UNIVERSITY OF LIVERPOOL

School of Engineering

PhD Thesis

Blown Powder Laser Cladding for Additive Manufacturing - Generation of Uniform Material Properties

Thesis submitted in accordance with the requirements of

University of Liverpool for the degree of Doctor of Philosophy

By

Jing Liu

Jul 2020

School of Engineering

The University of Liverpool

Brownlow Hill

Liverpool, UK

L69 3GH

Email: n00u0064@Liv.ac.uk

Declaration

I hereby certify that this dissertation constitutes my own product, that where the language of others is set forth, quotation marks so indicate, and that appropriate credit is given where I have used the language, ideas, expressions or writings of another.

I declare that the dissertation describes original work that has not previously been presented for the award of any other degree of any institution.

Signed: Jing Liu

Date: 25/07/2020

Abstract

Additive manufacturing (AM) is attracting significant interest in industry and research. Blown powder laser cladding (BPLC) for additive manufacture is a technique for manufacture of fully dense 3D components in a rapid process. This can be applied for the creation of novel quasi-hollow structures. The aim of the work presented in this thesis is to investigate the production of AM parts by BPLC with uniform material properties and the possibility of producing parts at low average power using stainless steel 316L and super alloy Inconel625.

This work was performed using a CO_2 laser system and has examined the process characteristics, the microstructure and mechanical performance of the clad layers. Process characteristics studies were carried out by visual observation of the cladding process within a set of process windows including laser power, cladding speed, powder feed rate, gas flow rate and step height.

Two test structures were designed with different build methods, using two types of materials: stainless steel 316L and super alloy In625. Both these designs consist of two intersecting circles. The first was produced with a linear build method, with the laser indexing upwards by the step height after each layer is produced. The second was produced in a helical manner, with the laser constantly indexing upwards. To examine the quality of cladding results, specific dog bone geometry components were manufactured by two different cladding track directions against tensile force direction.

The optical microscopy work yielded microstructures which were primarily equiaxed cellular but suffered from microstructural variations. Areas of epitaxial growth were found with some dendritic structures also noted. A key result was to determine the influence of power on the microstructures; low power can help with a better distribution of homogenous microstructures through specific processing parameters. For this work it was found that the power could be reduced to 320W.

Using an analytical method an increase in cladding speed was specified for the optimised microstructure to be produced at both the intersection and non-intersection points. Overall, the production of an optimised microstructure to achieve uniform material properties for blown powder laser cladding AM for both 316L stainless steel and IN625 was largely successful with further optimisation possible.

Keywords: Blown power laser cladding, Additive manufacturing, low power, uniform material

List of Publication to Date by Author

Blown powder laser cladding for isotropic material properties (Conference Paper)

Liu, J., Fearon, E., Dearden, G., & Edwardson, S. (2017). Blown powder laser cladding for isotropic material properties. In Proceedings of the 5th UK Industrial Laser Symposium Vol. Additive Manufacturing 4 (pp. AM2-03). Grantham, UK.

Low power blown powder laser cladding for uniform equiaxed micro-structures (Conference Paper)

Liu, J., Dearden, G., & Edwardson, S. (2017). Low power blown powder laser cladding for uniform equiaxed micro-structures. In Proceedings of 39th MATADOR Conference Vol. Session LCM, Laser Cladding and Melting (pp. Paper #046). University of Manchester, Manchester, UK.

Blown Powder Laser Cladding with Novel Processing Parameters for Isotropic Material Properties (Peer-Reviewed, Conference Paper)

Liu, J., Fearon, E., Dearden, G., & Edwardson, S. (2017).28th Annual International Solid Freeform Fabrication Symposium--An Additive Manufacturing Conference −2017, Austin, Texas, USA

Acknowledgement

I would like to extend thanks to the many people, who so generously contributed to the work presented in this thesis.

Special mention goes to my enthusiastic supervisors, Dr Stuart Edwardson and Prof Geoff Dearden. My PhD has been an amazing experience and I thank them wholeheartedly, not only for their tremendous academic support, but also for giving me so many wonderful opportunities for laboratories work.

Similar, profound gratitude goes to Mr Andy Snaylam, who has been a truly dedicated technician. I am particularly indebted to Andy for his constant faith in my lab work especially in samples sectioning. And I'd like to thank Mr Dave Atkinson who always helped me to prepare the acid solutions for etching samples and offer me great metallic knowledge.

I am also hugely appreciative to Dr Eamonn Fearon, especially for sharing his nozzle design and cladding expertise so willingly, and for being so dedicated to his role as research fellow at the first year of my PhD and valuable suggestions later.

Special mention goes to Mrs Teresa Qiao and Miss Suyi Fan, for unconditional help and support during my PhD period as my best friends. I am also very appreciated another friend, Dr Yan Zhou for her kind guidance on my thesis writeup and prof-reading. And, I am very appreciated for the help from Laser Group members, Qianliang Li, Dunia Lopez Espiricueta, David Rico Sierra and Yue Tang. I would like thank Zhengning Zhang as well to help me on 3D simulation and modelling.

Finally, but by no means least, thanks go to mum, dad and other family members for almost unbelievable support. They are the most important people in my world and I dedicate this thesis to them.

Contents

List of Figures

List of Tables

List of Symbols

C_p	Specific Heat	J/kgK
E	Engergy Density	J/m^3
G	Temperature Gradient	K/m
h	Step height	mm
L_m	Latent Heat	J/kg
m	Mass of the powder	g
P_{laser}	Laser Power	W
R	Solidification Speed	mm/s
S	Clad Shape Factor	
T_m	Melt Temperature	K
t	Time taken for a cladding track	min
V	Volume	mm^3
q_{cond}	Energy Conducted Through Material	W
v	Cladding speed	mm/s
w	Clad Width	mm
z_m	Melt Pool Depth	mm
η_P	Powder Catchment Efficiency	
η_w	Efficiency of Laser	
ρ	Density	Kg/m^3
ϕ_m	Powder Flow Rate	g/min

List of Abbreviations

AM	Additive Manufacturing
BPLC	Blown Powder Laser Cladding
BCC	Body Centred Cubic
C	Carbon
Cr	Chromium
DED	Directed Energy Deposition
DLF	Directed Light Fabrication
DMD	Direct Metal Deposition
DMLS	Direct Metal Laser Sintering
EBM	Electron Beam Melting
FCC	Face Centred Cubic
FGMs	Functionally Graded Materials
IN625	Inconel 625
LBM	Laser Beam Melting
LC	Laser Cladding
LFFF	Laser Free Form Fabrication
LMD	Laser Metal Depostion
LPBF	Laser Powder Bed Fusion
Mn	Manganese
Mo	Molybdenum
Ni	Nickel
Nb	Niobium
PBF	Powder Bed Fusion
SFF	Solid Freeform Fabrication
SLM	Selective Laser Melting
SLS	Selective Laser Sintering
Si	Silicon
WLAM	Wire-Laser Additive Manufacturing
316L SS	Stainless Steel 316L

Chapter 1 Introduction

Blown powder laser cladding is an emerging laser aided additive manufacturing technology, which combines direct metal deposition into a solid freeform fabrication process that can be used to manufacture near net shape components from their CAD files. This technology has been successfully used to fabricate a series of samples of metal materials for various applications such as in aerospace for aero engines and aero blade and in biomedical industry for personal health.

In this chapter, the history and development of additive manufacturing and blown powder laser cladding will be introduced followed by producing two types of material groups stainless steel 316L and Inconel 625 that will be used for this work. In the end, the state of art and the challenges will be summarized. Hence the motivation for this work is established. To achieve the aim, several objectives are delivered.

1.1 Background

Additive manufacturing (AM) is recently receiving unprecedented attention from the mainstream media, the investment community and national governments around the world. This technology is often referred as 3D printing as well. AM can be used in many industries for example, aerospace for lightweight design and biomedical for personalised healthy products [1].

The clue to the basics of additive manufacturing technology, rather than producing a component by taking material away, it adds to it instead [2]. Traditional manufacturing methods involve a material being carved or shaped into the desired product by parts of it being removed in a variety of ways. Additive manufacturing is the pole opposite, structures are made by the addition of many layers which can be combined to create a product [3]. AM technologies have been developed for many different materials including metals, polymers and ceramics [4-6].

Potential benefits of AM can provide a great reduction in overall product development and manufacturing time leading to quicker transfer to market. As it is typically a CAD driven process, changes can be made quickly with an associated potential saving in time and cost overall (Table 1-1).

Table 1-1: Potential time saving of AM techniques against conventional manufacturing techniques [7].

Industry	Conventional Techniques	Time Savings
Industrial Design	Clay models	96%
Education	Outsourced machining	87%
Aerospace	2D laser cutting and welding	75%
Automotive	Aluminium tooling	67%
Aerospace	Injection moulding and CNC tooling	43%

Conventional manufacturing techniques can produce a great range of shapes and designs, but additive manufacturing takes production to the next level. One of the greatest benefits of this more advanced technology is that more flexible and lightweight component or with hollow and lattice structures can be produced [8, 9]. In addition, parts from micro to macro can be produced. Designs that cannot be manufactured in one entire piece with traditional means can easily be achieved [1, 10]. For example, shapes with a scooped out or hollow structure can be produced as a single piece, without the need to weld or attach individual components together therefore no additional tooling or manufacturing cost [11]. This has the advantage of being stronger, no weak spots which can be compromised or stressed. In the past, the limitations of production have all too often influenced design, ruling out ideas because

they were not practically achievable [12, 13]. The introduction of AM technology and its development means the process has been spun on its head, with design now driving the production.

Due to these advantages, AM techniques are widely used by car manufacturers for precision and the ability to facilitate the creation of complex components [14]. AM has helped the Bentley design team to produce small-scale models as well as full-size parts easily, for assessment prior to production on the assembly line [15]. The weight reduction of AM products is attractive for the aerospace industry as well. Equally critical is the reduction of storage space and material resources, which means a reduction in maintenance cost. Boeing has already made use of laser-sintering based AM for cooling ducts on the F18 around 10 years ago [16]. As a summary, the most significant feature of AM implementation within aeronautical industry is the advantage of weight reduction. Equally critical is the reduction in storage space for stock and material resources. On the other side, it helps to reduce the maintenance cost.

Recent advances in this technology have seen its use become far more widespread and it offers exciting possibilities for future development. There are numerous laser-based AM technologies and techniques that have been developed in recent years including laser and non-laser based methods. Laser cladding is the focus of this research. The Laser Cladding (LC) process can be known by many different names such as Laser Free Form Fabrication (LFFF), Direct Metal Deposition (DMD) or Directed Light Fabrication (DLF) [17, 18] which all essentially refer to the same process with the possible addition of atmospheric chambers or closed loop control systems. In the laser based AM process material is typically added to a substrate via a laser generated melt pool. Most laser cladding techniques involve overlaying of one metal onto another to achieve a surface layer with desirable dimensions and mechanical properties. The laser acts as a concentrated heat source to create a melt pool which allows the added material to be fused to the substrate. Material can be added in the form of pre-placed powder, blown powder or a wire feed [17, 19] which introduces two main families of additive manufacturing technologies for production parts, powder bed fusion (PBF) and direct energy deposition (DED) [20, 21]. Blown powder laser cladding (BPLC) is the most popular technique of DED, which is the subject of this research. In this process, metal powder is blown either coaxially or via a side feed into a laser generated melt pool, adding to its volume to form a fusion-bonded raised bead when cooled [22]. This can then be built up layer by layer in a net shape process (Figure 1-1). This offers all the advantages of AM such as increased design freedom, light weight structures, new functionality and short production cycle times [23]. In addition to powder bed technologies, BPLC also offers the addition of functionalities on existing parts with either the same or a different material,

compositional variation, repair of high value parts and no dimensional limits apart from machine size [24, 25].

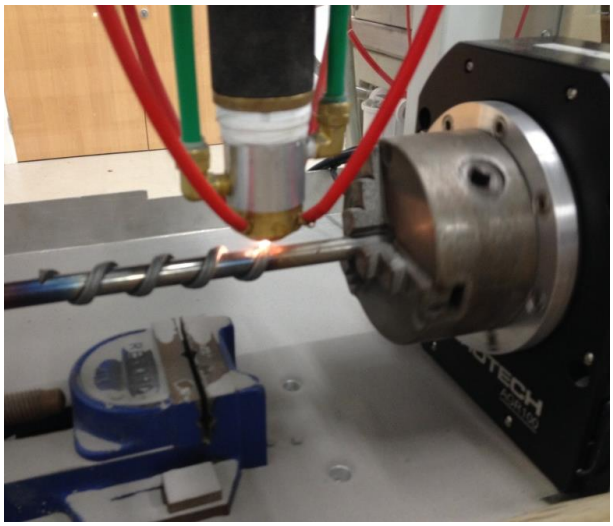

Figure 1-1: Apparatus of Laser Cladding at Liverpool with customised 4-port directional nozzles.

The application of BPLC also brings several advantages over conventional fabrication in aerofoil manufacturing with lower weight but high strength to weight ratio [26]. This helps with shortening processing periods by around 80% as well as 20-50% reduction in cost [27]. This technique can be also used in the aerospace and automotive industries to create wear and corrosion protective in addition to repairing wear damaged turbine parts or as a rapid prototyping process [28]. Compared with conventional processing, laser cladding can provide high wear and corrosion resistance in terms of coatings that can be applied in the aero engine manufacture by Rolls-Royce and General Electric [29, 30].

The various process parameters for BPLC can have a large effect on the microstructure and mechanical properties of the part produced. These include but are not limited to: laser spot size, laser power, powder feed rate, cladding speed, step height and layer distance from the substrate [31-33]. The microstructures created in the BPLC process tend to suffer from microstructural variations throughout a build. This has an adverse effect of the mechanical properties of the part causing variations in areas of a build. Control over process parameters can minimise these microstructural variations and can therefore improve the mechanical properties. The minimisation of microstructural variations in parts produced using BPLC for additive manufacture, and the effect of this on the mechanical properties, is the main subject of this research.

1.2 Challenges and Limitations

1.2.1 Challenges

Despite the promise of AM, there are still a number of impediments to its widespread utilisation, particularly in industries that produce low production volume and high value components like aerospace. Quality control and mechanical characterisation remains a major challenge [34-36]. The quality and mechanical properties of the manufactured parts are influenced by the generation and existence of microstructural features and potential defects [37, 38]. The inhomogeneities of the microstructure and material properties could lead to failure of the component [39-41]. These can be initially dominated and affected by the variations in process parameters and powder attributes. Laser power, nozzle cladding speed, cladding strategies, step height, powder feed rate, powder size distribution and powder types are among main parameters that influencing the quality of a part.

From available heat source, high power lasers are extensively used in AM, especially for metals, to form fusible liquid metals. Typically these range from around 1kW to as high as 5kW in power [42-44], which has a cost implication. A greater energy input may also lead to a greater risk of surface vaporization and poorer surface quality, however higher power is equally likely to facilitate increased mass deposition rates and thicker layer height. As current manufacturing research is concerned with the environmental impact of a process, reduction of the energy usage and material consumption is of increasing interest. A potential driver for AM future development is the generation of less pollution and landfill usage. Currently the amount of energy consumed when producing the same part by AM can still be greater than conventionally produced part, often due to longer process times. If increasing energy is applied, higher energy consumption is therefore required. Taking all these challenges into consideration, exploring a lower power option for AM would be of interest. Consequently, if the process can be performed at lower average power and hence lower cost but to the same quality, this could be potentially significant for the technology acceptance in industry. Producing similar components or even better components at lower average laser power with uniform mechanical characteristics and quality is a significant challenge for this research.

1.3 Aim and Objectives

The aim is to investigate the production of AM parts by BPLC with uniform material properties at lower average power.

To achieve this, the specific objectives include:

i) Investigate the effect of laser power, step height, cladding speed powder mass flow, gas flow rate and part geometry on the BPLC process for 316L Stainless Steel in terms of metallurgy and mechanical properties for material anisotropy.

ii) Develop and optimise processing parameters and part geometries based on acquired data to promote the generation of predominantly equiaxed grain structures and hence potentially uniform material properties in 316L Stainless Steel AM parts; confirming effects through metallurgical analysis and mechanical testing.

iii) Investigate processing parameters for the production of 316L SS parts at lower average power (sub 600W).

iv) Based on the findings above, investigate the generation of equiaxed grain structures and hence potential uniform material properties in other relevant engineering metals.

1.4 Thesis Structure

This thesis is focused on how to develop lower power processing conditions for blown powder laser cladding and to potentially achieve uniform material properties of AM parts.

Chapter 1 deliveries the background and context for the work and chapter 2 provides a literature review of AM technologies and current challenges and in particular blown powder laser cladding.

Chapter 3 provides a briefing of the laser types, CNC platform, nozzle designed, and powder feeder used in this research. In addition, the CADCAM software for 3D part production is explained.

Chapter 4 and 5 introduces the two types of metal materials selected SS 316L and IN 625; with detailed investigation of processing parameters on cladding results. Mechanical tests are performed to qualify the clad components. COMSOL has been used to offer a simulation on cladding performance in terms of thermal cycles and cladding height effect on the substrate.

Chapter 6 draws the main conclusions from the work and possible future research directions.

Chapter 2
Literature Review on Powder-based Additive Manufacturing Process

From a review of literature, it is possible to present a comprehensive background to the theory of laser cladding for additive manufacture and processing of austenitic stainless steel and super alloy Inconel 625. Following this numerous research papers have been reviewed regarding the effect of process parameters as this is the focus of this research. Variations in process parameters and powder attributes influence not only the microstructural features present in AM components (e.g., grain size, texture, solute distribution), but may lead to the generation of defects. Laser power, scan speed, step height, spacing of scan lines, powder feed rate, powder size and distribution, and surface chemistries are among the many parameters that influence the quality of the deposited material [45]. Many studies have been conducted which seek to understand and quantify the effects of these parameters on the final microstructural characteristics, e.g., Rombouts *et al*.[46] and Lévesque *et al.*[47]. However, as the combined influence of all related parameters is not completely understood, robust process models still need to be developed ([46, 48, 49]) and other critical experiments are required.

2.1 Introduction to Additive Manufacturing (AM)

Laser cladding is a process of adding material to a substrate in which a strong fusion bond is created, and dilution is minimal. This material can be added in a blown powder format. Alteration of this process to produce parts in an additive process is possible, known in this research as laser cladding for additive manufacture. This technique can be used as a rapid prototyping process to create fully functional prototypes, a method of direct fabrication and a method of repair [50].

Cladding operations involve overlaying one metal with another to form a surface layer with a strong surface bond. This allows surface layers to be created with good wear, corrosion, oxidisation or erosion properties onto a substrate which, for various reasons including cost and mechanical, may not have these properties. The process can also be used in the repair and refurbishment of high value components. In the process the cladding material is fused to the substrate via a heat source to create a surface bond. The aim of the cladding operation is to create this surface layer without dilution of the cladding material into the substrate. Thick clad layers (>0.25mm) are often produced by welding methods. Significant melting of the substrate occurs, using welding methods, and with this dilution [51]. This dilution requires thick sections to be laid down to achieve the required clad properties. Laser cladding can be used to create thin clad layers with low dilution [52].

Significant research has taken place on the in the field of laser cladding over the past 15 years with a variety of potential applications arising such as the additive manufacture application used in this research. Despite this industry has been reluctant to adopt this technology due to the high investment costs of the laser cladding system and high running costs. Significant progress has been made in laser cladding over recent years, particularly in the repair of components and rapid prototyping technology. Laser technology is now available for the precise fabrication of functional and protective coatings on components with complex shapes and forms as well as the production of complex shapes and forms in an additive manufacturing process [53].

Rapid prototyping is being increasingly used within industry to give a representation of a design before it goes into manufacture. A rapid prototyped part can be produced before a design is finalised and before any necessary tooling etc. has been purchased. Typically, these prototype parts are non-functional and a functional prototype will have to be produced later in the design process [54]. Laser cladding can be used as an additive manufacture process to create fully dense 3-dimensional parts [55]. This is a fairly recent development which can be adopted in industry to create functional prototype parts. This would allow new design concept parts, which previously may have required

specialist tooling or moulds to be purchased, to be produced at a low expense within a rapid timescale. Rapid prototyping technology has been growing in popularity in industry as a method of producing non-functional parts. The use of rapid prototyping can significantly reduce the time to market new products whilst also allowing a designer to realize their designs and provide reasonable patterns for processes such as castings [56]. Typically, these rapid prototypes are produced from low strength polymers. The use of laser based direct fabrication technology, which has been recently developed, allows parts to be produced with properties close to the desired properties of the final cast or wrought product [57]. The ability to create functional prototypes has the potential to significantly reduce the costs and timescales in a product development cycle.

The alloy addition can be before laser processing in the preplaced powder method or during processing by either the blown powder method or wire feed. If the preplaced powder method is adopted the melt front moves rapidly through the powder layer until it reaches the interface with the substrate in which a small amount of the substrate is melted causing the fusion bond. If blown powder or wire feed is used a melt pool is generated on the substrate by the laser and the cladding material added. In both cases the substrate acts as a heat sink causing rapid solidification [58]. Figure 2-1 shows the preplaced powder and blown powder method. Other relevant laser-based AM techniques are summarised in the following sections.

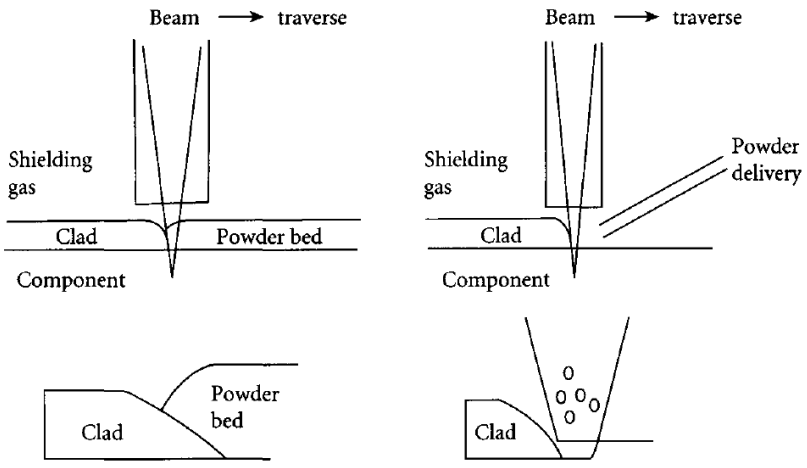

Figure 2-1: Preplaced powder (left) and blown powder (right) laser cladding [58].

2.1.1 Powder Bed Fusion (PBF)

Selective Laser Sintering (SLS), Direct Metal Laser Sintering (DMLS) and Selective Laser Melting (SLM), now called powder bed fusion (PBF) [59], are three of the most common techniques.

In the PBF process, a laser or an electron beam is used to melt the powder to form a fused bond on the platform. Normally, a layer with typical payer height of 0.1mm is spread over the working platform [60]. A new layer is fused on top of the previous track using a roller continuously until the entire model is created [61]. Figure 2-2 shows the powder bed fusion process.

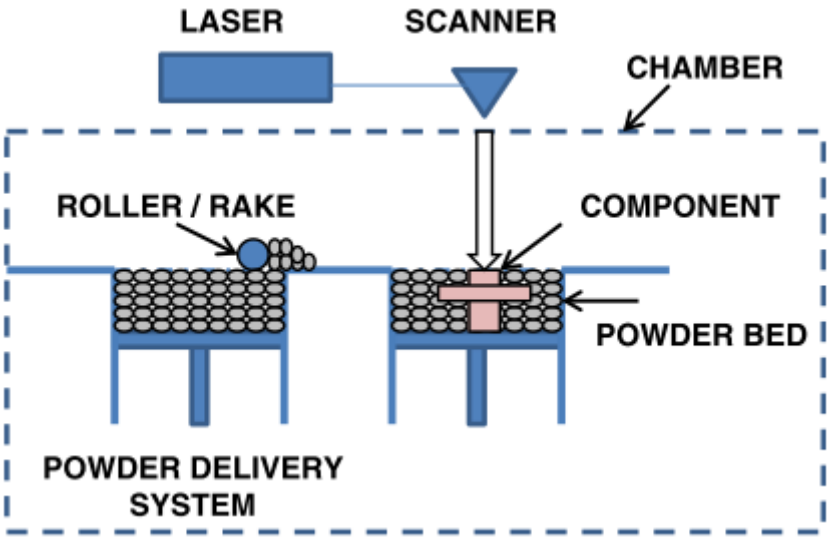

Figure 2-2: Powder bed fusion example setup [62].

SLS (selective laser sintering) and DMLS (direct metal laser sintering) are essentially the same process; both involve sintering rather than full melting. The only difference between the two is that SLS is normally used to describe the process when used for other materials. SLS is used in conjunction with materials such as plastics, nylons and ceramics whereas DMLS is used exclusively with metal and metal alloys. SLS is used to describe the sintering process in conjunction with materials such as plastics, nylons and ceramics, whereas DMLS used for metal [63]. SLM (selective laser melting) is straightforward and used only when the powder is being melted rather than sintered. Although considered by many to be a subcategory of SLS, with SLM the metal part is fully melted into a new 3D solid part. LPBF (laser power bed fusion) is slightly different because it involves a full melt with the metal heated and then cooled to fully consolidate. Although very similar, this full melting process means that the results should not be porous, unlike with DMLS [64].

In Bartolomeu's work, a comprehensive study on the influence of three different processing technologies (Selective Laser Melting, Hot Pressing and conventional casting) on the microstructure, mechanical and wear behaviour of an austenitic 316L Stainless Steel. The high wear and mechanical performance of 316L Stainless Steel fabricated by Selective Laser Melting are mainly due to the finer microstructure, induced by the process. In this sense, Selective Laser Melting seems a promising method to fabricate customized 316L SS implants with improved mechanical and wear performance [65].

Any powder based materials can be used in LPBF process, typically metals such as stainless steel, Titanium and Aluminium, and polymers such as Nylon, which means large range of material options can be chosen from [66]. The cost is relatively inexpensive and suitable for visual models and prototypes. This powder bed techniques are good for part building especially small scale and integrating into office sized machine but not for part repair [67]. In addition, high power and relatively slow speed are used which indicated high cost and low efficiency for industry. Due to the size limitation, there is lack of structural properties in materials [12].

2.1.2 Wire-Laser Additive Manufacturing (WLAM)

Wire-laser additive manufacturing (WLAM) is a technology in which 3D components are built by continuously feeding a wire into a melt pool generated by a laser beam [68] (Figure 2-3). This process enables costs and time saving in comparison with traditional methods, which include either precision castings or machining from oversized forgings, through substantially reduced material waste and lead times [69]. Fully dense components can be produced at high deposition rate [70]. The high-power density and flexibility of lasers enables sufficient control to build medium to small features with near-net shape characteristics, thus enabling further cost savings as well as increased design freedom [71, 72].

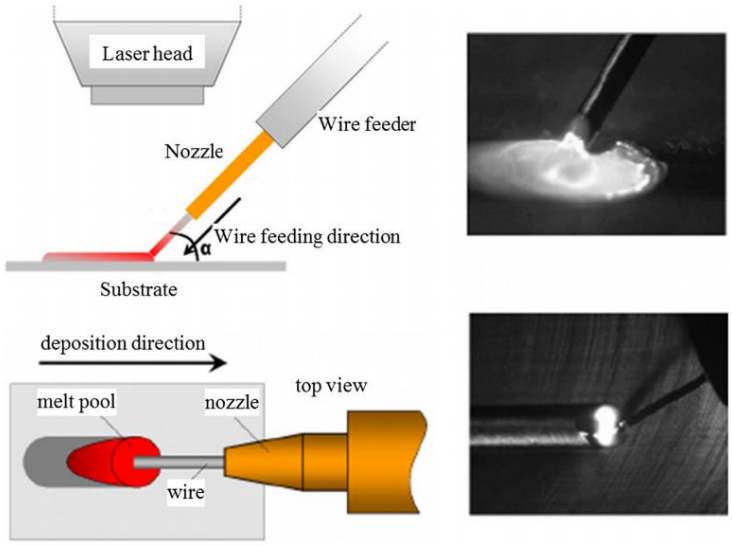

Figure 2-3: (a) Schematic drawing of the laser wire-feed process. (b) Top and Side View images of the real process[68].

The influences of process conditions, such as energy input, wire-feed rate, welding speed, deposition pattern and deposition sequences, etc., on thermal history and resultant residual stresses of AM processed components needs to be further understood [73, 74]. In addition, poor accuracy and surface finish of the process with 'stair stepping' effect limit the applications of wire-feed AM technology [75-78].

2.1.3 Blown Powder Laser Cladding (BPLC)

The blown powder method for laser cladding is generally assessed as the better option compared with wired feed and preplaced powder techniques [79]. With the preplaced method a certain power is initially required to melt through the preplaced powder [80]. Also, when the melt pool reaches the substrate interface thermal conduction increases resulting in freezing of the molten powder [81, 82]. This leaves only a weak interfacial bond and remelting must occur to create a strong fusion bond. The main advantage with blown powder laser cladding lies in the melting sequence [83]. Melting occurs at the substrate interface and powder is trapped in the melt pool [84, 85]. The energy must be high enough to melt the powder without too much of the substrate being melted [86]. Clad dilution (shown in Figure 2-4 is kept at a minimum due to the well-defined heated region [87].

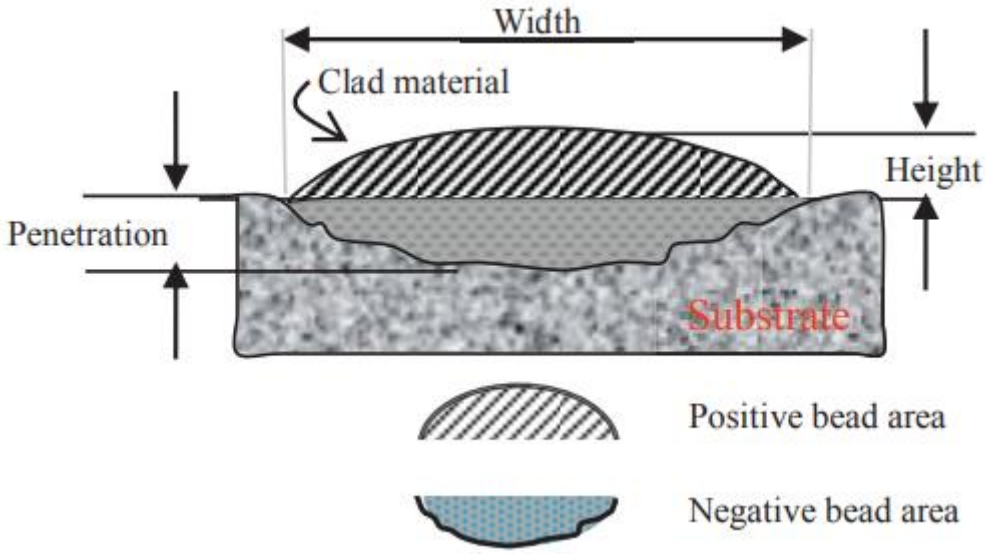

Figure 2-4: Cross section view of a single bead notation[87].

In the process of blown powder laser cladding, powder is fed via a powder feeder system and blown into a laser generated melt pool on a stream of inert gas through a nozzle of various designs and types [88, 89]. Primarily there are two types of powder feed nozzle the side feed nozzle, and the coaxial nozzle [90, 91] as shown in Figure 2-5. The coaxial powder feed nozzle can clad in multiple directions however the nozzle can be prone to blockage [84, 92, 93]. The single side feed nozzle has the disadvantage of only being able to clad in a single direction, however blocking of the powder feed nozzle is not possible and the powder stream can be shaped by a gas stream flowing coaxially to the laser [94, 95]. Coaxial powder streams are also shaped by the gas stream. Both within the annular powder outlet and outside the powder outlet.

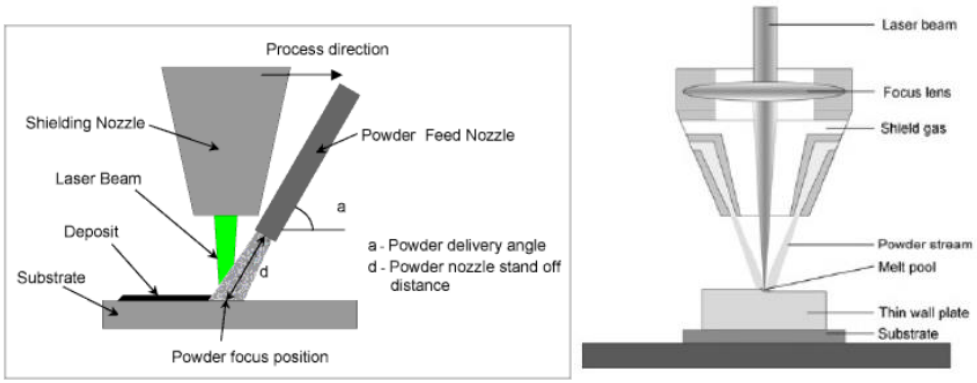

Figure 2-5: Nozzle Arrangements: Side Feed (left and coaxial nozzle (right).

The advantages of a side feed nozzle can be combined with multi directionality using a multiple side feed system such as the system developed by Fearon as shown in Figure 2-6[96].

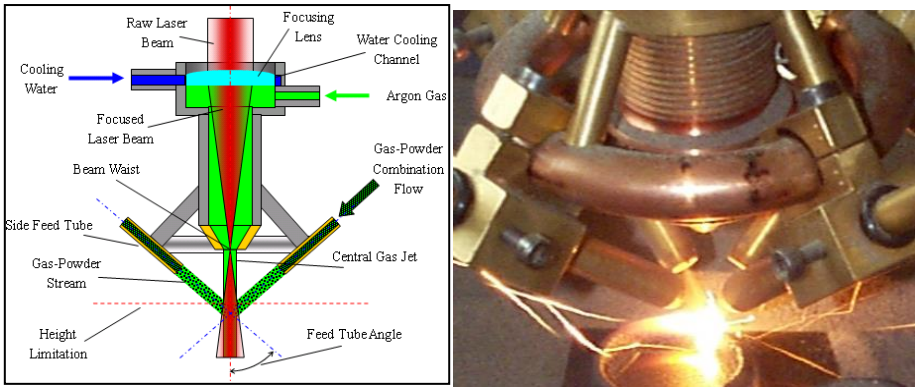

Figure 2-6:Omnidirectional laser cladding nozzle [96].

2.1.4 Optomec Lens Nozzle

In the early days of Optomec, Lens processing typically included laser powers of around 300 to 500W. Nowadays with technical advancements in lasers and processing capabilities, coupled with industry's desire to process larger and larger parts at faster rates, Optomec LENS systems have increased available laser power ranges in their systems from 500 W to 1 kW, 2 kW, and now even 3 kW systems, making higher-powered laser capability available to all users.

Faster speeds and improved deposition rates are the key criteria for AM applications to maximize production without sacrificing the quality of the build part. To operate current laser power range, it is significant to be able to control power density. Consequently, the ability to vary the focused laser spot size in order to control power density during processing becomes a critical factor.

With increasing laser powers introduced into its systems, Optomec faced the challenge of how to keep a consistent power density and thus a stable conductive process over a wide range of laser powers. Since power density is defined as power applied over a given area (in this case laser power delivered through a laser spot size area focused at the substrate), the solution would be to increase the laser spot size.

There are three key factors determining the focused laser spot size which are the laser cable diameter, the collimator lens focal length and the focus lens focal length. If a customized design requires an identify the power range of their application, then a suitable fiber cable size, collimator, and focusing lens could be chosen for optimal processing at that given laser power based on the requirement.

2.1.5 Blown Powder Laser Cladding for Additive Manufacturing (AM)

Laser cladding for additive manufacture was derived from the base laser cladding process. The laser group at Liverpool began research into the build-up of clad layers in 1992 [97] whilst at around the same time Mazumder and co-workers at the University of Illinois started investigating the layer by layer deposition of aluminium alloys and tool steels [98]. Instead of a surface layer being added to a substrate, a fully dense 3-dimensional part is produced by the repeated deposition of material on the previously deposited layer. In the build-up of a part motion paths are developed in CNC tool-path format from a CAD model. The motion path provides the control logic for the motion controller (CNC table), powder feeder and laser. A layer of material is laid down in the required shape, the laser then indexes away from the part by the step height, controlled by the motion controller, to form the next layer. Laser power, powder feed rate and cladding speed are controlled to produce a fully dense 3-dimensional part [99].

Along with use in rapid manufacture, laser cladding for additive manufacture is a manufacturing option for low volume parts [12]. The process can potentially be used to produce large scale metal parts in the aerospace industry such as pylon ribs or spars of wing components for aircraft [100, 101]. The use of laser cladding for additive manufacture has the potential to lighten the aircraft whist significantly reducing the processing time by about 80%, and the cost by around 20-50% [27]. Additive manufacture has also been proposed as a means for fabricating spares on an as-needed basis [102, 103]. For example, an aircraft carrier could carry an AM system to fabricate spares for the aircraft at sea. The process could also be applied on space missions for producing critical spares [104].

2.2 Process Parameters

2.2.1 Heat Source Characteristics

Two types of laser are widely used in laser materials processing, gas based and solid-state lasers. An example of a gas based laser is Carbon Dioxide (CO_2) laser which is used for this work and solid-state lasers such as the fiber laser and Nd:YAG. CO_2 lasers use a mixture of CO_2, Nitrogen and Helium as an oscillating medium [105, 106]. The exact mixture depends on the laser in question i.e. laser design, operating pressure and operating mode (CW or pulsed) [107]. The volumetric concentrations of each gas vary in the range 2-5% CO_2, 10-60% N_2 and 40-90% He [108, 109]. CO_2 lasers offer the highest power available for materials processing with capabilities of up to 50kW average power however most industrial systems are below 15kW with the majority under 3kW [31, 79]. The typical output wavelength is 10.6µm and the beam can be focused down to about 0.3mm diameter depending upon mode structure.

Nd:YAG lasers have a lasting medium based around in Nd3+ ions. Neodymium is doped into Yttrium Aluminium Garnet crystals to create the oscillating medium. The Nd:YAG takes the form of a cylindrical rod. Most single rod designs are 600W or lower, to achieve higher powers multiple rods tend to be used. In comparison to the CO_2 laser it is more difficult to achieve the higher power ratings with a Nd:YAG laser. The typical output of the Nd:YAG laser is 1.064µm which is generally absorbed better than the higher wavelength CO_2 laser [110].

High-power fibre lasers are widely used in cladding application because of their high robustness, high reliability and especially high efficiency, all of which contribute to markedly lower operation costs. Arias *et al.* found that fibre laser offers a greater wall-plug efficiency than CO_2 lasers that can be delivered using optical fibre [111]. Fibre laser can also prove a necessary near-infrared (NIR) wavelength. However, it reduces much cost of operation and provides much longer service intervals compared to other laser types, such as flash lamp-pumped Nd:YAG [112].

In general, the different types of laser are widely used in specific applications. The selection of the laser has an important influence on the consolidation of powers due to the laser abusability of materials significantly depends on the laser wavelength. Moreover, the input laser energy density has a significant effect on metallurgical mechanism of cladding components [55].

2.2.2 Beam Mode Structures

The laser is a resonant cavity containing an active medium which, due to the presence of a pump creating a population inversion, radiates light [113]. Within this resonator the electromagnetic waves

have well defined modes transverse to the cavity axis. These modes, which depend upon a multitude of factors including geometry of the cavity and the gain distribution of the active medium, are referred to as Transverse Electromagnetic Modes (TEM) modes [114]. Long thin cavities will produce 'low order' mode structures with one or two peaks in the transverse intensity of the beam. A typical CO2 laser used for laser cladding will have a TEM^{00} or a TEM^{01*} mode structure [115]. A Nd:YAG laser can have a similar mode structure to other lasers however due to the lower wavelength the Nd:YAG laser can be transmitted through optical fiber whereas the CO2 laser cannot. Transmission through optical fiber can create a 'top hat' beam mode structure [116, 117].

The different beam modes will affect the thermal distribution in a part and hence will also affect the melt pool shape during laser cladding. The effect of the beam mode on the isotherms generated in materials during laser processing is shown in Figure 2-7 for low order beam mode structures. These modes on the heating of materials can be estimated by performing burn prints on a suitable material such as Perspex or by calculating the isotherms and their interactions within the materials. Differences in beam mode structure will affect the cooling rates within the clad bead and hence the microstructure [118].

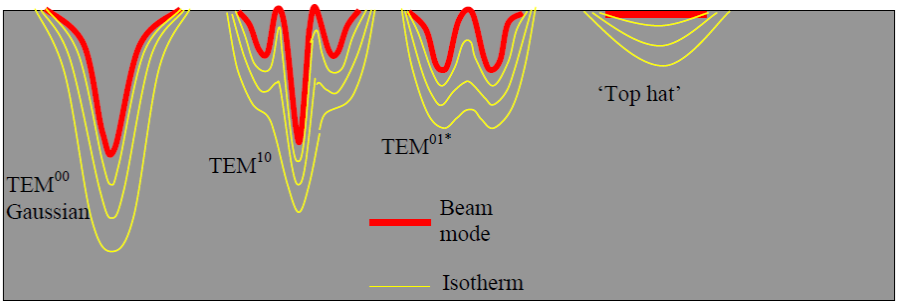

Figure 2-7: Material isotherms associated with low order beam mode structures [119].

In 2009, J.del Val et al. have taken a comparative study between Nd:YAG laser and fiber laser on laser cladding of Co-based super alloy coatings [120]. There are two different laser sources used in his research. Firstly, a Rofin-Sinar RSY500P type lamp-pumped Nd:YAG laser which can offer a maximum power of 500 W with a wavelength of 1064 nm, was used. It was guided by means of a 600 µm core diameter fiber and coupled to the working station via expanding and collimating optics. A high brightness monomode Ytterbium doped fiber laser (SPI SP-200) was used as a second laser source, which can provide a maximum power of 200 W and a wavelength of 1075 nm. Figure 2-8 shows an example of the analysis carried out for both lasers after the expanding and collimating optics. The measured value of the M^2 factor is M^2= 10 for the Nd:YAG laser and M^2= 1.8 for the fiber laser.

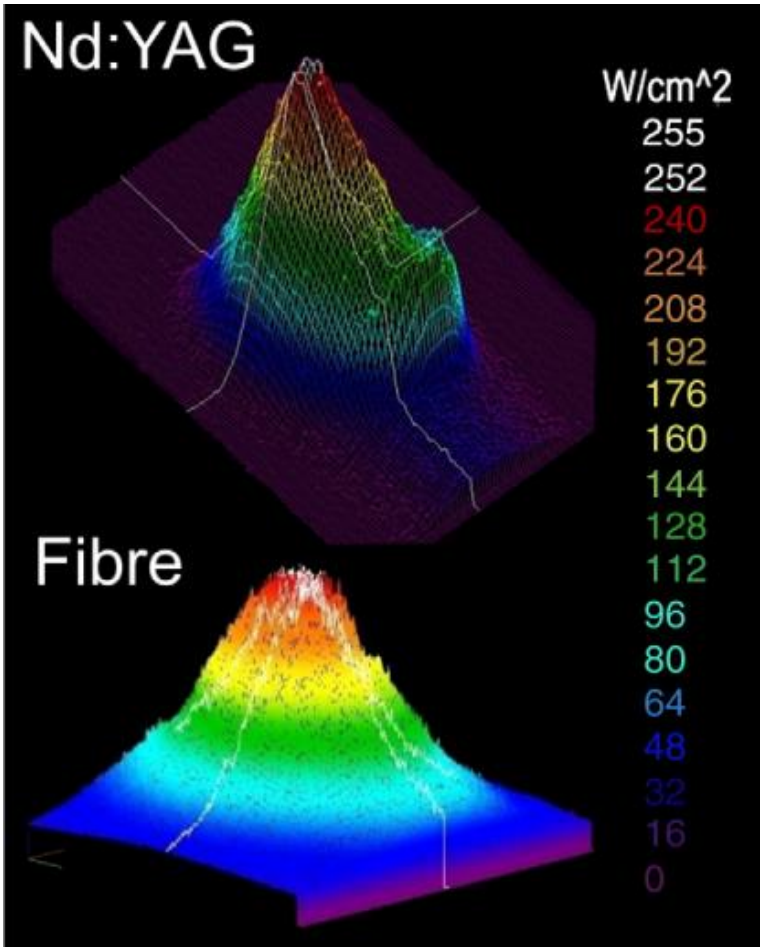

Figure 2-8: Three-dimensional profile of the laser beam for Nd:YAG and fiber lasers [120].

2.2.3 Laser Parameters

For the laser cladding operation, the laser is used as a concentrated heat source [115]. The intensity of the laser beam is key to its use in this application. A high-power laser beam can be focused to power densities of up to 10^6 - 10^7 W/cm^2 and can rapidly heat a metal surface layer up to 10^5K which then rapidly cools at a rate of up to 10^6 - 10^7K/s. The only intense beams comparable to the laser are such as ion and electron beams which also allow high energy deposition over a small area. The laser however can be focused down to a very small spot size creating a localised area of heat affected material. These unique properties create a situation where the laser is a very useful tool for cladding. Lasers for cladding can be used in either the Continuous Wave (CW) mode or can be pulsed [121]. For this research, only CW lasers will be considered due to available hardware.

2.2.4 Cladding Characteristics

Cladding speed (mm/s), spot size and the pattern of the cladding spot are all important parameters in the AM process. The energy density [122] can be defined as:

$$E = \frac{\mathrm{P}}{\mathrm{v}*\mathrm{d}} \qquad \text{Eq.2.1}$$

where P is the average laser power (rate of energy flow averaged over one full period), v is the scan speed, and d is the beam diameter. In practice, the equality in this equation should more correctly be a proportionality, given variations in the shape of the molten pool. It has been observed that there is a minimum energy density above which the properties of the material are acceptable [123]. Thus, energy density is directly proportional to the average laser power and inversely proportional to the cladding speed. Balancing these parameters generally leads to an operational window within which the systems can be operated to give desired part characteristics. The optimum scan speed may be correlated with the thermal gradient experienced by the material and desired production rate of the machine. The former can be related to microstructure, texture, compositional homogeneity [124] while the latter is limited by the capability of the positioning or control systems for beam placement while maintaining process parameters within the optimal operational window that results in desired and ideally optimised material properties.

While laser-based AM methods typically use a single beam, multi-beam laser-based AM techniques have been demonstrated and shown to provide higher precision and improved deposition rates. In multi-beam laser-based AM, it is necessary to consider new process variables that influence the quality of the deposited material, including the percentage of beam overlaps, relative spatial positions, power and frequency variations [125]. During AM deposition, for each layer, the heat source melts or sinters the powder in a predefined cladding pattern which generally consists of sequential cladding vectors (although parallel cladding vectors are possible in multi-beam laser-based AM and electron-beam based AM) [126]. Cladding vectors are co-optimised with cladding speed by considering uniform heat flow in the part [127]. The cladding patterns and related cladding vectors greatly influence the thermal history of the part [128-130]. Their optimisation is dependent upon the part geometry and multiple material thermochemical properties (e.g., thermal conductivity, heat capacity and surface tensions) [131]. In addition, some common cladding patterns used in AM include zig-zag, parallel and hexagonal patches [132].

2.3 Powder and Substrate Characteristics

2.3.1 Powder

Both pure metal and alloy powders have been used in AM processes. However, powders of metal alloys are more commonly used for high value parts. A critical assessment of the literature indicates that most of investigations have focused on titanium [37, 133] and aluminium [134-138] in pure powder

processing, while Ti, Ni and Fe-based materials are typical for alloy powders [139]. Ti-based alloys are used extensively in aerospace applications due to their high tensile strength and toughness, lightweight and the ability to withstand extreme temperatures [140, 141] and in medical applications [142-147] due to their biocompatibility. Ni-based alloys have superior creep, tensile strength, and corrosion resistance properties which make them ideal materials for jet engine and gas turbine components [148, 149]. Powder attributes, such as morphology, surface chemistry, size, internal porosity and any entrained defects or foreign materials have a significant influence on the quality of the as-deposited material, the transmission of prior defects, generation of new defects, and the attending mechanical properties [150, 151]. Thus, the characterisation of powder is critically important when seeking to measure and/or predict the presence of inhomogeneities in the final product [152, 153]. Regarding the measurable attributes of powder, the particle shape, average size and particle size distribution are important for packing and processing [154, 155] in powder bed fusion (PBF), while flowability is important for both direct energy deposition (DED) or blown powder laser cladding (BPLC) [62, 156].

2.3.2 Substrate

Due to large temperature gradients created between the molten pool and surroundings in powder based additive manufacturing, parts are usually made on a base plate or substrate which acts as both a mechanical support and a heat sink. The substrate and its thermal characteristics are therefore important to provide adequate cooling and support during the forming process. In general, there is a significant economic advantage if the substrate can also be incorporated into the final shape of the additively manufactured component. The incorporation of the substrate into the final component can reduce build time and cause the process to consume less energy. In contrast, for cases when the substrate is not included in the final structure, it must be removed at the end of fabrication process using some form of cutting or machining.

2.4 Material Properties

2.4.1 Absorptivity

Absorptivity is the ratio of the absorbed radiation to the incident radiation and is a function of both the material and the wavelength of the incident radiation. Based on current research, it can be concluded that the absorptivity of the materials in their powder form is significantly higher than their absorption in dense form [157]. This is due to multiple scattering of the laser beam in the powders [158, 159]. In addition, for powder bed AM, the physical depth where the intensity of the radiation falls to about 37% of the original radiation intensity is called the optical penetration depth and depends

on the absorptivity of the powders and packing density [22, 159, 160]. Although rarely possible, ideally the laser wavelength would be matched with the powder characteristics as energy density will change with both the powder absorptivity and frequency (wavelength=10.6µm) of the laser [161].

Moreover, the reflectance of the material (R) is a [principal parameter in determining the energy input to the surface with a relationship with absorptivity (A) shown in following equation Eq. 2.2:

$$A = 1 - R \qquad \text{Eq. 2.2}$$

As a result, the laser power P_L will be partly reflected and partly absorbed, according to the following:

$$P_L = P_{Reflected} + P_{Absorbed} = RP_L + AP_L \qquad \text{Eq. 2.3}$$

2.4.2 Surface tension/wettability

In both sintering and fusion-based AM processes, the liquid-solid surface tension impacts the resulting product. This tension is a temperature and composition dependent variable. The surface tension of the solid-liquid interface (γ_{sl}), solid-vapour interface (γ_v), and liquid-vapour interface (γ_l) influence wettability which can be measured by the contact angle (θ). As $\cos\theta \rightarrow 1$, the liquid completely wets the solid [162]. The Figure 2-9 illustrates the angles relations.

$$\cos\theta = \frac{\gamma_v - \gamma_{sl}}{\gamma_l} \qquad \text{Eq. 2.4}$$

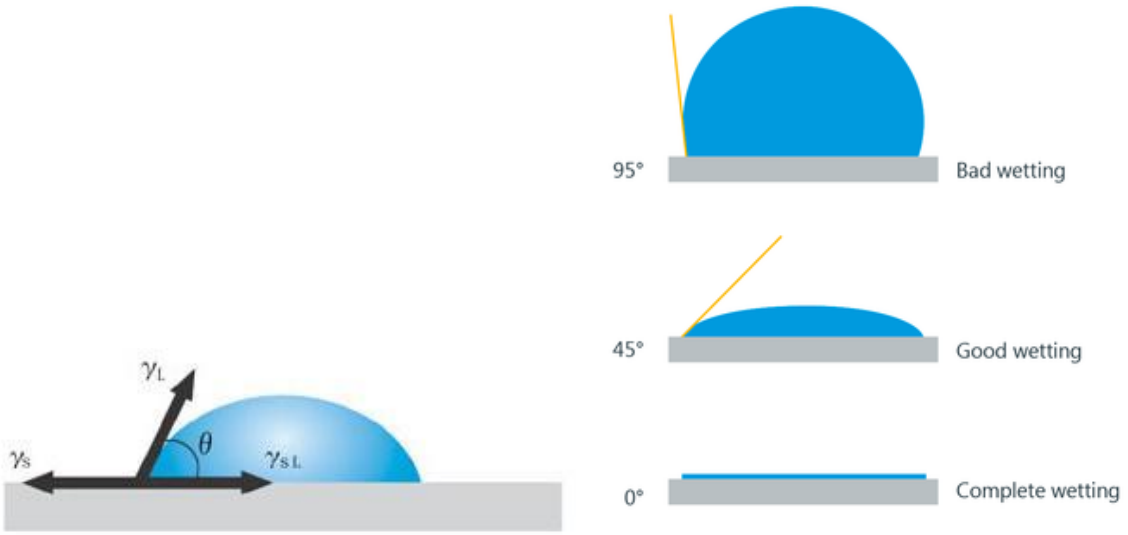

Figure 2-9: Illustration of contact angles formed by sessile liquid drops on a smooth homogeneous solid surface(left) and wetting conditions (right) [163].

2.4.3 Thermal Conductivity

The effective thermal conductivity of a packed powder can be estimated by [162]:

$$Kp \cong (1 - \omega)K \qquad \text{Eq. 2.5}$$

where ω is the packing density of the powder bed and K is the conductivity of the dense material. This effective thermal conductivity strongly depends on particle-to-particle contact. Based on experimental measurements, Fischer et al. (2003) found that a loose pack has thermal conductivity that can be more than one order of magnitude smaller than for fully dense materials [164]. Thermal conductivity for different metal powders was measured in several studies [165, 166]. More recently, other researchers have used simulation and found that conductivity for an AM material is almost decoupled from bulk properties [167]. It was found that the combination of the thermal characteristics of the material, substrate and environmental processing conditions affect the cooling and solidification rates that strongly influence the resulting part microstructure [168].

2.5 Processing Mechanisms

2.5.1 Powder Bed Fusion Mechanism

Powder bed fusion (PBF) systems normally include a heat source, an automatic powder layering mechanism, a computer control system and related sensors and accessories [169]. Such a system is shown in schematic form as Figure 1. An electron beam source requires a vacuum environment while laser sources typically utilise an inert gas environment or gas shielding to prevent excessive oxidation. Powder is spread over the previous layer in each step of production using a roller or a blade [170]. After each step of layering, the build platform lowers the part so the process can be repeated for subsequent layers. Typically, melting processes are faster than sintering, but require higher energy expenditure[171].

2.5.2 Direct Energy Deposition Mechanism

The concept of direct energy deposition (DED) is very similar to the other additive manufacturing methods [22]. However, the powder is supplied through feed nozzles into an inert gas shielded delivery system. The beam and powder nozzles are focused coincidently at the deposition plane. It is possible to incorporate up to 6 degrees of freedom for the position and motion of the deposition head, allowing for deposition to occur below a part in an unsupported geometrical sense. The incoming material is heated prior to deposition as it passes through the beam, and may be melted either during this pass through the beam or by thermal conduction once the powder is in the molten pool through the nozzles into the path of a laser or electron beam. Figure 2-10 shows a schematic of a DED process and representative configuration of the nozzles relative to the beam. DED may be used to repair high value components where the existing high value components act as the substrate.

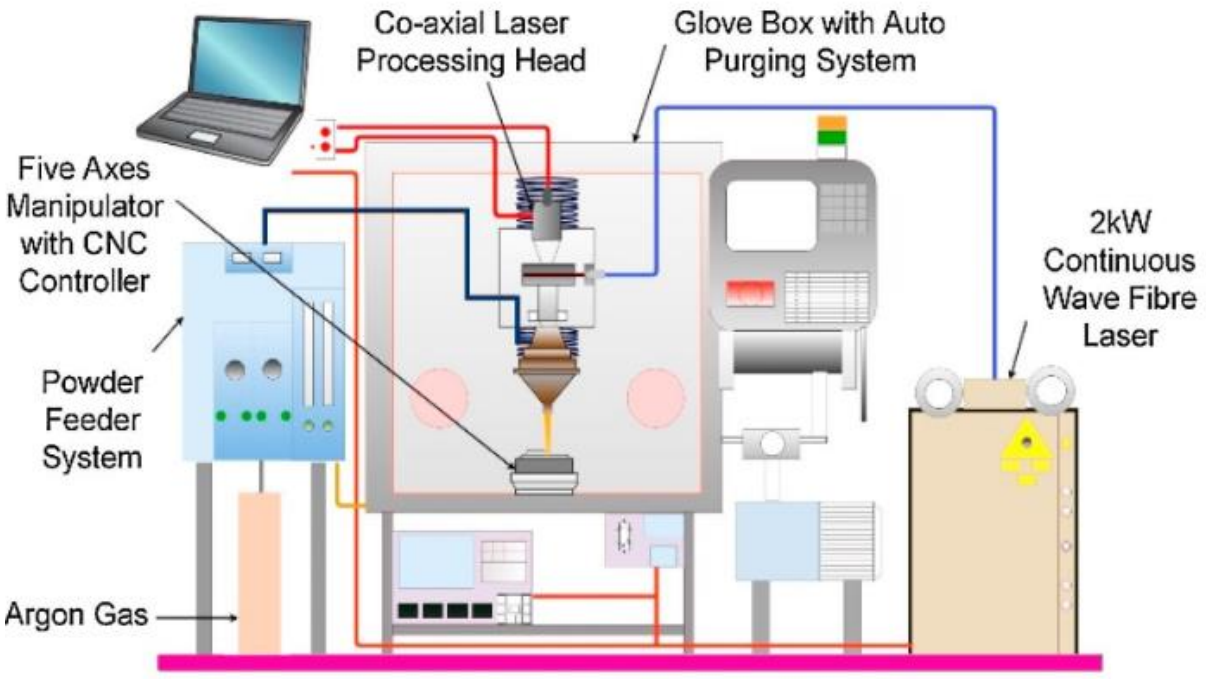

Figure 2-10: Laser assisted direct energy deposition set up presentation [172].

2.6 Types of Inhomogeneities and their generation mechanisms in AM parts

Variations in process parameters and powder attributes influence not only the microstructural features present in AM components (e.g., grain size, texture, solute distribution), but may lead to the generation of defects. Laser power, scan speed, step height, spacing of scan lines, powder feed rate, powder size distribution, and surface chemistries are among the many parameters that influence the quality of the deposited material. Many studies have been conducted which seek to understand and quantify the effects of these parameters on the final microstructural characteristics [46]. However, as the combined influence of all related parameters is not completely understood, robust process models still need to be developed [48, 49] and other critical experiments are required.

2.6.1 Microstructural Anomalies

Any feature seen in the microstructure of AM parts that deviates from what is desired can be considered as an anomaly depending upon the end application. As noted previously, in this work, 'defect' is about any structural deviation away from an otherwise uniform, fully dense solid of the target alloy. Examples are seen in the form of: porosity, lack of fusion (LOF), microcracks and hot-tears, variations in crystallographic texture and grain size, unwanted variations in composition, unexpected or metastable phases, and non-metallic inclusions [173].

2.6.2 Porosity

Porosity is a common defect found in AM parts. Many process parameters and feed material attributes have been associated with porosity. Further, the porosity that exists can occur at different length scales. For sintering-based AM processes, micro-porosity (sub-powder scale) is generally related to pores inside the starting powder that are transmitted to the final deposition. For both sintering-based and fusion-based AM, porosity that is present at the macroscale may be categorised into two main classes: gas porosity and LOF [48]. Most of the porosity occurs from gas porosity and the porosity due to LOF.

2.6.3 Anisotropy and Phase Stability

Changing process parameters such as laser power and cladding parameters, specifically cladding speed and its effects on energy density, has been shown to cause a considerable change in the grain structure [49], the phases present (including the promotion of metastable phase formation), their distribution within the microstructure [174], and tendencies for defect generation in AM parts [175, 176]. The variation in the temperature gradient in the melt pool result in variation in the solidification rate, resulting in concurrent variations in microstructure, including phase stability [177]. Further, the atmosphere can have an influence on phase stability, microstructural features/morphology, and defects. For example, even a small amount of oxygen contamination can cause oxidation changing the resulting texture and adding impurities to the microstructure in some AM methods which are processed under inert gas shielding or environments [178]. Several studies have reported the anisotropy seen in material properties caused by the different cladding patterns and process parameters used [35] and has also been shown to be dependent upon the material employed [179].

2.6.4 Geometrical Anomalies

Dimensional inaccuracy for an AM produced part can be problematic, particularly when considering a prototype or high value part where the end use is for a component requiring fine dimensional control [180]. The layering process used in AM methods can result in rough surfaces and possible deviations from specified CAD model tolerances or other geometrical anomalies in the final part. Typically, the CAD model is converted to a stereolithography (*.stl) file format where the designed geometries and surfaces are discretised into geometric meshes. A macro-level ‘stair-case’ effect can occur on part surfaces due this discretisation [181]. In addition, it has been shown that melt pool dynamics have a large influence on sidewall dimensions for the finished parts [182]. The risk of occurrence for curling, waviness and surface roughness are also all influenced by the previously discussed process and material parameters.

Melt pool dimensions and fluid flow have been shown to influence the sidewall dimensions and surface finish in deposited parts [183].To minimise geometrical anomalies, a stable melt pool size/shape is required [182]. The Marangoni effect has a strong influence on melt pool size and shape and can introduce anomalies in deposited layers due to its dependence on composition and the local thermal gradients.

2.6.5 Cracks and Similar Linear Features

Several different physical factors and process parameters can cause cracking in AM parts. Melted powder can merge with the closest surface contact point, often a solid or liquid neighbouring particle and not the previous layer. Continuation of this phenomenon can cause a change in the distribution of thermal energy and generation of large channels devoid of material bound to the substrate that resemble cracks in the final part [174]. Melt pool movement also causes mass transfer/movement along the interface due to surface tension gradients (known as the Marangoni effect) and can cause entrapped gas porosity, or cracks [184]. Thermal gradients can generate cracks in the parts when there are differences in thermal properties between the substrate and the build material, or when there are large thermal gradients in the molten pool while solidification is proceeding (i.e., hot tearing) [185].

In addition to these cracks that can form during service, it is possible to have cracks form during service. Powder contamination, especially inclusions or un-melted particles originating from the feedstock, can cause subsequent cracking in service due to stress concentrations around inclusions under fatigue loading. Geometric anomalies can form stress concentrators that can potentially form the starting point for crack growth in service.

2.6.6 Defects in Powder Materials

As noted previously, internal voids in feedstock powder materials have been identified as a source of defects in AM components. Poor packing density during consolidation can create internal voids in as-deposited materials. Impurities in the powders can also lower the quality of the final part and generate porosity and inclusions [186]. Sieving the gas-atomised powders and triboelectric separation [187] are reported as potential methods for removing impurities from powder feedstock. The particles themselves can also contain geometric defects including voids [188]. One such example is that of an X-ray image of titanium particles that exhibit internal voids, as well as powder particle size and shape variations is shown in Figure 6. Smaller sized powder particles exhibit better compaction and lower defect rates than when compared with larger particle. However, smaller particles may also lead to increased interstitial contents in the final components or safety issues during powder processing and

handling. It has also been found that the final part surface roughness increases with larger particle and consequently larger layer height is employed [189].

2.6.7 Defects in Functionally Graded Materials Manufactured by AM Methods

One opportunity in application of AM technology is the fabrication of functionally graded materials (FGMs). FGMs are formed by mixing different alloy powders during the laser sintering or melting process. Producing controlled gradients in mechanical properties enables opportunities for new designs and products which utilise these tailored properties [176]. For such materials the spatial control of chemical composition becomes an additional design parameter, and consequently new approaches to material testing and evaluation need to be developed.

Thermal stresses due to the AM process are the main cause of defects, primarily cracking, in FGMs due to a systematic variation in the thermos-physical properties and the presence of large thermal gradients. This cracking commonly occurs in brittle ordered phases that form during the fabrication process, and is the result of transitioning across phase boundaries as a result of the compositional variation [138]. This kind of cracking has been reported in several studies for different compositions of materials. Such transitions are not surprising when the thermodynamics of materials are considered. While FGMs offer tremendous promise in designing a material whose properties can be engineered for a given set of requirements at a specific location within a component, in reality it is necessary to incorporate a detailed materials design component to realise effective and defect free FGMs. The local composition will influence the attending microstructure and properties [176]. In addition to cracking due to brittle ordered phases, it is possible to have differences in the coefficients of thermal expansion lead to cracking in some FGMs, especially those with abrupt changes in composition. One additional type of defect that can be found in FGMs is un-melted particles formed when mixing materials with different thermos-physical properties and melting points [190].

2.7 Influence of processing Parameters and Inhomogeneities on Mechanical Properties

Parts produced using the BPLC process have a multivariable dependency on the processing parameters selected. A change in any variable of the laser cladding process affects the properties of parts produced. The key variables include laser power, laser spot size, cladding speed, beam mode structure, powder feed rate, step height and distance from substrate. This multivariable dependency results in a very complex situation in which the melt pool size and shape can vary resulting in varying cooling rates. A solid liquid interface is maintained during build-up of a part. The size of the molten zone needs to be controlled by the processing parameters to maintain uniformity in parts produced.

Further to this the reheating of previously deposited layers occurs as each new layer is deposited in a multilayer build. Multiple temperature gradients are created in a BPLC build affecting the material properties. These gradients result from a repeated non-uniform heating and cooling process. This process results in complex microstructural evolution within parts. The most important parameters to control are laser power, cladding speed and powder feed rate which have a significant effect on the microstructure and mechanical properties of parts built.

2.7.1 Effect of Processing Parameters on Microstructures

As mentioned, the process parameters have a large effect on the microstructures of parts built by BPLC. The microstructure strongly depends on the cooling rate for austenitic stainless steels. Variations in the cooling rate during production of a part caused by processing parameters will cause significant microstructural variations. It has been discovered strong variations in microstructures from parts produced from a mixture of AISI 316L stainless steel and Inconel718 powders [191, 192]. Various proportions of dendritic, cellular and columnar structures were observed as shown in Figure 2-11.

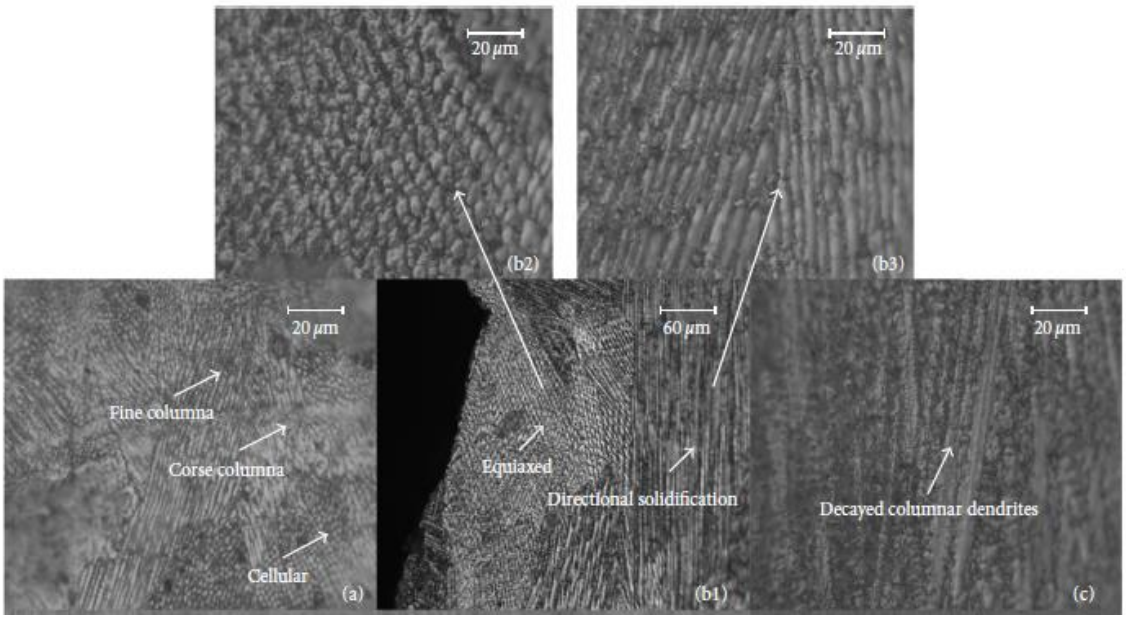

Figure 2-11: Microstructural variations in laser cladding parts of AISI 316L[193].

Dendritic structures that grow in an epitaxial manner towards the surface of the melt pool are common in BPLC parts. Cellular structures can form however the remelting process creates a situation where the cooling rate is lower leading to a dendritic microstructure as appose to an equiaxed cellular microstructure. In a typical clad microstructure, the cooling rate at intermediate layers is epitaxial whilst the microstructure at the top, where the no remelting has occurred, is equiaxed. With no remelting the cooling rate is much faster leading to this effect [194]. Thomas et al. (1995) discovered dendritic growth in 316L stainless steel wall and rod structures produced by BPLC. It was observed that

there is a constant solid/liquid interface occurring during the process causing dendrites to continuously grow within the process material. These dendritic structures were linked to cooling rates of the order 102K/s for rods and 104K/s for plates [195]. For cellular structures to form higher cooling rates are required.

A laser clad microstructure morphology can be said to be dependent on the ratio between the temperature gradient (G) and the solidification speed (R). When the ratio of G/R is high the solidification front is stable otherwise instabilities occur [196]. Ocelik et al. (2010) observed columnar dendrites towards the bottom of a laser clad sample where the solidification speed is low and the ratio G/R is therefore high [197]. Towards the top of the sample where solidification speed increases short cellular dendrites were noted and attributed to instabilities in the solidification front. Similar observations were found in which a dendritic microstructure was observed to change from coarse to fine with an increase in cladding speed. This was attributed to a decrease in the ratio G/R [193]. The solute content of an austenitic stainless steel can be related to the ratio G/R to predict the microstructure as shown in Figure 2-12[198].

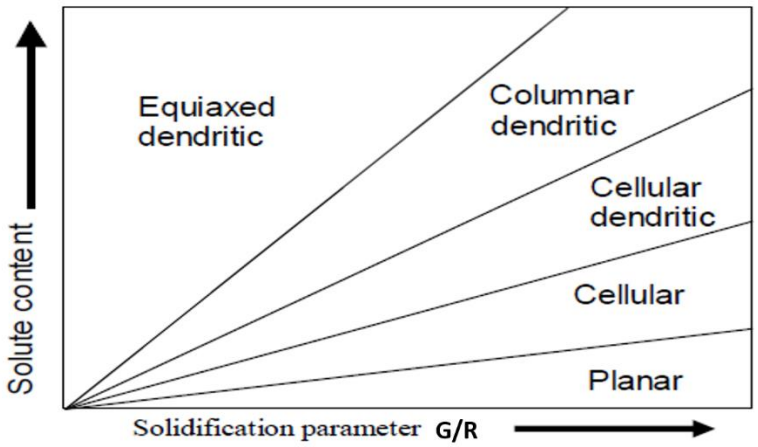

Figure 2-12: Dependence of solidification mode on solute content and G/R parameter.

The presence of porosity is another key factor in the microstructures of parts produced by laser cladding with can be controlled by process parameters. Majumdar *et al*. discovered micro-porosities in clad builds. It was found that the area fraction of porosity could be reduced by altering the process parameters. By increasing the cladding speed, it was possible to reduce the porosity. The presence of micro-porosities was attributed to entrapment of gas from the surrounding atmosphere hence higher process velocities reduced the porosity due to the lower interaction times [107].

It is possible to adapt the process parameters to achieve an 'optimised' microstructure. To achieve uniform mechanical properties minimal microstructural variation is necessary. It can also be deemed

desirable to have an equiaxed microstructure and to therefore prevent directional solidification. Therefore, the optimum microstructure will be both equiaxed and homogeneous. Amine *et al*. achieved a homogeneous microstructure, however one that was not equiaxed, by manipulating process parameters [199]. The microstructure deposited was entirely defect free. Majumdar *et al*. used a parametric optimisation technique to generate ideal processing parameters at various power densities [107]. Considering the independent effects of laser power, cladding speed and powder feed rate on porosity and homogeneity within the microstructure 'ideal' processing parameters were established. The microstructures obtained from these process parameters were either a mix of cellular and dendritic or mainly cellular depending upon the power density. It can be suggested that these 'ideal' processing parameters failed as a homogenous microstructure was not achieved however for some of the parts the microstructures were equiaxed.

2.7.2 Effect of Processing Parameters on Mechanical Properties

The mechanical properties of any material are strongly related to the microstructure. The laser cladding process puts the material through a melting and rapid solidification thermal cycle. As mentioned in section 2.4.1 it is not possible to strengthen an austenitic stainless steel via a further heat treatment process following initial processing. However, due to the excessive cooling rates involved, thermal stresses around the melt pool causes some work hardening to occur within the material.

Microhardness profiles have been conducted by many and appear to relate strongly to the process parameters. Majumdar *et al*. note hardness variations between 170 to 280HV depending upon the process parameters for 316L stainless steel cladding samples with predominantly cellular microstructures. The typical wrought hardness of 316L stainless steel is 170-220HV therefore a clear increase is noted. Variation is shown to depend upon cladding speed and power density mainly. It was discovered that as power density increases that microhardness decreases. The distance from the substrate was seen to have very little effect. This is contrary to that found by Amine *et al*. [199], for dendritic microstructures, in which similar hardness values were achieved however hardness was found to decrease as distance from the substrate increased. As power was increased microhardness was seen to decrease as found by Majumdar *et al*. and Wu *et al.* compared the hardness values in dendritic areas and cellular areas and found a comparative increase in microhardness where the microstructure transitioned from dendritic to cellular equiaxed compared to where the microstructure was purely dendritic [195].

2.8 Standardisation of Materials and Methods

2.8.1 Austenitic Stainless Steels

Material of interests are presented in this thesis is austenitic stainless steel due to availably.

The high temperature form of Iron (between 910 and 1400°C) is known as austenite. Austenite can be maintained a room temperature by alloying. Austenitic stainless steels use nickel as an austenite retainer with a nickel content of around 8% [200]. Other alloying elements are chromium for corrosion resistance along with multiple other additions including carbon, silicon, molybdenum and manganese for strength, formability and added corrosion resistance. Austenitic grades of stainless steel tend to be used due to their very predictable levels of corrosion resistance and excellent mechanical properties. The composition of an austenitic alloy can be visualized on the Schaeffler-Delong diagram as shown in Figure 2-13. This diagram was designed to show which phases are present in the as-solidified condition such as found in welds and as such will be useful for the laser clad alloy composition. Key to the Schaeffler-Delong diagram are the Chromium (Cr) and Nickel (Ni) equivalences defined in equations Eq.2.6 and Eq.2.7

$$Cr_{eq} = Cr + Mo + 1.5 * Si + 0.5 * Nb \quad \text{Eq. 2.6}$$

$$Ni_{eq} = Ni + 30C + 0.5 * Mn \quad \text{Eq. 2.7}$$

The chromium and Nickel equivalences are not just relevant for the Schaeffler-Delong diagram in Figure 2-13 but also for the solidification modes of austenitic stainless steels. Using the Chromium and Nickel equivalences allows simplification of a complex austenitic stainless-steel alloy to a Fe-Cr-Ni alloy. This simplification allows the alloying elements Molybdenum (Mo), Silicon (Si) and Niobium (Nb) to be classed as having a similar effect to adding their equivalence in chromium and the alloying elements Carbon (C) and Manganese (Mn) to be classed as having a similar effect to adding their equivalence in Nickel.

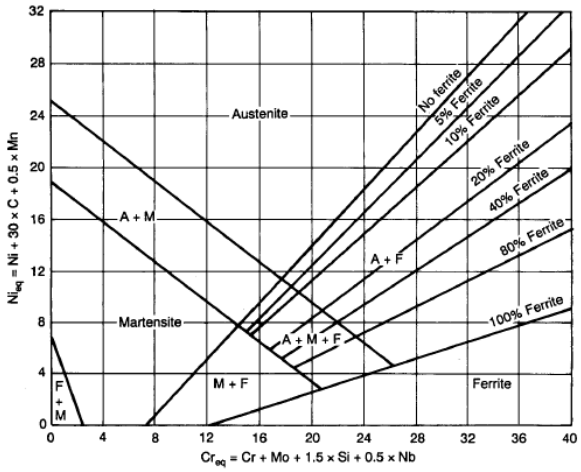

Figure 2-13: Schaeffler-Delong diagram for austenitic stainless steels [122].

Austenitic stainless steels can be divided into 5 groups (in Appendix 4): Conventional austenitics, Stabilized compositions, Low-carbon grades, High-nitrogen grades and High alloyed austenitics. A table of the common grades included within these bands can be found Figure 2-13. Austenitic stainless steels of the low-carbon grades will be the focus of this section and the rest of this report.

2.8.2 Microstructure and Metallurgy

The austenite structure is a face centred cubic (fcc) lattice which, in austenitic stainless steels, is present throughout the whole temperature range from room temperature to the melting point. The wrought form tends to be subjected to a high-temperature solution anneal to create a fully equiaxed austenitic microstructure. Post this initial forming heat treatment further heat treatment to strengthen the alloy is not possible. It is however very possible to strengthen austenitic alloys by work hardening [201].

The microstructure of austenitic stainless steel can vary quite significantly depending upon the cooling rate and hence the solidification mechanism. Stainless steel alloys solidify in one of five different primary solidification modes. These are as follows: single phase austenite, primary austenite with second-phase ferrite, eutectic ferrite and eutectic austenite, primary ferrite with second-phase austenite and single-phase ferrite. For the case of the low-carbon grades the primary solidification modes can be of the single-phase austenite or primary austenite with second-phase ferrite. The secondary phase structure which can be found in these alloys is classed as delta-ferrite (δ-ferrite). These phase structures have a body centred cubic (bcc) lattice structure and occur alongside the primary austenite (fcc) phase structure [202, 203].

2.8.3 Cellular and Dendritic Microstructures

Dendritic and cellular microstructures can occur in austenitic stainless steels dependant on the cooling rate. These microstructures exist due to constitutional undercooling. During solidification, as a solute-rich layer forms in the liquid adjacent to the advancing solid interface the temperature at which freezing takes place is reduced. The diffusion of solute is much lower than the diffusion of heat. A condition in which the temperature of the liquid is below the equilibrium liquidus temperature can occur in a limited distance near the substrate. This situation is referred to as constitutional undercooling [204].

In the creation of a cellular microstructure, if the zone of constitutional undercooling is narrow freezing occurs on a cellular interface. The centre of each cell projects into the liquid. The formation of a cellular

interface is accompanied by lateral diffusion of solute from the cell tips to the cell boundaries. As a result, the cell boundaries freeze at much lower temperature than the cell tips producing an interface contour in which liquid regions extend far into the solid. Dendritic microstructures occur with an increase in constitutional undercooling. The continued change in shape of cell structures results in the appearance of a branched dendritic structure.

2.8.4 The Effect of Cooling Rate

The rate at which austenitic stainless steels solidify has a large effect on the microstructures produced. Work by Fu *et al*. allows visualisation of the phase changes that occur as cooling rate increases for austenitic stainless steels [205]. In their experiments an ingot of AISI 304 stainless steel was cast into a water-cooled wedge-shaped copper mould. Where the rate of cooling is at its lowest a skeletal δ-ferrite structure form. As the cooling rate increases transformation from primary dendritic δ-ferrite to primary dendritic austenitic occurs and then from primary dendritic austenitic to fine cellular austenitic. These transitions are shown in Figure 2-14 [205].

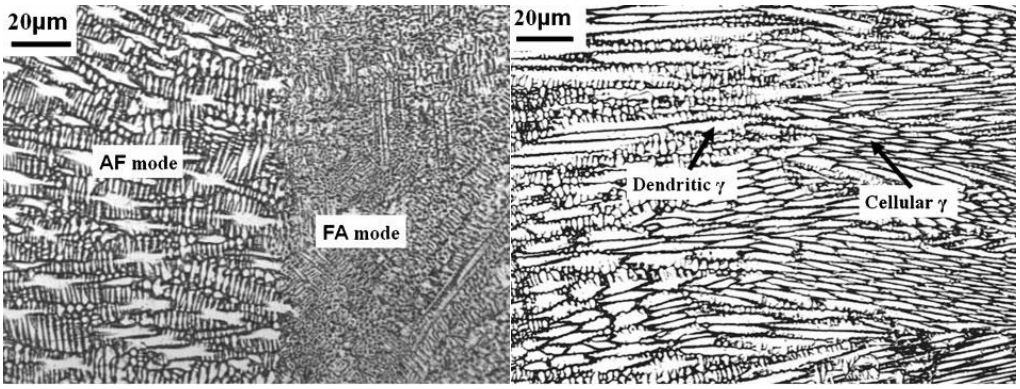

Figure 2-14: Transition microstructures in AISI 304 stainless steel FA to AF (left), dendritic to cellular (right).

The phase transformation during solidification of austenitic stainless steels depends strongly on the chemical composition, most notably the Ni/Cr equivalence. As such Fu's group [205] found that the solidification mode could be characterised by the four following groups, where L, δ and γ represent liquid, δ-ferrite and austenite respectively:

i. A mode: $L \rightarrow L+\gamma \rightarrow \gamma$ $Cr_{eq}/Ni_{eq} < 1.25$

ii. AF mode: $L \rightarrow L+\gamma \rightarrow L+\delta+\gamma \rightarrow \gamma+\delta \rightarrow \gamma$ $1.25 < Cr_{eq}/Ni_{eq} < 1.48$

iii. FA mode: $L \rightarrow L+\delta \rightarrow L+\delta+\gamma \rightarrow \gamma+\delta \rightarrow \gamma$ $1.48 < Cr_{eq}/Ni_{eq} < 1.95$

iv. F mode: $L \rightarrow L+\delta \rightarrow \delta \rightarrow \delta+\gamma \rightarrow \gamma$ $Cr_{eq}/Ni_{eq} > 1.95$

AISI 304 stainless steel has a Cr_{eq}/Ni_{eq} of around 1.77 which gives the FA mode as the primary

solidification mode. It was found that this solidification mode occurs at the base of the sample however did not occur further up where cooling rate were higher. When cooling rate was sufficiently high transition from FA to AF mode was found to occur. As the cooling rate was increased further dendritic austenite forms and then cellular austenite [206, 207].

Increasing the cooling rate to a large extent so that the primary solidification mode is altered is something which is likely to happen during laser cladding in which rapid cooling is a key characteristic. Further increases in the cooling rate alters the microstructure from one that is a uniform dendritic to one that is uniform cellular.

2.9 Key Research Topics and Issues with Blown Powder Laser Cladding for Additive Manufacture

Development of the laser cladding for additive manufacture process has uncovered several problems with the process each with varying solutions. The key issues, in terms of producing fully functional parts, include geometrical inaccuracies, efficiency of the process and the control of microstructures.

2.9.1 Step height Control

One of the key issues with the BPLC process or any of its variations is geometrical accuracy. As the part is built up, typically laser power, cladding speed and powder feed rate are kept constant [84]. For certain geometries which include features such as corners, i.e. a square cross-section, the cladding speed is reduced in these areas. This creates a situation where, as the laser is centred over these areas for a longer time, the step height builds up at the corners eventually affecting the height of the final part. With an open loop system, with no method of step height control, the layer height is proportional to powder feed rate and the cladding speed [208]. This effect increases as the height of the part increases. This problem also affects the clad widths resulting in poor geometrical accuracy. If no layer height control method is adopted parts tend to require significant post machining to achieve the necessary geometrical accuracy of the final part [209].

A group from Spain tried to geometric model the cladding process to simulate the clad geometry in order to calculate the layer height. They were using the coaxial nozzle to produce a model from concentrating the injected material, real energy distribution and melt-pool geometry and lately the cladding height was estimated with an averaged error between modelling and actual cladding measurement under 8% [210].

Methods to prevent geometrical inaccuracies include the use of a closed loop system to control deposit thickness and height. Mazumder *et al*. [118] used sensors to provide dynamic feedback on the height of the part as it is being built. This allows the process parameters to be altered to ensure the layer height is kept constant. Another method was developed at the University of Illinois which used reflective topography to visualize and measure the surface deformation of the melt pool and feed this into a closed loop system [211, 212].

An open loop system to optimise layer height by controlling step height has been developed by Fearon [97] which utilizes the multiple side feed nozzle system described earlier. This method utilizes the shape of the powder stream to control the step height. Using a balance between the powder feed gas flow and the coaxial gas flow the shape of the powder stream can be controlled with the interface between the multiple powder streams at the limit of the step height. This can be visualized in Figure 2-15. With this, the step height can be simply programmed into the height at which the laser moves up after each layer is deposited. This method requires the step height and cladding speed to be programmed to allow for build up to the interface between the powder streams to be achieved.

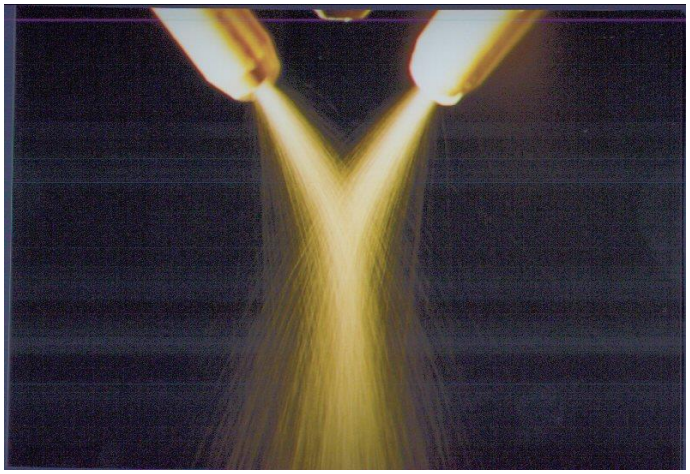

Figure 2-15: Multiple side feed nozzle with step height control [213].

2.9.2 Process Efficiency

The laser cladding process is not particularly energy efficient. A large proportion of the laser power is reflected or reradiated away from the cladding zone. Doro *et al*. investigated the energy distribution during laser cladding via the single side feed method. Energy in varying proportions was found to reflect off the cladding zone, radiate from the cladding zone and reflect off the powder particles along with being absorbed by the process [214]. The amount of energy which is absorbed in the process (useful energy) is dependent on the laser used. For a carbon dioxide laser, the energy absorbed was found to be 40% of the incident energy [215].

Another factor which limits the efficiency of the BPLC process is the catchment efficiency. Only some of the powder particles blown into the substrate will adhere to the melt pool, others will ricochet and be lost. The catchment efficiency is very dependent on process parameters, particularly cladding speed and powder feed rate. The effect of theoretical can be reduced by the reusing of powder however some powder will always be lost due to oxidisation with the high temperatures involved.

According to Lee's work, laser powder cladding process and related powder catchment efficiency are influenced by many mutually dependent parameters. A single track of 40mm length was cladded on the workpiece surface and the related powder deposition efficiency was evaluated for each run. To characterize the powder cladding efficiency a powder cladding efficiency η_p was define by the ratio:

$$\eta_P = \frac{\mathrm{m}}{\phi_m * t} \qquad \text{Eq. 2.8}$$

Where *m* denotes the mass of the cladding track measure by a scale, and the product $(\phi_m * t)$ defines the estimated powder mass fed during the time t with a constant powder flow rate ϕ_m in unit of g/min. Kuznetsov *et al*. did a similar investigation on the exploring annular laser beam focus position and related beam spot diameter, powder mass flow, cladding speed and laser beam intensity effects on the powder catchment efficiency in 2016. Both research results agreed that mentioned process parameters have similar influence on the powder catchment efficiency via conventional cladding heads. The catchment efficiency is increasing with the increasing mass flow and average laser beam intensity while decreasing with increasing cladding speed. [216].

2.9.3 Microstructural Control

For BPLC to be a success it is necessary for parts to be built with properties like that of the wrought material. Parts produced using the BPLC method can suffer from porosity along with having directionally solidified grains. Depending upon the application these characteristics tend to be undesirable leading to poor mechanical properties. It is possible to control the microstructure using the process parameters to reduce these effects as is further discussed in following reviews.

2.10 Software Modelling and Simulation

There are lots of influencing factors closely connected with laser cladding results, a 3D finite element simulation model of the laser cladding process has been developed taking into account heat source, heat transfer, fluid flow, surface tension and free surface movement. All input parameters and data,

which are independent of the process parameters but depend not only on the materials but also machine properties, have been obtained from analysis and modelling by different research groups around the word. In addition, the laser cladding process gains importance, as it does not only allow the application of surface coatings, but also additive manufacturing of three-dimensional parts. In both cases, process simulation can contribute to process optimization. Ravi.*at al* [217]confirmed that the simulation modelling on exploring the relationship between laser cladding process parameters and results is very helpful to optimize the final stage manufacturing process based on Copper and SS316L studies. They found that the laser power is the main affecting process parameter to clad geometry. The power and mass flow rate would affect the clad height, dilution, temperature, and stresses and furthermore, there are in proportional relations. While cladding height and dilution increases with increasing laser spot diameter, but temperature and stress are decreasing. Another group from University of Manchester lead by Prof Lin Li and Dr Andrew Pinkerton has investigated the interaction of the substrate and coaxial powder stream as they are playing important roles in determination how the material is deposited. Initially, they were explored some models of the coaxial powder stream concentrated on mass flow dynamics and steam heating, regardless of the effect of substrate, which can predict the stream geometry and shape as well as velocity and trajectory of flying particles. This conclusion was fully agreed with their experimental observations. Later, they developed a comprehensive numerical model including the substrate material analysis which modelling a realistic cladding configuration [218].

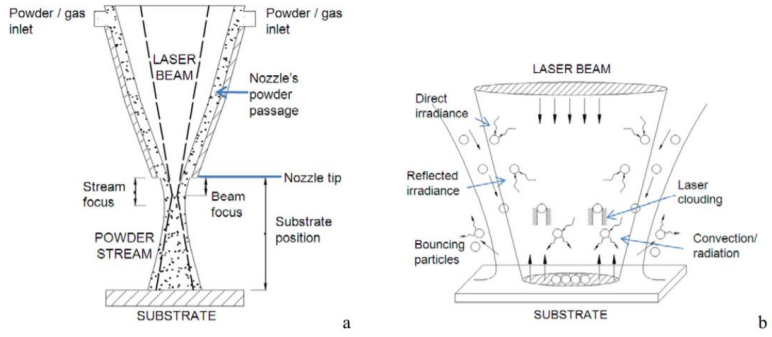

Figure 2-16: Schematic of the laser cladding process (the nozzle comprises four powder inlets), (b) Schematic of thermal processes in laser cladding.

There are large number of researches on modelling on laser cladding, including approaches to the direct metal deposition, powder steam process, melt pool process, microstructures, stress and final geometry using ANSYS, ABAQUS and COMSOL [219]. The development of this modelling is positive and trends to provide sufficient simulations references for laser community in multiple ways.

2.11 State of the Art

Man *et al*. [27] used a 5 kW CO2 laser to produce thick (up to 4 mm height) 316L clads on 316L substrate. Using a CNC table, the authors produced 97.5% dense clads at 1.4 m/min speed using a feed rate of 32 g/min. However, only 20% of the impingent powder was effectively added to the surface. Tensile specimens obtained from the as-deposited clad plus substrate attained the following maximum values: tensile strength 510 MPa, yield stress 450 MPa, total elongation 20% and hardness 260 HV.

Dadbakhsh *et al*. [220] studied the effect of gas flow on the consolidation of 316L steel clads. The authors' results show that the part layout and gas flow condition have a negligible influence on porosity formation, however they notably affect the thermal stress and bonding strength between particles which consequently influences the mechanical properties of final parts.

Abouda *et al*. [221] did a comparison research between laser cladding and plasma arc-transferred cladding using 316L stainless steel through a broad parameters including laser power, powder feed rate, cladding speed and preheating to optimise the cladding properties such as adhesion, compactness, microstructure and dilution rate. As a result, they found that laser cladding induces a significant strengthening mechanism for hard-facing alloy which results from a finer dendritic structure with a modified Chromium and Molybdenum precipitations distribution in the eutectic inter-dendritic phase. In other word, laser cladding exhibits a refinement of the cladding microstructure and provides a homogeneous distribution of different carbides in the inter-dendritic structure.

A recent study on blown powder laser cladding by Song*. et al* has proved that addition of graded structures on existing part of different materials can clad. They applied Ni50Cr as blown powder cladding on 304 stainless steel successfully [222]. In terms of different exploration purposes such as wear resistant, corrosion resistant and porosity, lots of materials have been used in BPLC like aluminides of titanium, nickel and iron [223]. For experimental researches, numerical modelling will always be a good prediction for results since they are many factors affecting the cladding. Mazumder et. al [224] developed a self-consistent 3D transient model to examine the physical phenomena including heat transfer, melting/solidification phase change and liquid metal flow using a coaxial powder injection laser cladding process. The numerical results provided a good prediction to form a good metallurgical bonding by optimising the processing parameters. However, computational software and hardware still have limitations in simulating a model of accurate blown powder dynamics, melt pool morphology and melt pool fluid dynamic [225-227]. Mechanical properties such as tensile,

fatigue and impact testing are common applied to examine and evaluate the performance of the cladding structures. It's found that DLD parts gave similar or higher values of properties compared to wrong and cast materials [228-230].

Two criteria used to evaluate the quality of laser cladding are based on macroscopic and microstructural analysis. In terms of macroscopic aspect, the shape of the cladding structure, the uniformity of the surface, cracking and porosity are the main considerations for exploration. Whether qualified microstructure can be formed, and the required properties can be met are summarised as microcosmic criterion.

During the process, powder feed rate and clad speed can be controlled as constant; but the power may be varied and fluctuated which will cause the variation of rapid solidification. In terms of structural geometry, the step height was determined by the G-code from the programme directly. However, the step height would be affected by actual geometry such ad at the corner and intersected area due to changing speed and cooling rate.

Another issue with blown powder is the efficiency on catchment that the vast majority of it depends on the powder feed rate and processing parameters [231, 232]. How to improve the catchment efficient and reduce the waste and cost need to be further studied by altering and optimising processing speed and powder feed rate.

To sum up, although the cladding approach is advantageous, the current limitations in achieving predictable and repeatable material and structural properties, geometric and surface roughness characteristics, and the occurrence of deformations due to residual stresses results in significant variations in quality and reliability.

There are numerous research groups and companies working on additive manufacturing by exploration different directions in UK (2018-2019). Laser direct metal deposition for interlayer porosity generation behaviours has been studied in the University of Manchester and they also developed an optimum combination of process parameters/conditions and characteristics of the initial power to minimize the intralayer for practical engineering applications. They also implicated the study on the effects of melt pool variables. The main equipment used was a 1.5kW Laserline LDL diode laser and materials were Inconel 718 and Ti-based aerospace alloys. A significant research effort is taking place between the MTC (Manufacturing Technology Centre) and the University of Nottingham. They are

working on in-process monitoring for laser powder bed fusion to reduce occurrence of over-melted zones and resulting spherical pores for coaxial melt pool. And for non-coaxial, they can identify any deviations during the build which could result in pores or voids. Some laser additive manufactured components were successfully simulated using an embedded 3D circuit system and microstructures manipulation using Gaussian and holographic optical elements reconstructed beams in Loughborough University Additive Manufacturing Research Group. In addition, the majority of their research activities have been conducted in collaboration with industrial partners and encompass a broad range of sectors including aerospace, defence, design, health, medicine, and electronics. The researchers from Cranfield University have manufactured large-scale products like projectiles, wind tunnel models, bombardier landing gear rib and wing rib produced of different materials such as steel, aluminium, titanium using wire and Arc additive manufacturing (WAAM) technology. Not only academic area, laser cladding attracts industry's attention as well. TWI is a decent company in cladding techniques. For example, it has been developing the laser metal deposition (LMD) process for the last decade, exploring its use for everything from repair of high-value parts to fabrication of large freeform components. These can prove that laser cladding for additive manufacturing is a promising technology.

Laser systems for laser cladding with wire or with powder can currently be purchased from a few companies such as Coherent (Orlaser), Kuka, Irepa Laser and TLM Laser based on specific demands like component scale, powder types and main applications. Their turn-key systems still face several challenges to improve industrial take up of the technology, to be discussed later.

2.11 Motivation for Current Work

Key problems with the blown powder laser cladding for additive manufacture process include the issue of controlling the layer step height, the efficiency of the process and the control over microstructure. The process has a multivariable dependency on process parameters such as layer step height, laser power, cladding speed, powder feed rate and the beam mode structure of the laser. Benefit from the omnidirectional nozzle design in our group, step height can be high precision in this work. Moreover, various step height can be designed.

Austenitic stainless steel has been chosen as one of the group materials in the cladding process as its microstructure is strongly related to the cooling rate during solidification. The as clad microstructure of austenitic stainless steels has been found to be either cellular or dendritic depending upon process parameters. An increasing of hardness is also noted on austenitic stainless steels during laser cladding for additive manufacture. It will be a great opportunity to investigate of the process parameters to

control the microstructure and mechanical properties. Inconel 625 was selected as a second study material as its solid solution strengthened alloy is favourable for AM due to its high weldability and low titanium and aluminium content. As it has been widely used in many applications such as aerospace and biomedical field, more possible designs and applications will be generated if optimised processing parameters of blown powder laser cladding are studies.

Following on from the research of others in this field, the achievement of an equiaxed, homogeneous microstructure by manipulating process parameters is limited so it will be significant improvement if uniform material properties could be obtained and non-uniform characteristics could be eliminated. The quality of BPLC components can be tested by the mechanical properties, particularly in a tensile and compressive test, compared to a directionally solidified clad microstructure would be of particularly interest. Moreover, the possibility to lower the power will be a great help in cost reduction. As a consequence, the work will be designed to achieve equiaxed microstructures of cladding components and eliminated non- uniform material properties at a lower average power (currently 600W as other research group undertaking using similar workstation).

Chapter 3 Experimental Equipment and Techniques

This chapter will mainly introduce the cladding equipment used in this work. As laser is used as the heat source during cladding process, a ready-to-use PRC CO_2 laser station is introduced in detail. It is followed by cladding system including hopper system, control system, powder delivery method and nozzle designs. A CNC working platform is controlled by the NView to produce the cladding path and this will be explained in detail.

There are two main groups of materials used for cladding: stainless steel 316L and Inconel 625, of which properties will be listed and provided. To qualify the cladding components, micro-analysis is taken. How the samples being designed and sectioned for micro-hardness and micro-images taken will be introduced. Some investigations on mechanical testing such as tensile and compressive tests will be undertaken as well. This will be related with cladding routes and specific geometry designs.

3.1 Introduction

Solid state and gas-based lasers are the most common types of lasers being used for materials processing. Solid state lasers such as CO_2 and fibre-based lasers tend to be used for thinner components while CO_2 based lasers tend to be used for the thicker components although high power fibre lasers are increasing used. The choice of the laser for any application depends on the thickness and physical properties of the material to be processed. The main advantage of the CO_2 laser over the other type lasers, for instance, is that it can be scaled efficiently to high laser powers with good beam quality to achieve high penetration, which is good for melt pool formation during the cladding process.

3.1.1 Laser Equipment

The laser used for this work was a PRC 1.5kW CO_2 laser, shown in Figure 3-1. This laser is a fast axial flow type delivering a TEM01* mode structure focused through a powder delivery nozzle arrangement mounted on the z-axis of a 4axis workstation.

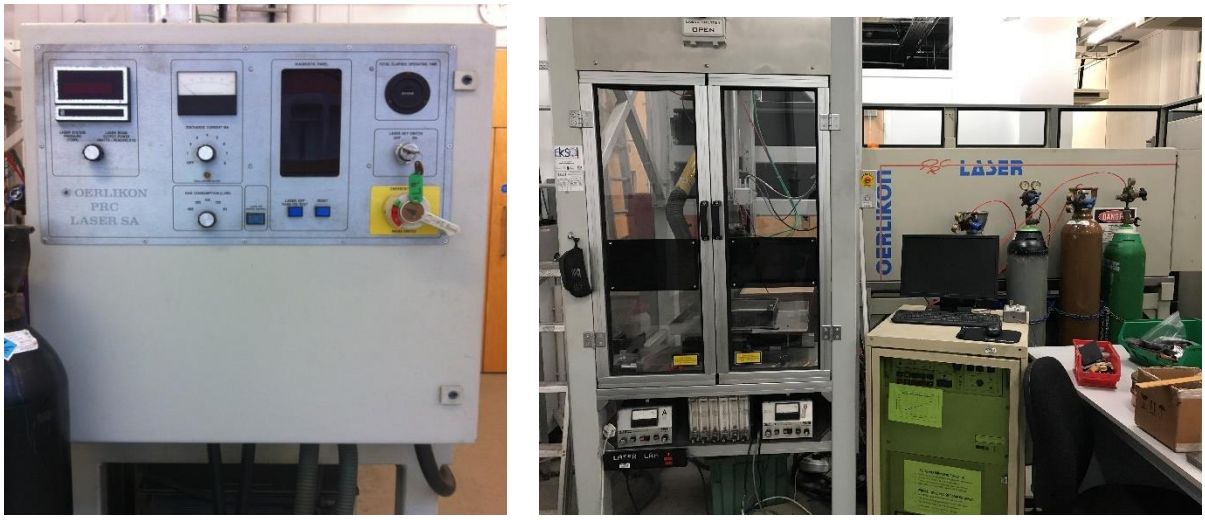

Figure 3-1: PRC 1.5kW CO2 laser used in experiments.

The output from the laser with a wavelength of 10.6µm and M^2 of 1.954 with a raw beam diameter of 18mm, is delivered via gold-coated copper water-cooled turning mirrors to a workstation at the top of the vertical Z-axis. The beam is then focused using a 2-inch diameter ZnSe lens with a focal length of 190mm mounted in a water-cooled beam delivery assembly on the Z-axis. The laser has a focused spot diameter for this lens of approximately 200µm. Typically for laser cladding this is the defocused to a 1.98mm beam diameter at an offset in Z-axis of 15mm. The laser runs with an active heating exchanger coupled to an external chilled water supplier. The constituent gases, CO_2 (10%), N_2 (12%) and He (78%) [113] are supplied via gas bottles in the lab (Figure 3-1).

3.1.2 Laser Power Calibration

It is important to calibrate the power readings to verify the accuracy of the output laser power. Especially for CO_2 lasers, the laser power is controlled by the discharge current through the gas and can be selected using dial on the control panel. The power reading on the control panel is monitored in the laser using a sensor on the back mirror. A power puck meter has then been used to measure the actual power output before the laser beam enters the focusing lens. Gold plated mirrors have a reflectivity of 98.8% approximately which indicates that a small amount of the incident laser beam will be absorbed. Figure 3-2 shows the results of the power calibration. The differences in power between the actual output and indicated on the machine is likely due absorption losses on the turning mirrors and loss of laser calibration for the internal measurement.

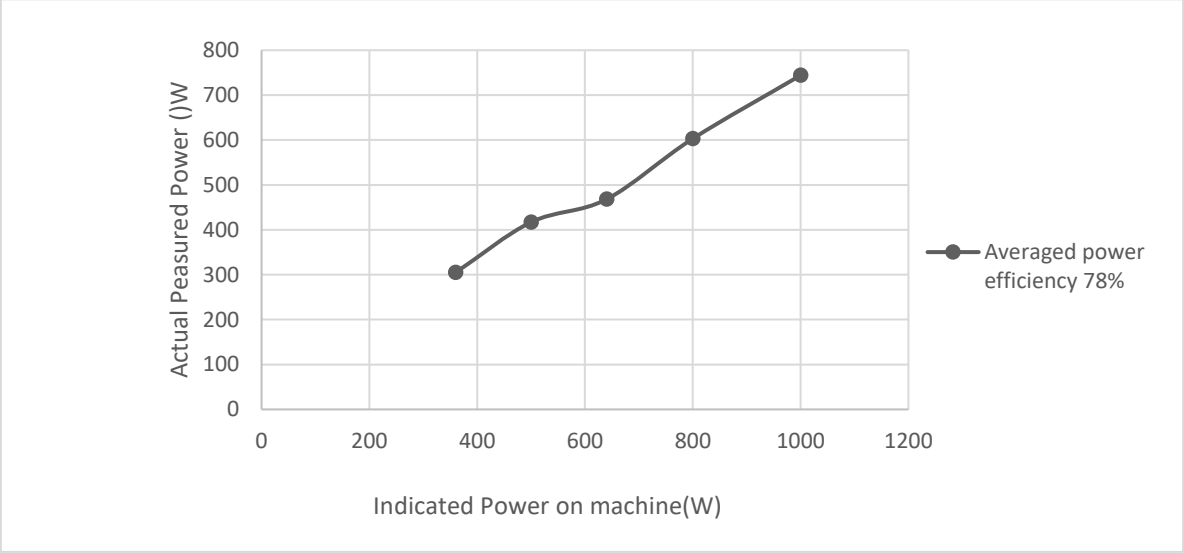

Figure 3-2: Laser Power Calibration on CO2 Laser Station used in this Work.

3.1.3 Laser Beam Alignment

It was necessary to check the alignment of the laser to ensure it was delivered vertical downwards through the optical lens and nozzle arrangement.

The misalignment of the laser beam would result in damage to the nozzle aperture and would affect the beam spot; further influencing the interaction cross sectional area between laser beam and powder which would have a detrimental effect on powder catchment efficiency. The vertical alignment of the laser beam was checked by inspecting burn prints on wood after firing the laser beam through a set of cross-hairs. The cross-hair burn print should be presented with a symmetrical shape indicating good alignment, which can be altered by adjusting the turning mirrors; shown in *Figure 3-3*.

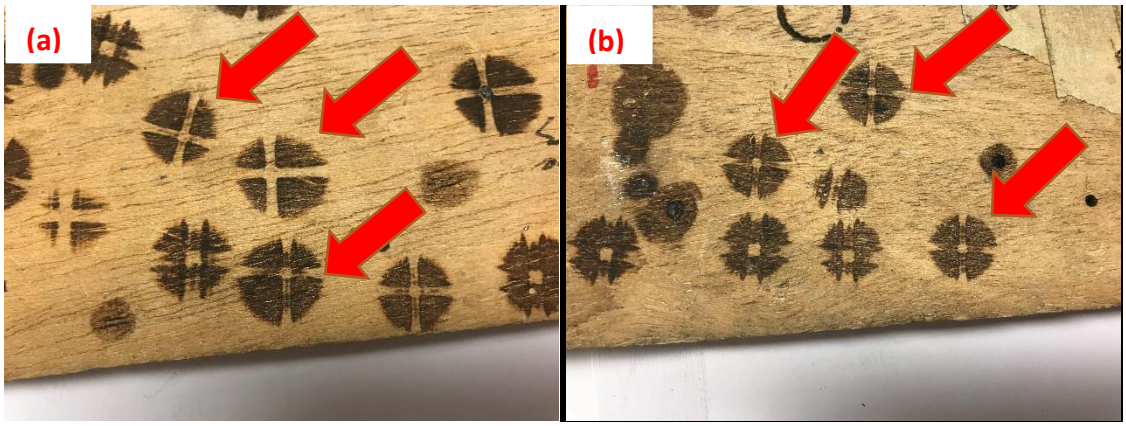

Figure 3-3: Comparison of Burn Print to calibrate the Laser Beam: (a) Misalignment Beam, (b)Aligned Beam.

Beam mode is associated with various isotherm shapes which gives variation in heating that affects the size and shape of a melt pool. With regards to the cladding process, the beam mode can affect the cladding layer width due to the melt pool size and shape. Variations in speed and in cooling rates will affect microstructures across the clad bead as well. The circled beam mode in *Figure 3-4* demonstrates the real TEM01* mode produced by the PRC laser used in this work.

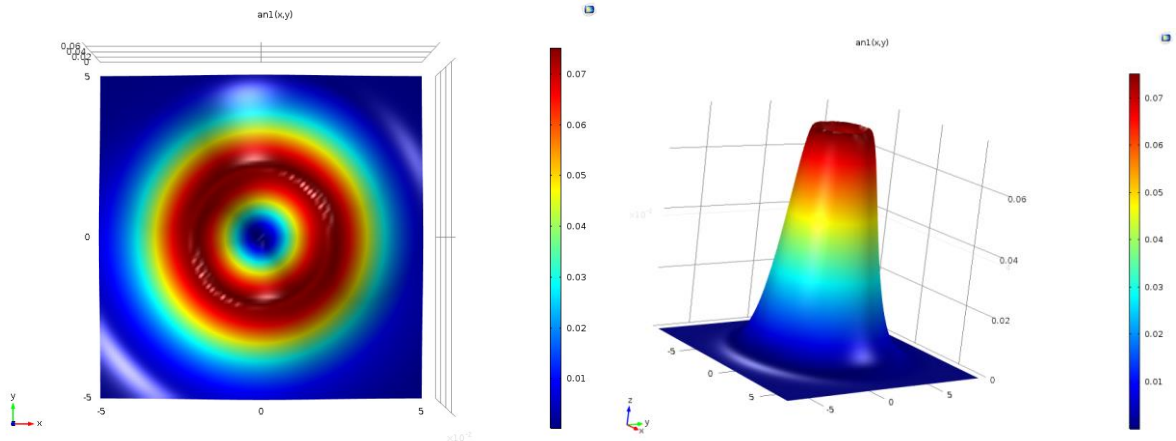

*Figure 3-4: Simulation Donut Beam Mode of type TEM01*by COMSOL.*

The experimental burn print on polyvinyl chloride is shown in *Figure 3-5* with an actual TEM01* beam mode during this experiment. It can be seen that the real beam is somewhat different. Before each experiment starts, beam mode and beam size calibration would undertaken to ensure the accuracy of the beam properties.

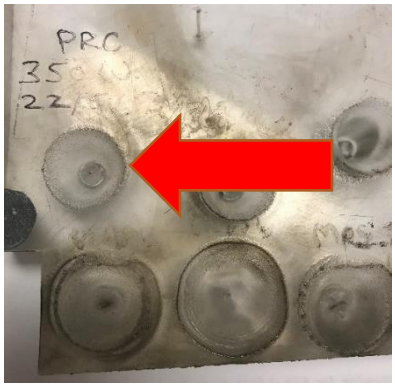

Figure 3-5: Calibrated Laser Beam Mode of type TEM01- burn print on polyvinyl chloride.*

Using this burn print technique, it was confirmed that the stand-off distance of 15mm from nozzle exit to substrate surface gave a beam size of 1.98mm for cladding process. It is important to introduce a factor qualifying the beam in terms of its divergence, M^2, which helps to calculate the beam spot size at this distance. The optimum M^2 is 1 and the theoretical beam spot size is 1.44mm at the distance of 15mm from the central nozzle exit which appeared to agree with measurement of the burn print on the wood by Vernier calliper. And it was calculated for the laser beam used in this work was 1.954. The beam quality factor M^2 for this laser is 1.954 for theoretical value references.

3.2 Powder Feeder System

Powder is fed into the nozzle using a screw feed system. It has been [222] found that the feed rate of the powder is dependent on the screw size, screw speed, particle size and hopper pressure. As the screw was fixed and uniform material filled in the hopper, the only variation possible is the screw speed during this work. Consequently, the powder feed rate is related to the screw speed. As demonstrated in *Figure 3-6* and *Figure 3-7* the screw feed is driven by a motor such that the powder feed rate is related to the motor speed.

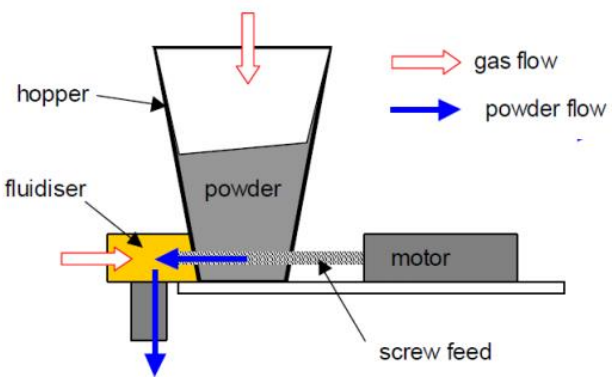

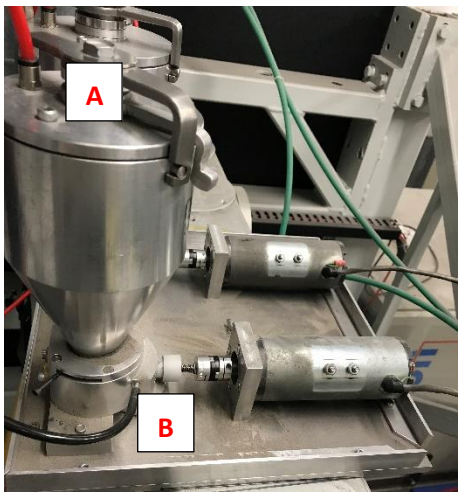

Figure 3-6: Powder Hopper/Screw Feed used in the research.

Figure 3-7: Motor Rare Controller in a unit of rpm.

The actual powder mass being driven down was measured over 1-minute at various speed settings on the controller. The relationship between the powder feed rate and motor speed can be seen in *Figure 3-8*.

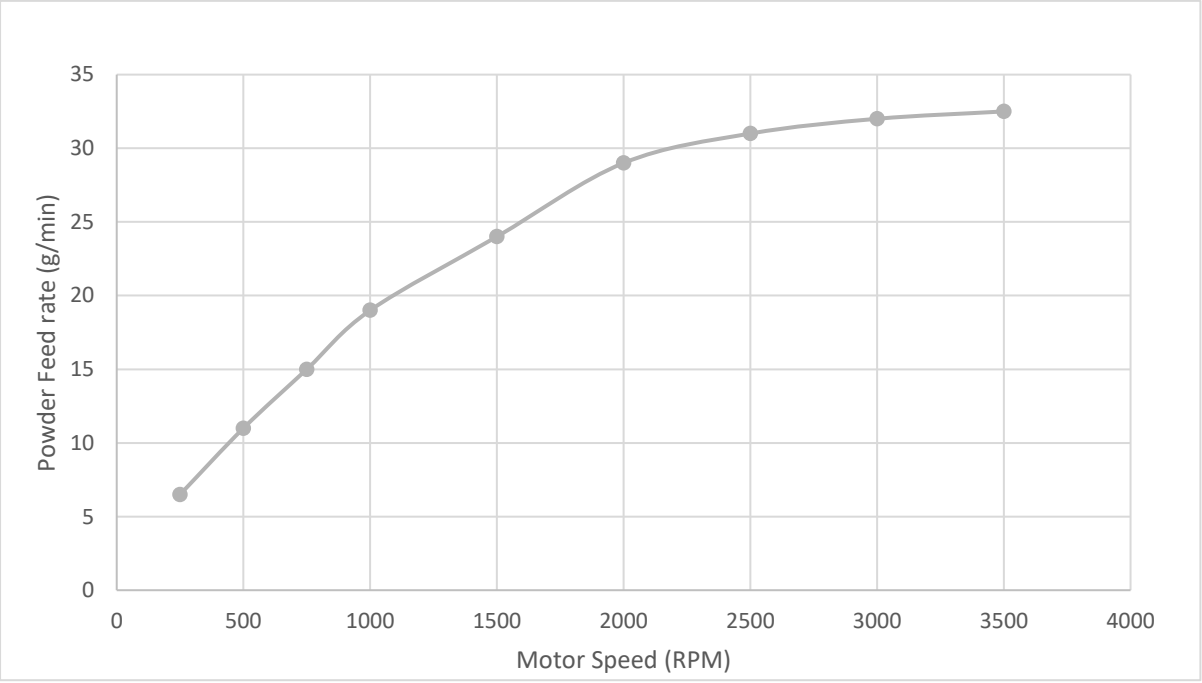

Figure 3-8: The relationship between powder feed rate against motor speed.

3.3 Powder Flow System

To avoid a blockage at the nozzle exit and provide a smooth flow of the powder, an assist gas is necessary. This helps the powder to be distributed evenly to the pipes after the splitter to make sure equal amounts of powder are delivered through each powder feed tube. The melted pool was shielded using Argon gas for preventing from oxidation. Argon is significantly cheaper and therefore costs can

be reduced.

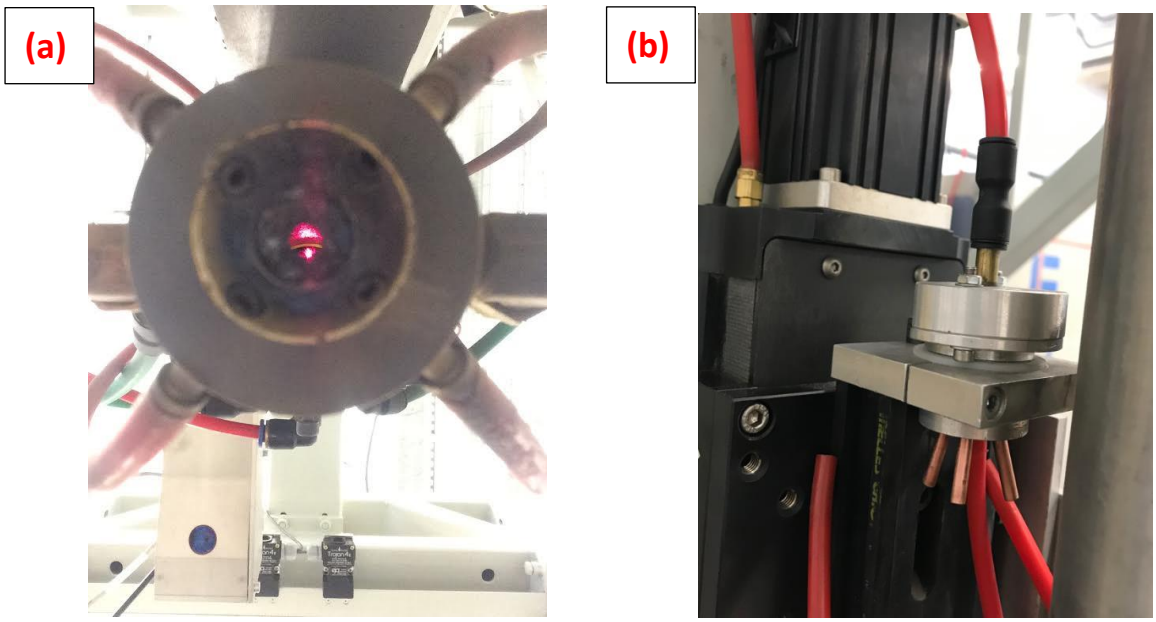

Figure 3-9: (a) Top-view of nozzle head, (b) Splitter insert dividing powers into 4 pipes uniformly.

The Argon is fed into the hopper system from two places, one from the top of the hopper above the powder level and the other is at the end of the hopper where the powder exists.

Figure 3-10: Gas Flow Rare Controller in the Middle used in this Work.

There are two gas system in this nozzle: G1 is the central gas and G2 is the pipe gas; by altering the two gas pressures, the 'Y' configuration shown in Figure 3-11 can be varied, which then affects the powder catchment efficiency and cladding beam volume.

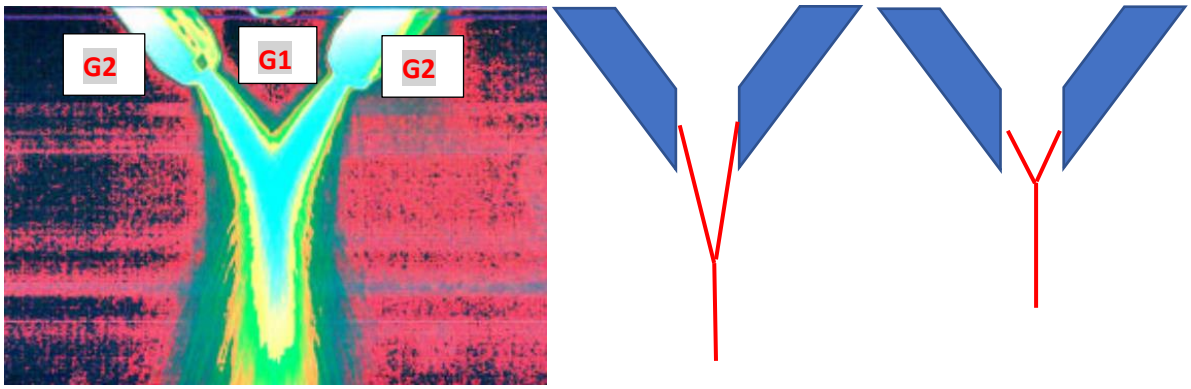

Figure 3-11: Example of powder cloud vertical collimation and Schematic of different 'Y' shape.

3.4 Specific Laser Nozzle Design

Powder is typically fed into the melt pool on a stream of inert gas whilst a secondary gas stream flows in parallel to the laser to prevent oxidation during the high build temperatures (Figure 3-12). A layer can be created in the shape of the part to be produced using a Computer Numerical Control (CNC) table. After each layer is produced, the laser and powder feed nozzle are moved up and followed by depositing a further layer on the previously produced layer. This process is repeated until the full-size part is created. The system can be said to act like a 'metal pencil' laying down a track of specified height and width determined by laser spot size [122]. The beam and powder nozzles are focused coincidently at the deposition plane. It is possible to incorporate up to 6 degrees of freedom for the position and motion of the deposition head.

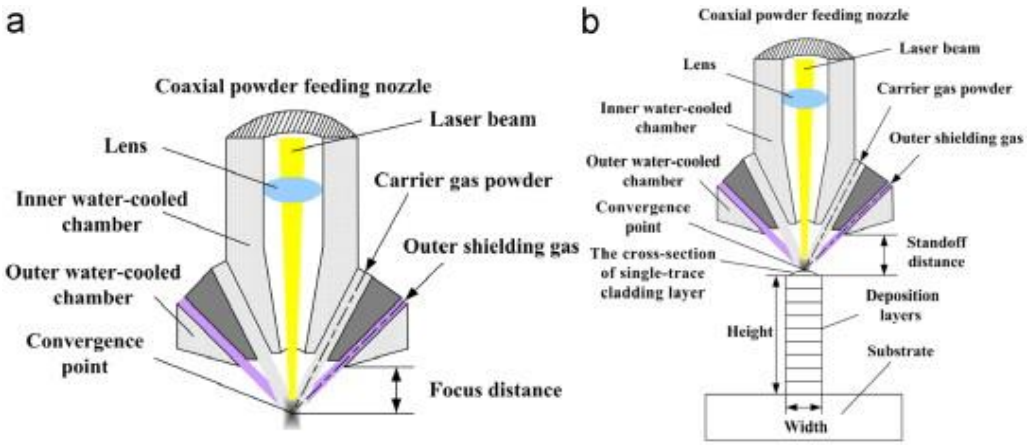

Figure 3-12: Schematic of co-axial powder feed nozzle (a) and existing deposited layers under nozzle.

As the incoming material is heated prior to deposition as it passes through the beam, it may be melted either during this pass through the beam or by thermal conduction once the powder is in the molten pool.

An improvement was made based on the coaxial nozzle system in Liverpool shown in Figure 3-13. This provides higher catchment efficiency of powder mass deposition with non-feedback step height control. This updated nozzle ports system can introduce omnidirectional cladding with low angle powder feed and low speed powder feed. In addition, this system reduces the costs and associated equipment. It is worth noting that the step height can precisely controlled and can produce different step height s like 0.2mm, 0.6mm or 1mm, respectively.

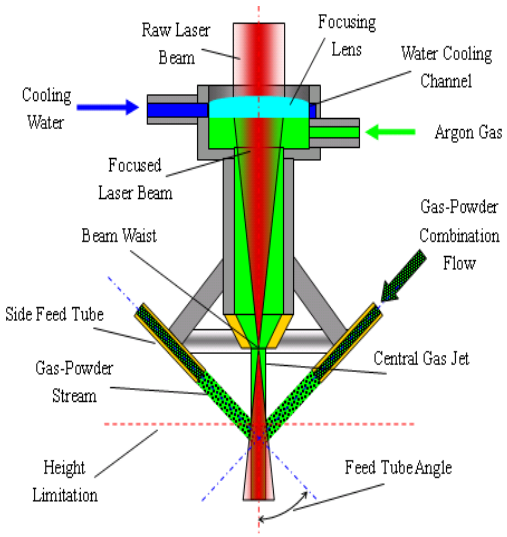

Figure 3-13: Schematic of Four-port powder feed nozzle and nozzle apparatuses used in this work.

3.5 CNC Workstation

The workstation consists of 4 axis CNC controlled stages, X-Y-Z and a rotation state. These are Aerotech AVS (Marix Churchill MAC V2E controlledusing a NUM1060) combined with NPIO drive amplifiers. The system is controlled with the Aerotech A3200 software-based system. A widow based NView application is used to jog a programme the system (Figure 3-14). An Aerobasic G-code is used to programme with either directly or by a post-processor.

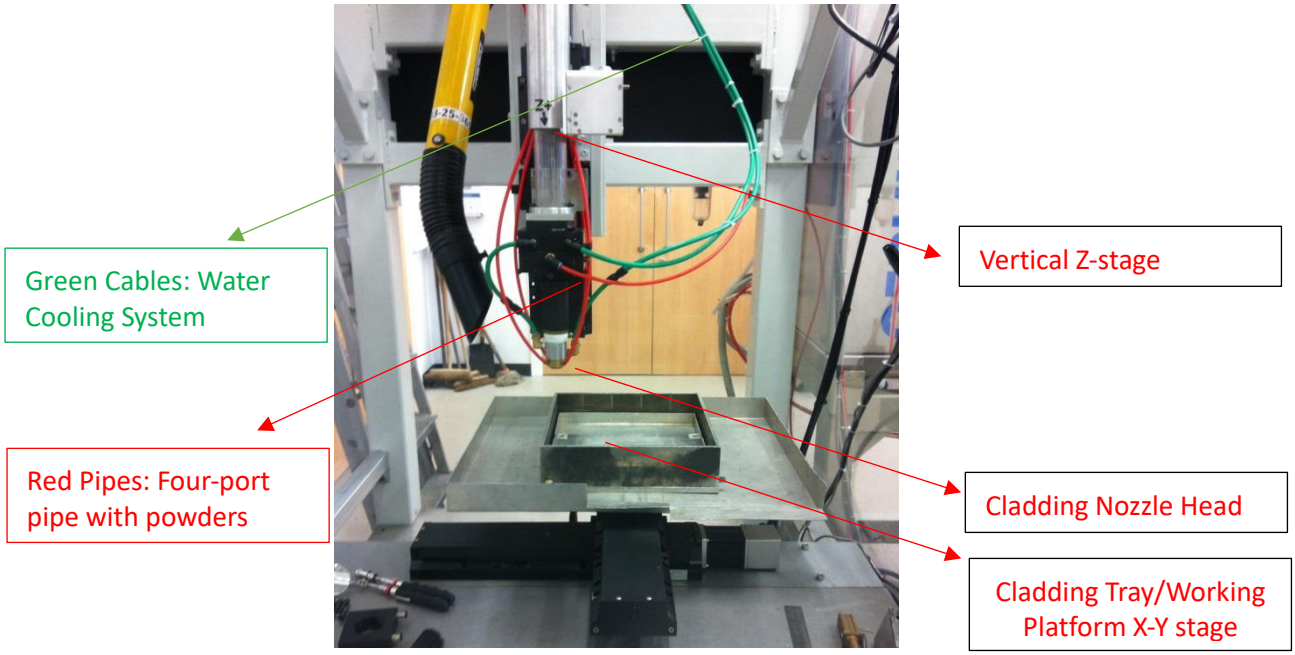

Figure 3-14: Schematic of Four-port powder feed nozzle and CNC table used in this work.

Design concepts are prepared and presented through a 3D CAD software like Solidworks, Creo and Catia etc. The CAD model can then be converted into a Parasolid or Tessellation Language (STL) file and imported into an AM setup with the help of a CADCAM software such as Alphacam Mill. The geometric shape in the Parasolid or other format files is sliced into thin layers (Figure 3-15). The movement of the depositing or fusing unit, and substrate, as well as other parameters are programmed by a post processor that deduces the G-code. The CNC table can be controlled using the G-code. The step height can be altered through the slicing macro by a selection box. Alphacam Mill offers a tool path generation for milling system, it has been re-tasked here for a reverse willing operation.

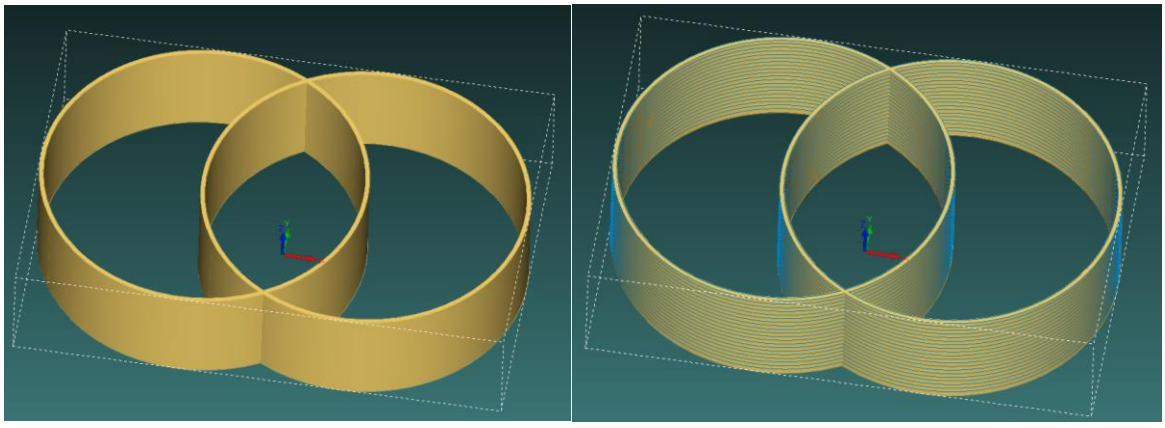

Figure 3-15: 3D model open in Alphacam Mill (a) and model sliced (b).

3.6 Cladding Material Selection and parameters

Regardless of laser beam, machining parameters and production properties, power is the critical factor that influences the physical process and processing results. A good understanding of the material

properties is essential help to realize the aim and objectives of this work.

3.6.1 Stainless Steel 316L (SS 316L)

Steel grades available for laser based additive manufacturing are mainly common austenitic stainless steels (AISI 316L/EN:1.4404/X2CrNiMo17-12-2) [233] and AISI 304L/EN: 1.4306/X2CrNi19-11 [234], maraging steel (18Ni-300/1.2709/X3NiCoMoTi18-9-5) [235], as well as precipitation hardenable stainless steels (17-4 PH/EN: 1.4542/X5CrNi- CuNb16-4/AISI: 630 and 15e5PH/EN:1.4545/X5CrNiCu15-5 [236]. Besides, a martensitic cutlery grade (AISI 420/EN:1.4034/X46Cr13) has also been investigated for Laser beam melting (LBM) usage [237], while in Electron beam melting (EBM) mainly tool steels (H11/EN: 1.2343/X37CrMoV5-1 and H13/EN: 1.2344/X40CrMoV5-1 [238] as well as austenitic SS 316L have been used. For LMD, the use of austenitic SS 316L [239] is also reported. The alloys described above satisfy typical requirements of general-purpose applications, as well as increased requirements on strength and hardness.

The material properties for stainless steel 316L are available in a number of studies in the literature. Abouda *et al.* conducted microhardness on simple wall structures fabricated from 316L stainless steel with varying process parameters [240].

The wrought values for 316L stainless steel was selected lately for this research which are shown in Table 3-1. When comparing these to the results achieved by both Fenandes de Lima and Zhang *et al [92]*. It is clear the cladding process can have a strengthening effect depending upon process parameters.

Table 3-1: Mechanical properties of wrought 316L stainless steel [241]

Yield Stress (MPa)	Ultimate Tensile Stress (MPa)	Total Elongation %	Elastic Modulus (GPa)
170	485	40	193

The material used for both test structures was 316L stainless steel powder with the composition (in % weight) shown in Table 3-2.

Table 3-2: Composition of 316L stainless steel used in experiments

C	Si	Ni	Cr	Mo	Mn	Fe
0.03%max	1%max	10-14%	16-18%	2-3%	2%	balance

3.6.2 Inconel 625 (IN625)

Due to the high corrosion and oxidation resistance properties of Inconel 625 alloy which contains Ni-Cr-Mo-Nb (shown in Table 3-3), Inconel 625 has always been a material of choice for cladding components exposed to seawater for long-term protection with high resistance of corrosion. Table 3-4 presents the typical properties of IN625.

Table 3-3: Chemical compositions (wt.%) of the alloy matrix powder (Inconel 625) and substrate material used.

Materials	C	Cr	Mo	Fe	Mn	Nb	Al	Si	Ti	Ni
Inconel 625 powder	0.02	19.6	5.8	1.6	–	3.9	0.1	0.4	0.15	Balance

Table 3-4: Typical properties of IN625.

Property	Value
Density	8.44g/cm3
Melting point	1350°C
Coefficient of expansion	12.8µm/m.°C (20-100°C)
Modulus of rigidity	79000 MPa
Modulus of elasticity	205.8K MPa

It is a non-magnetic nickel-chromium-molybdenum nickel-based superalloy strengthened and also precipitation hardenable due to the precipitation of fine metastable phase γ'' (Ni3Nb) after annealing over a long period in the temperature range 550-580°C. It is known for its high temperature strength and excellent corrosion resistance in a wide range of corrosive media, being especially resistant to crevice and pitting corrosion.

3.7 Substrate Material and Preparation

A good fusion zone and solid metallic bond of the first layer are essential. There are determined by the processing condition and material selection of the substrate and the surface condition. Brittle intermetallic compounds between cladding layer and substrate should be avoided as insufficient metallic compounds can result in poor dilution and an unsolidified melt pool causing a cladding failure in the Z-axis. In addition, different thermal expansions of different metals would cause insufficient fusion bonding and delamination would occur under this incoherent condition. Last but not the least, the cladding process would deform a thin substrate.

As a result, substrates are normally selected with the same or similar mechanical properties of the cladding material and with sufficient thickness to avoid deformation during the cladding process.

The substrate material selected in this work was 43A mild steel in the form of flat plates of dimensions 100X100X10mm. This material was chosen based on ready availability, cheapness and the most important fact was that it would not produce intermetallic with the cladding materials (316L Stainless Steel and Inconel 625). Thermal expansion mismatching existed between the substrate material and cladding material as stainless steels expand by roughly 50% greater than mild steels, but the fusion bond between them was sufficient to avoid delamination occurring from the substrate.

The surface condition of substrates was essential for cladding. The first layer needed to be clad with a sufficient fusion zone and a good melt pool generation so that it can provide solid support to the following layers. It was found that roughness, surface films, oxidation and contamination of the substrate surface would result in a variation on the reflectivity and uneven distribution of layer height and volume. For more reflective substrates, these need to be coated with graphite or a similar material to enhance absorption of the laser beam.

To make sure the substrates are oil free and do not have excessive oxidation, they were cleaned with ethanol and better sandblasted so that to remove contaminants and provide a roughened surface to increase coupling of the laser beam to the substrate as well as reduce the reflectivity of the surface.

3.8 Analysis Equipment

The microstructures for all samples were analysed using optical microscopy techniques (shown in Figure 3-17) and microhardness tests. Using Infinity Capture software several images were taken at key places. Due to the bulk number of samples to be analysed images were taken at specified datum points for all samples and limited to low magnification (50x, 100x and 200x). Analysing the samples in this way allowed an efficient investigation of the three key parameters: layer step height, distance from the substrate and intersection points which labelled in green cross-section in Figure 3-16.

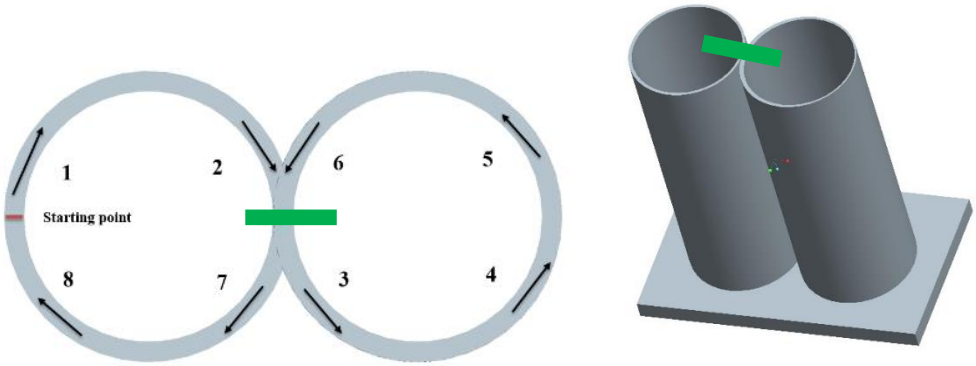

Figure 3-16: An Example of the cladding part top view (left) and standard view (right).

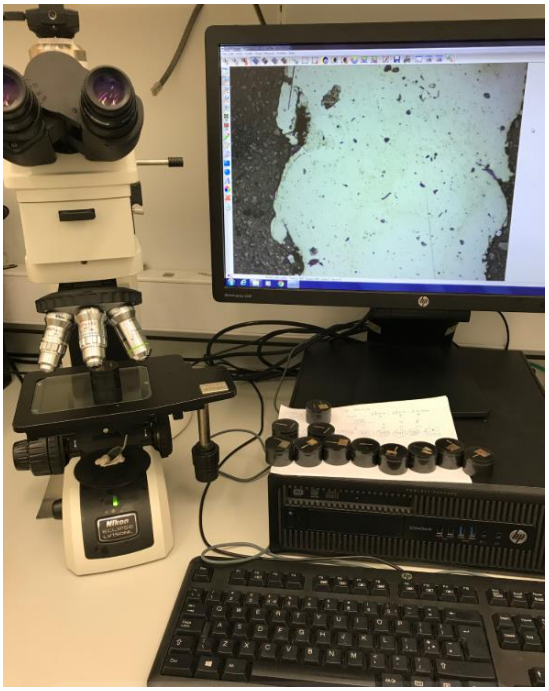

Figure 3-17: A Nikon eclipse LV150NL machine used to collect microstructures.

The microhardness tests involved taking two hardness readings at every datum point and averaging the result to try and reduce the experimental error. A Vickers hardness measurement was taken with a 500g load on the indenter of a Mazurek hardness tester. This hardness tester is displayed in Figure 3-18.

Figure 3-18: Mazurek hardness tester used for this work.

Compressive and tensile tests were performed using a 5kN Instron load cell. The samples were mounted longitudinally within the load cell as shown in Figure 3-19. This was partially due to fears that the samples might overload the load cell if mounted axially, however it was also believed this mounting would provide better results for comparison. The samples were tested to display the first yield point.

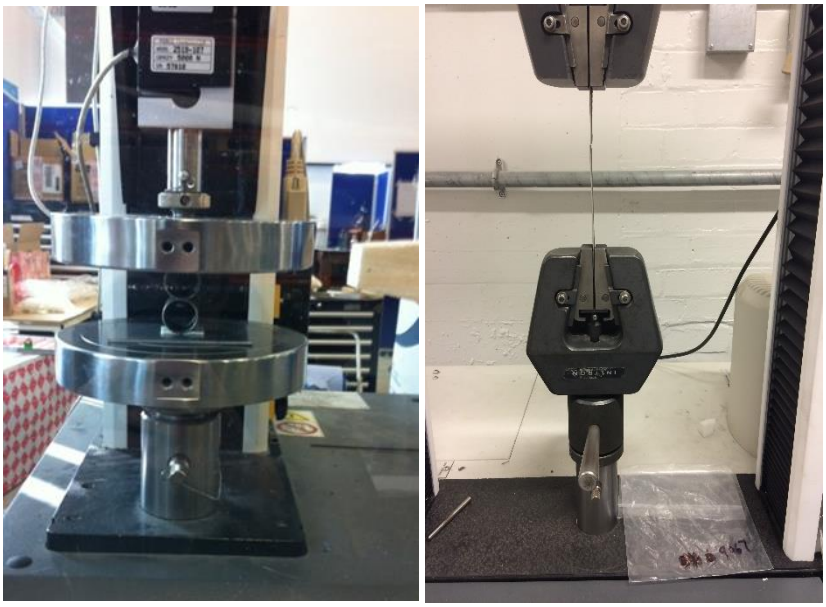

Figure 3-19: Compression and Tensile testing arrangement using INSTRON machine.

Chapter 4 Blown Powder Laser Cladding of Stainless Steel 316L

Laser cladding has attracted extensive research over the past 40 years. Research in laser cladding covers many scientific issues, including processing techniques, physical and chemical properties of deposited materials and clad—substrate interfaces, microstructure and phases, rapid solidification phenomena, modelling and simulation, and systems engineering and applications. In details, there are lots of factors affecting blown powder laser cladding results in terms of microstructures and mechanical properties, such as cladding speed, gas flow rate, motor speed which is related to feed rate and power.

This chapter, focusing on these influencing factors and material properties, summarizes the state of the art on two fundamental scientific aspects: laser power and the material characteristics. A review of the microstructural refinement extended solid solution, metastable phases, amorphous structure, and directional solidification has been introduced in Chapter 2. In this chapter, 316L stainless steel was selected as the cladding material on the mild steel substrate. Steel is still the most common engineering material. Therefore, steel is obviously also a material of high interest for AM. Various factors were investigated to different degree influences on the microstructures. In the end, it was found that lower powder about 320W was possible for cladding components and capable of producing materials with designed homogenous macro/microstructures and uniform properties.

4.1 Study on Blown Powder Laser Cladding of Single Tracks

Although lots of experiments with different materials have been carried out to investigate microstructure characteristics, microhardness, residual stresses distributions independently in the components through laser cladding, there are few detailed reports focused on the quality of the wall according to the processing parameters. However, the single clad geometry is important to control the cladding procedure accurately and build a component lately. Besides, it will be meaningful to integrate multi-layer geometry predictions with microstructures characteristics and mechanical behaviours identification, for instance microhardness, which are beneficial for the precise cladding of complex components and offer bases for numerical simulations of the laser cladding process. In this section, single cladding track is built and discussed. The cladding time is taken into account in order to find the best parameters. The microstructure morphology is analysed.

4.1.1 Exploration of Influencing Factors on Cladding Bead

A series of clad tracks will be made using Stainless Steel 316L on a mild steel substrate using the following parameters: 3cm long clad tracks are to be created at speeds of 2mm/s to 18mm/s (in 2mm/s increments), for powers of 600W to 1200W (in 200W increments) at a fixed motor speed of 1k rpm which means powder feed rate is 19g/min (Figure 3-8), A carrier gas (Argon) flow, fixed at 4L/min, carries the powder while a secondary gas flow, fixed at 2.5L/min, shapes the powder stream. The laser beam is focused on the substrate surface while the working distance between the nozzle and focus plan remains constant at 5mm.

Figure 4-1 shows the cladding tracks under changing power and cladding speed. It was obvious to be observed that the cladding bead with and volume were affected by laser power and cladding speed.

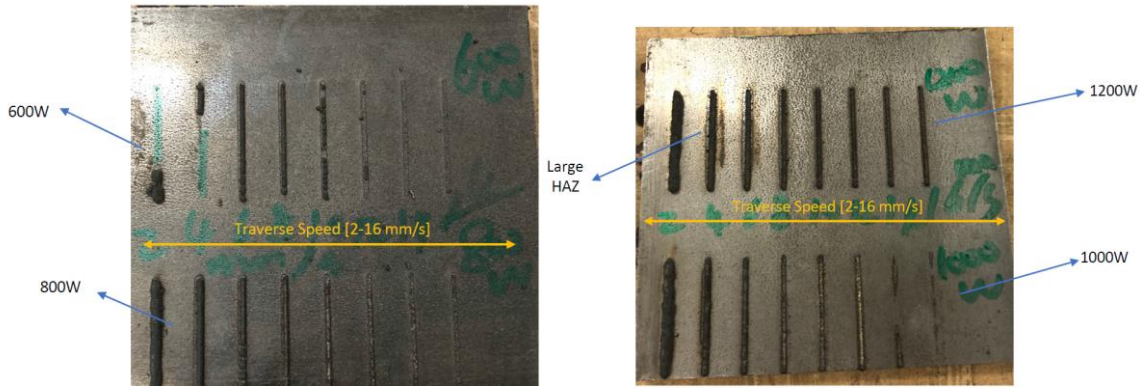

Figure 4-1: Cladding profiles for 600W, 800W, 1000W, 1200W, with varying laser speed from 2-18mm/s.

It can be from the figure that some cladding track was not deposited succeed on the substrate as the energy absorbed was not enough for the formation of melt pool. However, excessive

laser power would lead to the remelting of the cladding, affecting its mechanical property such as the hardness, the grain structure and the geometry characteristics of cladding track width and height.

The clad bead profile generated by the interaction of the laser beam and the delivered powder is defined according to three types dependent upon its cross section. These are shown in Figure 4-2 below[162]:

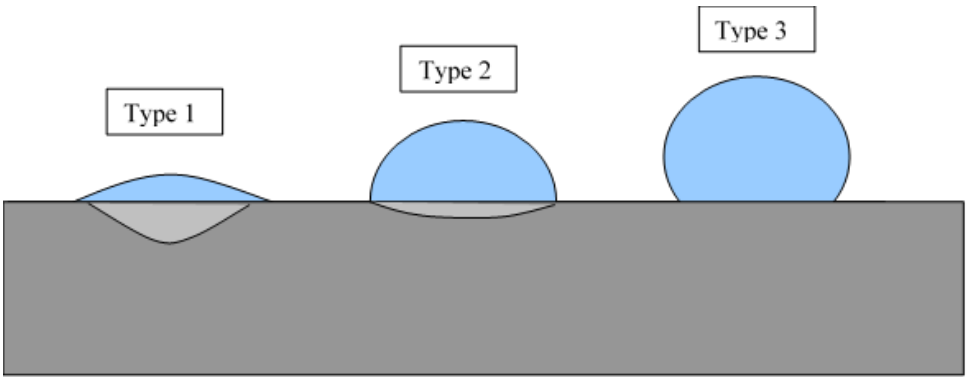

Figure 4-2: Cladding bead profiles and types classification.

Type 1 occurs when there is a greater amount of laser power than is required to generate the clad with the powder available and is characterised by excessive dilution of the clad into the substrate material. It is detrimental to laser surface cladding due to the fact that alloying of the clad material with the substrate has taken place to an extent greater than the minimum dilution consistent with fusion bonding. However, when the substrate material is of the same alloy composition of the clad bead, as is the case of a clad bead being deposited upon earlier layers in laser cladding, dilution ceases to be a relevant consideration from an alloying viewpoint.

Type 2 is the best type of clad profile from a layering standpoint as it has the minimum dilution consistent with fusion bonding mentioned above and would therefore correspond to the highest catchment efficiency during a layered build. Its aspect ratio, however, would not be best from the point of view of area coverage due to the likelihood of incomplete fusion at the edges. For area coverage a width: height ratio of 5 has been found to be the most suitable.

Type 3 occurs when there is an excess of powder compared to the laser power necessary to create the clad bead. It is characterised by a lack of fusion between the generated bead and the substrate or preceding layer. In cladding or in building this will result in a discontinuous clad bead and/or delamination from the substrate or preceding layer.

To verify the cladding bead quality, a section was made cross the middle of the cladding track and micrographs (Figure 4-3) were taken to be analysed in the terms of cladding track volume and cladding bead types. And Table 4-1 explains the cladding bead conditions and results respectively for these 3 types.

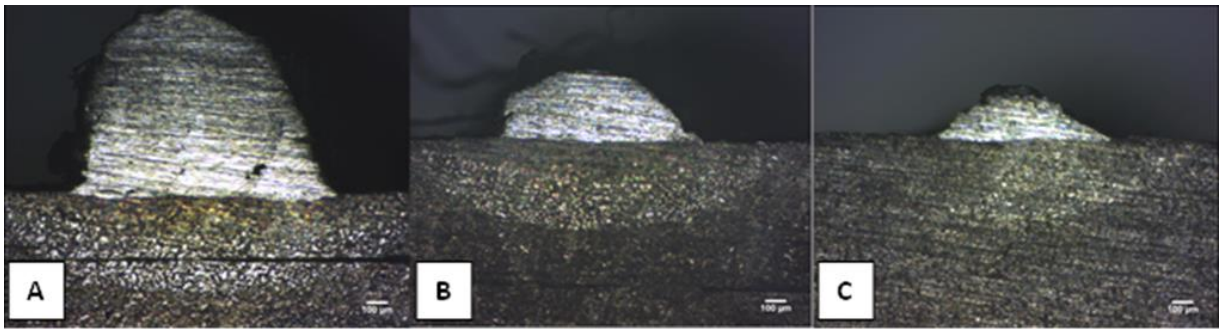

Figure 4-3: Cladding bead of stainless steel 316L taken from A (type 3), B (type 2) and C (type 1).

Table 4-1 demonstrates the analysis on single cladding bead from the cladding conditions and deuces the relevant cladding result generally.

Table 4-1:Laser cladding bead conditions and analysis for 3 types.

Profile	Conditions	Result
Figure 4-3 (A)	High powder feed rates or low power densities	Aspect ratio (AR) incorrect for overlapping (AR = width/height)
Figure 4-3 (B)	Optimum parameters (powder feed rate, power density and cladding speed)	Good, low dilution, fusion bonded track. Favoured for overlapping tracks to cover an area.
Figure 4-3 (C)	Low powder feed rates or high-power densities	Excessive and (in this case) irregular dilution

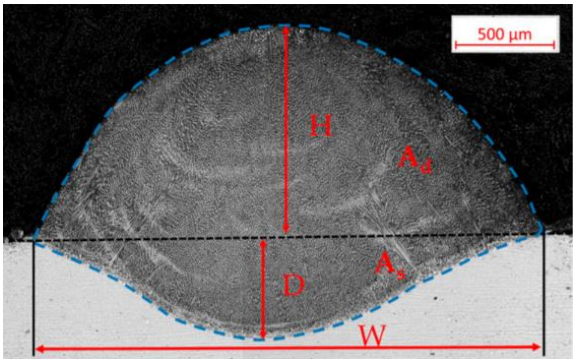

Figure 4-4: A typical directed energy deposition deposit depicting geometric measurements of interest.

A typical cross-section of a single-track DED (directed energy deposition) deposit depicting geometric measurements of interest is illustrated in Figure 4-4. The DED material showed a distinct appearance compared to the wrought microstructure present in the substrate region. The horizontal dotted line marked in the figure is indicative of the original substrate surface before deposition. The values of height (H), width (W) and depth (D) were obtained by measuring dimensions. The measurement of area of deposition and dilution was done using Image-J software (version 1.5). The area above the fine dotted line indicated the area of deposit (A_d) and the area below indicated area of dilution (A_s), measured in mm^2. Dilution percentage was obtained by the equation:

$$\%Dilution = \frac{\mathrm{As}}{\mathrm{As+Ad}} \qquad \text{Eq 4-1}$$

Table 4-3, Table 4-4 and Table 4-5 shows the measurement results on each cladding bead under different powers starting from 600W as the referencing of current researches from other groups.

Table 4-2: Volumes and cladding type classification for cladding tracks for 600W.

Cladding Speed [mm/s]	Cladding Bead Width [µm]	Cladding Bead Height [µm]	HAZ Height [µm]	HAZ Width [µm]	Aspect Ratio
2	1261	N/A	N/A	N/A	N/A
4	1253	N/A	479	N/A	N/A
6	1248	N/A	448	N/A	N/A
8	1175	857	453	1832	1.371
10	1003	545	388	1785	1.840
12	890	322	379	1660	2.764
14	605	90	355	1492	6.722
16	581	112	314	1455	5.188
18	N/A	N/A	275	1311	N/A
20	N/A	N/A	269	1306	N/A

Table 4-3: Volumes and cladding type classification for cladding tracks for 800W.

Cladding Speed [mm/s]	Cladding Bead Width [µm]	Cladding Bead Height [µm]	HAZ Height [µm]	HAZ Width [µm]	Aspect Ratio
2	1181	N/A	N/A	N/A	N/A
4	1143	N/A	501	N/A	N/A
6	1176	1233	470	N/A	0.954
8	1145	862	451	1210	1.328
10	982	707	412	1015	1.389
12	899	610	388	990	1.474
14	623	298	331	889	2.091
16	536	285	301	967	1.881
18	N/A	187	279	889	N/A
20	N/A	N/A	258	967	N/A

Table 4-4: Volumes and cladding type classification for cladding tracks for 1000W.

Cladding Speed [mm/s]	Cladding Bead Width [µm]	Cladding Bead Height [µm]	HAZ Height [µm]	HAZ Width [µm]	Aspect ratio
2	1703	N/A	572	N/A	N/A
4	1688	N/A	553	N/A	N/A
6	1611	4487	548	N/A	1.357
8	1555	1101	503	N/A	1.412
10	1413	850	489	N/A	1.662
12	1378	620	473	1879	2.223
14	1323	430	433	1830	3.077
16	1288	312	406	1812	4.128
18	1202	298	360	1603	4.034
20	1274	289	N/A	N/A	4.408

Table 4-5: Volumes and cladding type classification for cladding tracks for 1200W.

Cladding Speed [mm/s]	Cladding Bead Width [µm]	Cladding Bead Height [µm]	HAZ Height [µm]	HAZ Width [µm]	Aspect ratio
2	1729	N/A	762	N/A	N/A
4	1680	N/A	665	N/A	N/A
6	1654	1398	562	N/A	1.183
8	1613	1018	534	N/A	1.584
10	1514	860	491	N/A	1.760
12	1428	573	473	1799	2.492
14	1380	553	454	1790	2.495
16	1301	402	404	1782	3.236
18	1152	300	292	1753	3.840
20	1129	247	279	1748	4.571

*N/A: not available to measure because the microstructure is beyond the magnification zoom.

In addition to the three types of profile mentioned above, the aspect ratio of the bead profile can be affected by the cladding speed in that increased cladding speeds will reduce the clad step height independently of the level of dilution of the type of clad bead generated. This was initially noted by Weerasinghe [242]. Hence cladding step height can be controlled by suitable selection of cladding speed in conjunction with in-process monitoring as a means of compensation for retained heat effects during a build.

As cladding speed is one of the most important process parameters in laser cladding which attracts lots of researchers' attention. And Gu's group also concluded the same findings that the cladding bead height, width and HAZ decrease accordingly with the increase of cladding speed [243]. They also had the same conclusion that the cladding tack width increased monotonically with the increasing laser power.

As a sufficient cladding track, it should be with a minimum dilution into the substrate concomitant with low or negligible porosity. A measurement on HAZ width and height was taken to investigate the effect of cladding speed and laser powers (Figure 4-5 and Figure 4-6).

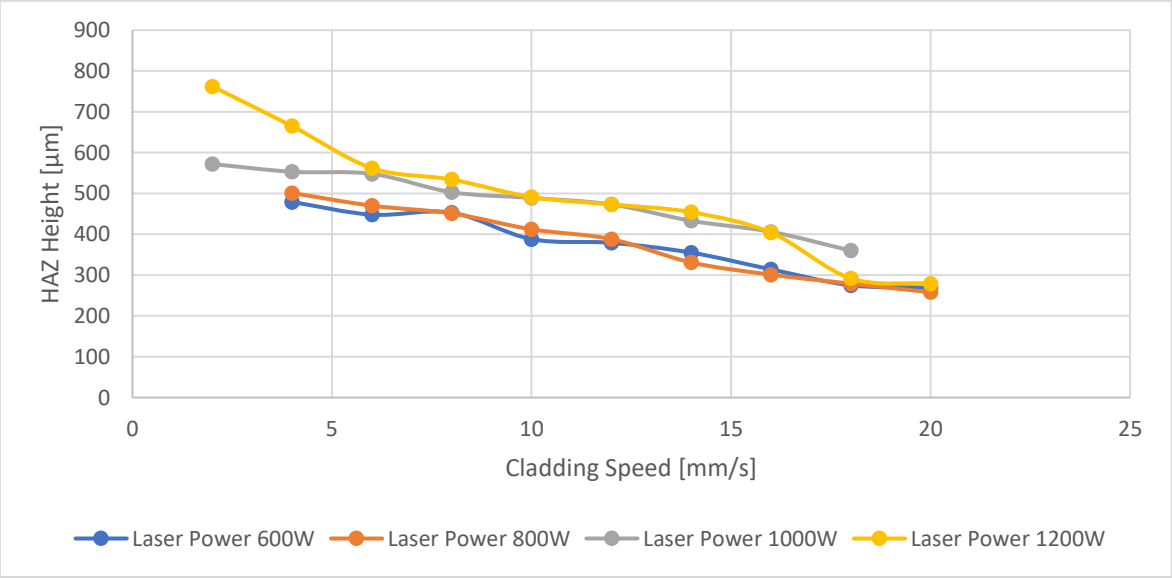

Figure 4-5: HAZ height against cladding speed under different powers.

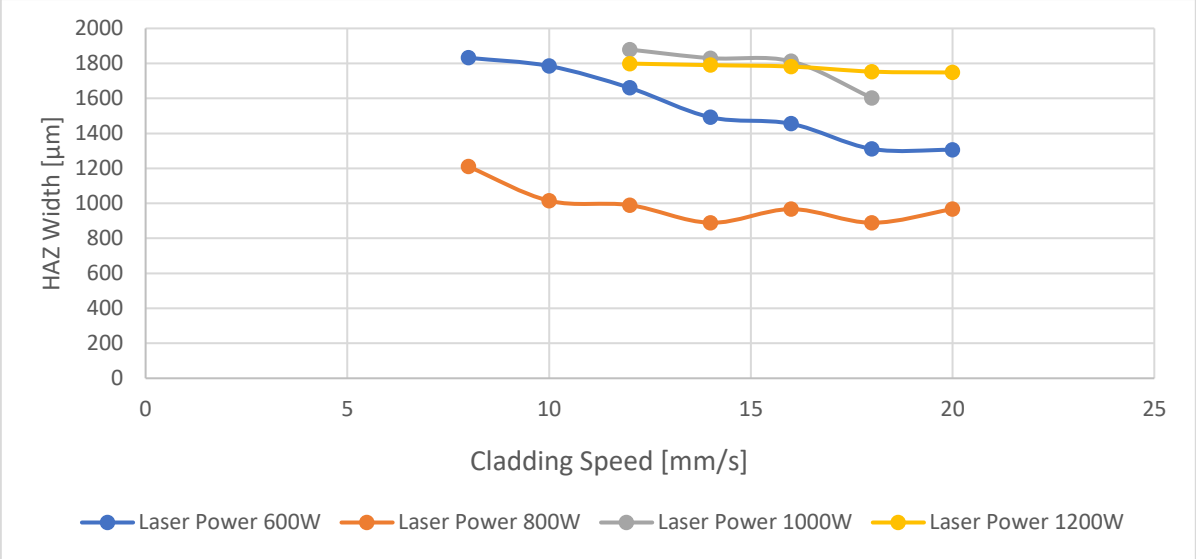

Figure 4-6: HAZ width against cladding speed under different powers.

Although the results for the HAZ are much more varied, there is still a clear trend. As the cladding speed increases the HAZ height and width both decrease. There is also a general trend that as the laser power increases, the HAZ width and height also increase. It is desirable to have as small a HAZ as possible as it causes a change within the metal's microstructure thus weakening the zone around which the cladding is deposited.

From the results in Table 4-2 to table 4-5, the optimal laser power and cladding speed chosen were those that produced the best cladding. A good clad is one that has low dilution; produces a small HAZ; bonds well to the surface; and has a good height to width ratio, much like in type 2 bead profiles.

Therefore, the optimal settings chosen were a 1000W laser power and a speed of 10mm/s under a fixed powder feed rate of 19g/min, coaxial gas flow rate of 8L/min and powder gas flow of 2.5L/min.

Another set of cladding parameters was designed to investigate the varying metal powder mass effect on the cladding bead profiles using selected powder 1000W and speed of 10mm/s. To achieve this, the laser power and cladding speed were kept constant whilst the rotational speed (RPM) of the powder delivery system was varied from 250 rpm to 2000 rpm in steps of 250 rpm.

Table4-6 presents the details of each cladding tracks and Figure 4-7 shows the cladding track volume against powder delivery mass in unit time.

Table 4-6: Cladding track properties measured for different powder feed rates.

Powder Feed rate [g/min]	Motor Speed [rpm]	Cladding Bead Width [µm]	Cladding Bead Height [µm]	HAZ Height	Aspect Ratio	Cladding Volume [mm^3]
6.5	250	1202	273	469	4.403	7.731
11	500	1228	238	449	5.160	6.886
15	750	1399	417	458	3.355	13.746
19	1000	1392	523	404	2.662	17.153
22	1250	1435	602	471	2.384	20.354
24	1500	1398	647	409	2.161	21.312
27	1750	1479	689	N/A	2.147	24.010
29	2000	1425	742	N/A	1.920	24.913

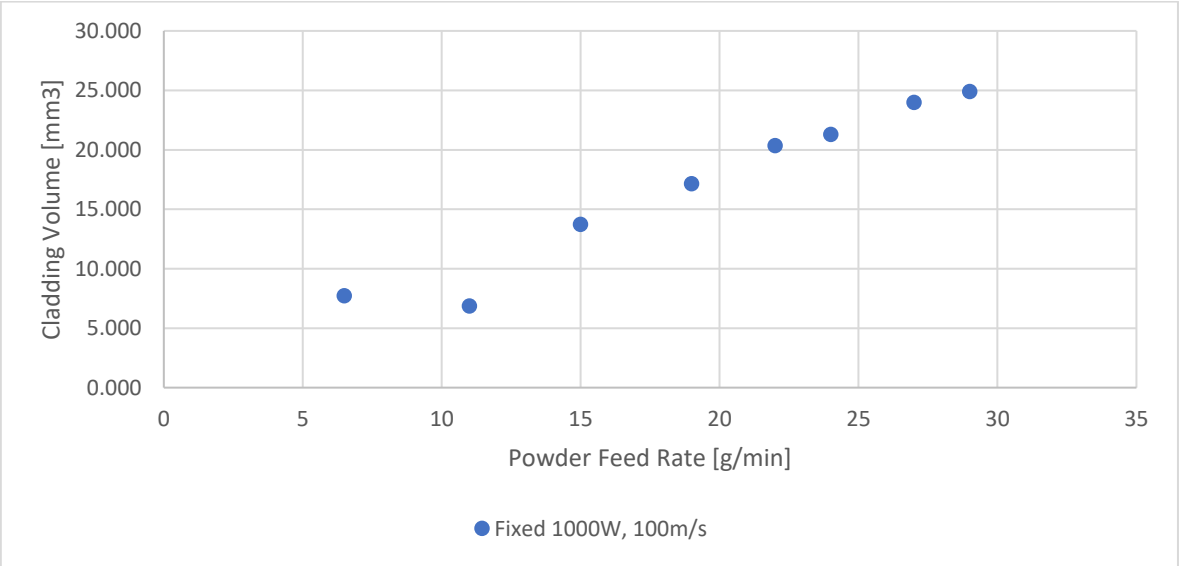

Figure 4-7: Cladding track volume against powder mass delivered.

It is clear from the results in Figure 4-7 that as the powder delivery rate increases, the track volume also increases. This is expected as all other laser settings were kept constant, so more metal powder is melted during a track application. The relationship however is not linear as the track volume begins to plateau. This is because the laser power is not sufficient to melt all the powder after a specific flow rate. The excess powder is deposited to the edges of the cladding, where some of it melts through conduction with the cladding and the substrate. An example of this can be seen in Figure 4-8.

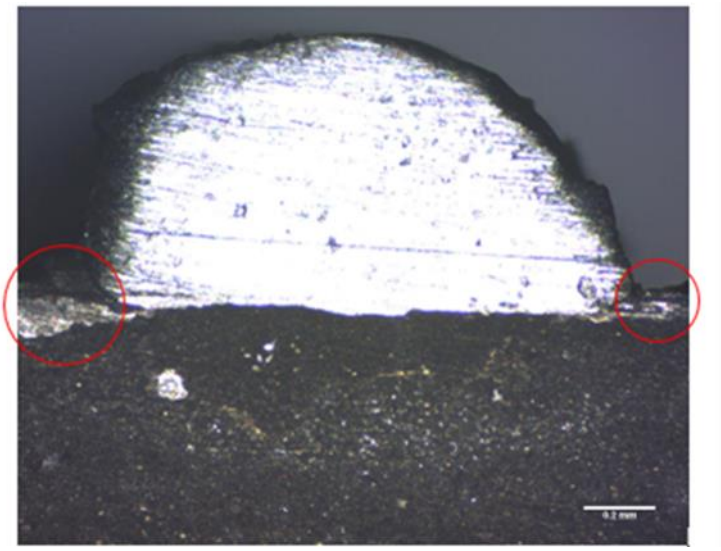

Figure 4-8: Cladding bead taken with power of 800W, speed of 8mm/s, 18g/min of feed rate, 8&2.5L/min coaxial and powder gas flow rate.

Figure 4-7 also clearly shows that as the metal powder mass increases, so does the clad volume. The bead type again ranged from type 3 to type 1 over the range of powder feed rates. This is because a larger flow rate of powder is being fed to the laser per unit time so a larger clad is formed. However, at a set power and cladding speed, the clad volume plateaus because there is too much powder present for the laser to melt per unit time. If the powder rate is too high, the laser does not have enough energy to melt all the powder, resulting in it falling to the sides of the cladding as shown in Figure 4-8. This is an unwanted effect as the cladding and substrate still contain enough thermal energy to melt the excess powder creating an unwanted deposit which would affect the aesthetics of the clad. From the results, the best feed rate for the setting used was 18g/min.

HAZ height and width for each cladding bead under fixed power and cladding speed were also plotted in Figure 4-9. It can be observed that the powder delivery mass increases, the HAZ height decreases as more thermal energy is removed from the laser by the powder. Note it was not possible to assess the HAZ width as it was larger than all provided images. It is predicted that the HAZ width would decrease in a similar pattern to the HAZ height for the same reason which need to be further addressed if possible.

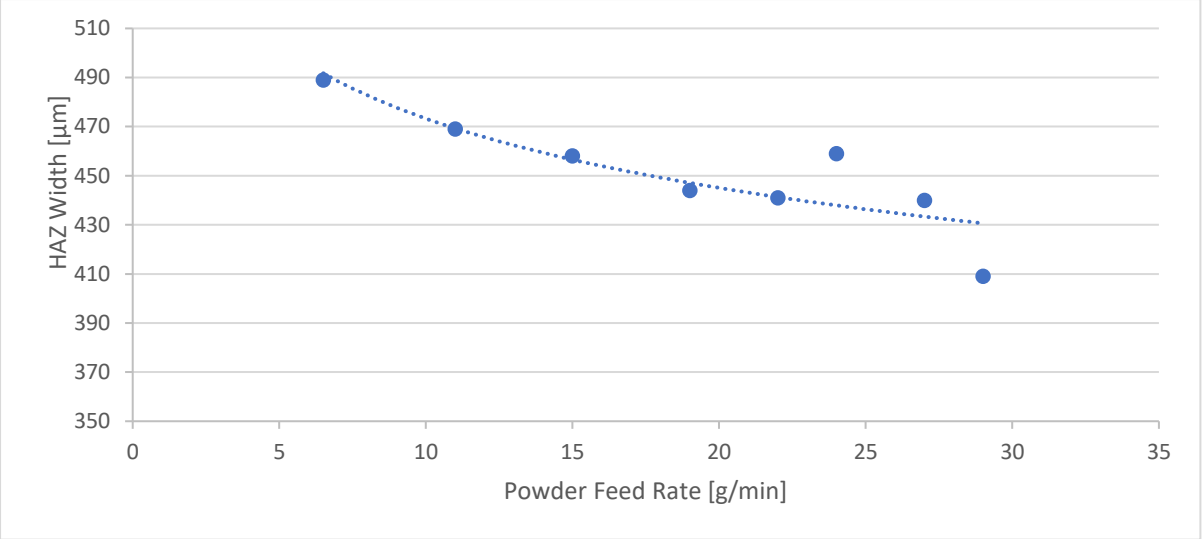

Figure 4-9: HAZ height vs powder feed rate (power of 1000W, cladding speed of 10mm/s).

In industry, being lean is the main aim for any manufacturing process, therefore minimal waste is desired. The excess powder is a waste of material which is a detrimental cost as well as the potential for post machining being needed to remove the melted powder. The optimal powder flow rate must also be considered alongside the laser power and head speed to produce the most efficient process with the best clad at a minimal cost.

4.1.2 Grain Structure Development During Solidification

The grain structure in most castings has three distinct zones: the chill zone, columnar zone, and equiaxed zone, shown in Figure 4-10. Solidification starts with fast nucleation of equiaxed crystals with random orientation in extremely supercooled liquid near the mould wall. The narrow band of small equiaxed crystals near the cold mould wall is called the chill zone. Due to the latent heat released by the first forming equiaxed grains, the nucleation rate dramatically decreases. Grains with preferred crystallographic orientation <100> which are most parallel to the direction of maximum temperature gradient grow fastest in the direction of heat flow usually normal to the mould wall. Those grains with a strong preference in orientation normal to the mould walls form the columnar zone. At the same time, spherical, randomly oriented crystals with isotropic properties are formed by nucleation in the most constitutionally supercooled inner liquid and on broken dendrite arms from columnar zone crystals transported by liquid flow into the centre [244]. The equiaxed zone in the centre of the mould consists of equiaxed grains with much larger size than those in the chill zone.

The transition from columnar grains into equiaxed grains called CET plays a very important role in the formation of centreline segregation and inner cracks, in the continuous casting process. Increasing the

area of the columnar region can worsen the centreline segregation [245].

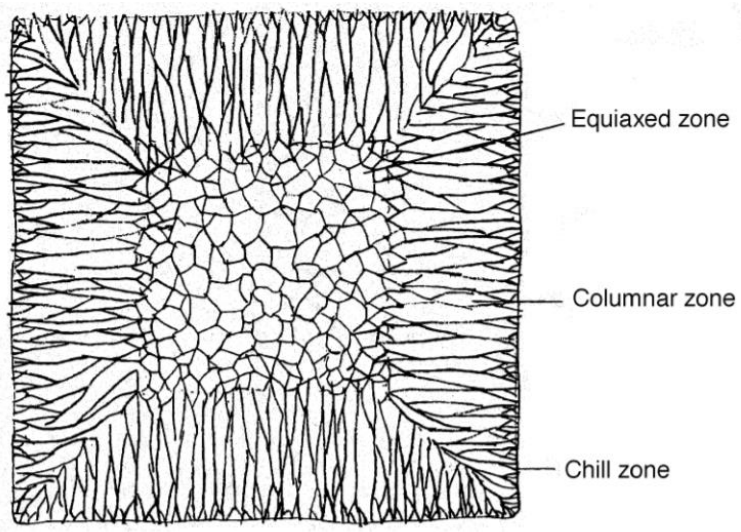

Figure 4-10:Characteristic grain structure in a cross section of as cast steel[246] .

4.1.3 Single Cladding Bead Morphology

The cross-sectional morphology for one-half of a single-track deposit is shown in Figure 4-11, as the other half of the cross-section was semi-symmetrical. The deposit can be broadly distinguished into three separate regions, the top, the middle and the bottom areas based on morphological differences observed in microstructural feature present in these discrete regions depicted respectively.

The bottom and middle regions closer to the substrate can dissipate heat much faster compared to the top region, and hence yielded columnar dendritic microstructures and relatively lower segregation of Nb-rich phases [247]. An interplay between thermal gradient (G) and growth rate (R) determined the cooling rate and substructure formation during solid-liquid (S/L) transformation. The G is higher in the bottom region where relatively cooler substrate was in contact with the melt-pool which led to a high G/R ratio which preferentially formed columnar dendritic structures as the planar and cellular growth fronts terminated prematurely [248]. The G value gradually decreased towards the top region of the deposit where equiaxed grain morphology was noticed [249]. The dendritic growth at the top edge of the deposit indicated a secondary growth front that nucleated from partially melted powders and also due to shielding gas interaction with the melt-pool, that provided a suitable condition for heterogeneous nucleation away from the solidification front [250]. The heat dissipation by partially melted powder particles is minimal as compared to the substrate, and the cooling rates achieved in this region are low compared to the bottom of the deposit.

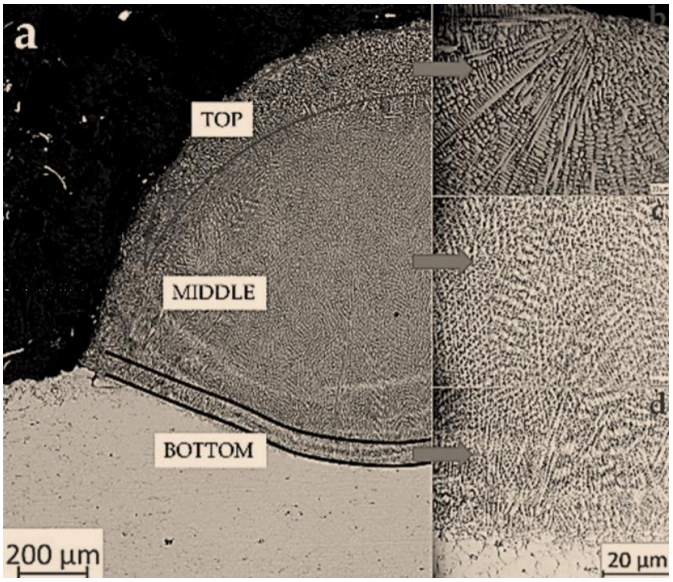

Figure 4-11: (a) A typical morphology of a deposit; magnified images of (b) top; (c) middle; (d)bottom regions of the bead.

4.1.4 Conclusions on Influencing Factors on Cladding Bead

The quality and profile of laser cladding are affected by many processing parameters and it can be quantified by changing three main parameters: laser power, cladding speed and powder feed rate. In general, it was found that increasing the laser power and powder feed rate while decreasing the cladding speed would increase the clad volume due to more powder being melted onto the substrate per unit time.

Decreasing the cladding speed or increasing the laser power applied more laser energy onto the substrate per unit time, thus melting more powder and increasing the volume of the cladding. Increasing the laser speed results in an overall faster process however a higher laser power is required to maintain a consistent clad of good quality. In industry, a balance must be made between these parameters depending on cost, speed, and clad quality.

During first testing design, it was concluded that the laser, at a power of 1000W and a speed of 10mm/s, produced the best clad due to its excellent bond, good uniformity, good height to width ratio and small HAZ – as is found in type two bead profiles. Increasing the powder feed rate also increases the volume of the cladding up to a maximum value of 24g/min for the laser setting of 1000W, 10mm/s. This is because more material could be melted onto the substrate by the laser per unit time as more powder was delivered. A feed rate greater than 24g/min would create powder which would not be melted during the process. Within industry this waste would incur a greater cost during the laser cladding application which is undesired.

During second testing design, it was found that at a laser power of 1000W and a laser speed of 10mm/s the optimal flow rate of the powder was 19g/min due to the clad's excellent bond, good uniformity, good height to width ratio and small HAZ – as is found in type two bead profiles.

4.2 Comparison between High Power and Low Power Cladding Results

An investigation has been conducted into BPLC with lower laser power and processing speed to potentially reduce material anisotropy due to reduced thermal gradients. A comparison has been made for single wall structures with typical higher power conditions and low power.

Figure 4-12 shows the cladding walls of stainless steel sectioned micrographs taken from high power of 1000W at 10mm/s cladding speed, 8&2L/min for coaxial and powder gas flow and 19g/min feed rate but (a) 1mm per step height and (b) 0.8mm per step height. Almost, everywhere in the walls, directional solidification or columnar dendrites can be seen. Their direction growth is almost perpendicular to the solidification front and so depends on the local solidification conditions. In Figure 4-12 (a), it can be seen that more microstructure variations/types compare with Figure 4-12(b). In Figure 4-12(a), the microstructure study shows columnar dendrites grains with different growth directions, and at the top of the components, short dendrites. In Figure 4-12(b), the directional solidifications grow more in the central and along the cladding direction. With the cladding height higher, the directional solidifications transferred to columnar or short dendrites until disappeared. It can be seen that more uniform grain size or equiaxed structures were observed. These can be conclusion that firstly step height has critical effect on the cladding results; and most significantly is that decreasing the power in cladding was possible to achieve.

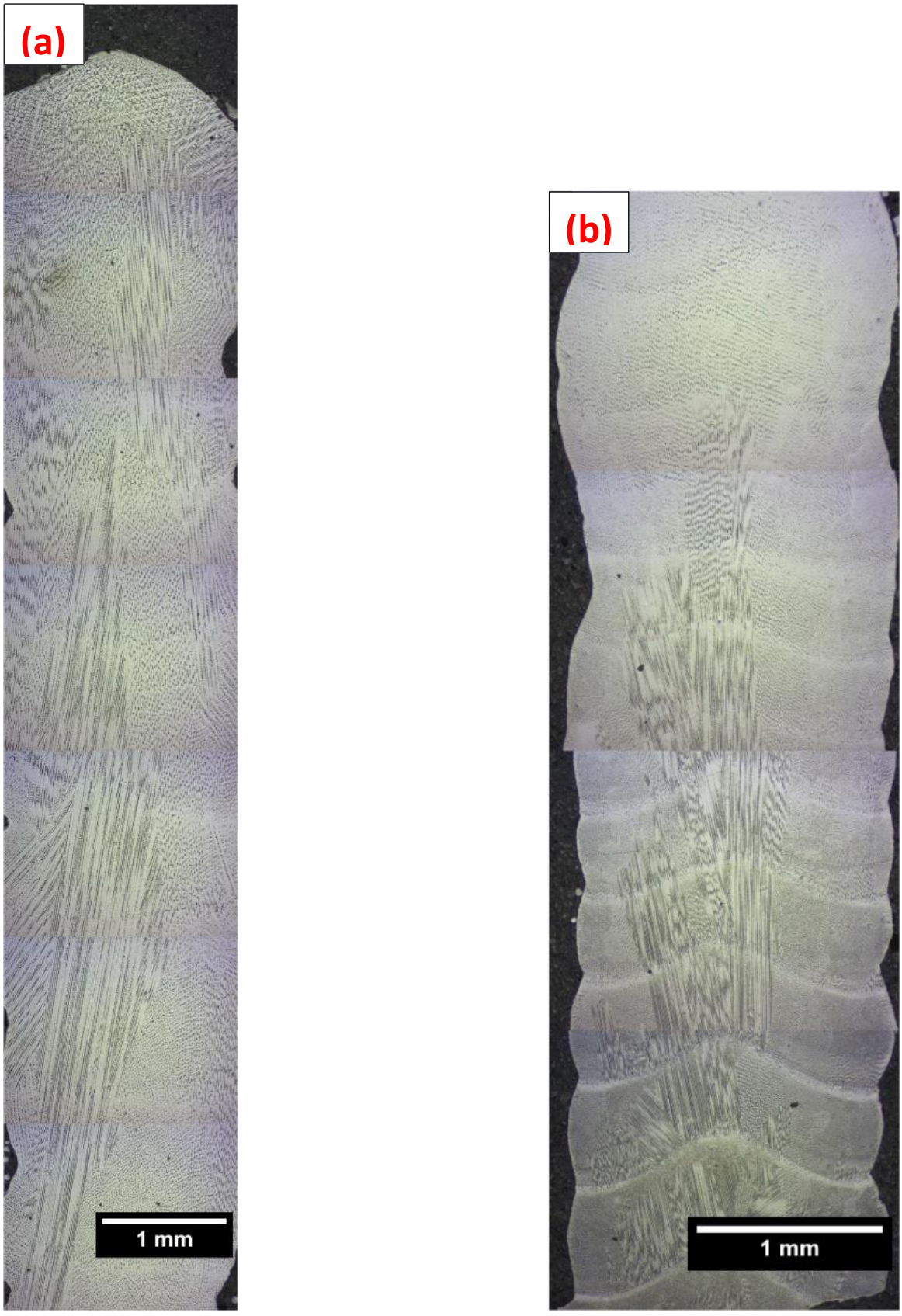

Figure 4-12: High power of 1000W cladding wall (316L SS), (10mm/s, 8&2.5L/min), (a) step height of 1mm, (b) step height 0.8mm.

Figure 4-13 shows tensile test results for cladding walls with different step height (0.4mm, 0.6mm, 0.8mm and 1mm per step height respectively) at 1000W, 10mm/s, 19g/min feed rate, 8&2 L/min for coaxial and powder gas flow rate. Compared to standard averaged stainless steel 316L tensile strength of 485MPa, the results were lower. It is easy to explain that first of all, the cladding track built perpendicular to the tensile force direction which indicates easier to be pulled apart; secondly the processing parameters were not optimised which means the microstructures were not presented in a fine grain size distribution so the properties were negatively affected.

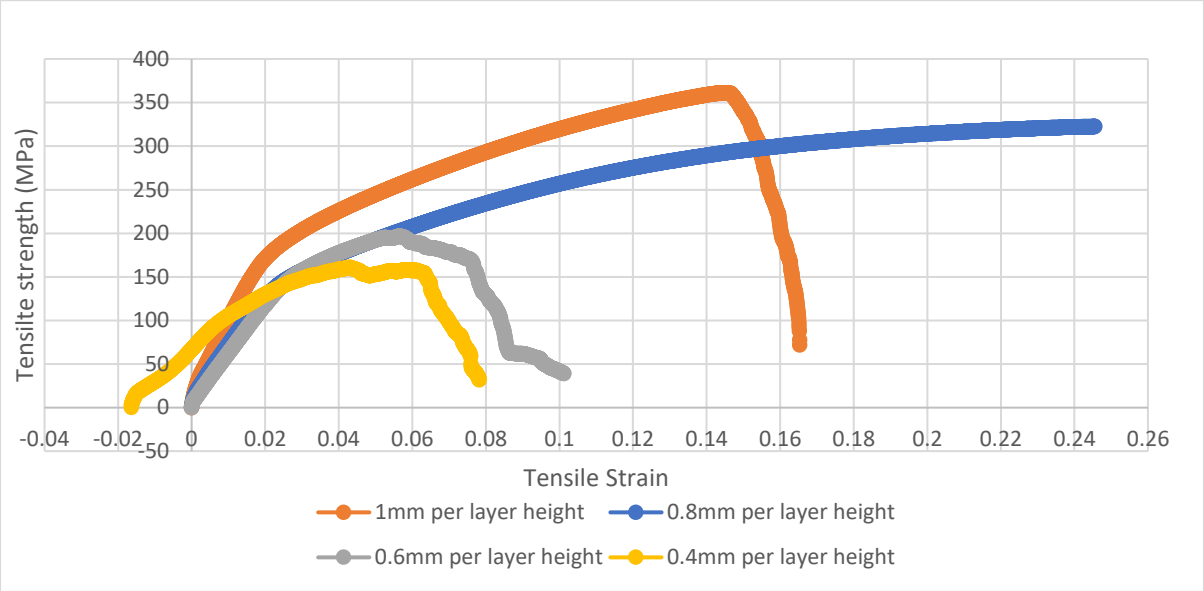

Figure 4-13: Tensile test results from high power cladding components (316L SS) of different step height.

Figure 4-14 shows the microstructure variations in low power of 320W of a 17-layer cladding wall under the condition of 40mm/s cladding speed, 8&2L/min coaxial and powder gas flow, 0.8mm per step height at 18g/min powder feed rate. It can be seen that there still exists part of directional solidifications growing from the solute bond but significantly reduced. The top of each laser track was slightly re-melted by the next layer at a lower power and so the upper dendrite zone disappears.

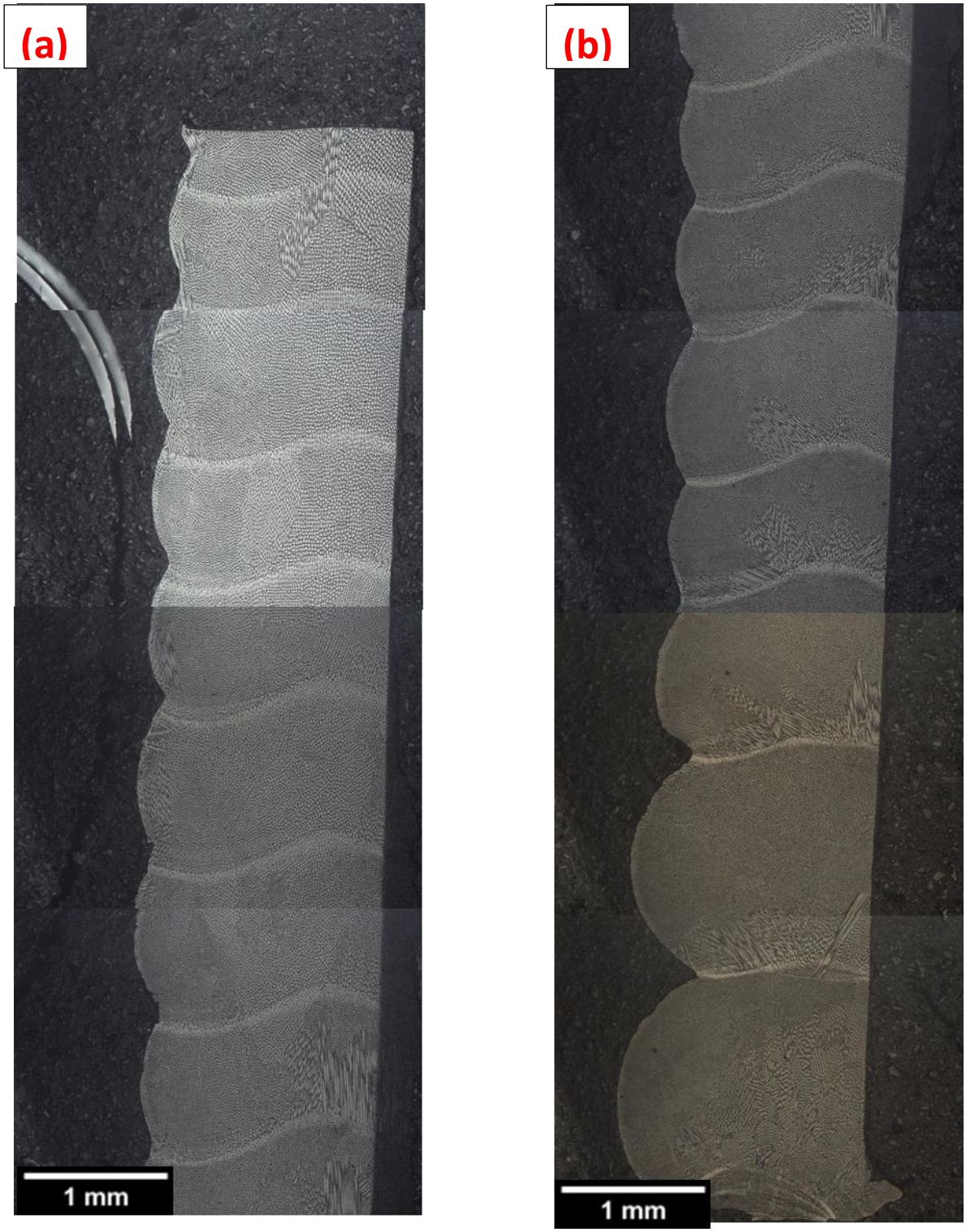

Figure 4-14: Low power of 320W cladding wall (316L SS, 4mm/s, 8&2.5L/min, 0.8mm/ step height), (a) 9-17th layer from the substrate, (b)1st -8th layer from the substrate.

From the comparison between grains morphologies shown in Figure 4-12 and Figure 4-14, it can be seen that the laser power decrease improves the microstructure distribution.

4.3 Geometry Design for Cladding Samples made of 316L SS

4.3.1 Part Production

Cylinder structures have been selected for this study based on the literature survey and analysis of typical components that could be manufactured by additive manufacturing. These structures would also typically exhibit a significant material anisotropy during building in an upright orientation.
A study has then been advised to look at the effect of remelting and reheating by interesting and interlocking multiple cylinder structures. In addition, BPLC with lower laser power has also been investigated.

4.3.1.1 Structure A – Interlocking Hollow Cylinders

As can be seen the design of test structure A is that of two interlocking hollow cylinders. Key to this design are the two overlapping points, important for the investigation stage. Each cylinder is 30mm in diameter with a height of 60mm and the overlapping region has a maximum width of 10mm. In producing test structure A - a model was first produced in Creo software as shown in Figure 4-15.

Following the design, the model was then imported into the CAM software Alphacam where, using a section of the software designed for milling operations, the model was sliced and G-code produced for the CNC table. The output from this was unsuccessful as the milling software attempted to create 2 clad layers side by side. It was then decided that a separate section of the Alphacam software should be used, one designed for laser cutting operations, so that just the 2-D profile could be automatically created in G-code. This would result in just one layer being created therefore the code was altered manually to add a repeat and set parameters such as step height in order that a multi-layer part would be produced. The G-code for test structure A can be found in appendix 1.

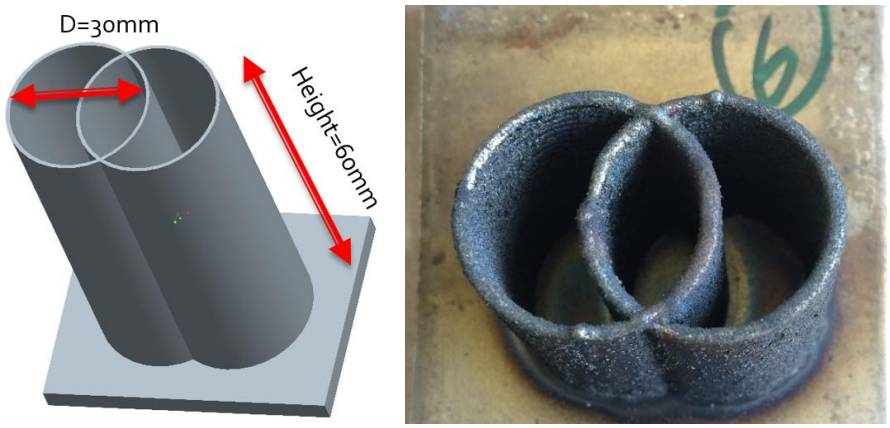

Figure 4-15: Test structure A (left)CAD model – Interlocking Hollow Cylinders and (right) actual cladding sample.

In creating this test structure initially one circle is produced; the other circle is then produced separately from a different point. The laser shutter is closed during the transition from one point to the other point. The start points of each circle in the build are shown in Figure 4-16. The process is repeated continuously with the laser indexing upwards until the final part height is reached. The process parameters for the structure A builds are displayed in Table 4-7, only 1 pass per layer has been used. The second circle is a full circle and cladding path is cladded on top of the previous layer of first circles.

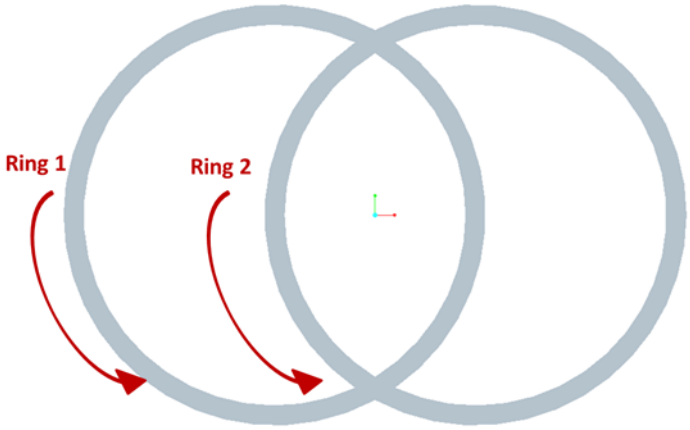

Figure 4-16: Test structure A build method showing starting points.

Table 4-7: Process parameters for test structure A builds.

Indicated Power (W)	Cladding speed (mm/s)	Powder Feed Rate (rpm)	Powder Gas Flow (L/min)	Coaxial Gas Flow (L/min)
320*	4	1000 (18g/min)	2	8

320*: Averaged power, it was damping slightly during the process.

The BPLC process parameter can be combined into an energy per unit volume (E/V) that can be defined as shown in Eq. 4-2.

$$\frac{E}{V} = \frac{\eta_W P_{laser}}{hvw} \qquad \text{Eq. 4-2}$$

Four variations of test structure A were built with different step height s; these were classed as separate samples as shown in Table 4-8. Clad widths were subsequently measured and the energy per unit volume calculated, also displayed in Table 4-8. By producing samples with different step heights and completing the analysis allows the investigation into the effect of the different process parameters. Each sample was built on a 10mm thick mild steel substrate.

Table 4-8: Sample classification for structure A builds

Sample	Step height (mm)	Width (mm)	Energy per unit Volume (J/mm^3)
A1	0.4	1.20	135.42
A2	0.6	1.31	82.70
A3	0.8	1.39	58.45
A4	1	1.45	44.83

4.2.1.2 Structure B – Edge Intersecting Hollow Cylinders

As before test structure *B* was first produced in CAD, the design is displayed in Figure 4-17. Test structure *B* consists of 2 hollow cylinders, each 25mm in diameter, 20mmin height, which intersect at the edge of each cylinder. Following the part design, the base 2-D profile was created in the Alphacam laser cutting application as before however the G-code was significantly altered to change the build method.

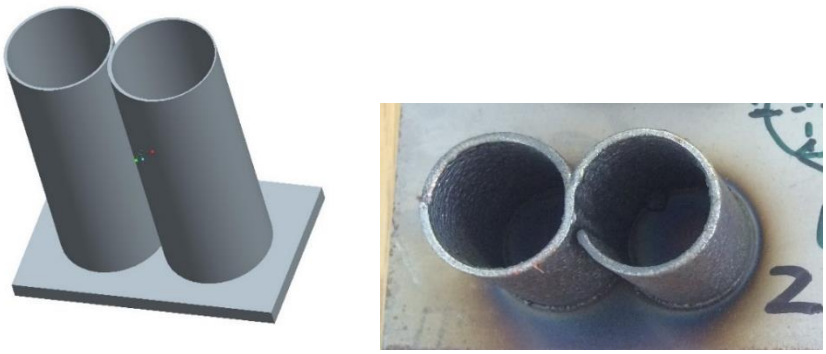

Figure 4-17: Test structure B (left) CAD model (right) cladding samples.

Along with the design, a key difference from test structure *B* to test structure A is the build method. As oppose to producing each circle separately and then the laser indexing upwards test structure B was produced in a 'figure of 8' style with the laser constantly travelling upwards. This results in a helical style build. Using this method, the laser shutter does not have to be operated during the process as the laser is constantly firing. This structure contained two circles tangential which cladded in a helical manner (like infinity symbol '∞') and the laser was constantly indexing upwards. The process parameters for the structure B builds are displayed in Figure 4-18. The G-code for the test structure B builds can be found in appendix 2.

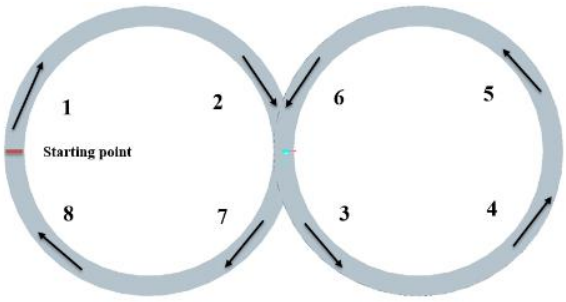

Figure 4-18: Test structure B build method showing starting points and overall routine.

Table 4-9: Process parameters for test structure B builds.

Indicated Power (W)	Cladding speed (mm/s)	Powder Feed Rate (rpm)	Powder Gas Flow (L/min)	Coaxial Gas Flow (L/min)
320*	4	1000 (19g/min)	2	8

320***:** Averaged power, it was damping slightly during the process.

Similar process parameters were used for test structures A and B to allow comparison between them. Using the same method as for test structure A several variations of test structure B were produced with different step heights and the energy per unit volume calculated. This is shown in Table 4-10. As before each sample was produced on 2.5mm mild steel substrate.

The height is measured from the top cladding surface to the substrate, and the width is taken the average value between cladding bead trough and peak aera as shown in Figure 4-19.

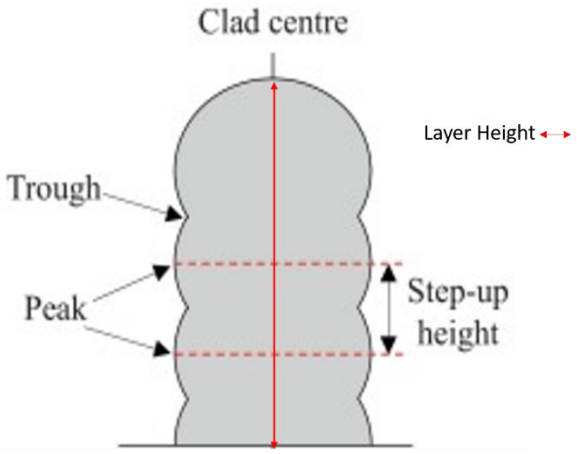

Figure 4-19: Front View of an Overlapping Cladding Wall.

Table 4-10: Sample classification for structure B builds.

Sample	Step height (mm)	Width (mm)	Energy per unit Volume (J/mm^3)
***B* 1**	0.4	1.18	137.71
***B* 2**	0.6	1.29	83.78
***B* 3**	0.8	1.39	58.58
***B* 4**	1	1.42	45.77

4.2.2 Sample Sectioning Methodology

Following production of the test structures, samples were produced for analysis using optical microscopy and microhardness tests. This involved sectioning each clad build, mounting in resin, polishing and etching. For each cladding sample a section was taken at an intersection point and a non-intersection point. Figure 4-20 shows how both test structure A samples and test structure B samples were sectioned with the green labels pointing in the direction at which they were viewed on the microscope. The sample naming convention was altered at this point. Samples at the non-intersection points were as before, in Table 4-8 and Table 4-10. Samples at the intersection points were as before but with the postfix I i.e. sections taken from the sample A3 build were referred to as follows: Sample A3 for the non-intersecting section, Sample A3I for the intersecting section.

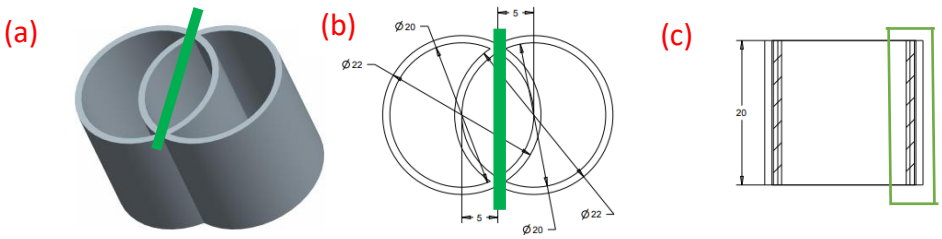

Figure 4-20: (a) Sectioning of test structure A-model, (b) engineering drawing top view,(c)side view with cross-aera.

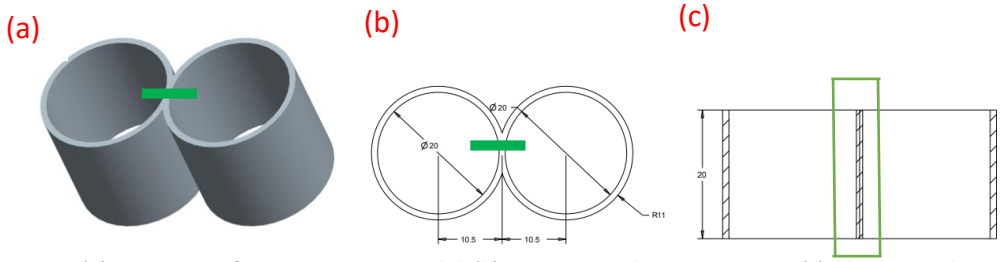

Figure 4-21: (a) Sectioning of test structure B-model, (b) engineering drawing top view,(c)side view with cross-aera.

The green bar in the middle of the cladding geometry indicates where the samples were sectioned and viewed on the microscope. The right-hand side engineering drawing also presents the sectioned part with side view. After the samples were sectioned, the cross-section areas indicated by the greenline fram were mounted in conductive resin and polished using both an automatic polishing machine, to

achieve an initial finish, and then manual polishing disks to achieve a 1micron finish pre- etching. Some initial microscopy work was done prior to etching to ensure any defects in the samples were not misconstrued and to view the relative porosity. An electrolytic etch was then conducted using a 10% oxalic acid solution.

4.4 Investigation of Structure A at Low Power

Microstructure is a very important characteristic of the laser cladding because it has a strong impact on the mechanical properties.

4.4.1 Microstructural Analysis of Non-Intersecting Area of Structure A

To complete the investigation, it was decided that the samples at the intersection point and the samples at the non-intersecting points would be investigated separately for the purposes of analysing the effect of step height and distance from the substrate.

In general, the microstructures were found to be cellular in majority for all samples. These microstructures are a result of the very high cooling rates that must have occurred during the build process. This leads to very large temperature gradients and an increase in the ratio G/R. Microstructural variation is present in all builds with a mix of epitaxial columnar cells, directionally solidified dendritic structures and equiaxed cells in the microstructure as can be seen from Figure 4-22.

Figure 4-22: Sample A3 microstructure 40mm from substrate, x100 magnification (316L SS, 0.8mm per step height, 18g/min feed rate, 2&8 L/min of powder and coaxial gas flow rate).

Solute banding is very clear when viewing the microstructures. This occurs because of the solidification profile of the melt pool. The outside of the melt pool cools quicker than the inside. This results in two

solidification velocities which, when they meet, cause large levels of solute to form resulting in the banding affect. Throughout the microstructures epitaxial growth was seen to occur from the solute banding. This growth was then seen to dissipate into fine equiaxed cells.

A fine cellular equiaxed microstructure is unusual for a part produced using BPLC. This can be compared to the primarily dendritic epitaxial structure found by Fearon [96] using essentially the same laser cladding workstation. This clad was produced with a laser power of 1040W and a cladding speed of 15mm/s. A study of the microstructure shows different grains morphologies shown in Figure 4-23 [251]. AISI 304L stainless steel was used in this case however this is a very similar grade to 316L. It can be seen that the epitaxial growth occurs throughout and continues through several of the solute bands contrary to what has been found in the test Structure A samples. Where remelting has occurred the cooling rate is said to be slower and therefore cellular microstructures do not form. The test Structure A samples have a microstructure similar to what was found at the top of the clad shown in Figure 4-23 in which the cooling rate is said to increase due to the lack of remelting. Remelting has occurred in the test Structure A samples however cooling rates are still high enough for this fine equiaxed structure to form. It seems that with processing parameters changing significantly a significant microstructural change has also occurred.

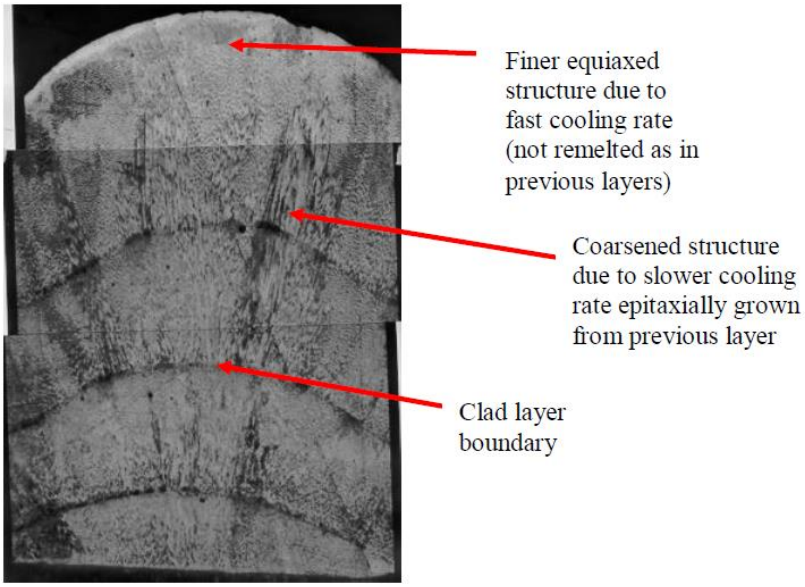

Figure 4-23: Cladding microstructure found by Fearon (magnification unknown).

The microstructures for the test structure A (interlocking) samples were found to have large levels of microstructural variation. As discussed earlier minimising this microstructural variation to achieve a homogenous microstructure is desirable. When finding the structure with the minimal microstructural variation it is possible to link this to the process parameters and discover the 'optimum' process parameters

4.4.1.1 Distance from Substrate

The changes in the microstructure as the distance from the substrate increased were found to be very low. Usually with a part produced using laser cladding for additive manufacture the substrate acts as a heat sink causing a higher cooling rate at the base. This would have the effect of creating a finer microstructure. Figure 4-24 shows the microstructure for sample A1 (0.4mm per step height, 4mm/s cladding speed, 2&8L/min powder and coaxial gas flow rate, 18g/min feed rate) at varying distances from the substrate. The microstructure in general and the microstructural variation can be seen to have very little correlation to the distance from the substrate.

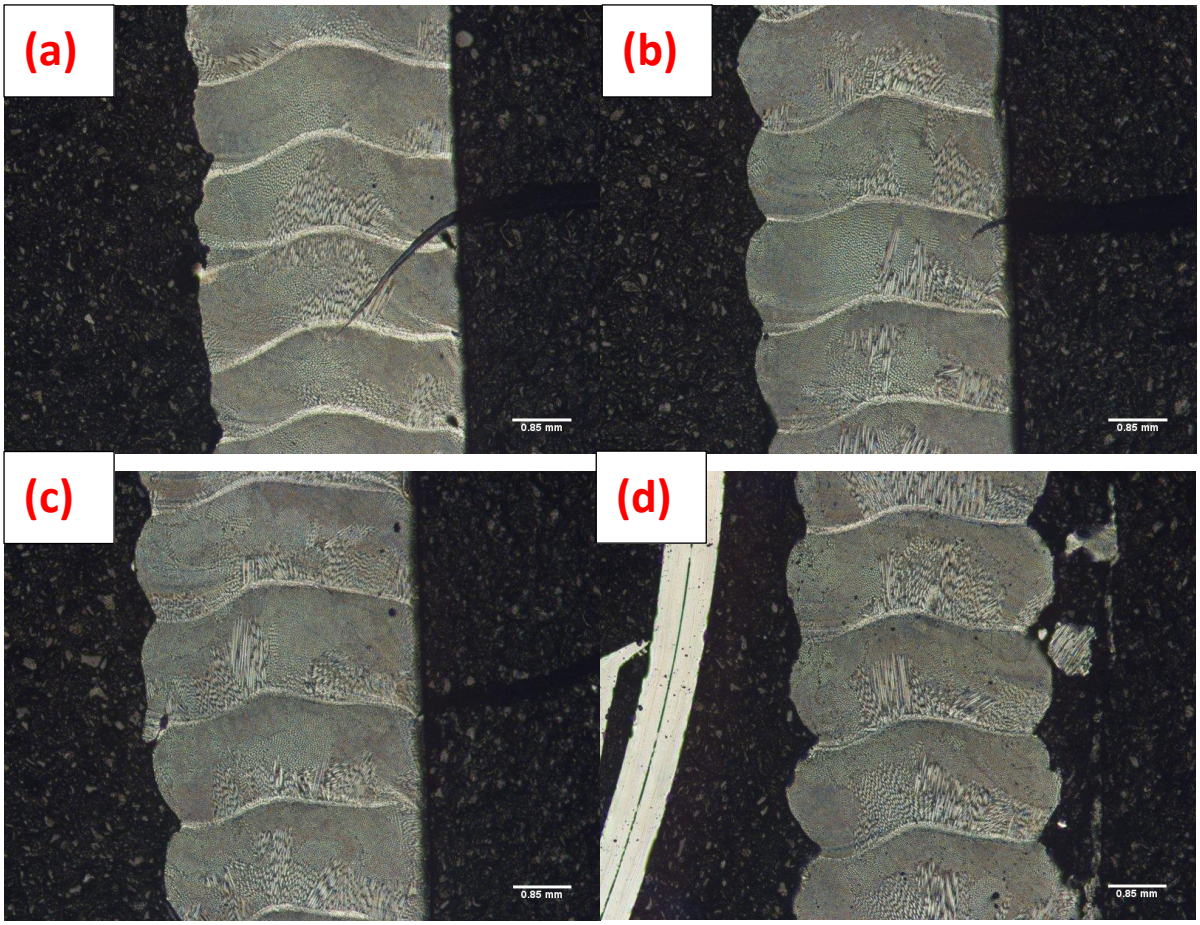

Figure 4-24: Sample A1 microstructure 5mm (a), 10mm(b), 15mm(c) and 20mm (d) from substrate, x50 magnification (316L SS ,0.4mm per step height, 4mm/s cladding speed, 2&8L/min powder and coaxial gas flow rate, 18g/min feed rate).

The process parameters used create a situation where the laser power is relatively low but so is the cladding speed. This results in a low power but high interaction time. Creating a comparison again to clads done by Fearon [252], which, given the cladding speed and step height, the energy per unit volume can be estimated at around the 138 J/mm^3. The energy per unit volume for the Structure A clad builds are comparatively low (44-135 J/mm^3). With such low energy per unit volume being used it can be expected that the clad builds are quite efficient with very little excess energy other than that required to create a melt pool and strong fusion bond. In fact, it can be seen in Figure 4-25 that for

sample 4 the energy input is barely high enough to create a strong fusion bond. Sample A4 (1mm per step height, 4mm/s cladding speed, 2&8L/min powder and coaxial gas flow rate, 18g/min feed rate) is the only sample for which the distance from the substrate appears to have any affect. As the distance from the substrate is increased the fusion bond between consecutive layers increases significantly. Despite this there still appears to be no appreciable change in the microstructure.

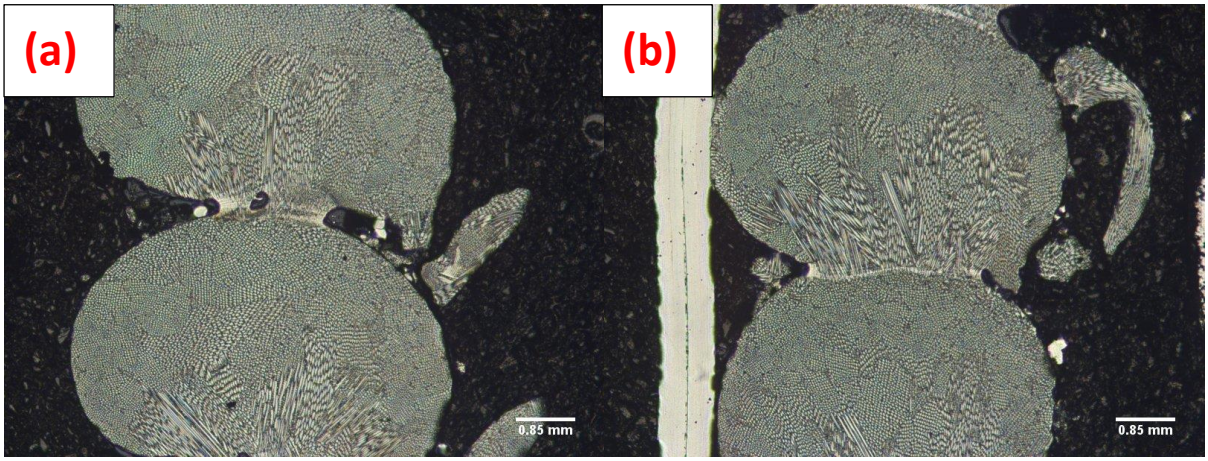

Figure 4-25: Sample A4 microstructure 10mm (a) and 20mm (bt) from the substrate, x50 magnification (316L SS , 1mm per step height, 4mm/s cladding speed, 2&8L/min powder and coaxial gas flow rate, 18g/min feed rate).

It can be noted that the energy per unit volume is probably not the only driving factor in the microstructures found. The energy per unit volume to produce sample A1 is quite close to that estimated for the sample produced by Fearon [252]. Therefore, it can be suggested that the interaction time is also an important factor in the creation of the microstructures found.

4.4.1.2 Step height

Changing the step height hence changing layer height of the samples appears to have the largest effect on the microstructure. Variations in the microstructure are significantly different with the variation in layer height along with the relative coarseness of the microstructures. This investigation was focused into finding the 'ideal' microstructure, or as close as possible to the ideal, i.e. an equiaxed homogeneous microstructure.

Coarsening may happen during dendritic solidification by two main mechanisms: (1) growth of larger dendrite arms at the same time as smaller dendrite arms disappear, also called ripening; (2) filling in the space between two adjacent dendrite arms to merge them into one larger dendrite arm (coalescence). During the early stages of solidification, ripening happens by dissolving the small dendrite arms as shown in Figure 4-26, while at the final stage of solidification, coalescence occurs by filling in the space between two dendrite arms [253].

The ripening happening at the earlier stage of solidification should reduce the level of micro-segregation in the solid [254]; the latter stage of coalescence was expected to have little effect on the level of segregation. The effect of coarsening on micro-segregation is small compared with the back-diffusion in solid [255].

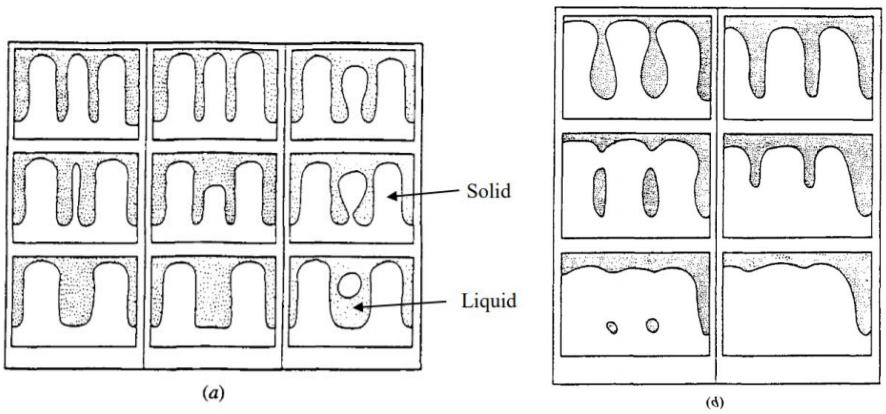

Figure 4-26: Schematic diagrams of coarsening mechanisms: (a) ripening and (b) coalescence.

Figure 4-27, Figure 4-28, Figure 4-29 and Figure 4-30 display representative images of the microstructures for samples A1 to A4 respectively. Sample A1 can be seen to suffer from strong microstructural variations with large areas of epitaxial columnar growth propagating from the solute bands. Towards the outside of the sample the microstructure is fine cellular whereas towards the centre the microstructure is mixed columnar dendritic and relatively coarse cellular. This will be due to the outside of the melt pool cooling at a faster rate than the centre of the melt pool causing fine cells to form at the outer regions. This effect is less prominent in the other samples which all have less microstructural variation. Sample A2 appears to have the least microstructural variation, a fine cellular structure present throughout with a small amount of epitaxial growth propagating from the solute bands. Sample A2 is also mostly equiaxed. Samples A3 and A4 are mostly equiaxed but suffer from greater levels of epitaxial growth from the solute bands. Samples A3 and A4 can also be seen to have a coarser microstructure in general, than samples A1 and A2 which, would lead to lower strength. This coarsening effect is as expected as samples A3 and A4 have had a lower energy input compared to sample A1 and A2. This would create an effect where the thermal gradients are lower and there is a decrease in the ratio G/R, leading to a coarser microstructure.

During the cladding process, where the molten pool is moved through the material, the growth rate and temperature gradient vary considerably across the melting pool. Geometrical analyses have been developed that relate cladding speed to the actual growth rates of the solid at various locations in the melting pool. Along the fusion line the growth rate is low while the temperature gradient is steepest. As the cladding centreline is approached, the growth rate increases while the temperature gradient

decreases. Consequently, the microstructure that develops varies noticeably from the edge to the centerline of the cladding. Most of these microstructural features can be interpreted by considering classical theories of nucleation and growth.

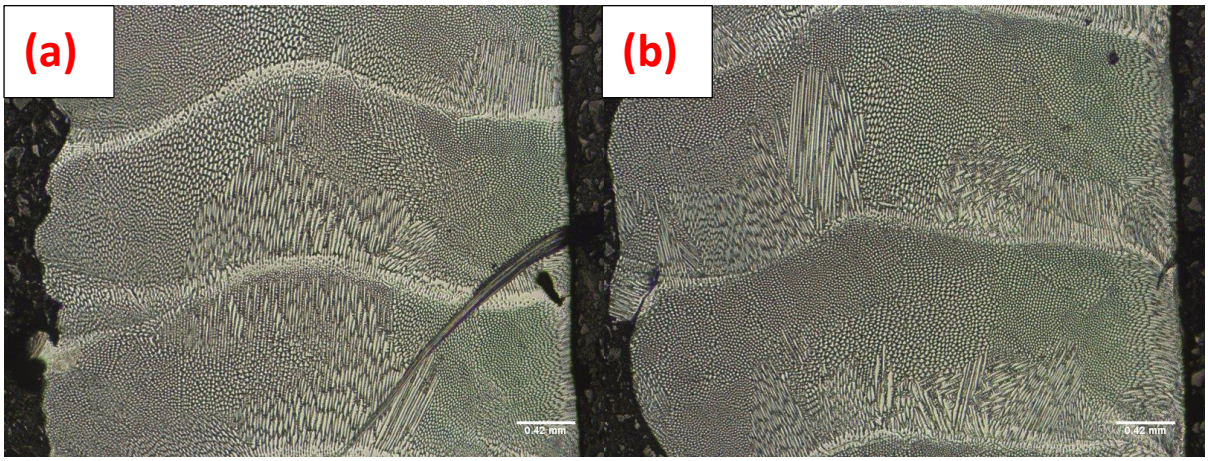

Figure 4-27: Sample A1 microstructure 5mm (left) and 15mm (right) from substrate, x100 magnification (0.4mm per step height, 4mm/s cladding speed, 2&8L/min powder and coaxial gas flow rate, 18g/min feed rate).

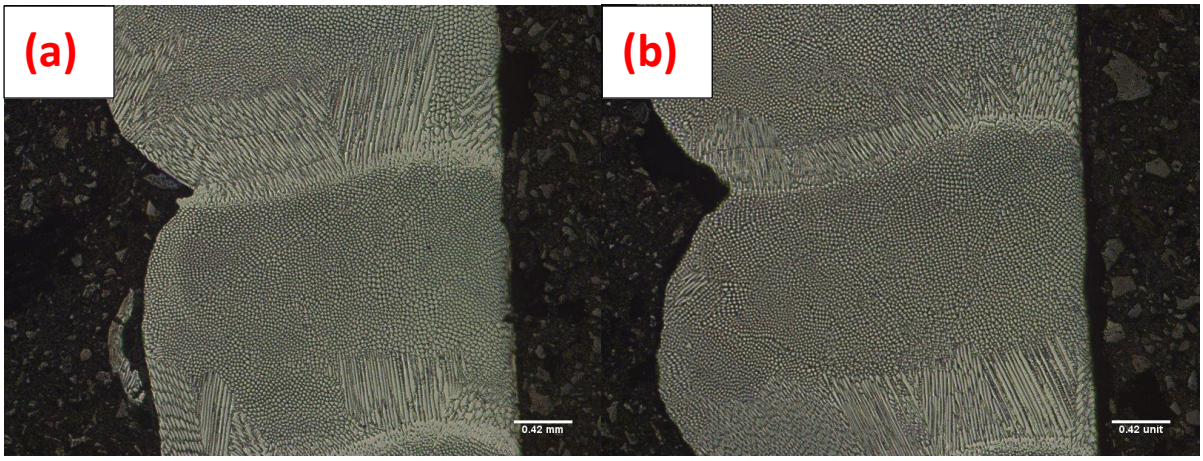

Figure 4-28: Sample A2 microstructure 5mm (left) and 15mm (right) from substrate, x100 magnification (316L SS, 0.6mm per step height, 4mm/s cladding speed, 2&8L/min powder and coaxial gas flow rate, 18g/min feed rate).

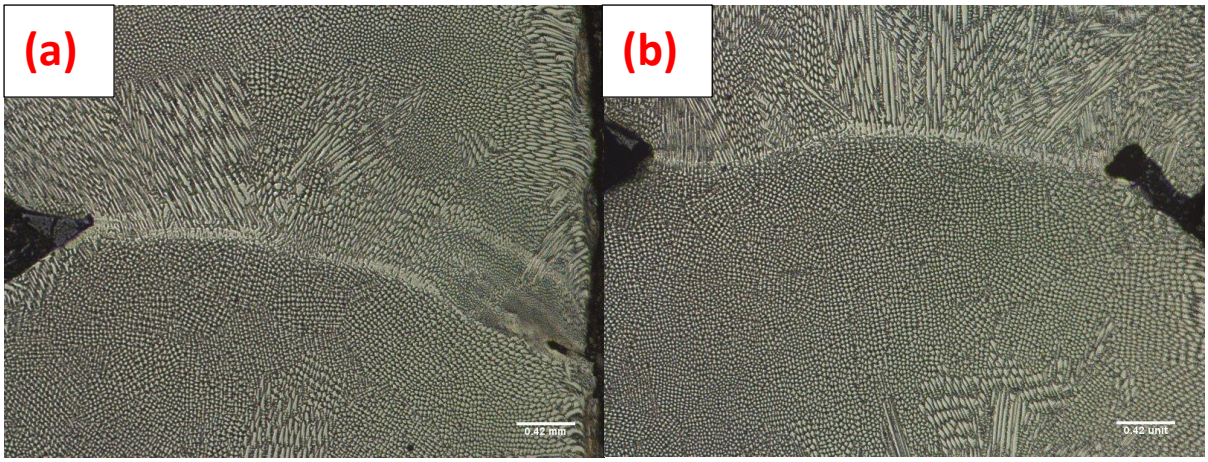

Figure 4-29: Sample A3 microstructure 5mm (a) and 15mm (b) from substrate, x100 magnification (316L SS, 0.8mm per step height, 4mm/s cladding speed, 2&8L/min powder and coaxial gas flow rate, 18g/min feed rate).

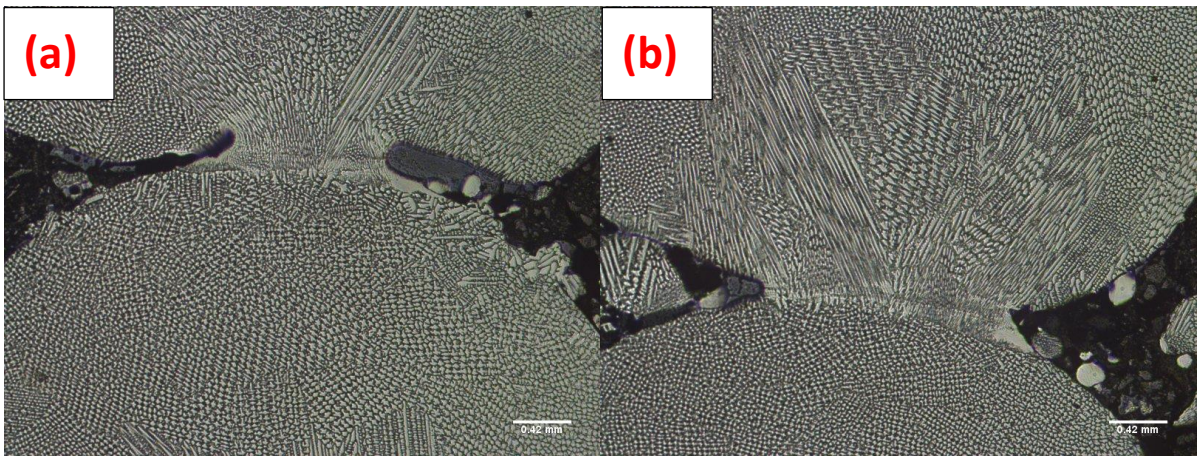

Figure 4-30: Sample A4 microstructure 5mm (a) and 15mm (b) from substrate, x100 magnification (316L SS, 1mm per step height, 4mm/s cladding speed, 2&8L/min powder and coaxial gas flow rate, 18g/min feed rate).

4.4.1.3 Micro-Porosity

The relative porosity of the samples can have observed from pre-etch images as shown in Figure 4-31. All samples have a low porosity with sample A2 having the lowest. Based on this and the previous analysis on the microstructural variation sample A2, 0.6mm lay step height er height with an E/V of 82.70J/mm^3, appears to be closest to the optimum microstructure.

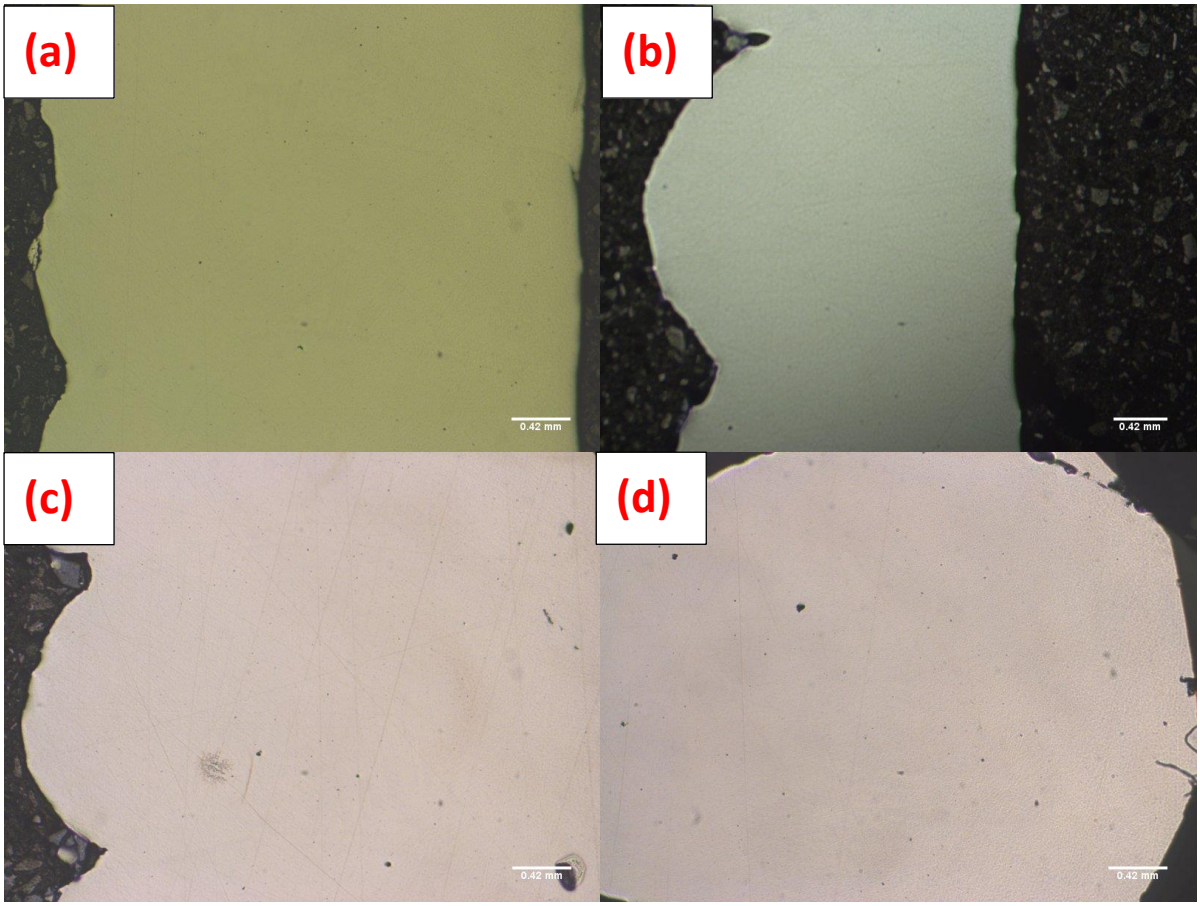

Figure 4-31: Pre-etch images – samples A1 (a), A2(b), A3(c) and A4 (d), non-intersected area, x100 magnification.

In terms of the porosity all samples were seen to be quite similar. Low levels of porosity were found as can be seen in Figure 4-32. As the porosity does not alter significantly with step height, based on the microstructural investigation sample A3I, a 0.8mm step height sample with an E/V of 58.45J/mm^3, is the ideal sample for a crossover point.

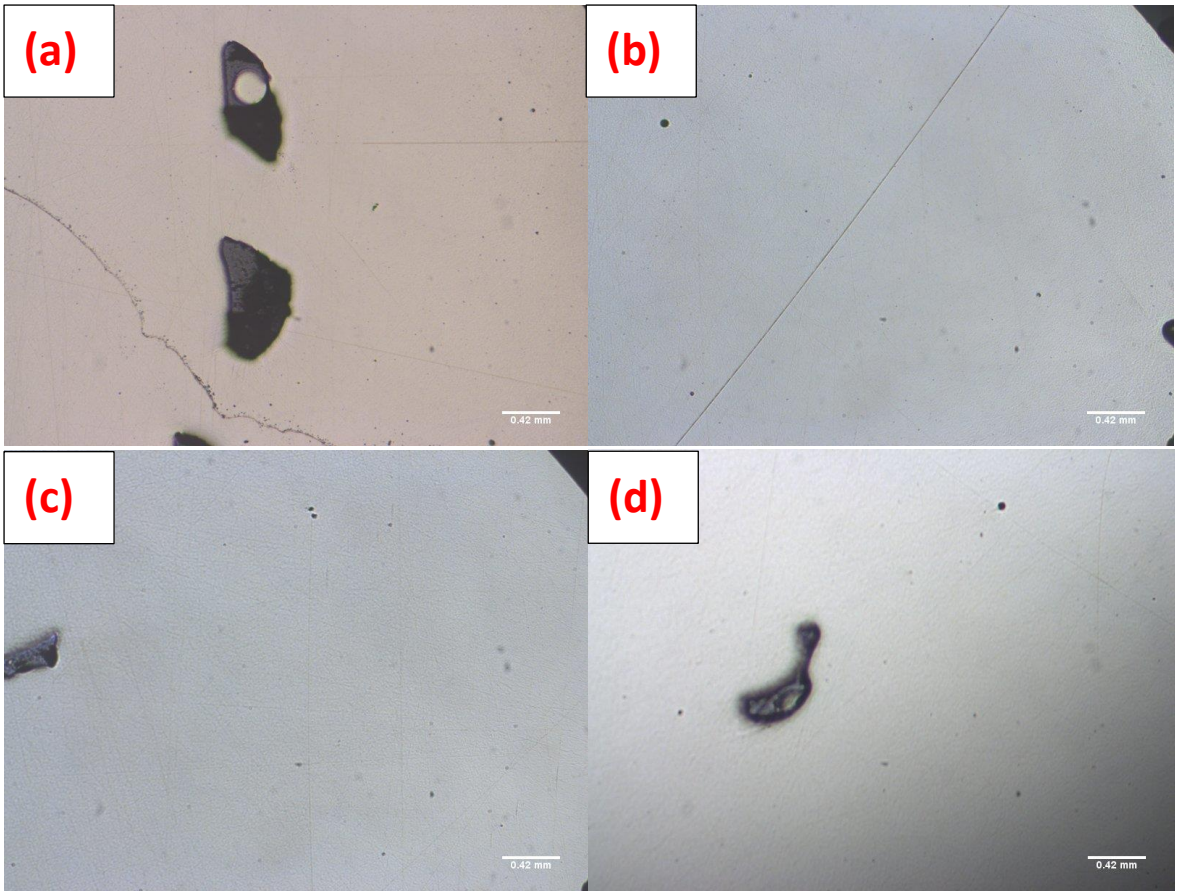

Figure 4-32: Pre-etch images – Sample A1I (a), A2I(b), A3I(c) and A4I (d), intersected area, x100 magnification.

4.4.2 Microstructural Analysis of Intersecting Area of Structure A

The intersecting samples were found to also display a microstructure that is cellular in the majority. Vast microstructural variations were present throughout all samples. Some of the samples proved difficult to mount and the intersecting sections could not be viewed directly on the microscope. This has had the unfortunate effect of making any conclusions gained from the investigation process less accurate. For the samples which were viewed directly the effect of the intersection point is quite interesting. A typical sample is displayed in Figure 4-33. The result of the crossover point in the clad build has had the effect of creating the odd oval shaped solute banding displayed in the figure. This is a result of complex melting and remelting process in which multiple solidification fronts meet from cladding occurring in two separate directions. Resultant from this is a complex microstructure comprising a several phases of columnar dendritic, epitaxial cells and fine equiaxed cells.

During growth of the solid in the melt pool, the development of microstructure can be affected by the shape of the solid-liquid interface. The thermal and compositional conditions (compositional supercooling) can determine the nature and the stability of the solid-liquid interface. Depending on these conditions, the interface growth may be planar, cellular or dendritic. Dendritic growth of the

solid, with its multiple branches, is shown in Figure 4-33. This figure also shows morphology changes from cellular to dendritic as the growth velocity increases toward the centre of the intersection part.

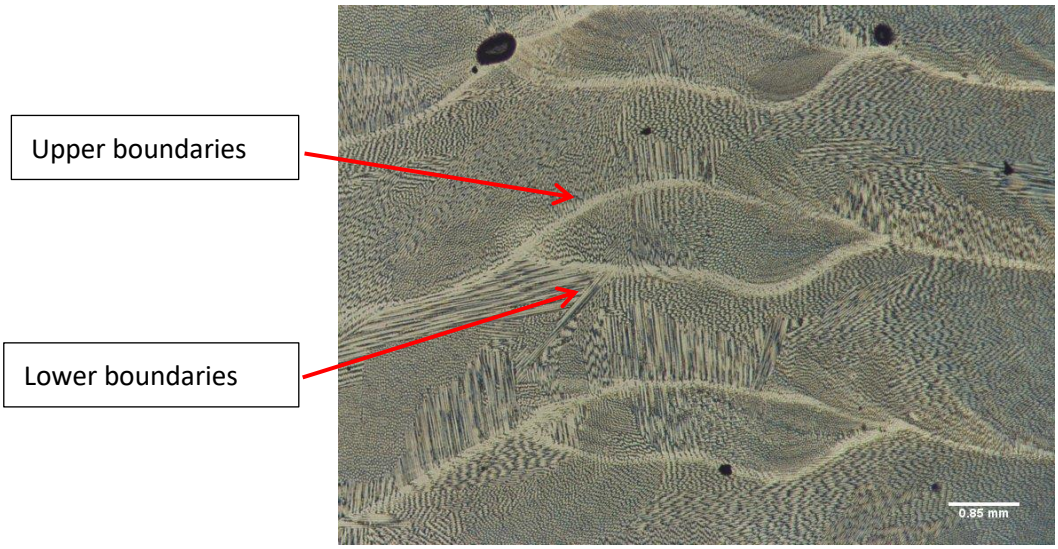

Figure 4-33: Sample A2I microstructure A-5mm from substrate, x50 magnification (316L SS, 0.6mm per step height, 4mm/s cladding speed, 2&8L/min powder and coaxial gas flow rate, 18g/min feed rate).

It is worthy to note the two boundaries were observed in Figure 4-33. A possible explanation is that the upper boundary is the original boundary, and the lower boundary occurs due to re-melting of the inner layer. The outer surface of the melt pool may be intact during re-melting due to the existence of an oxide layer.

Also, the dendrite arm spacing is inversely proportional to the solidification rates according to Flemings formula:

$$\lambda = a(G * R)^{-n} \qquad \text{Eq. 4.3}$$

where λ = dendrite arm spacing

a = constant

G = thermal gradient at melt pool interface (K/m)

R = velocity of solidification interface (m/s)

n = constant equal to approximately 0.5 for primary dendrite arms and 0.3 – 0.5 for secondary arms

As a result, a high cooling rate will result in smaller dendrites with smaller arm spacing resulting in finer dendrites.

Constitutional supercooling has important effects on the solidification morphology. Due to solute

partitioning between the solid and liquid during solidification, the solute rejected to the liquid produces a solute-enriched layer in front of the solidifying interface. Epitaxial growth was not seen to propagate from the solute bands as before. Instead the location of the solute banding, in the vertical direction, appeared to have very little effect on the epitaxial growth. At the edges of the solute bands, where the cooling rate was likely to be faster, a very fine cellular microstructure was found whereas towards the centre of the oval shaped structures cells coarsen and directional solidification was seen to occur. The result of this is a microstructure with large variations.

As mentioned earlier, since solidification of the cladding metal proceeds spontaneously by epitaxial growth of the partially melted grains in the base metal, the intersection cladding grain structure is mainly determined by the base metal grain structure and the cladding processing parameters. Crystallographic effects will influence grain growth by favouring growth along crystallographic directions, namely the easy growth directions. The cellular structures are stable only in a certain temperature gradient range. Normally cells grow normal to the interface at relatively low growth rates and reject solute element atoms which pile up in the intercellular regions. With increasing growth rate, crystallographic effects start to make a difference and the cells grow towards the preferred crystallographic growth direction (<100> for cubic structure). Therefore, secondary dendrites or even tertiary dendrites start to form on the stem of columnar structures to form dendritic geometry.

In continuous cladding, dendritic solidification in steels occurs in both columnar and equiaxed zones. G and R are important in optimising the operational parameters in terms of decreasing the risk of internal defects. Both the growth rate R and thermal gradient G depend on the cooling rate and decrease with increased distance from the surface [256] If the dendrite growth rate is too slow, the shell thickness is thin enough so that break-out may happen. If the dendrite growth is too fast, defects may form in the final product.

4.4.2.1 Distance from Substrate

As with the non-intersecting samples it proved difficult to find any form of correlation in the microstructure with varying distance from the substrate. It would be expected that, at the crossover points, the thermal energy input is much greater due to the reheating/remelting occurring with twice the frequency than at the at other areas in the clad builds. This can be akin to applying a larger energy per unit volume. Due to this it would be expected that the heat sink caused by the substrate would have a larger effect.

Figure 4-34 shows the microstructure at varying distances from the substrate for sample A4I. It is evident that there is very little appreciable variation with varying distance from the substrate, microstructural variation in this regard appears random. There is also no evidence of a coarsening or thinning of the microstructure in correlation with the distance from the substrate. This was found to be the same for all samples. These are likely to be related to, as before, the low energy per unit volume values and the low cladding speed. The substrate, being 2.5mm thick, is also likely to be too thin to have a large influence in creating a heat sink.

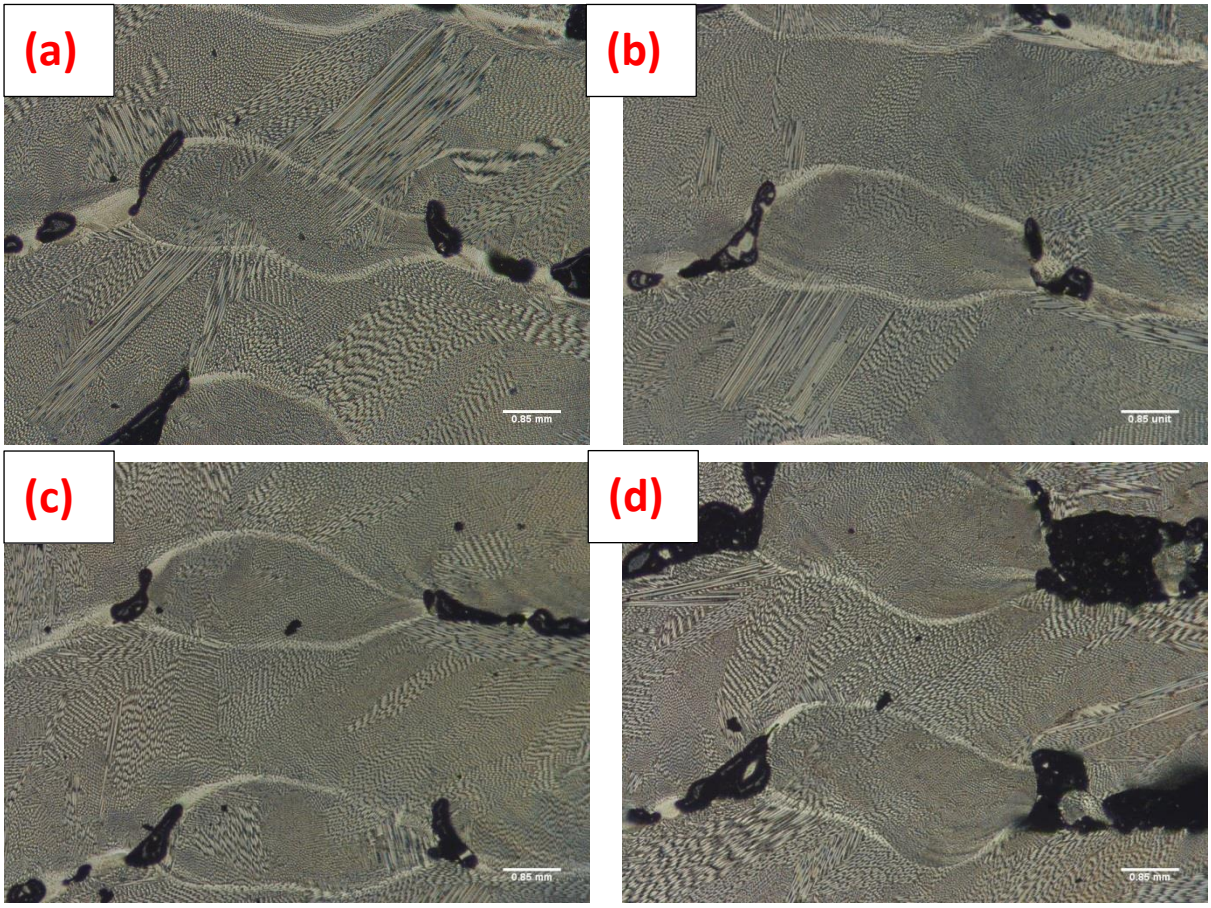

*Figure 4-34: Sample A4I microstructure 5mm (a), 10mm(b), 15mm(c) and 20mm (d) from substrate, x50 magnification (*316L SS*, 0.4mm per step height, 4mm/s cladding speed, 2&8L/min powder and coaxial gas flow rate, 18g/min feed rate).*

4.4.2.2 Step height

Varying the step height has influenced the microstructure. Figure 4-35, Figure 4-36, Figure 4-37 and Figure 4-38 display the microstructures for samples A1I to A4I respectively. It is difficult to analyse sample 1I as it suffered from the mounting problems previously mentioned. From what can be seen, throughout the sample variations from coarse epitaxial cells to fine equiaxed cells is most prominent with large areas of dendritic structures also noted. Sample A2I is seen to have less microstructural variations however large areas of columnar dendritic and epitaxial cellular structures are present. This

is also true of sample A4I. Sample A3I is seen to display the least microstructural variation however variations are still present. The microstructure is a very fine equiaxed cellular one in general with areas of coarser cells and columnar epitaxial growth. It is difficult to note any coarsening of the microstructure as step height increases due to the large microstructural variations except for sample A4 in which the general microstructure is clearly coarser than that found in the other samples. Sample A3I displays a microstructure closest to a purely equiaxed homogeneous microstructure. These micrographs also show the partly elimination of a poorly aligned dendrite.

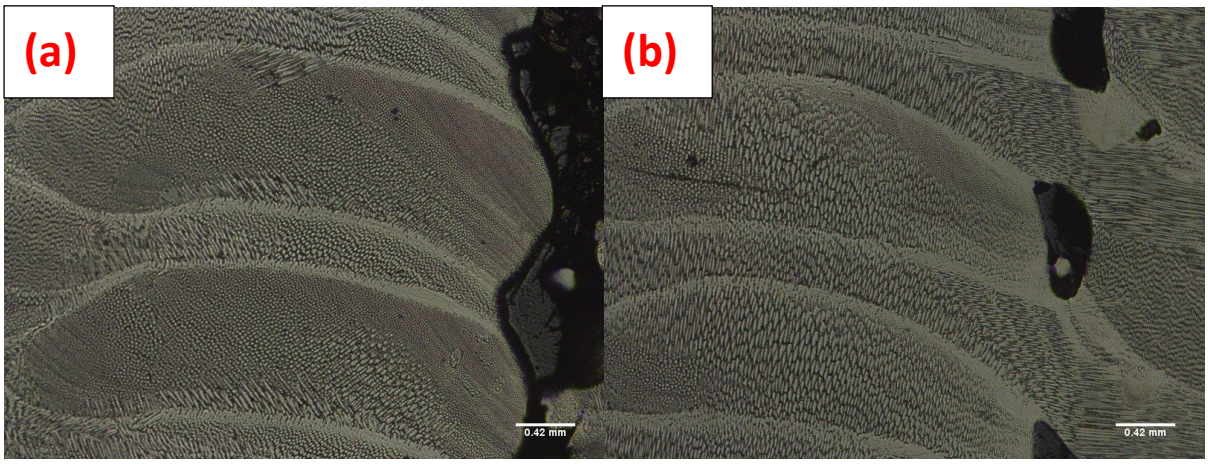

*Figure 4-35: Sample A1I microstructure 5mm (a) and 15mm (b) from substrate, x100 magnification (*316L SS*, 0.4mm per step height, 4mm/s cladding speed, 2&8L/min powder and coaxial gas flow rate, 18g/min feed rate).*

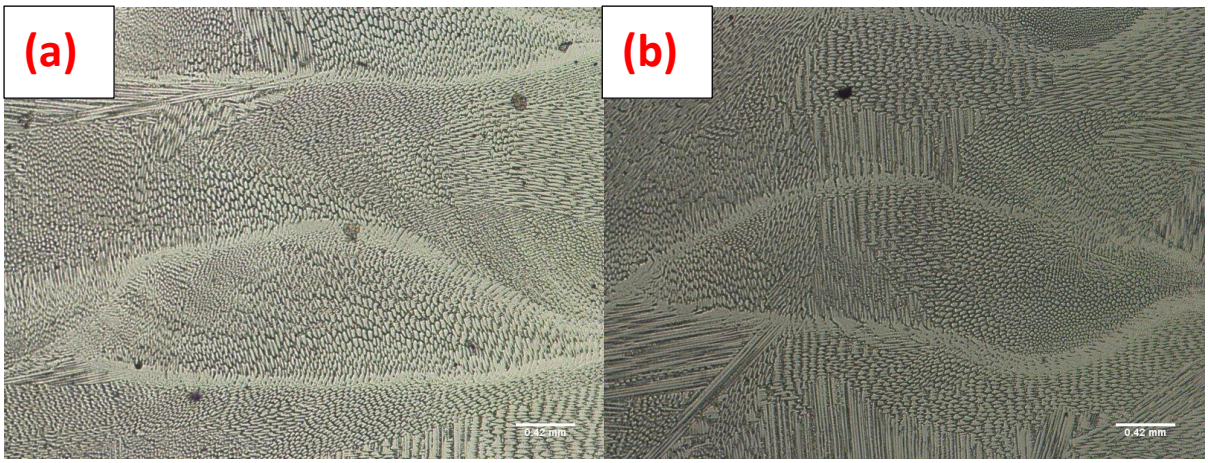

*Figure 4-36: Sample A2I microstructure 5mm (a) and 15mm (b) from substrate, x100 magnification (*316L SS*, 0.6mm per step height, 4mm/s cladding speed, 2&8L/min powder and coaxial gas flow rate, 18g/min feed rate).*

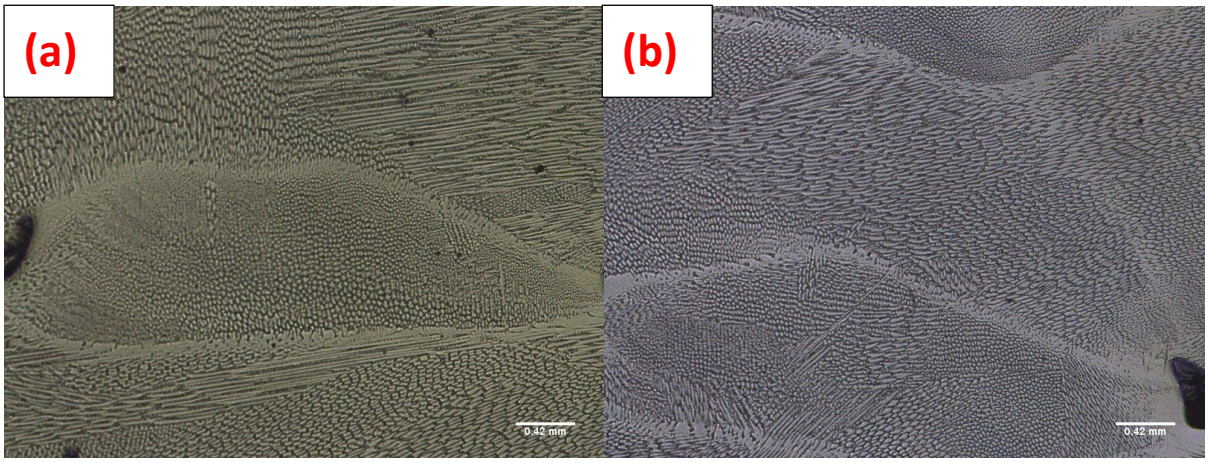

Figure 4-37: Sample A3I microstructure 5mm (a) and 15mm (b) from substrate, x100 magnification (316L SS, 0.8mm per step height, 4mm/s cladding speed, 2&8L/min powder and coaxial gas flow rate, 18g/min feed rate).

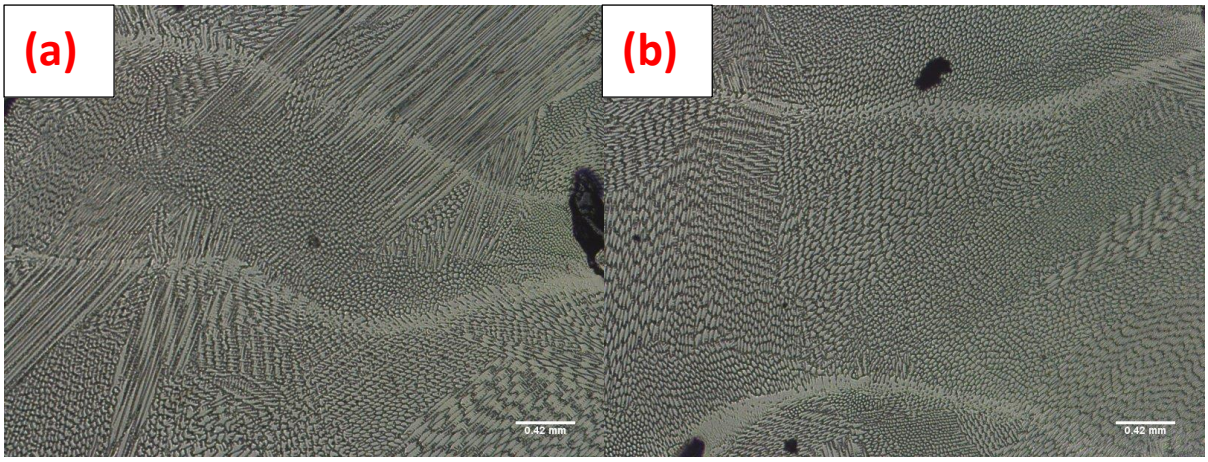

Figure 4-38: Sample A4I microstructure 5mm (a) and 15mm (b) from substrate, x100 magnification (316L SS, 1mm per layer step height, 4mm/s cladding speed, 2&8L/min powder and coaxial gas flow rate, 18g/min feed rate).

4.4.3 Comparisons between Intersecting and Non-Intersecting Microstructures

The main difference between the microstructures of the intersecting regions and the non-intersecting regions lies in the microstructural variations. Variations are far more prominent in the intersecting regions. Overall the general microstructure is fairly similar with a fine cellular microstructure mixed with coarse cells and columnar dendritic structures evident in areas. It seems that achieving an optimised microstructure in a BPLC structure which intersects is very difficult. Where the non-intersecting samples have a fairly homogeneous microstructure with only a few areas of varying structures the intersecting points have a very inhomogeneous microstructure with varying structures throughout. It seems that the added thermal cycle at the crossover points has had a detrimental effect on the microstructure and its ability to be controlled by process parameters.

4.4.4 Microhardness

The results of the microhardness test can be seen in

Figure *4-39*. In general, the microhardness was found to vary from 170-240VH. Microhardness readings were taken at the midpoints of the solute bands at the varying distances from the substrate. The typical hardness for wrought AISI 316L stainless steel is 170-220VH [257]. The hardness values achieved are very similar to the wrought condition value for the material suggesting that changes of hardness of the material has not occurred to any great extent in the test Structure A builds. This result can be explained that given the fine cellular microstructures, a higher hardness would be expected. The E/V values are possible too low to cause a significant increasing of hardness in the material.

Due to the different thermal cycles taking place at the non-intersecting areas and intersecting areas it would be expected that the hardness value would differ between these. This was found not to be the case as can be seen from Figure 4-39. This was found to be the case for all the clad builds in test structure A. Neither a coarsening nor thinning of the microstructure was observed between the intersecting and non-intersecting explaining the lack of hardness variations between the two.

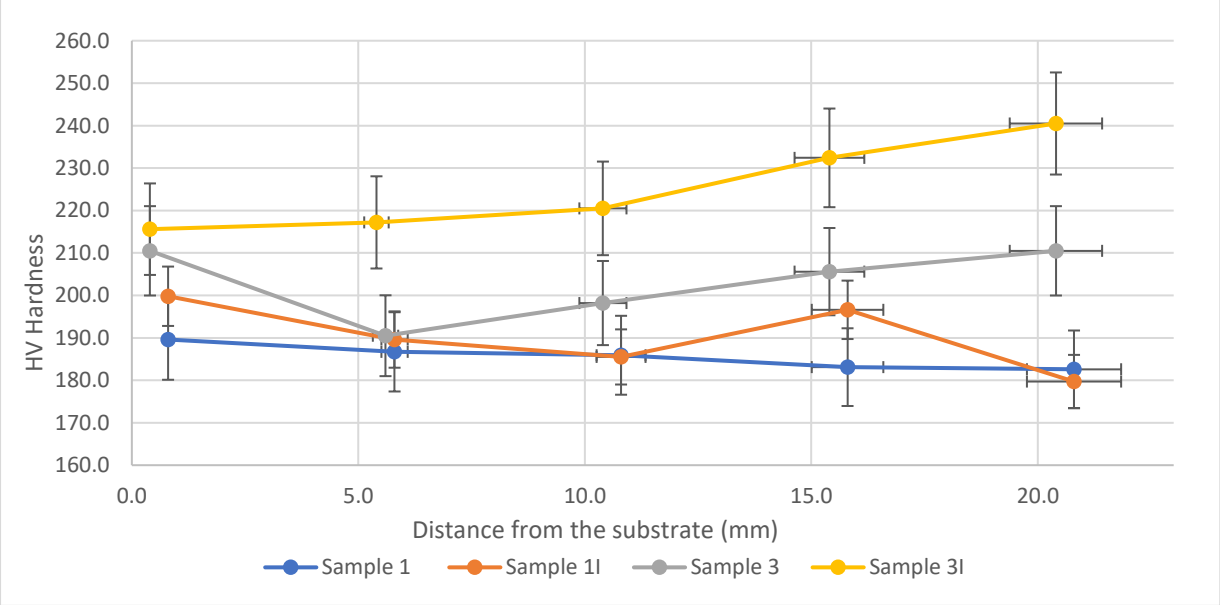

Figure 4-39: HV hardness of Structure A with 0.4mm step height (sample A1) and 0.8mm step height (sample A3) both intersected and non-intersected area (320W, 4mm/s cladding speed, powder feed rate 3000rpm, coaxial and powder gas flow are 8 and 2L/min).

Another key point is the fact that the hardness values do not vary significantly as the distance from the substrate increases. The hardness variations can be understood that within the experimental error band and therefore the microhardness is uniform throughout all the samples. This, combined with the

previous point, is further evidence that no significant hardness changes are occurring during the clad builds leading to properties similar to that of the wrought material. As there is no significant variation in microhardness with distance from the substrate an average can be taken from all data points. Table 4-11 displays the average microhardness value for all samples.

Table 4-11: Microhardness and E/V value for Structure A both non-intersected and intersected area.

Sample	Average Vickers's Hardness (HV)	E/V (J/mm^3)
A1 (Non-intersected, 0.4mm/layer)	189.5	159.18
A1I (Intersected, 0.4mm/layer)	195.6	159.18
A2 (Non-intersected, 0.6mm/layer	210.5	98.23
A2I (Intersected, 0.6mm/layer)	220.3	98.23
A3 (Non-intersected, 0.8mm/layer	207.6	71.31
A3I (Intersected, 0.8mm/layer)	223.4	71.31
A4 (Non-intersected, 1mm/layer	201.4	54.02
A4I (Intersected, 1mm/layer)	215.6	54.02

Samples A2I and A3I display the highest hardness values. From the microstructural investigation these samples were seen to have the minimal microstructural variations suggesting that minimising microstructural variation improves the mechanical properties as assumed at the start of the research. The increase, however, is minimal – in the region 20-30HV compared to the other samples.

4.5 Investigation of Structure B made under Low Power

The test structure B samples were investigated in much the same way as test structure A. It would be expected that the microstructures and mechanical properties are fairly like that found for test structure B as the process parameters did not vary significantly.

4.5.1 Microstructural Analysis of Non-Intersecting Area of Structure B

The microstructures found for the test structure B were, as expected, similar to that found for test structure A. A microstructure which is primarily equiaxed cellular was observed, with some epitaxial cells and dendritic structures propagating from the solute bands as can be seen from Figure 4-40. A key difference in this microstructure compared to that found for test structure A is in the level of microstructural variation. The test Structure B samples, in general, suffer from fewer variations than that found for test structure A. This suggests that changing the build method to the helical one used for test structure B along with reducing the powder feed rate has had a positive effect on the microstructure.

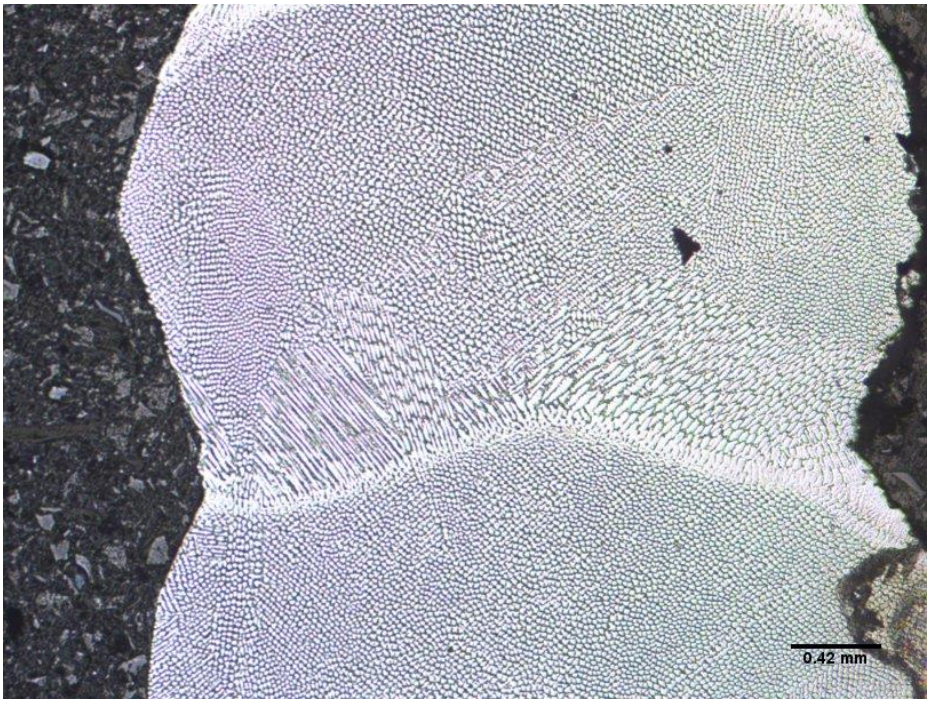

Figure 4-40: Sample B2 microstructure a 2mm from substrate, x100 magnification (316L SS, 0.6mm per step height, 4mm/s cladding speed, 2&8L/min powder and coaxial gas flow rate, 18g/min feed rate).

The cellular structure for the test structure B samples was seen to be coarser than the cellular structure for test structure A. This suggests the cooling rates for the test structure B samples were slightly lower than test structure A however a greater uniformity in cooling rates was achieved throughout each clad build.

4.5.1.1 Distance from substrate

The variation in the microstructure with the varying distance from the substrate was found to be negligible. The reason for this will be the same as for the test Structure A samples in that the E/V values and cladding speed are low and the substrate is thin. Figure 4-41 shows the microstructure for sample B2 at varying distance from the substrate. It is evident that there is no correlation between the microstructure and the distance from the substrate.

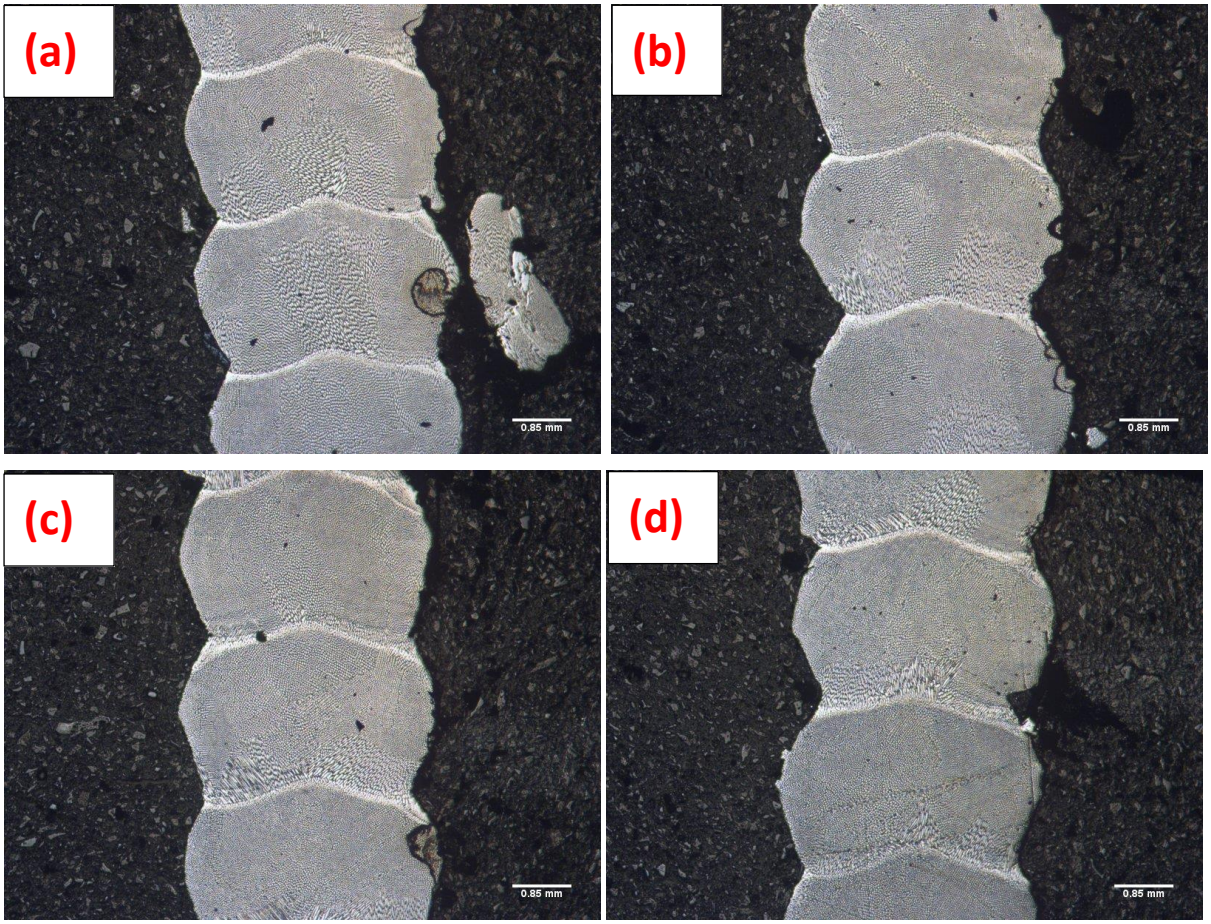

Figure 4-41: Sample B2 microstructure 4mm (a), 8mm(b), 12mm(c) and 16mm (d) from substrate, x50 magnification (316L SS, 0.6mm per step height, 4mm/s cladding speed, 2&8L/min powder and coaxial gas flow rate, 18g/min feed rate).

As before the only effect the distance from the substrate has is in the creation of a strong fusion bond for the 1mm step height sample: sample B4. Initially a strong fusion bond is not created, whereas as the distance from the substrate increases the bond length increases. This can be seen in Figure 4-42. It can be observed that this effect is reduced compared to sample A suggesting the lower powder feed rate, or helical build method, promotes a stronger bond between layers.

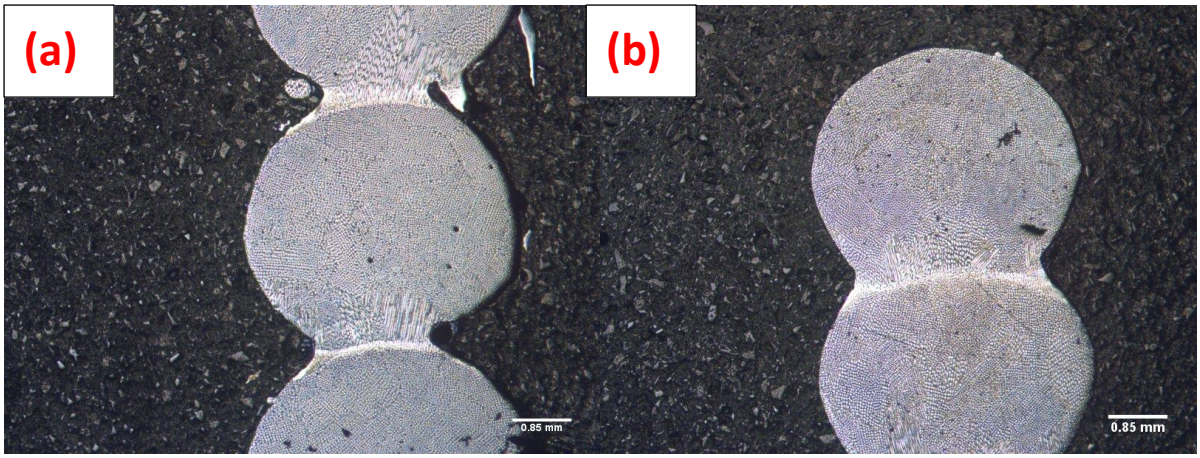

Figure 4-42: Sample B4 microstructure 4mm (a) and 20mm (b) from substrate, x50 magnification. (316L SS, 1mm per step height, 4mm/s cladding speed, 2&8L/min powder and coaxial gas flow rate, 18g/min feed rate).

Solidification rate R and thermal gradient G are the major parameters affecting the directionally solidified microstructure. Thermal gradient is the rate of temperature change with distance in the axial direction. Figure 4-42(b) shows the 3-D dendrite structure in the zone: the primary dendrite grows along the axial direction from bottom to top, a small deviation in the primary dendrite orientation was found. Near the edge, a few dendrites starting to grow from the wall towards the centre were observed indicating the faster cooling rate near the wall area. The morphology in the mushy zone is determined by the ratio of G/R in terms of critical values related to the transition between different microstructures. The morphologies related to microstructure of nickel-based super alloy as a function of G and R are shown in *Figure 4-43*.

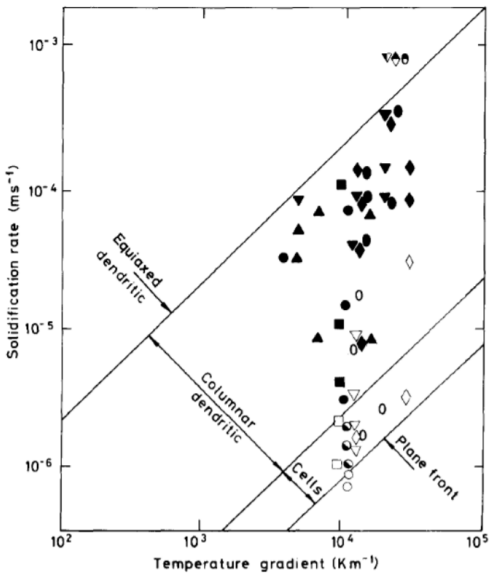

Figure 4-43: Solidification morphologies of Ni-based superalloy by DS displayed on a plot of log R [258].

If keeping G constant and increasing R, the morphology will change from a planar front through cellular, columnar dendritic to equiaxed dendritic solidification structures. Lee et al. found that for Fe-18Cr stainless steels, dendritic microstructures can be obtained at solidification rates of 50 µm/s or over at G = 10.0 K/mm [259].

The temperature gradient associated with the cooling rate is not constant along the axial direction, but is larger at the bottom, constant in the middle and above. The primary dendrite arm spacing increases with the decreased temperature gradient in the direction of the temperature gradient.

4.5.1.2 Step height

As before, altering the step height influences the microstructures found. The microstructures for samples B1 to B2 can be seen in Figure 4-44 to Figure 4-47 respectively, with varying step heights for these samples from 0.4mm, 0.6mm, 0.8mm and 1mm respectively. Sample B1 was seen to have microstructural variations from fine equiaxed cells at the outer edges to coarse epitaxial cells at the centre. Some dendritic structures were noted but very few. Sample B2 displays a very similar microstructure. Samples B3 and B4 have an essentially equiaxed fine cellular structure throughout except for small areas of directional dendritic growth propagating from the solute bands. There is a slight coarsening of the microstructure as step height increases. In terms of finding the 'ideal' microstructure a compromise must be reached. Sample B3 appears to have the closest to the ideal microstructure however the cohesion between separate layers is low which will weaken the part. Sample B2 cannot be considered optimised due to the large levels of microstructural variations therefore the 'ideal' sample can be said to occur at a step height between samples B2 and B3. T optimised sample for the given process parameters will occur at a step height of 0.8mm.

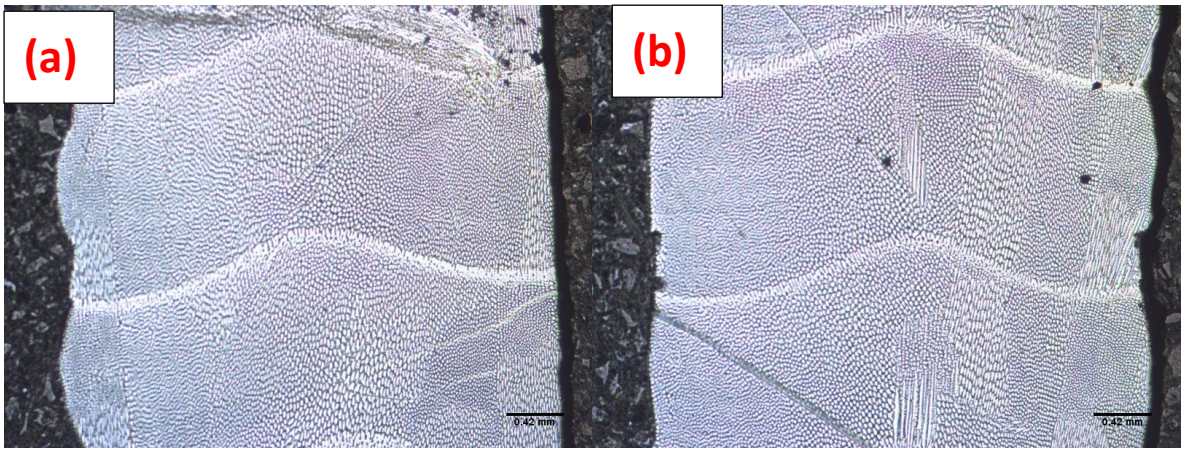

Figure 4-44: Sample B1 microstructure 4mm (a) and 12mm (b) from substrate, x100 magnification (316L SS, 0.4mm per layer step height, 4mm/s cladding speed, 2&8L/min powder and coaxial gas flow rate, 18g/min feed rate).

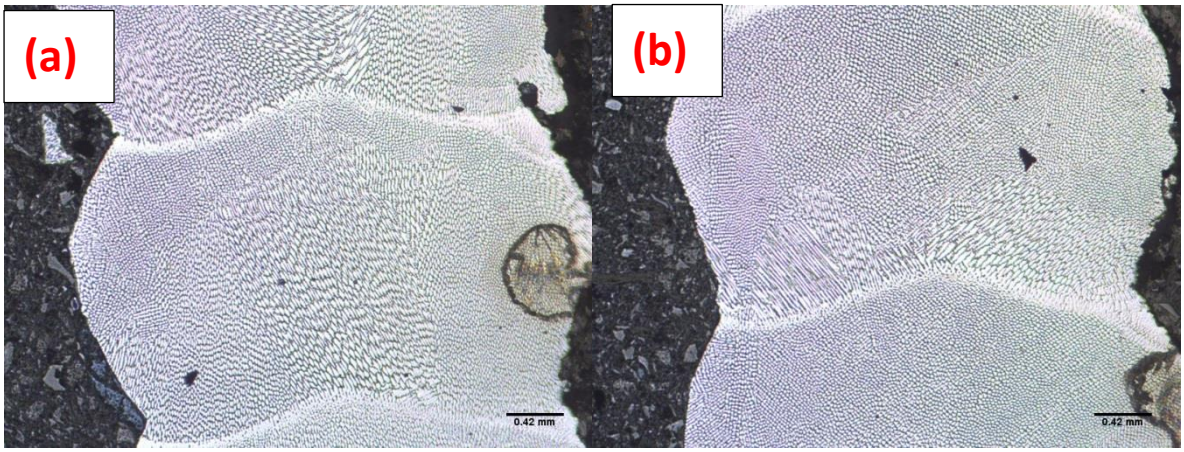

Figure 4-45: Sample B2 microstructure 4mm (a) and 12mm (b) from substrate, x100 magnification (316L SS, 0.6mm *per step height, 4mm/s cladding speed, 2&8L/min powder and coaxial gas flow rate, 18g/min feed rate).*

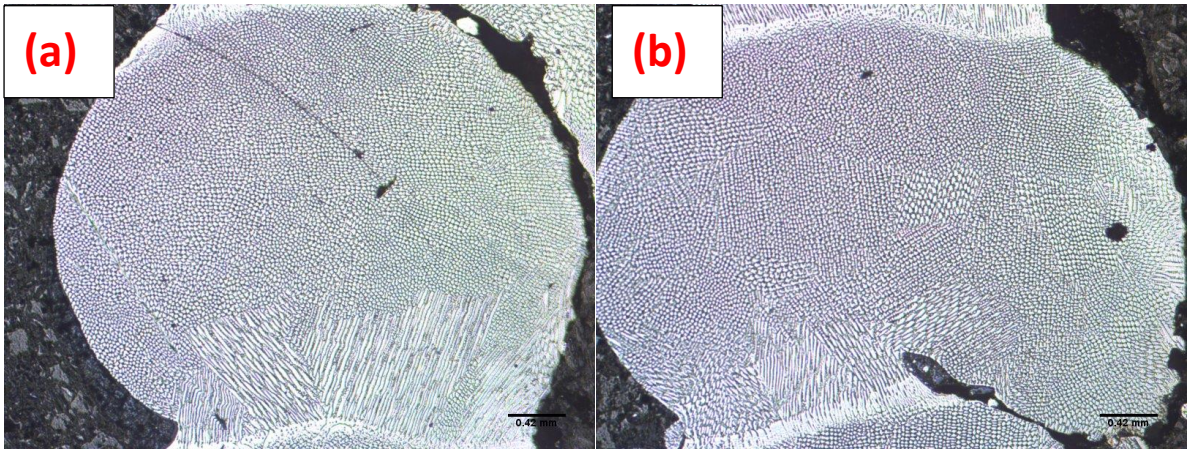

Figure 4-46: Sample B3 microstructure 4mm (a) and 12mm (b) from substrate, x100 magnification (316L SS, 0.8mm *per step height, 4mm/s cladding speed, 2&8L/min powder and coaxial gas flow rate, 18g/min feed rate).*

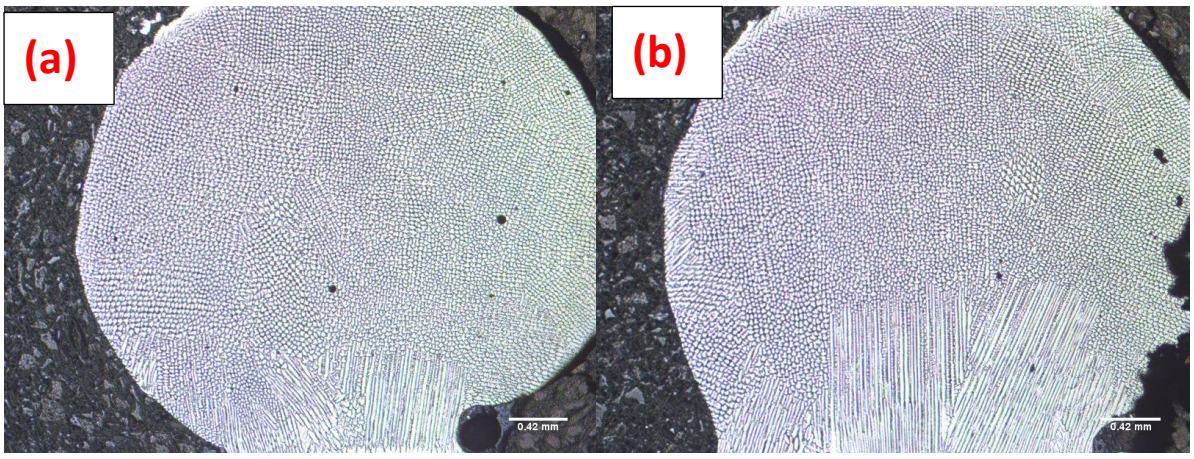

Figure 4-47: Sample B4 microstructure 4mm (a) and 12mm (b) from substrate, x100 magnification (316L SS, 1mm *per step height, 4mm/s cladding speed, 2&8L/min powder and coaxial gas flow rate, 18g/min feed rate).*

4.5.1.3 Micro-Porosity

The porosity can be seen from Figure 4-48, to be relatively low with minimal porosity noted for sample B1 and a minor increase in samples B2 and B3. Sample B4 however can be seen to be very porous. This is contrary to the findings for the test Structure A clads suggesting that either the lower powder feed rate or the helical build method have a significant effect on the porosity for samples with a low E/V.

It was suggested that porosity was caused by the entrapment of gas during cladding [260]. As a constant step height is maintained during a clad build using the test Structure B method it is unlikely that build method is the driving factor in this porosity. Therefore, the lower powder feed rate, in which less powder particles are fed into the melt pool, seems to have caused this porosity. With the test Structure A builds, an excessive amount of powder was fed into the melt pool which is undesirable. As excessive porosity is only noted on the 'unoptimized' sample B4 it can be ignored to an extent in term of achieving the 'ideal' microstructure however is worth noting.

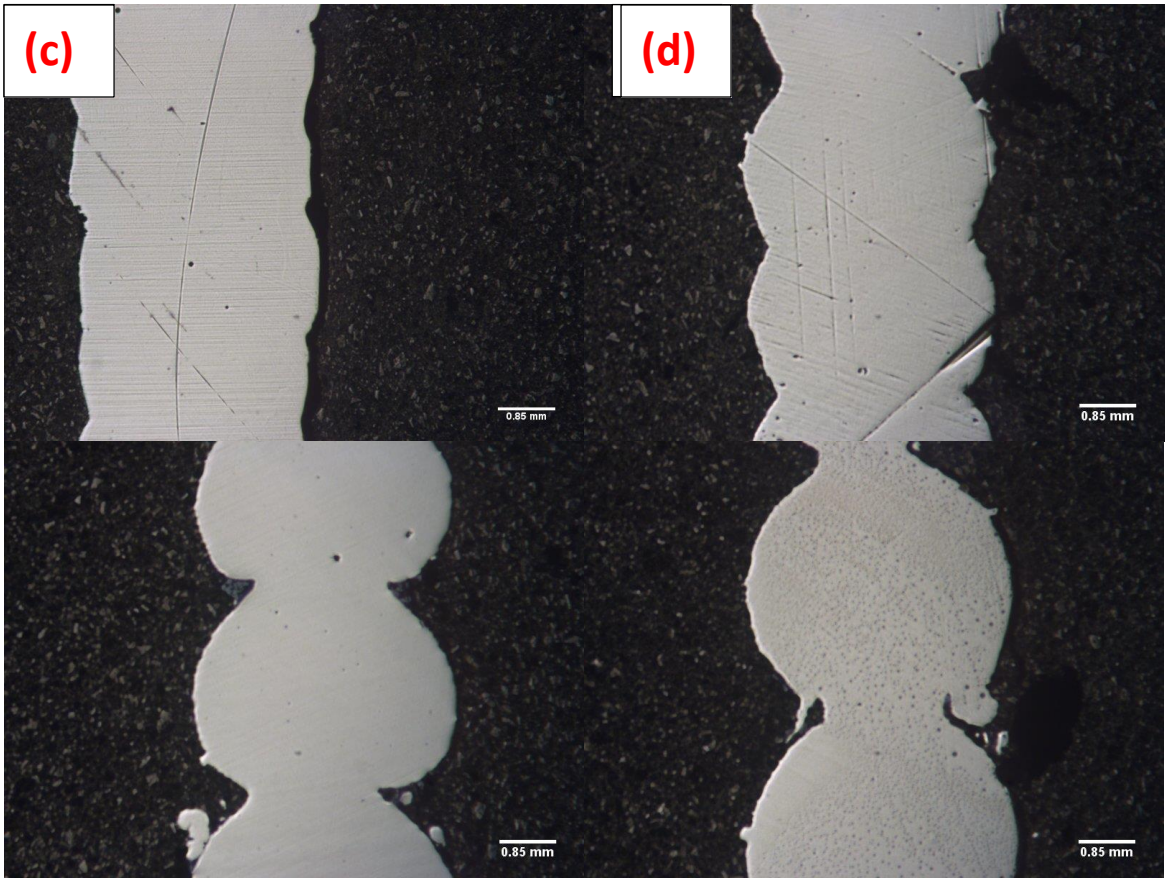

Figure 4-48: Pre-etch images – Samples B1 (a), B2(b), B3(c) and B4 (d).

4.5.2 Microstructural Analysis of Intersecting Area of Structure B

The general microstructure for the intersecting samples was found to have the same basic microstructure as all previous samples, a mix of fine equiaxed cells, coarse epitaxial cells and columnar dendritic structures as can be seen from Figure 4-49. Dendritic structures are seen to propagate from the solute bands. This contrary to that found for the test structure A intersecting samples in which the dendritic regions were found to be relatively independent of the location of the solute banding. The banding structure is different to that found for the test Structure A intersecting samples. The nature of the overlapping region is different leading to the different microstructure. Very fine cells can be found at the edges of the areas between the solute bands whilst towards the central 'hump' coarser epitaxial cellular and columnar dendritic structures can be seen.

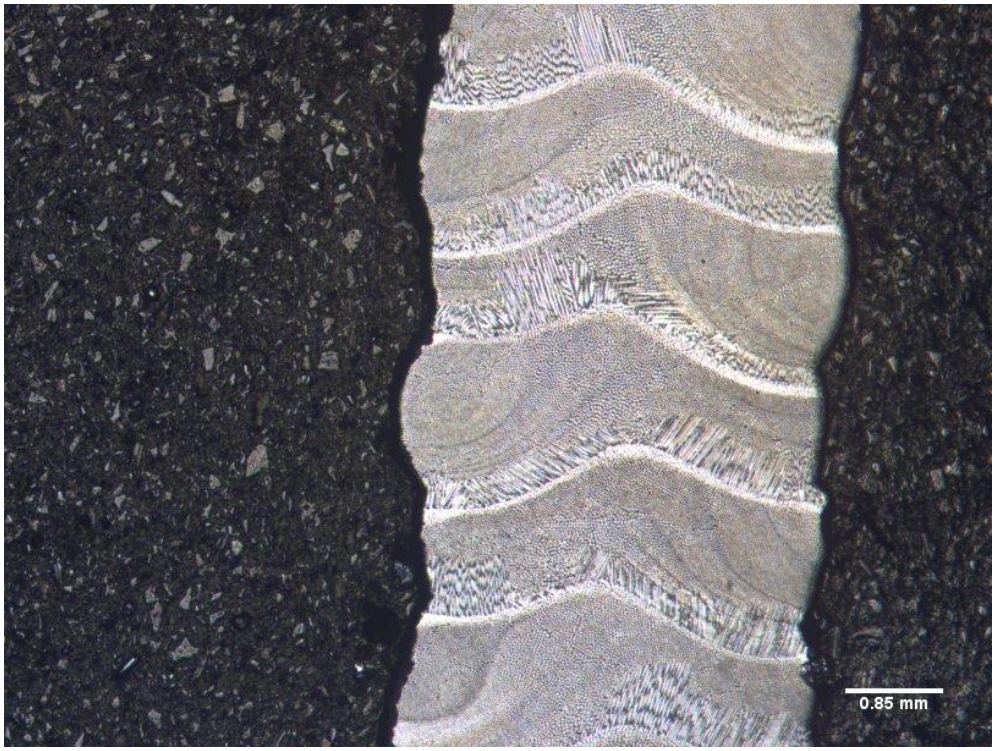

Figure 4-49: Sample B2I microstructure 8mm from substrate, x50 magnification (316L SS, 0.6mm *per step height, 4mm/s cladding speed, 2&8L/min powder and coaxial gas flow rate, 18g/min feed rate).*

4.5.2.1 Distance from Substrate

No appreciable correlation could be found relating the microstructure to the distance from the substrate. This is evident from Figure 4-50. This will be for similar reasons to those stated in section 4.4.2.1.

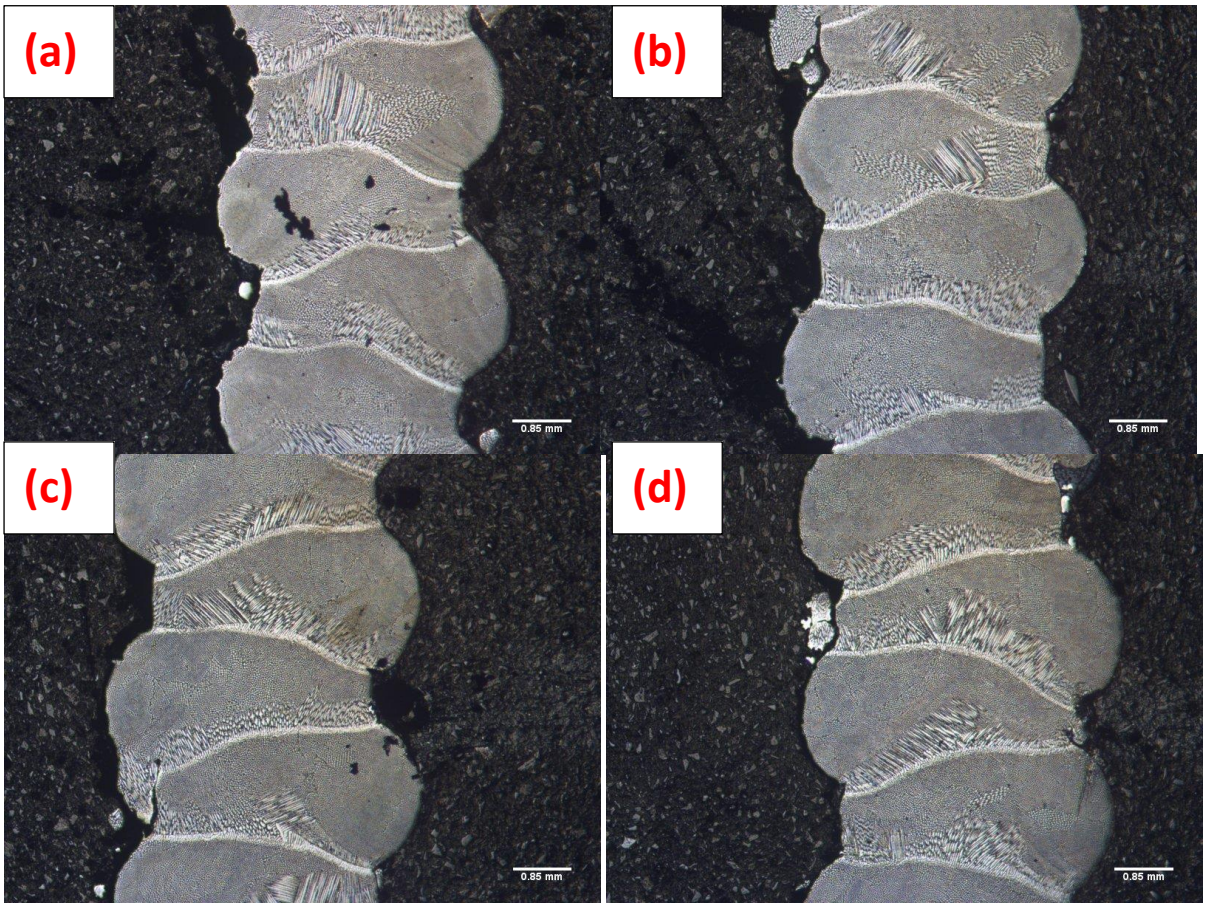

Figure 4-50: Sample 316L SS, B3I 4mm (a), 8mm(b), 12mm(c) and 16mm(d) from substrate, x50 magnification.

4.5.2.2 Step height

As for all other samples it was found that the step height affects the microstructure. The microstructures for samples B1I to B4I (I stands for intersection part) can be found in Figure 4-51 to Figure 4-54 respectively. Sample B1I can be seen to have large areas of directional growth and microstructural variation. Much of the microstructure for this sample is dendritic, more so than any other sample. The E/V is highest for this sample, 137.71J/mm^3, suggesting that to avoid a dendritic microstructure a lower energy per unit volume should be used for the clad build. Sample B2I also suffers from significant microstructural variation with several regions of epitaxial growth; sample B3I is similar but was observed to have slightly less microstructural variation. Sample 8I is the closest to a homogeneous equiaxed microstructure. A slight coarsening of the microstructure can be seen

occurring as the step height increases but is difficult to see due to the large microstructural variations in the low step height samples.

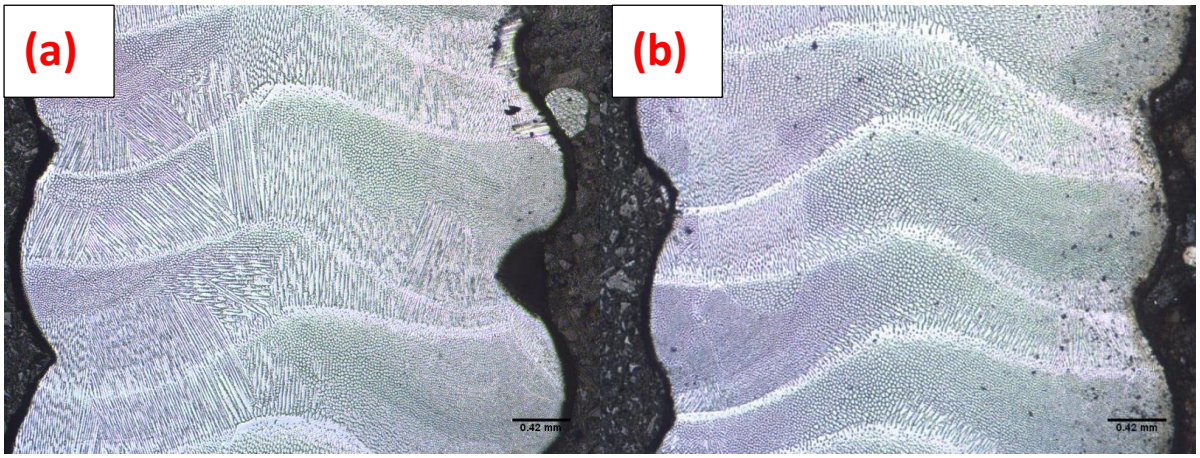

Figure 4-51: Sample B1 8mm (a) and 16mm (b) from substrate, x100 magnification (316L SS, 0.4mm *per step height, 4mm/s cladding speed, 2&8L/min powder and coaxial gas flow rate, 18g/min feed rate).*

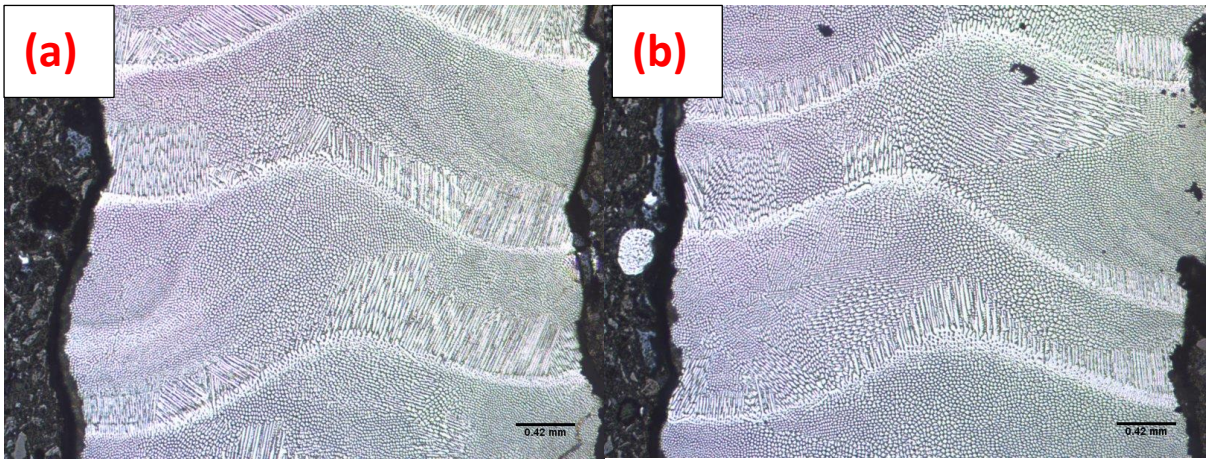

Figure 4-52: Sample B2I 8mm (a) and 16mm (b) from substrate, x100 magnification (316L SS, 0.6mm *per step height, 4mm/s cladding speed, 2&8L/min powder and coaxial gas flow rate, 18g/min feed rate).*

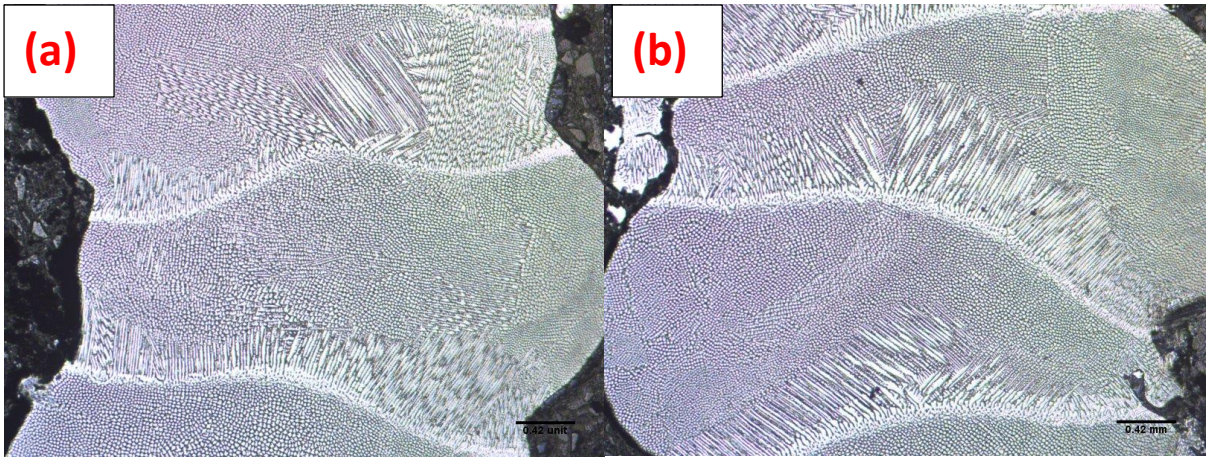

Figure 4-53: Sample B3I 8mm (a) and 16mm (b) from substrate, x100 magnification (316L SS, 0.8mm per step height, 4mm/s cladding speed, 2&8L/min powder and coaxial gas flow rate, 18g/min feed rate).

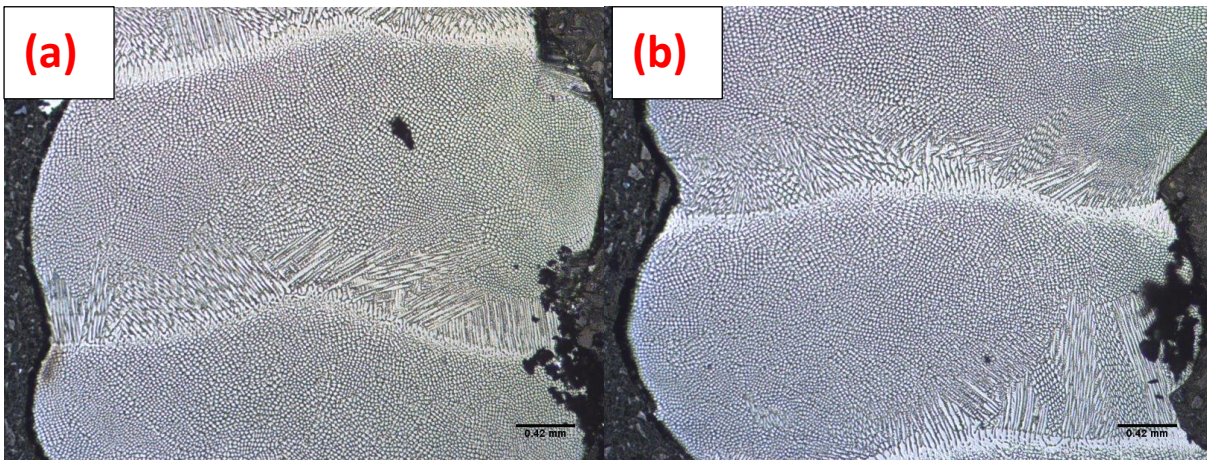

Figure 4-54: Sample B4I 8mm (a) and 16mm (b) from substrate, x100 magnification (316L SS, 1mm per step height, 4mm/s cladding speed, 2&8L/min powder and coaxial gas flow rate, 18g/min feed rate).

4.5.2.3 Micro-Porosity

Pre- etch images for the interesting samples are shown below in Figure 4-55. Porosity is minimal in samples B1I, B2I and B4I however sample 8I displays some significant porosity in areas. Due to this sample 8I cannot be considered optimum for the intersecting samples. Sample B3I still displays some significant microstructural variation. The optimised sample can be considered to occur at a point between samples B3I, 0.8mm step height, and B4I, 1mm step height. The closest to achieving the 'ideal' microstructure will be a 0.9mm step height (further analysis in section 4.10.3).

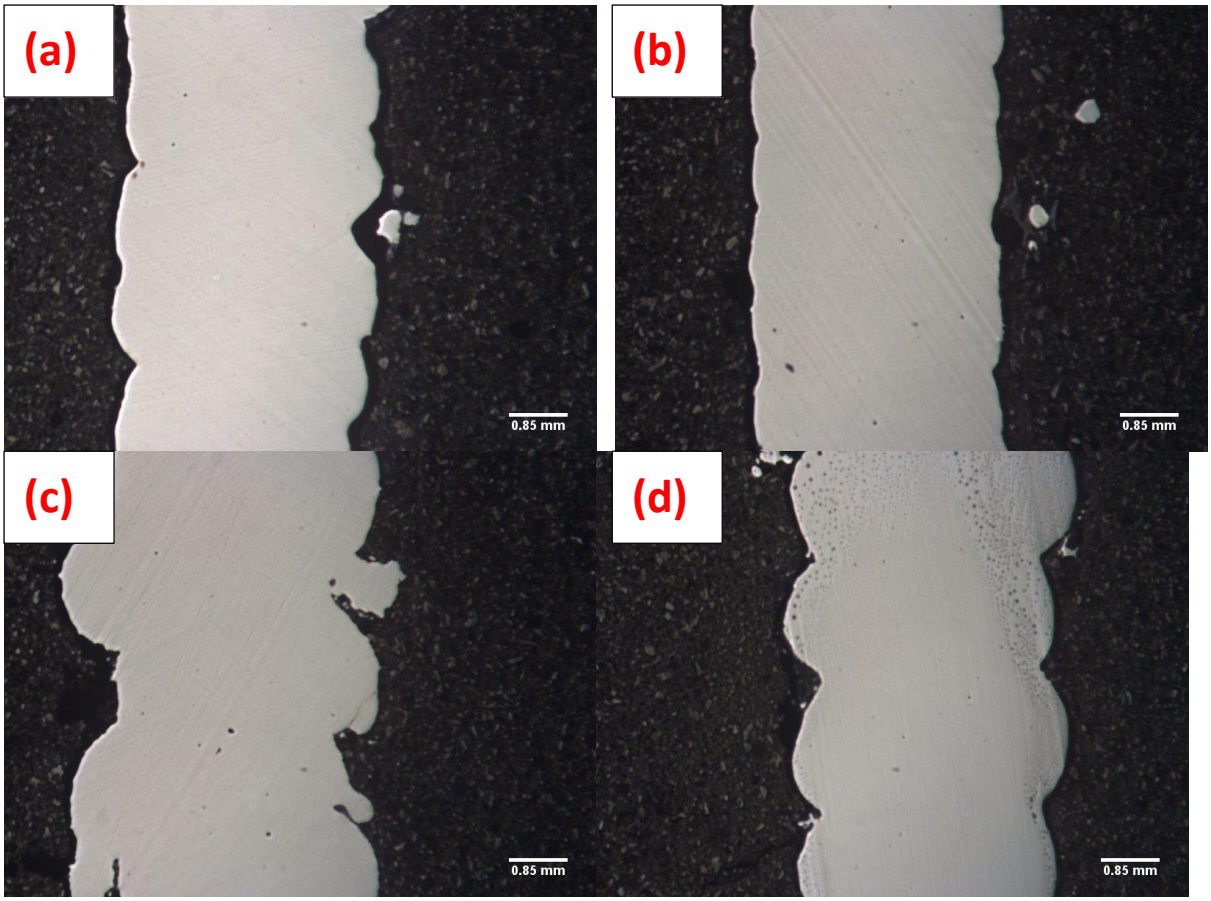

Figure 4-55: Pre-etch images – samples316L SS, B1I (a), B2I(b), B3I(c) and B4I (d), x50 magnification.

4.5.3 Comparisons between Intersecting and Non-Intersecting Microstructures

Microstructural variations were found to be greater in the intersecting samples than the non-intersecting samples. As previously mentioned, this will likely be due to the greater complexity of the reheating/remelting processes taking place as the structure overlaps. Dendritic structures were seen to propagate from the solute bands to that found for the non-intersecting samples. This is likely due to the higher heat input. A slight thinning of the microstructure can be noted from sample B4 to B4I however is not apparent in the other samples. This may be due to the low E/V value however was not noted in sample B4 and B4I.

4.5.4 Microhardness of Structure B

The microhardness for the structure B test samples was found to vary from 190-260HV (Figure 4-56). Higher hardness performance of the material can be noted in some of the test structure B builds. Comparing this to the hardness values found for the test structure A builds (170-220HV), it is evident that the test structure B build process has caused hardness increased. The cellular structure for test structure B was seen to be coarser than that for test Structure A therefore an increase in hardness is surprising. However microstructural variations are lower with less directionally solidified structures.

This suggests that the equiaxed cellular structures have higher hardness properties than directionally solidified structures. This agrees with what was found by Wu *et al [195]*.

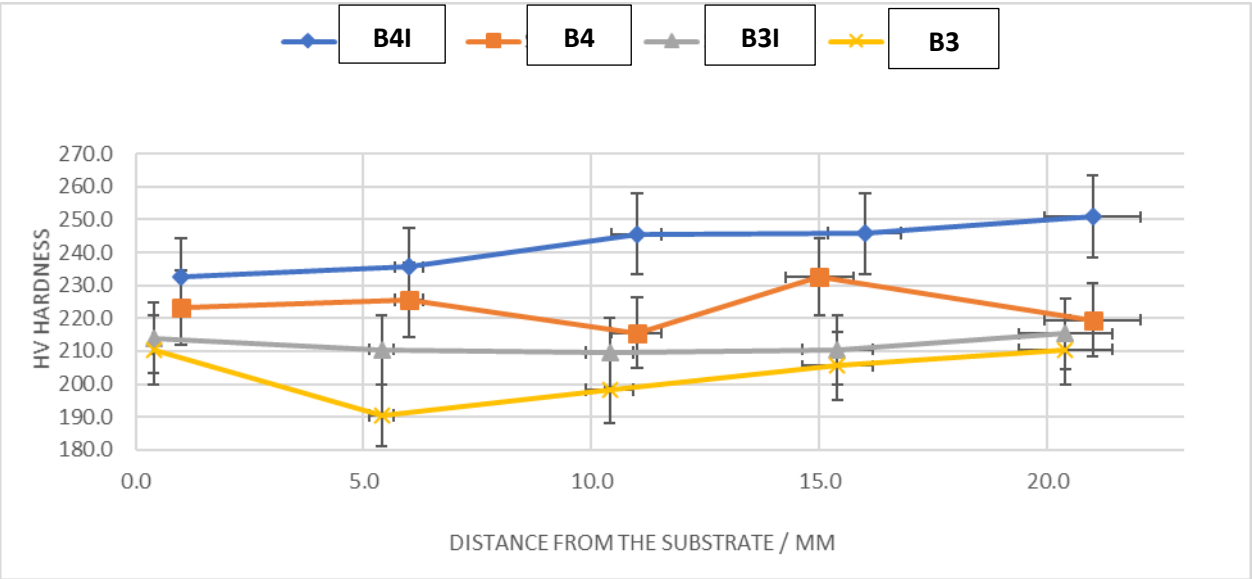

Figure 4-56: HV hardness of Structure B with 0.4mm step height (sample B1) and 1mm step height (sample B4) both intersected and non-intersected area (316L SS, 320W, 4mm/s cladding speed, powder feed rate 3000rpm, coaxial and powder gas flow are 8 and 2.5L/min).

The average microhardness values for each sample are displayed in Table 4-12. As can be seen, for the non-intersecting samples, sample B3 has the highest microhardness. Sample B3 displayed the lowest microstructural variation for the non-intersecting samples. For the intersecting samples, sample B4I displays the highest microhardness value; this was again the sample with the lowest microstructural variation.

Table 4-12: Microhardness and E/V value for Structure B both non-intersected and intersected area.

Sample	Average Vickers Hardness [HV]	E/V [J/mm^3]
B1 (Non-intersected, step height 0.4mm)	205.5	162.07
B1I (Intersected, step height 0.4mm)	210.6	162.07
B2 (Non-intersected, step height 0.6mm)	210.5	101.58
B2I (Intersected, step height 0.6mm)	225.6	101.58
B3 (Non-intersected, step height 0.8mm)	211.3	73.67
B3I (Intersected, step height 0.8mm)	234.1	73.67
B4 (Non-intersected, step height 1mm)	242.1	56.15
B4I (Intersected, step height 1mm)	254.2	56.15

4.5.5 Compressive Test of Structure B

Based on previous analysis, structure B (edge intersection like '∞') was selected for compressive testing to observe the possible uniform material properties due to the equiaxed microstructures as opposed to the typical directional solidification morphology. The test was taken in two directions: vertical (the same direction as cladding) and horizontal (perpendicular to the cladding direction); shown in Figure 4-57 and Figure 4-58. This was deigned to investigate the effect of the existence of directional solidifications growing from the solute bands. The diameter of each ring is kept constantly as 30mm and the total height was the same as 60mm.

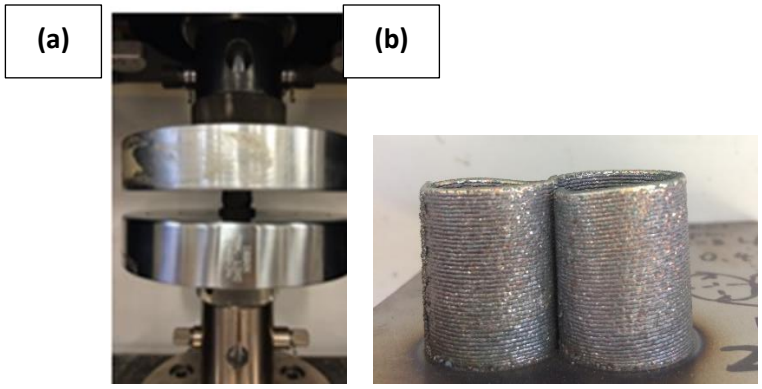

Figure 4-57: Compressive testing 1 (a) vertical placed (no holding gig needs) and (b) sample setting orientation upwards.

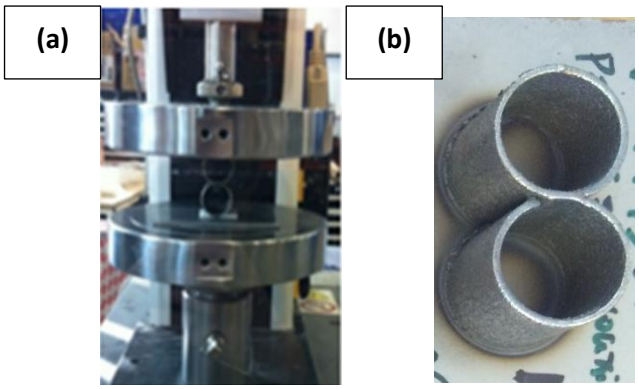

Figure 4-58: Compressive testing 2 (a) horizontal placed (holding gig needs) and (b) sample setting orientation, layers facing towards the paper.

It can be seen in Table 4-12 that the 1mm step height of structure B displayed the stress; which agreed with the microstructure observation that large amounts of equiaxed structures were observed with uniform distribution. In addition, the cladding structures performed better in the horizontal orientation which proved that the directional solidification microstructures growing from the solute bands affect the mechanical performance.

Table 4-13: Compressive Results for Structure B 316L SS, in two directions.

Step height (mm)	0.2% Proof Load (kN)		Stress (Mpa)	
	Vertical Direction	Horizontal Direction	Vertical Direction	Horizontal Direction
0.4	0.934	1.254	9.589	0.697
0.6	1.030	1.267	10.575	0.704
0.8	1.184	1.280	12.156	0.711
1.0	1.250	1.350	12.834	0.750

4.9 Investigation of Cladding Track Direct Effect on Cladding Results by Tensile Test

4.9.1 Design of Specific Dog-bone Samples

Another investigation into the mechanical property was achieved from tensile tests to obtain the ultimate tensile strength (UTS) and maximum load for the samples produced by laser cladding. To generate the tensile test coupons, the orientation of the deposited tracks in relation to the direction of the tensile force was designed in two directions, one was perpendicular to the tensile force (structure C) and the other parallel (structure D) shown in Figure 4-59.

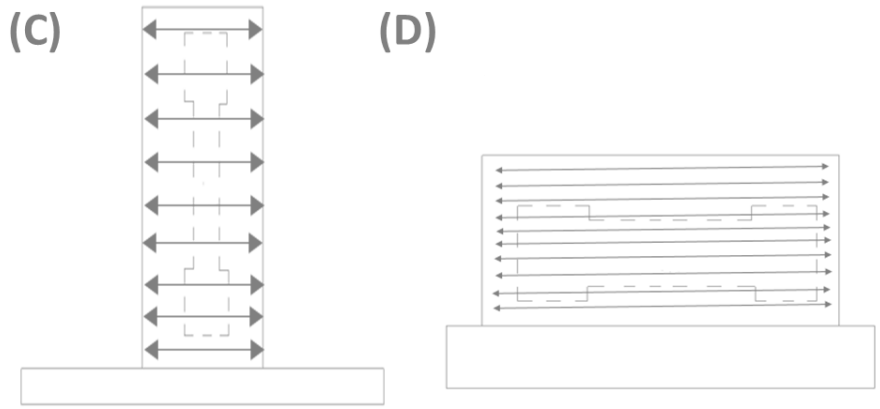

Figure 4-59: (C) Structure C: loading perpendicular to the cladding direction, and (D) Structure D: loading parallel to the cladding direction. These builds used for tensile test.

Table 4-14 and Table 4-15 display the processing parameters and related dimensions for the two orientations. The parameters set were to explore the power effect and two types of powder catchment efficiency combined by power feed rate and gas flow rate. All coupons were laser clad with 1mm step height.

Table 4-14: Processing parameters for structure C with vertical cladding tensile test samples and related dimensions (Figure 4-59 (C)).

Sample	**Processing Parameters**			**Sample width (mm)**	**Sample thickness (mm)**
	Power (W)	Powder feed rate (g/min)	Coaxial & powder gas flow (L/min)		
C1	320	8	4&2	29.92	1.38
C2	320	23	8&2.5	29.88	1.41
C3	400	23	8&2.5	30.61	1.46
C4	600	23	8&2.5	30.72	1.69

Table 4-15: Processing parameters for structure D with horizontal cladding tensile test samples and related dimensions (Figure 4-59 (D)).

Sample	Processing Parameters			Sample width (mm)	Sample thickness (mm)
	Power (W)	Powder feed rate (g/min)	Coaxial & powder gas flow (L/min)		
D1	320	8	4&2	29.21	1.38
D2	320	23	8&2.5	26.54	1.45
D3	400	23	8&2.5	25.97	1.83
D4	600	23	8&2.5	26.05	1.76

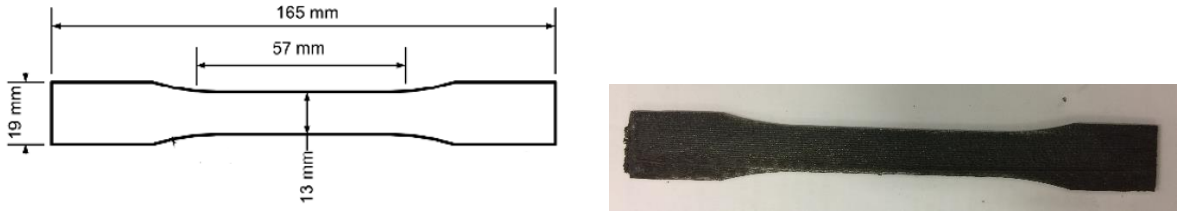

Figure 4-60: Dimensions for the Structure C and D (left) and actual sample (right).

4.9.2 Tensile Test of Specific Dog-bone Samples under Low Power Cladding

The structures C and D (*Figure 4-59*) were subjected to a tensile test. From the results generated in Table *4-16* and Table 4-17. It can be summarized that the horizontal samples which the track orientation was parallel to the tensile force show higher maximum breaking load and ultimate tensile stress and lower elongation than perpendicular ones.

Table 4-16: Averaged mechanical properties for samples with loading perpendicular to the cladding direction.

Sample	Max.Load (kN)	Ultimate Tensile Stress (MPa)	Elongation (%)
C1	12.15	394.26	38.88
C2	7.74	277.56	45.00
C3	7.00	256.63	30.37
C4	9.10	275.28	29.75

Table 4-17: Averaged mechanical properties for samples with loading parallel to the cladding direction..

Sample	Max.Load (kN)	Ultimate Tensile Stress (MPa)	Elongation (%)
D1	15.71	489.73	23.55
D2	14.05	465.10	16.96
D3	13.04	474.38	16.55
D4	15.38	435.46	17.97

Dendritic epitaxial microstructures were obtained for all process parameters. An increase in laser power resulted in a reduction in the hardness, yield strength and tensile strength. This was attributed to an increase in cooling rate leading to a quenching effect. As cladding speed was increased the hardness and strength properties were seen to increase. The cause being the reduced interaction time resulting in a more refined quenching effect due to higher solidification velocities in the build.

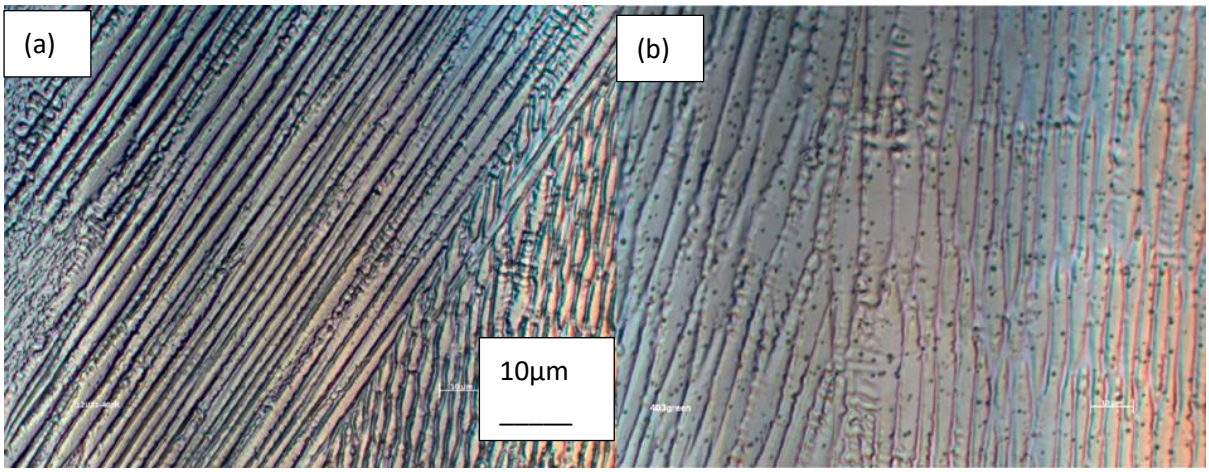

Figure 4-61: Cross sections of the sample.

One of the contributing factors might be the orientation of the grain/dendrite boundaries. After laser cladding most of the dendrites are oriented along the building direction. Upon loading parallel to the upwards-building direction into the plastic deformation region less barriers like dendrite/grain boundaries need to be crossed by the dislocations. This is reflected by a lower strength when loading parallel to the build-up direction. Another factor affecting the tensile strength is the size of grains or dendrites, as specified in the Hall–Petch relationship: $\sigma_s = \sigma_0 + k_y d^{-1/2}$, with σ_s the yield strength, σ_0 a materials constant for the starting stress for dislocation movement or the resistance of the lattice to dislocation motion, k_y the strengthening coefficient which is a constant unique to each material, and d the average grain/sub-grain diameter [261]. The dendrite spacing in the loaded region is larger for

the sample loaded parallel to the build-up direction. For this sample, an increase in dendrite spacing from 1–2 µm up to about 3–4 µm is observed from bottom to top of the sample (Figure 4-61: Cross sections of the sample.). This difference is also reflected by the hardness measurements: The hardness is about 30 HV higher and the microstructure finer near the baseplate than at the top because of the higher cooling rate. The lower hardness is attributed to the lower cooling rate near to the top as a result of heat accumulation in the slender sample. For the sample loaded parallel to the build direction the cooling rate in the loaded region is larger and consequently a smaller dendrite spacing, and higher strength is obtained.

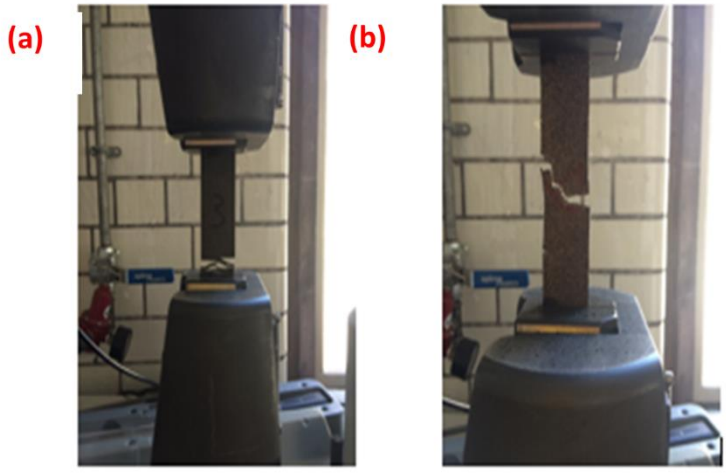

Figure 4-62: (a) Vertical build which tracks perpendicular to the tensile force; (b) horizontal build which tracks parallel to the force.

Further testing was conducted by Fernandes de Lima and Sankaré [262]. Several wall structures were produced from 316L stainless steel with overlapping clad tracks for microstructural analysis and mechanical testing. Process parameters were varied for these builds. Cracks and voids were found at the overlapping regions, which were assumed to be weak points in the mechanical testing. From an epitaxial fine dendritic microstructure tensile testing gave the mechanical properties shown in Table 4-18. It is important to note that the tensile tests were conducted in the direction parallel to cladding direction. The process parameters A, B and C can be found in Table 4-9 that conducted similar tensile testing on porous 316L stainless steel samples obtained from laser cladding. Ultimate tensile strengths were found to be in the region 400-500MPa dependant on process parameters, whilst 0.2% proof stress was found to be greater than 205MPa. The strongest samples were produced at a laser power of 1600W and a cladding speed of 23.3mm/s. Comparatively this is a very high laser power and cladding speed resulting in a high power over a low interaction time. The result of this was linked to a high cooling rate resulting in a refined microstructure with superior mechanical properties.

Table 4-18: Mechanical properties of 316L wall structures [262].

Process Parameters	Yield Stress (MPa)	Ultimate Tensile Stress (MPa)	Total Elongation %	Elastic Modulus (GPa)
A	229	414	37.8	3.5
B	261	530	43.4	3.7
C	207	539	45.0	3.4

Further to this Zhang *et al.* also conducted their tensile tests in both parrallel and perpendicular to the cladding direction. As the microstructures were epitaxial it would be expected that the mechanical properties would vary dependant on direction. As shown in Table 4-19 this is the case, it can also be seen that when loading in the parallel direction the speciment was seen to have superior mechanical properties. The values were much higher than the results generated here which may be due to the composition of the raw material and different processing parameter *et al*, however the final results appear to confirm my findings.

Table 4-19: Mechanical properties of specimens loaded in the parallel and vertical direction.

Loading Direction	Yield Stress (MPa)	Ultimate Tensile Stress (MPa)	Elongation (%)
Parallel	558	639	21
Perpendicular	352	536	46

This trend is also reported and agreed in other studies by similar investigation methods and analysis [263, 264]. In general, samples fabricated in 'horizontal' orientation (parallel to tensile loading direction) show higher strengths and lower elongation than 'slender' samples fabricated in perpendicular orientation of the tensile loading. This is attributed to the existence of a comparably weaker layer. Once the tensile force is perpendicular to the layers, the tensile force is applied directly to this weaker layer causing the failure; while the tensile force is parallel to the layers, the property of the specimen is averaged by all layers becoming stronger which resulting in higher strength. The reason behind the weakness can be the inter-layer porosity.

4.10 Further Evaluation and Discussion on 316L SS Cladding Samples

Using the experimental data accumulated it is possible to create analytical relationships between the cladding parameters. The ideal microstructures found for both test structures can be analysed in terms of their process parameters.

4.10.1 Test Structure A

For test structure A - a 0.6mm step height clad build (E/V=82.7J/mm^3) was found to produce the optimum microstructure where there is no crossover point. Where a crossover point occurs, the optimised microstructure was discovered to occur at a 0.8mm step height (E/V=58.45j/mm^3). It was theorised that an increase in cladding speed could be programmed into the CNC table to occur only at the crossover points so that the 'ideal' microstructure could occur throughout the clad build. By rearranging as shown in equation Eq.4-3, the cladding speed required to achieve an energy density of 58.45J/mm^3 during a 0.6mm step height clad build can be calculated. This cladding speed was calculated, using values for sample A2 displayed, to be 5.77mm/s. This is a 1.77mm/s increase in the cladding speed used for the builds.

$$v = \frac{\eta_w P_{laser}}{\frac{E}{V} * hw} \qquad \text{Eq. 4-5}$$

This analysis is not ideal and holds with many assumptions. The main assumptions are as follows: the microstructure is assumed to be affected only by the energy per unit volume, the clad width is assumed to be constant even when cladding speed increases and all areas of the sample which do not intersect are assumed to have the same energy input whilst the same is true of all the areas which do intersect.

4.10.2 Test Structure B

For test structure B the optimised microstructure was estimated to occur at a 0.7mm step height where the structure does not intersect and 1 mm where the structure does intersect and 0.9mm where the structure does intersect. As clad builds were not produced with these step heights an analytical relationship between the step height and the energy per unit volume can be used for the test Structure B process parameters, as shown in Figure 4-63. A second order parabolic relationship can be formed and is displayed in equation Eq.4-6.

$$\frac{E}{V} = 257.01h^2 - 510.33h + 299.9 \qquad \text{Eq. 4-6}$$

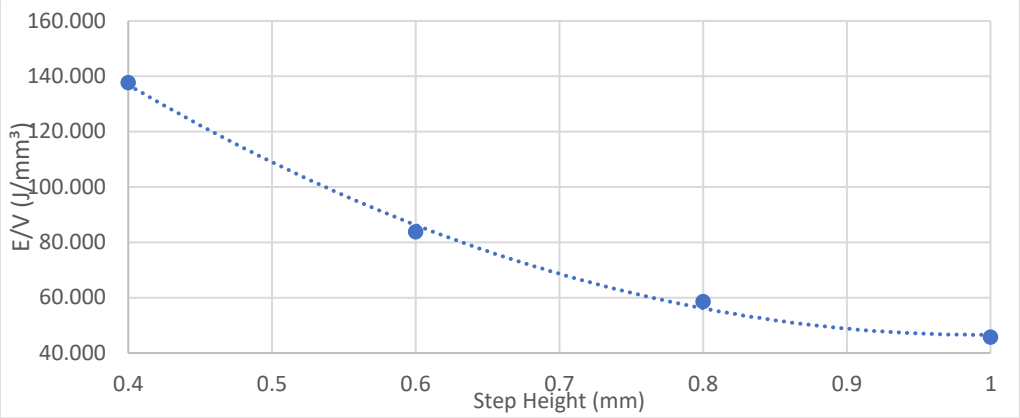

Figure 4-63: Structure B analytical relationship between cladding parameters

Using this relationship the E/V values can be calculated for step heights of 0.7mm and 0.9mm. These are 48.85J/mm^3 and 68.65J/mm^3 respectively. Equation 4-6 can be manipulated to find the clad width for a 0.7mm step height clad, given the E/V calculated and the original process parameters. This gives a clad width of 1.38mm. The required cladding speed at the intersection points to achieve the 'ideal' microstructure throughout can now be calculated. This was calculated as 5.70mm/s and 1.7mm/s increase.

4.10.3 Microstructural Investigation – The Optimised Clad Build

The 'optimised' sample was produced for the non-intersecting microstructure i.e. a 0.8mm step height clad build with the process parameters stated. The test structure B build method was chosen for production of the ideal sample as this method provided superior mechanical and microstructural properties. The cladding speed increase between the 'ideal' non-intersecting sample and the 'ideal' intersecting sample is also slightly lower than for test Structure A making this sample advantageous from an investigation viewpoint. Two further clad builds were produced also, one with a 1mm step height and one with a 0.4mm step height for comparison in a compression test.

This 'ideal' sample was sectioned as before and can be referred to as sample B5 or B5I (0.9mm per step height, 4mm/s, 18g/min powder feed rate, 2&8L/min powder and coaxial gas flow rate) to distinguish between the non-intersection and the intersection point respectively. Unfortunately, during the preparation stage, the samples were etched too deeply. No attempt was made to compare the microstructure with the distance from the substrate due to results obtained from all other samples. The clad width for sample B5 was measured as 1.36mm. This gives an E/V of 68.28J/mm^2. Comparing this with the clad width of 1.38mm and E/V of 68.65J/mm^3 calculated using the analytical relationship, it can be seen that a fairly high degree of accuracy was obtained using this relationship.

4.10.3.1 Non-Intersecting

The microstructure at the non-intersecting point can be seen in Figure 4-64. As is evident the microstructure is primarily equiaxed cellular and is homogeneous with only small areas of directional solidification. Slightly less microstructural variation is noted than that found for sample B3. As sample B3 was discovered to have a microstructure closest to the 'ideal' microstructure from all the test structure B samples. Sample B3 was not chosen as the ideal microstructure due to the lack of cohesion between layers. This seems to also affect sample B5 but to a lesser extent. It seems for the given process conditions sample B5 is as close to the optimum as possible.

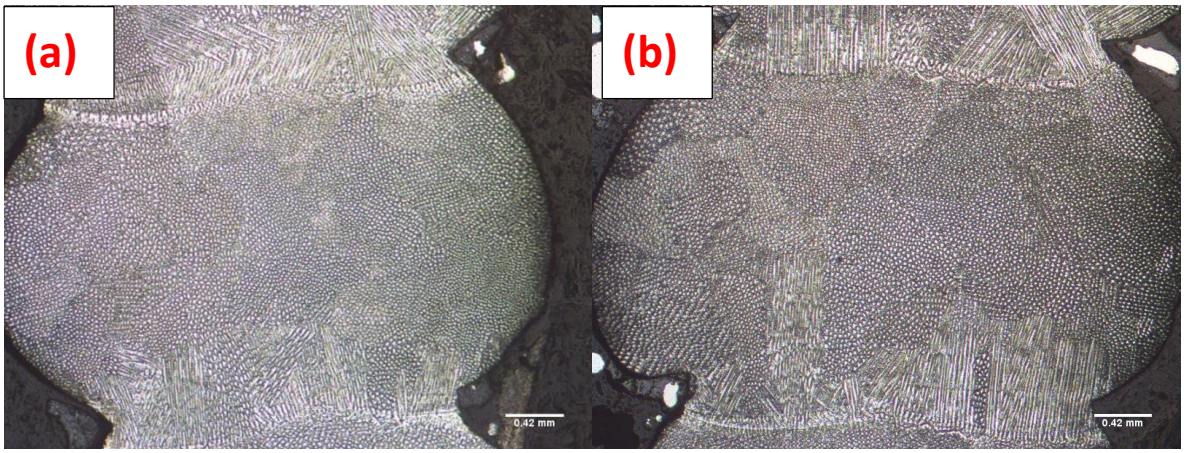

Figure 4-64: Sample B5 316L SS, microstructure 8mm (a) and 16mm (b) from substrate, x100 magnification

Some porosity is evident in sample B5 as is evident from Figure 4-65. Slightly more than is evident from samples B2 or B3. This is unexpected with the cause unknown requiring further research beyond this research.

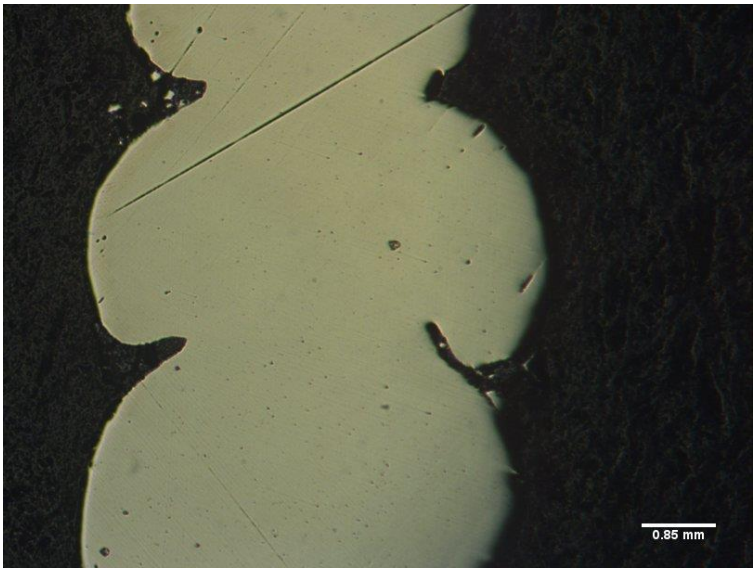

Figure 4-65: Sample B5 pre-etch image (316L SS, 0.9mm per step height, 18g/min feed rate, 2&8 powder and coaxial gas flow rate for edge intersecting hollow cylinder).

4.10.3.2 Intersecting

The intersecting sample is not considered optimum from the test structure B investigations. The microstructure for sample B5I can be seen in Figure 4-66. Microstructural variations were observed to be fairly high. Columnar dendritic growth is present but not in large amounts. Rather than displaying a uniform cellular structure sample B5I was observed to have large variations from coarse epitaxial cells and fine equiaxed cells throughout. The structure is far from homogeneous. This adds further evidence to the optimum cladding microstructure for an intersect point being at the lower E/V of 48.85J/mm^3.

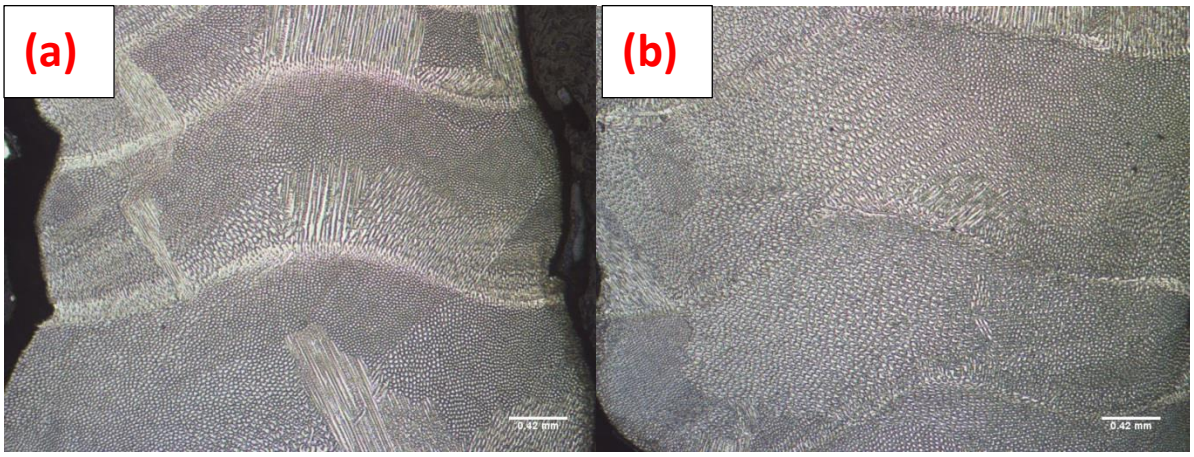

Figure 4-66: Sample 316L SS, B5I microstructure 8mm (a) and 16mm (b) from substrate, x100 magnification.

From Figure 4-67, a pre-etch image of sample B5I, it is clear that porosity is minimal. Porosity is similar to samples B1, B2 and B3.

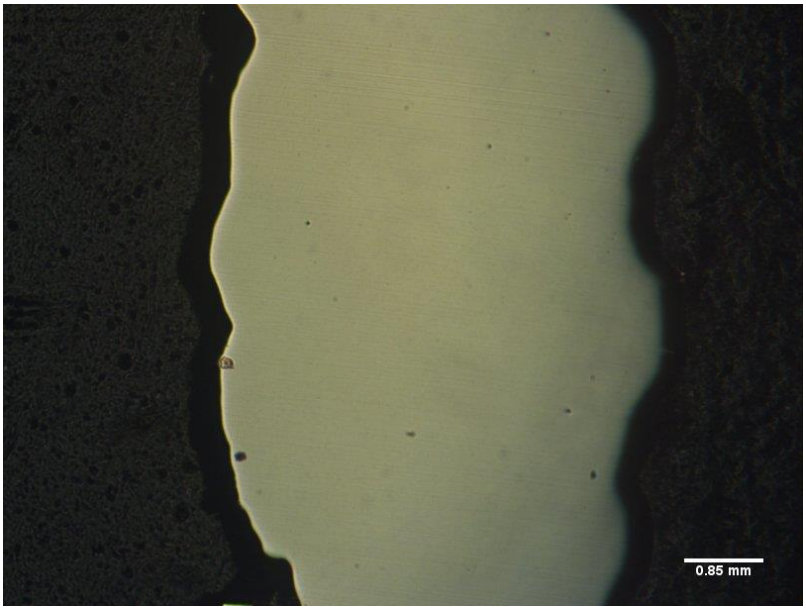

Figure 4-67: Sample 316L SS, B5I pre-etch image (0.9mm per step height, 18g/min feed rate, 2&8 powder and coaxial gas flow rate for edge intersecting hollow cylinder).

4.10.3.3 Conclusions of Microstructure Analysis

Microstructures found during the investigations were primarily equiaxed cellular, with secondary phases of epitaxial cellular and columnar dendritic structures. This was a result of high cooling rates caused by low E/V values and low cladding speed. The high cooling rates promote high temperature gradients and cellular microstructures result. Also caused by low E/V values, low cladding speed, and possibly also the use of a thin substrate, is the lack of microstructural alteration with increasing distance from the substrate. The step height does significantly affect the microstructure of part built by BPLC. Altering the step height, i.e. altering the E/V, was seen to cause a change in the microstructures and particularly the levels of microstructural variations. As the energy per unit volume decreases the microstructure coarsens due to a decrease in the cooling rate and an increase in the ratio G/R.

The microstructure at the intersection points was seen to differ from the microstructure at the non-intersection points due to the added thermal process taking place. Microstructural variations were seen to increase at the intersection points. The greater complexity of the reheating/remelting process which occurs at the crossover point results in greater variations in cooling rates within the melt pool. This leads to an increase in microstructural variation. The result of this is that optimum process parameters need be defined at non-intersection points and intersection points separately.

Optimum process parameters, in terms of the energy per unit volume, were defined for both test structure build methods for the intersection points and non-intersection points and are summarised in Table 4-20. Due to the nature of the test structure B investigations the analytical model was used to find the optimum E/V. From analysing the clad builds creation of the optimum microstructure at both the intersection and non-intersection points with a uniform step height can be done with an increase in cladding speed. This was calculated as 1.77mm/s for test Structure A and 1.7mm/s for test structure B2. It is important to note that the different build methods used for test structures A and B were seen to have a significant effect on the microstructure. The test Structure B build method was seen to display lower microstructural variations and is therefore superior to the test Structure A build method.

Table 4-20: Optimum process parameters.

Built Method	Intersection Optimum E/V (J/mm^3)	Non-Intersection Optimum E/V (J/mm^3)
Test Structure A	58.45	82.70
Test Structure B	48.85	68.65

The optimum microstructure is defined as a homogeneous equiaxed microstructure. Following production of the 'ideal' sample, using the test structure B build method, for the non-intersection points microstructural variations were reduced although directional growth was not eliminated. Therefore, a homogeneous equiaxed microstructure was largely achieved in this research on sample B5.

It is evident that the location and shape of the solute bands significantly affects the microstructure. A key observation from almost all the clad samples is the propagation of columnar epitaxial structures from the centre of the solute bands. The solute banding contained a central 'hump' in most situations from which directionally solidified growth was seen to propagate. The laser used has a TEM^{01*} beam mode structure. Relating this to the shape of the solute banding is very similar to the shape of the isotherm developed by TEM^{01*} beam mode. The areas towards the outside of the clad are heated and as such temperature gradients are greater and a fine cellular microstructure form. Towards the centre of the clad the temperature gradients are less allowing dendritic structures to form. The use of a different beam mode structure such as a TEM^{10} or 'top hat' mode might eliminate the dendritic epitaxial growth.

Porosity in the BPLC samples was minimal in most cases however was evident in samples B4 and B4I along with sample B5 to an extent. The cause of this porosity is possibly the low cladding speed in conjunction with very low E/V values for the 1mm step height samples and, since sample A4 and A4I appeared to have low porosity, the powder feed rate or build method. It is difficult to suggest the exact causation and is an area where further research may be required.

4.10.4 Microhardness

The microhardness for sample B5 and B5I (0.9mm per step height, 18g/min feed rate, 2&8 powder and coaxial gas flow rate for edge intersecting hollow cylinder) was found to vary from 200-260HV in Figure 4-68. This is similar to the hardness values found for the structure B test samples as would be expected. An increasing in hardness of the material has occurred. The average microhardness for samples B5 and B5I is 231.8HV and 225.0HV respectively. As found before there is very little variation between the crossover sample and the standard sample. It was suggested earlier that lower microstructural variation causes higher hardness. This would explain the sample B5I microhardness result being lower than B4I or B3I as microstructural variations are greater however sample B3 has a higher microhardness than sample B5 despite having greater microstructural variations. Microstructural variations were low sample B3 and only slightly lower for sample B5.

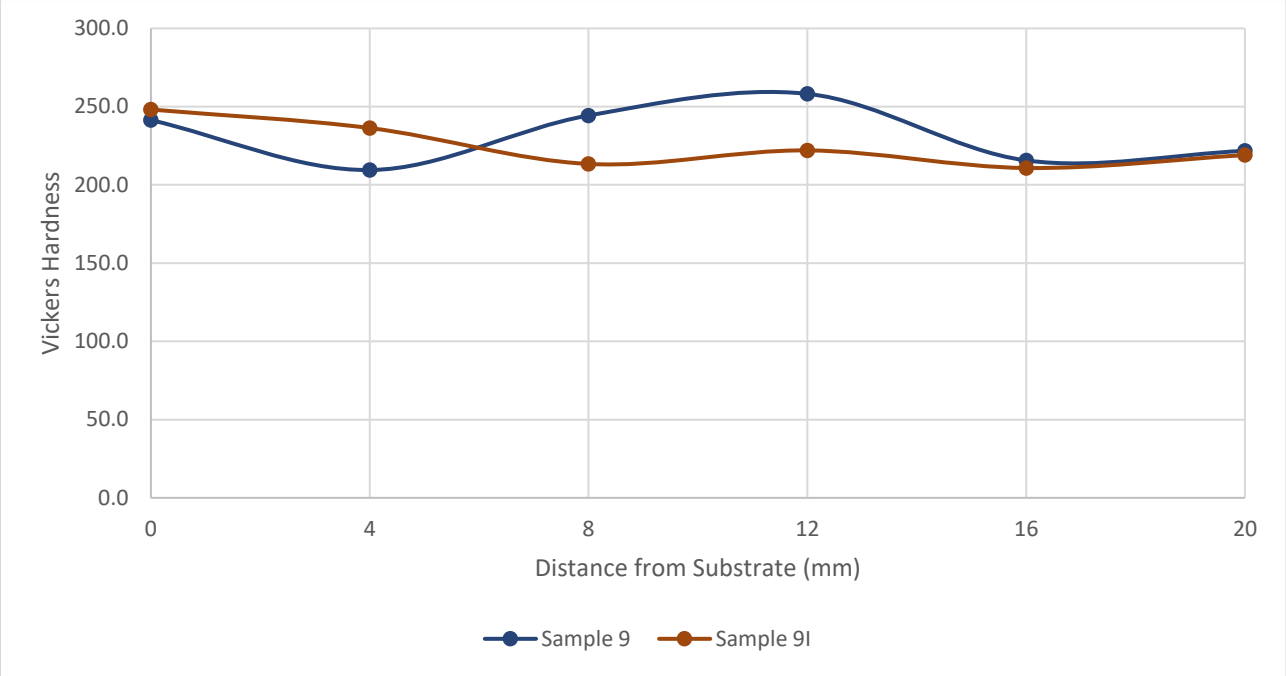

Figure 4-68: Sample B5 and B5I microhardness (0.9mm per step height, 18g/min feed rate, 2&8 powder and coaxial gas flow rate for edge intersecting hollow cylinder).

4.10.5 Mechanical Properties

The microhardness results can be linked to the microstructures. Varying the distance from the substrate was seen to have a negligible effect on the microhardness whilst altering the step height was seen to have an effect. The microhardness was seen to increase as the microstructural variation decreased. Where microstructural variation is high directionally solidified structures are present including dendritic structures and coarse cells. These structures have lower hardness values that the fine cellular equiaxed microstructure which occurs where microhardness is minimal leading to the microhardness increase.

The test structure B build method resulted in lower microstructural variations and as such a microhardness increase was observed from test Structure A to test structure B. The test Structure A samples were found to have hardness values similar to that of wrought 316L Stainless Steel whilst the test structure B samples were observed to have an increase in hardness compared to the wrought material. The fine cellular microstructure found because of high cooling rates, and therefore high temperature gradients and thermal stresses, is hardened.

From the compression test all samples displayed roughly similar values or the 0.2% proof stress. The

1mm sample was found to be the strongest sample. As the crush test samples were produced with a constant step height and cladding speed the microstructure for each sample will vary between the intersection and non-intersection points. The 1mm sample was found to have minimal microstructural and the maximum microhardness at the crossover point suggesting that the yielding occurred at the crossover points during the compression test. The 0.4mm step height sample was the weakest adding further evidence to this however only three samples were tested due to time constraints therefore any conclusions which can be gained are limited.

4.11 Effect of Deposited Walls Intersecting at Different Angles

The intersected area studies on two cylinders can give some ideas on how cladding strategies affecting the melt pool and microstructures of the cladding results besides the processing parameters. The extent to which crossover at different angles affects the microstructure is a function of the total energy absorbed into the inter-sectioned area.

A series of two simple walls deposited at different intersecting angles was designed and manufactured using the same processing parameters: 1mm per step height, 4mm/s cladding speed, 2&8L/min powder and coaxial gas flow rate, 18g/min feed rate at approximately 500W, which is shown in Figure 4-69 . Figure 4-70 shows the section path and cross-area mounted in the resin for microstructure analysis.

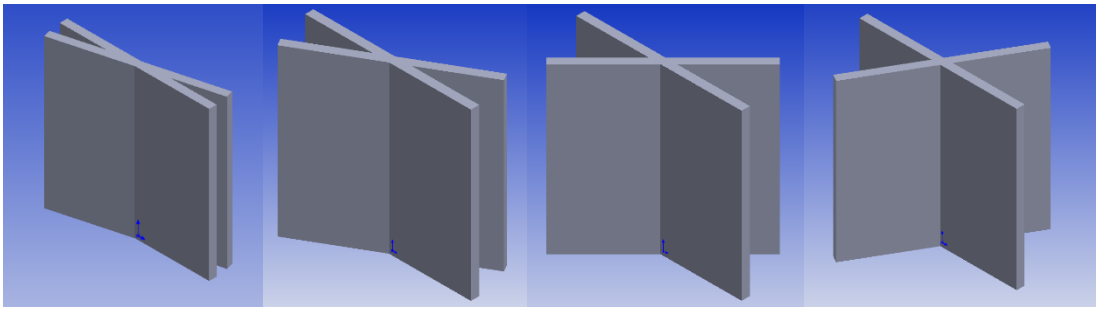

Figure 4-69: Deposited Walls Intersecting at Different Angles from left to right are 15^0, 30^0, 45^0 and 60^0 respectively.

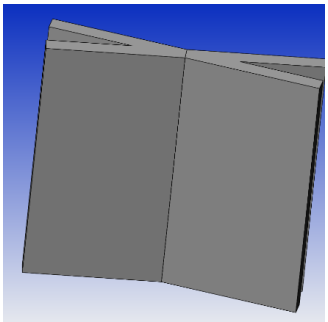

Figure 4-70: Cross-section with black line in the middle indicating the sectioning path.

Optical micrographs of the revealed microstructure of each intersecting aeras for different angles were shown from Figure 4-71 to Figure 4-74 respectively from 15^0 to 60^0. During the laser cladding processing, the overlapping zone was subsequently melted and a part of metal powder was fed into the melting pool and subsequently melted. Meanwhile, amount of metal powder was melted and cladded on the overlapped surface which resulted in the formation of cladding height, As shown in all 4 figures, the layer was free of defects, like holes, cracks or unmelted particles etc. According to the microstructure of cross section, the formed phase was uniform austenite. This was because of the content of Cr reached as high as 18% in weight which made it prone to obtain uniform austenite at low Ni element content (mostly 8%). In present study, the contents of Ni and Cr were 10-14% and 16-18% respectively in weight, which made the formation of uniform austenite microstructure. However, it can be seen that the microstructure feature was significantly various in intersecting at different angles.

As known, at the duration of re-solidification, the phase feature was intensively dependent on the value of G/R, which G presented the temperature gradient of liquid-solid line and R was the solidification rate, respectively. As the heat conductivity of metal was much more than that of air, the R was gradually increased from the top to the bottom of cladding layer. Therefore, the type of microstructure presented respectively equiaxed grain, columnar grain, cellular grain and plane crystal, which well agreed with the result found by Syed Haq *et al.[265].* What is more, it also can be found that a large number of secondary dendrite was formed along columnar grain and cellular grain, and a mass of carbide particle was precipitated at the space of dendrite arm, as presented in following figures.

In all cases columnar grains aligned with the major thermal gradients is clearly visible demonstrating from the metallurgical boundaries, which is mainly dendritic delta ferrite. Subsequent layers will nucleate from the previous layer continuing the grain structure beyond the clad layer boundary and into the next layer showing continuous epitaxial solidification in smaller angles like 15^0 and 30^0.

As indicated in Figure 4-71, the microstructure feature of former layer-overlapping was typically columnar grain, whose original microstructure feature was equiaxial grain as stated before. Here, it well manifested the phase transformation process of overlapping zone during multi-pass overlapping. Moreover, the direction of the regrown crystal was distinctly deflected compared to primary phase. The explanation was given as that the overlapping process offered the necessary drive energy to promote the secondary growth of the formed equiaxial grain. During this processing, the crystal was preferred to grow in the maximum temperature gradient, which was generally toward the centre of

laser facula [266]. Thus, the deflection of regrown crystal was following taken place in the direction of maximum secondary drive force. In this section, it should be noted that there was no visibly difference between original and solution treated cladding layer by means of OM.

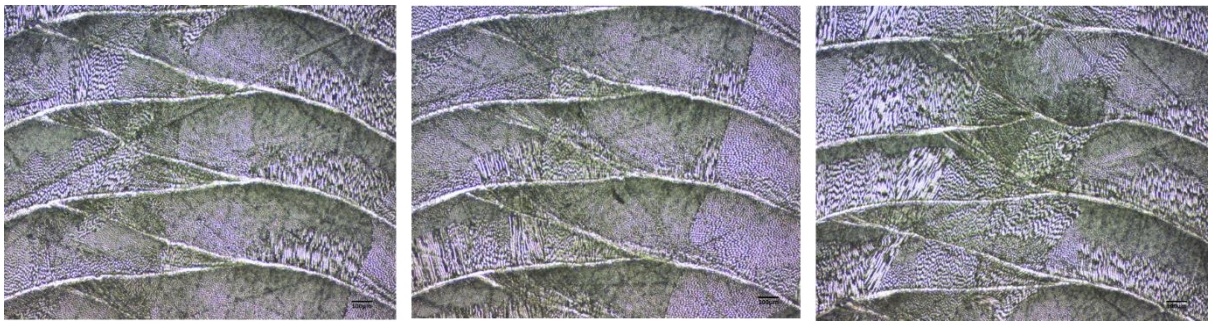

Figure 4-71: Two Intersecting Walls at 15^0, 3^{rd} layers above substrate from left upwards.

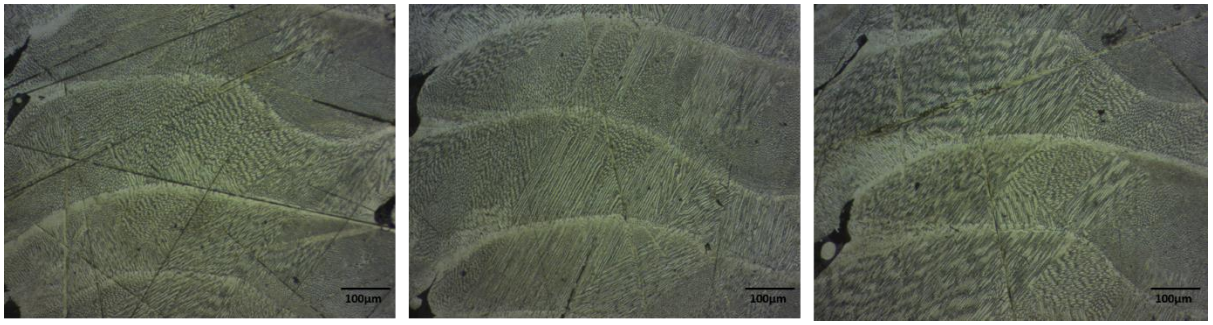

Figure 4-72: Two Intersecting Walls at 30^0, 3^{rd} layers above substrate from left upwards.

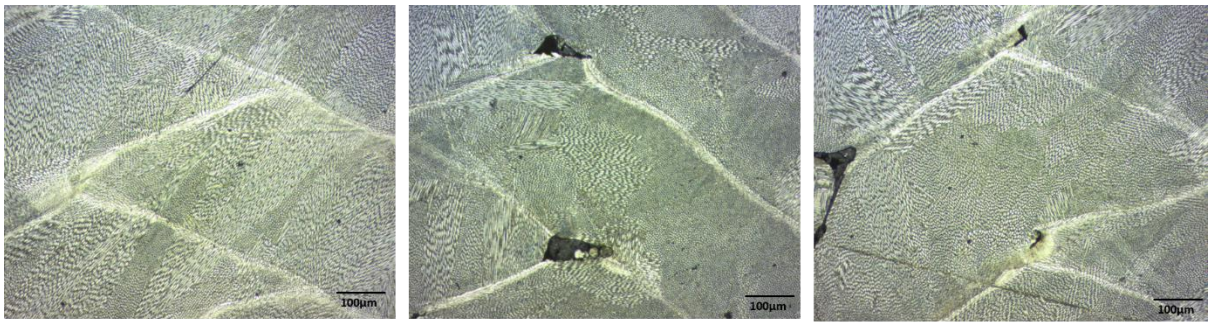

Figure 4-73: Two Intersecting Walls at 45^0, 3^{rd} layers above substrate from left upwards.

Figure 4-74: Two Intersecting Walls at 60^0, 3^{rd} layers above substrate from left upwards.

From the variation of the microstructures, it is easily found that intersecting angle at 60^0 showing better uniform grains distribution. It would normally be expected that a 90^0 crossover would have the shallowest associated melt pool which was similar to the two rings designed in the tangential way like structure B (Figure 4-17) and an acute angle crossover of say 15^0 would result in a deeper one, causing increased coarsening of the microstructure of the intersection. However, this is counteracted by the increased local volume of material in an acute angle intersection, allowing for more of the energy to be conducted away. It can be predicted that this counteraction is the cause of the similarity in microstructures. In addition, the study on the angle effect on the intersected walls shows no significant influencing on the interlayer and inner-layer porosity.

4.12 Analysis and Development of Energy Balance in the Laser Cladding Process

The laser cladding process is not particularly energy efficient. A large proportion of the laser power is reflected or reradiated away from the cladding zone. Gedda *et al.* investigated the energy distribution during laser cladding via the single side feed method. Energy in varying proportions was found to reflect off the cladding zone, radiate from the cladding zone and reflect off the powder particles along with being absorbed by the process. The amount of energy which is absorbed in the process (useful energy) is dependent on the laser used. For a carbon dioxide laser the energy absorbed was found to be 40% of the incident energy [215].

Another factor which limits the efficiency of the laser cladding process is the catchment efficiency. Only some of the powder particles blown into the substrate will adhere to the melt pool, others will ricochet and be lost which is agreed with Gedda *et al*. The catchment efficiency is very dependent on process parameters, particularly process velocity and powder feed rate investigated and proved by Pinkerton and Li *at al*.[267]. The effect of catchment efficiency can be reduced by the reusing of powder however some powder will always be lost due to oxidisation with the high temperatures involved.

It's studied that laser power in commercial blown powder cladding processing is eventually distributed with different portion to each sectors including 50% reflected off the cladding melt, 10% reflected off the powder cloud, 30% used to heat the substrate and 10% used to melt the clad layer [268]. Instead of approaching each processing parameter for the laser cladding process separately, as has been the technique of many, it is possible to group the process parameters using an energy balance for blown powder laser cladding as developed by Fearon. Equation 4-7 displays this energy balance for this

specific nozzle design to control cladding step height in this study.

$$\eta_w P_{laser} = (\rho Shvw + z_m vw)\left(C_p T_m + L_m\right) + q_{cond} \quad \text{Eq. 4-7}$$

Where $\eta_w P_{laser}$ is the energy coupled into the cladding track, ρ is the material density, S is the shape factor of clad, h is the cladding tacking step height, v is the cladding speed, w is clad width, z_m is melt pool depth, C_p is the specific heat of material, $T_m$is the material melting temperature and L_m is the material lantent heat of melting.

This can be re-written in a simpler manner as in equation 4.8.

$$\eta_w P_{laser} = (Volume\ of\ Clad + Volume\ of\ Melt\ Pool) * \left(C_p T_m + L_m\right) + q_{cond} \quad \text{Eq. 4-8}$$

The first two terms of the equation are the necessary factors in creating a clad whilst the q_{cond} term, energy conducted away through the material, is essentially waste energy. If this value is reduced the efficiency of the cladding process can be improved.

By applying equations into dog-bone specimens, the catchment efficiency can be deduced as illustrated in Table 4-21. It can be concluded that the powder feed rate is one of the factors influencing the catchment efficiency. Many other groups were exploring the relationship between processing parameters and catchment efficiency as well. Kuznetsov's work reported that a low averaged power of the laser would provide a relatively high powder catchment efficiency of 19.5% [216]. While an averaged 29.5% catchment efficiency can be achieved in this work. The results also confirmed that the nozzle designed and used for this work can provides higher catchment efficiency of powder mass deposition with non-feedback step height control, which is summarised as an advantage of this nozzle shown in Figure 3-13.

Table 4-21: Catchment efficiency for different sample clad under two powder feed rates.

Sample	Mass Weight (g)	Powder feed rate (g/min), ϕ_m	Time (min)	η_P
C1	35	8	15	0.292
C2	91	23	15	0.264
D1	39	8	14	0.348
D2	89	23	14	0.276

Chapter 5 Blown Powder Laser Cladding of Super Alloy Inconel625

316L austenitic stainless steel is widely used in corrosive environments like nuclear reactors as it has high corrosion resistance. However, its wear, cavitation and erosion resistances are poor due to low hardness (220HV), which restricts its use in many industrial applications. Austenitic stainless steels cannot be hardened through heat treatment due to it austenitic structure. Hence, to further apply this research to reality application. Another material Inconel 625 is selected.

As the advantages of the blown powder laser cladding, this specific complex component can be easily achieved. In the present study, uniform material properties for stainless steel 316L has been largely achieved at low laser power of 320W using blown powder laser cladding.

This chapter 5 will mainly be focused on the investigation on whether IN625 is a suitable material for BPLC and development on processing parameters to achieve uniform material properties at lower power.

5.1 Study on Blown Powder Laser Cladding Using IN625

The advantages of laser cladding for additive manufacturing have been widely stated and it has attracted a significant number of various laboratories throughout the world. The process development, processing parameters for controlling structural features and mechanical properties of specific structures and their customised applications have been explored and investigated many times. Numerous studies have been undertaken using stainless steel due to achievable microstructures, price and availability. The AM of nickel based super alloys has recently been developed and released as a commercially available material/process combination, capable of producing a material which matches relevant standards for a wrought material. Given the close resemblance between AM and welding processes, it is unsurprising that the alloys most readily developed for production by AM techniques are readily weldable solid solution strengthened and dilute precipitation strengthened alloys [269]. IN625 as a solid solution strengthened alloy is favourable for AM due to its high weldability and low titanium and aluminium content and significant research has been done to optimise the parameters needed for its production to provide the best results.

Inconel 625 (IN625) is a nickel-based super alloy strength-ended mainly and soon determined that the alloy is somewhat precipitation hardenable. In addition, it was found that it can be extensive used in many industries for diverse applications for a good combination of yield strength, creep strength, fatigue strength and excellent oxidation and corrosion resistance in aggressive environments. Moreover, its good weldability and fabricability have made it the choice from many advanced applications. Thus, over last half of century, IN625 has been widely used in aerospace, chemical, petrochemical and marine applications. However, many of the IN625 component are highly complex shapes that are very expensive to produce to extensive machining.

In 2012, Marleen *et al.* have concluded the optimized processing parameters of laser cladding using IN625 in terms of microstructures analysis [270]. Later, Lanlan *et al* and other research groups have reported the related studies on micro-structural and mechanical property characteristics using similar techniques and equipment [271]. It is well-known that fatigue and fracture toughness are two significant characteristics that influencing the properties, usage time and safe life operation of laser cladding components. Some reports related to fatigue and fracture toughness characterization have been summarised as review in Chapter 2.

Various processing parameters as well as system parameters will affect the cladding results, the

exploration of blown powder laser cladding of IN625 in this study followed the flow chart shown in Figure 5-1.

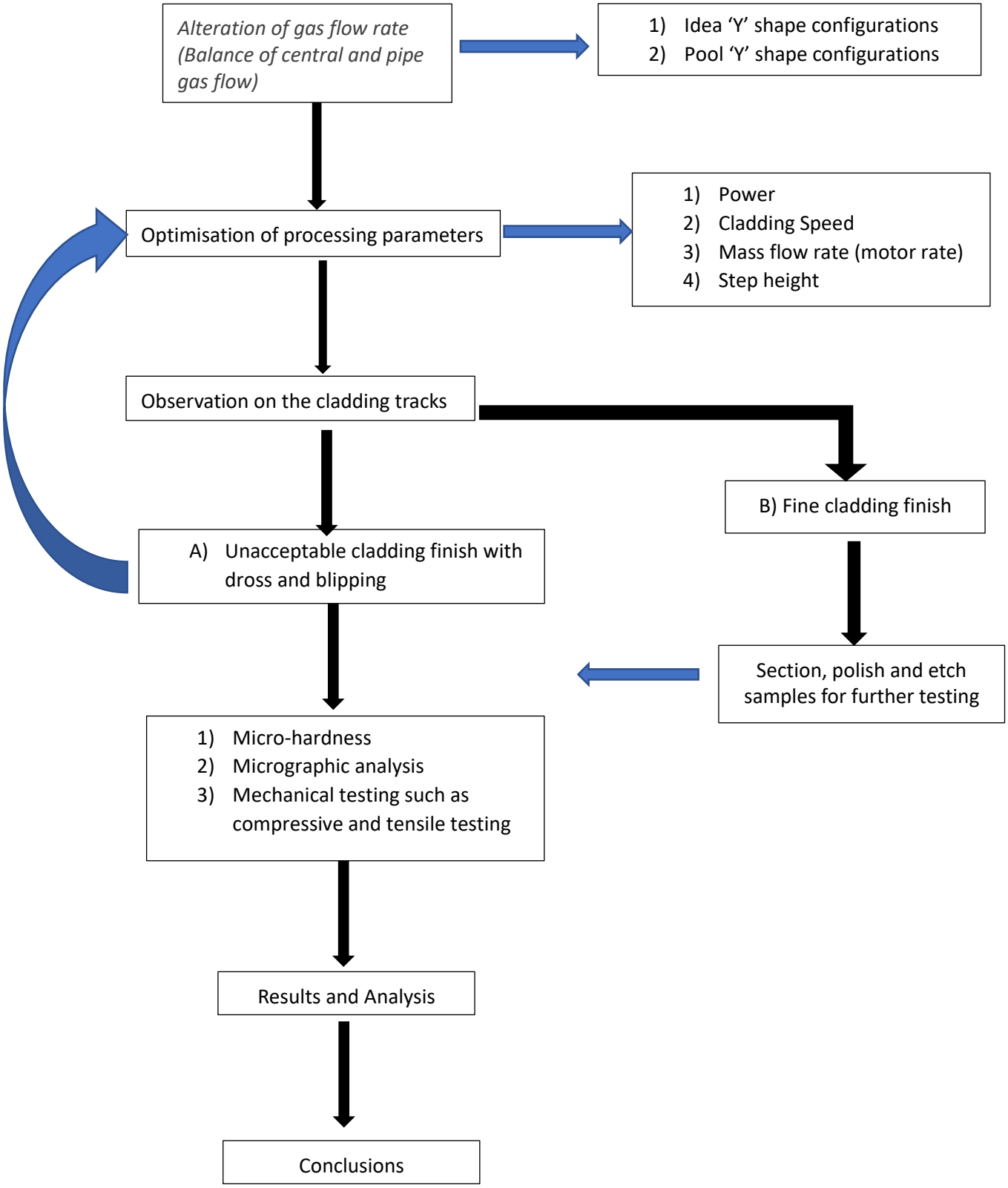

Figure 5-1: Investigation Procedures in the Research on Blown Powder Laser Cladding by IN625.

5.2 Blown Powder Laser Cladding Material Investigation of IN625

In the previous chapter, microstructures and mechanical properties of blown powder laser cladding components made of Stainless Steel 316L have been investigated. To investigate the effect of controlled directional solidification in other relevant materials, Inconels will select as a second material group for this study. IN625 was chosen as the length and width of the grains would give a good indication of the difference in cooling rates compared to regular laser deposition parameters.

IN625 is a Ni-Cr superalloy with significant mass fractions of molybdenum and niobium shown in Table 5-1. The addition of molybdenum and niobium gives the alloy high strength and toughness in the annealed condition. The alloy displays excellent resistance to a wide range of corrosive environments of unusual severity as well as to high-temperature effects like oxidation and carburization. High resistance of the alloy against localized corrosion, corrosion-fatigue and stress corrosion cracking (in chloride ion environment), along with high tensile strength, makes it an excellent choice for sea-water applications. Due to its good weldability and high oxidation resistance, IN-625 is an attractive material for aerospace applications, including aircraft ventilation systems, engine exhaust systems etc. The choice of IN-625 for the present study is because of its high temperature oxidation resistance, good mechanical strength and wide use in high temperature applications. Although IN625 is precipitation hardenable, it is primarily a solid solution strengthened alloy. As a consequence, it has superior properties compared with other superalloys in the 'as processed' state with blown powder laser cladding that requires additional heating treatment to achieve maximum mechanical properties.

Table 5-1: Main Chemical Composition of Nickel Chromium Alloy IN625 from LPW supplier.

Element	Cr	Ni	Mo	Nb+Ta	Fe	Co	Si	Ti	Al
Min wt%	20.0	Bal	8.0	3.15					
Max wt%	23.0		10.0	4.15	5.0	1.0	0.5	0.4	0.4

Table 5-2: Main Mechanical Properties of Nickel Chromium Alloy IN625 from LPW supplier.

Property		**As built**
Tensile Strength	Horizontal Direction (XY)	950 - 1050 MPa
	Vertical Direction (Z)	875 - 950 MPa
Yield Strength	Horizontal Direction (XY)	700 - 750 MPa
	Vertical Direction (Z)	575 - 625 MPa
Young's Modulus	Horizontal Direction (XY)	165 - 185 GPa
	Vertical Direction (Z)	135 - 155 GPa
Elongation	Horizontal Direction (XY)	30 - 35 %
	Vertical Direction (Z)	35 - 45 %
Hardness		300 - 330 VHV
Coefficient of Thermal Expansion		12.8×10^{-6} m/mK
Thermal Conductivity		9 - 10.5 W/mK

It is worth noting that the mean particle size of the IN625 selected have to be larger than current stainless steel 316L used of mean size around 44- 106µm (supplied from LPW technology Ltd), when cladding using the existing powder feeder to maintain due to partial shape. During the processing, the carrier gas and coaxial gas also needed to be reduced to compensate for the increased number of particles fully entrained within the gas stream. If not compensated for the catchment efficiency would go down substantially, negatively affecting the laser coupling efficiency. The powder utilised as the IN625 matrix material was supplied by LPW technology (LPW Technology Ltd, UK) and with a particle size specification of between 52-108µm, as reported by the supplier based upon a sieving test.

The SEM micrograph shown in Figure 5-2(a) shows spherical IN625 powder particles, as expected from a gas atomised powder. The spherical shape means that the powder runs more easily through the powder delivery system compared with 316L (Figure 5-2(b)). A high proportion of the particles do not approximate an ideal sphere, with spatter-like satellite particles or irregularities. These additions served to increase the average particle sizes measured in the powders original state, but were easily knocked off/smoothed during mixing, effectively reducing the observed powder size without significantly altering the primary morphology.

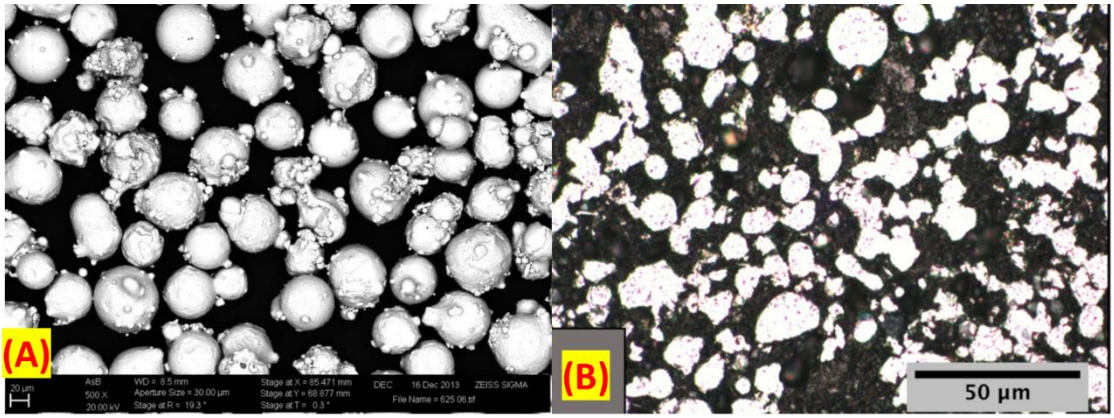

Figure 5-2: Back scattered electron image of (a) IN625 feedstock powder (LWP company), (b) 316L stainless steel [272].

5.3 Geometry Design for Cladding Samples made of IN625

5.3.1 Cladding Sample Preparation

As concluded from analysis on components made of stainless steel 316L, the optimised structure B containing two cylinders overlapping at the edge was selected for the following investigation on laser cladding of IN625.

Test structure B (labelled as 'INB' for 'IN625 B') consists of 2 hollow cylinders shown in Figure 5-3, each 25mm in diameter, 20mmin height, which intersect at the edge of each cylinder. Following the part design, the base 2-D profile was created in the Alphacam software as before however the G-code was manually altered to change the build method.

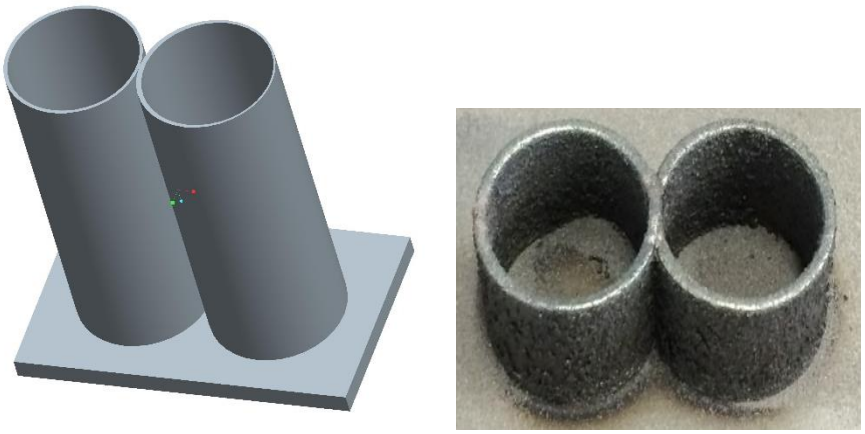

Figure 5-3: Test structure INB CAD model and actual cladding samples.

Rather than producing each circle separately and then the laser indexing upwards test structure B was produced with the laser constantly travelling upwards. This resulted in a helical style build as shown in Figure 5-4. Using this method, the laser shutter does not have to be operated during the build as the laser is constantly on. This structure contained two circles tangential which were clad in a helical manner (like an infinity symbol '∞') and the laser was constantly indexing upwards. The process

parameters for the structure B builds are displayed in Table 5-3. The G-code for the test structure B builds can be found in appendix 2.

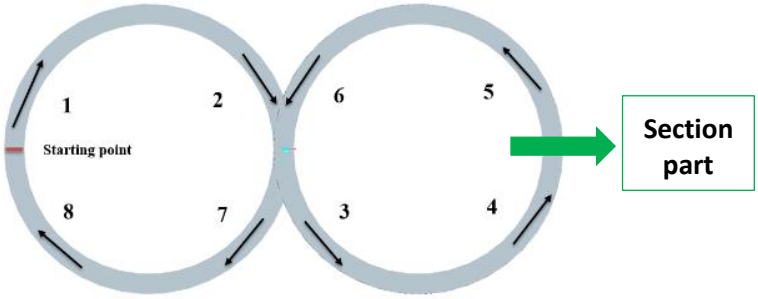

Figure 5-4: Test structure INB build method showing starting points and overall routine.

Table 5-3: Main Process parameters for test structure B builds of an example.

Indicated Power (W)	Cladding speed (mm/s)	Powder Feed Rate (rpm)	carrier Gas Flow (L/min)	Coaxial Gas Flow (L/min)
320	4	1000 (19g/min)	2	4

The samples were examined by sectioning the part which was then polished. Figure 5-4 also indicated are the regions for sectioning and analysis. Etched conditions were depending on material characteristic and microstructural features that intended to be studied. Polished samples were etched electrolytically with electrolytic etchant for nickel super-alloys of 90% 1.0M hydrochloric acid and 10% 0.1M oxalic acid in water with the cathode and anode being a stainless-steel plate and the sample respectively. The voltage was set at 4 V for 15-30 seconds depending on the time taken for the desired microstructure feature to be clearly revealed. The equipment used is shown in Figure 5-5.

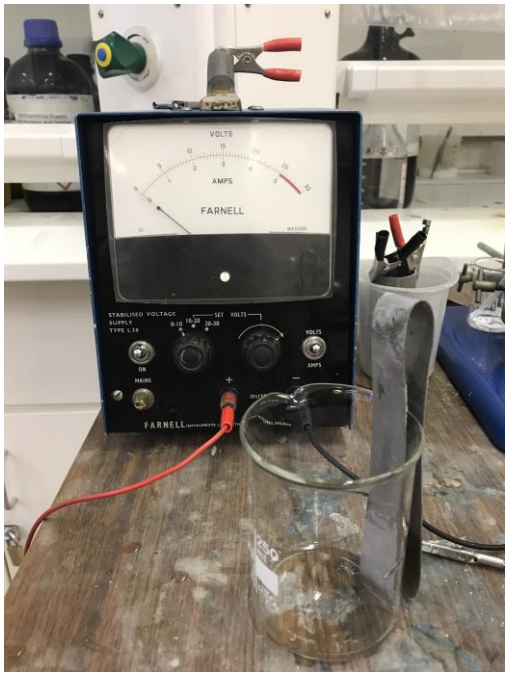

Figure 5-5: Etching Equipment used, red wire connecting samples and black wire connecting acid.

The same process parameters were used for test structures A and B to allow comparison between them. Using the same method as for test structure A several variations of test structure B were produced with different step heights and the energy per unit volume calculated. This is shown in Table 5-4. As before each sample was produced on 2.5mm mild steel substrate.

Table 5-4: Sample classification for structure INB builds.

Sample	Step height (mm)	Width (mm)	Energy per unit Volume (J/mm^3)
***INB* 1**	0.4	1.18	137.71
***INB* 2**	0.6	1.29	83.78
***INB* 3**	0.8	1.39	58.58
***INB* 4**	1	1.42	45.77

5.3.2 Sectioning IN625 Cladding Sample for Tensile Test

Following production of the test structures, samples were produced for analysis using optical microscopy and microhardness tests. This involved sectioning each clad build, mounting in resin, polishing and etching. For each cladding sample 2 sections were taken at an intersection point (b and a non-intersection point. Figure 5-6 shows how test structure B samples were sectioned with the arrows pointing in the direction at which they were viewed on the microscope. The sample naming convention was altered at this point. Samples at the non-intersection points were as before in Table 5-4. Samples at the intersection points were as before but with the postfix I i.e. sections taken from

the sample 1 build were referred to as follows: Sample 1 for the non-intersecting section, Sample 1I for the intersecting section.

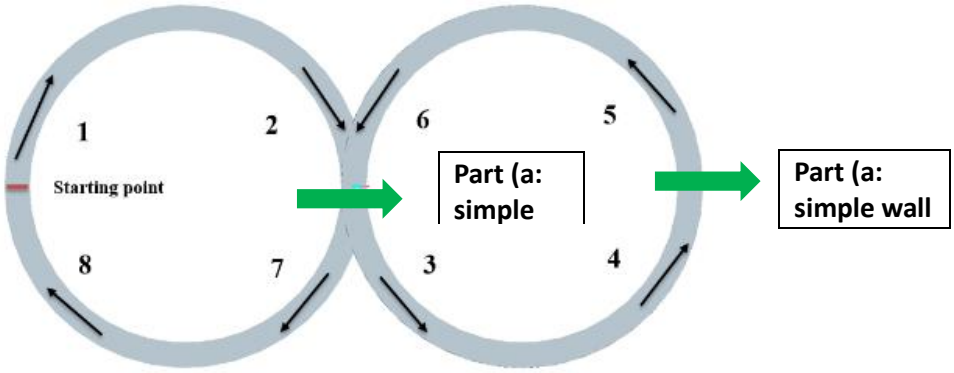

Figure 5-6: Sectioning of test structure B, part a for simple wall analysis and part b for intersection analysis.

After the samples were sectioned, they were mounted in conductive resin and polished using both an automatic polishing machine, to achieve an initial finish, and then manual polishing disks to achieve a 1micron finish pre- etching. Some initial microscopy work was done prior to etching to ensure any defects in the samples were not misconstrued and to view the relative porosity. An electrolytic etch was then conducted using a 10% oxalic acid solution.

5.3.3 Microstructural Analysis

Optical microscopy was utilised to reveal the microstructure of the samples. The grain growth and directions of the deposited samples were clearly revealed using a Nikon Eclipse LV150NL optical microscope with objective lens of 40X mainly. The DXM1200F digital camera of the microscopy was connected to computer acquisition software to clearly view, capture, record and store the micrographs of samples in digital form. To obtain optimum resolution of the track microstructures, contrast was enhanced by adjusting the dark field illumination, polarised light and the phase contrast of the microscopic system.

5.4 Microstructure Comparison between High Power and Low Power Cladding Results

As investigated and confirmed in Chapter 4, uniform material properties can be achieved using blown powder laser cladding of stainless steel 316L under low power at 320W approximately. To evaluate if this can be achieved using IN625 under low power, single cladding tracks were made as shown in Figure 5-7. It was important to noting that the total layer height and layer height per layer were both highly matching with the input of the step height controlled.

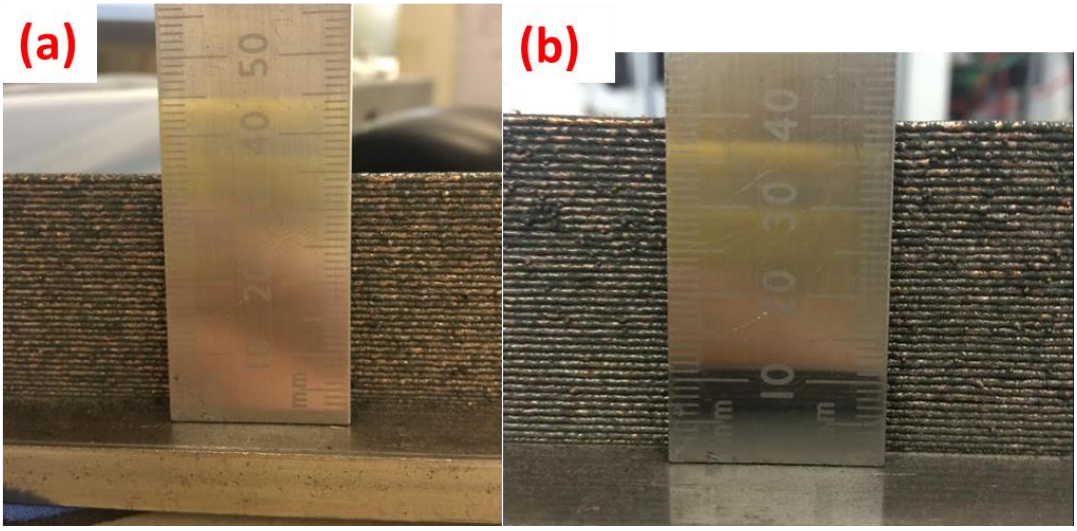

Figure 5-7: Simple walls clad for microstructure comparison between high and low power, (a)35 layers with 1mm/ step height, (b) 40 layers with 1mm/ step height.

It can be observed between Figure 5-8 and Figure 5-11 that the laser power has a significant influencing factor on the deposition results. In addition, the discontinuous tracks with non-uniform cross-section were presented at high laser power. On the other hand, excessive re-melting of the substrate was observed, when the laser power was more than 600W and the cladding speed 4mm/s and feed rate (18g/min). To qualify a standard cladding bead or cladding track, minimised dilution is essential, and this excessive re-melting was undesirable.

Figure 5-8 shows a micrograph of the polished and etched section of clad samples of IN625 at 1000W. Along the cladding upwards, the images show that the solidification mode is columnar and dendritic with outstanding directional solidification across layers. In other word, the direction of dendrite growth was along the direction of deposition. This is an indication that the thermal gradient was higher during solidification.

When each layer was deposited, the top surface of the previously solidified layer is re-melted and formed a good metallurgical bonding between two neighbour layers because of higher energy input by high laser energy density. Both (a) and (b) in Figure 5-8 show a strong metallic bonding of each layer which indicates that this group of processing parameters are capable to clad IN625.

The differences between (a) and (b) in Figure 5-8 is the averaged step height. Directional solidification growth is perpendicular to the solidification front and cladding direction and across the solute bond obviously in Figure 5-8(a). While in Figure 5-8(b), the size of directional dendrites shortened with thinner step height.

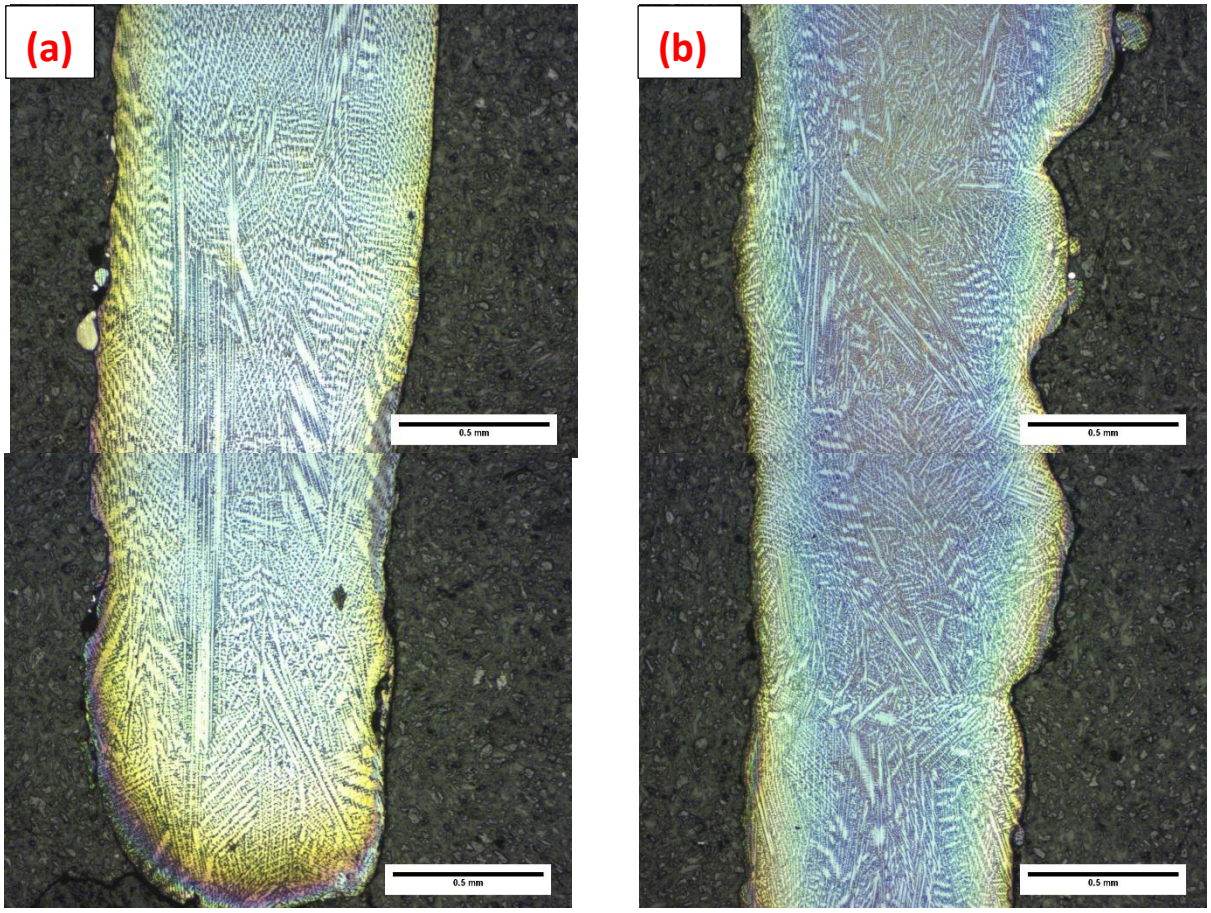

Figure 5-8: Cladding samples IN625 by power of 1000W, cladding speed of 10mm/s, carrier gas 2.5L/min, coaxial gas 4L/min, (a) step height of 0.4mm/layer, (b) step height of 0.6mm/layer.

To make a progress to approach aim of reducing cladding power, a lower power 600W was applied. Figure 5-9 shows the actual cladding component with oblivious defects. The metallic boundaries were not formed continuously along the single track may due to inefficiency power that cannot form a steady melt pool or the speed was too high to deposit the powder. This group of processing parameters were needed to be further optimised.

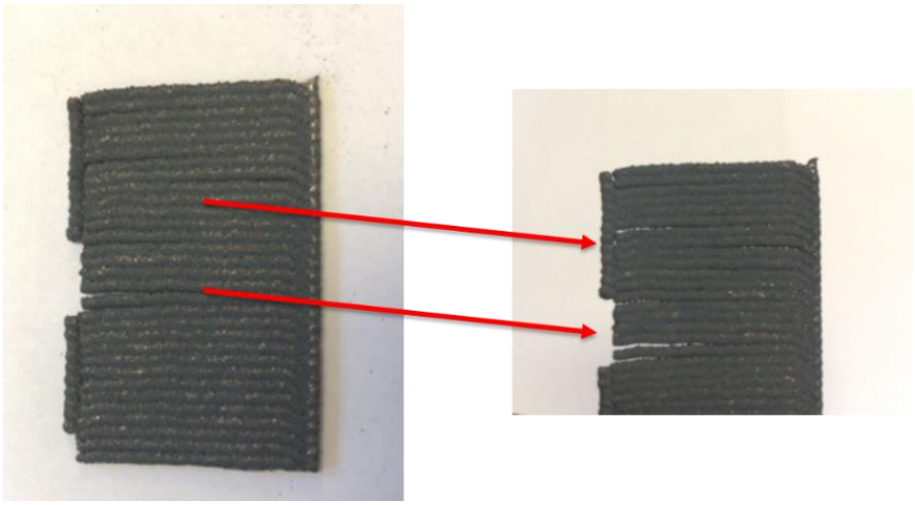

Figure 5-9: Actual cladding samples IN625 by power of 600W, cladding speed of 10mm/s, carrier gas 2 L/min, coaxial gas 4L/min, step height of 1mm/layer.

Figure 5-10 shows the micro graphs taken from a lower power of 600W with same other processing parameters. It can be overserved that the layer boundary between the two layers are not strong but part continuously which is a type of 'porosity' which will be explained in detail later in section 5.6.3. Another highlight of this micrograph is that liquation cracks are absent. These cracks are observed initiating near the fusion line between the layers, where is known as a weak site in the cladding process. During solidification, impurities have been pushed along with the last-to-solidify liquid towards the clad centreline and a solidification crack has formed and potentially expending from the centre to the side. This localisation of cracking may be due to a combination of grain boundary liquation due to re-melting od previous tracks and undesirable alignment of deposit microstructure with localised solidification stresses. However, the inter-layer cracking can be modified and improved by altering processing parameters and micro-cracks were seldom found in this work, so this work is considered free from relevant defects such as cracks, bonding error.

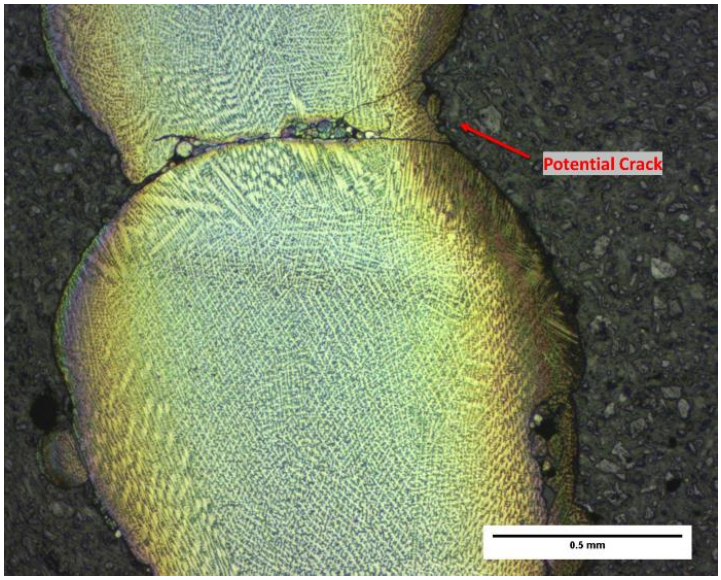

Figure 5-10: Micrograph of cladding samples IN625 by power of 600W, cladding speed of 10mm/s, carrier gas 2.5 L/min, coaxial gas 4L/min, step height of 1mm/layer.

Figure 5-11 presents the microstructure of blown powder laser cladding component processed at a much-reduced laser power of 320W. The microstructure examinations revealed that there were finely intermixed dendritic and cellular microstructures with high uniformity. The fine dendrite formation is likely due to the inherent rapid cooling rate during blown powder laser cladding, while cellular microstructure is attributed to relatively reduced cooling rate during multi-layer deposition. The fine microstructures with high uniformity are responsible for higher mechanical strength and hardness, while formation of cellular microstructure has helped in keeping ductility intact. The solidification has transformed to go in all directions, or in other words the solidification is equiaxed.

It can be summarised that optimised processing parameters for IN625 for an equiaxed structure can be confirmed as 4mm/s for cladding speed, carrier gas of 2L/min, coaxial gas of 4L/min and a low power of 320W.

The difference between (a) and (b) in Figure 5-11 is the image taken distance from the substrate. It can be seen that more shortened grains and fine microstructures were found on the higher cladding components compared to lower distance.

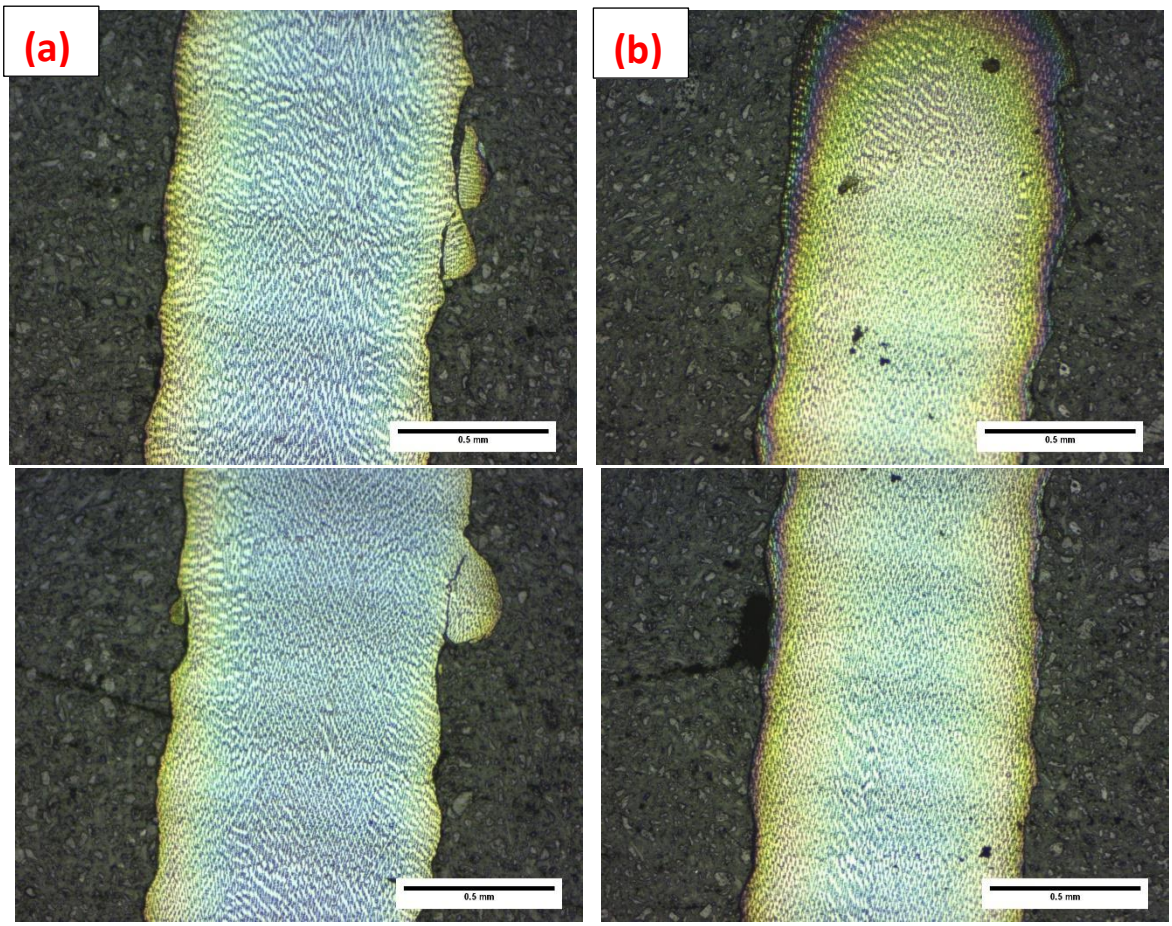

Figure 5-11: Cladding samples IN625 by power of 320W, cladding speed of 4mm/s, powder carrier gas 2.5L/min, coaxial gas 4L/min, step height of 0.4mm/layer, (a) section taken 2.5mm from the substrate, (b) section taken 5mm from the substrate.

5.6 Micro-Structure Investigation of Simple Wall with Single Direction Cladding of IN625 under Low Power

5.6.1 Influence of Cladding Speed

The scan speed affects the laser energy deposited and powder fed per unit length, as it is directly related to interaction time. Interaction time is the time duration for which the laser beam dwells at any point during the processing and is defined as the ratio of laser spot diameter to scan speed. It can be observed that for a single layer and overlapped track deposition, beyond the threshold laser power density, the deposition rate did not change with the variation in the interaction time for a given powder feed rate. Here, the deposition rate relates to total amount of powder deposited in unit time during the process. However, for multi-layer single-track deposition, the deposition rate remains constant with the increase in interaction time only for a couple of layers, then, it reduced. This is because, after a couple of layers the geometry of a previously deposited track changed to a semi-cylindrical shape. This semi-cylindrical shape reduces powder catchment efficiency and decreases laser power density on the deposited track. This results in a reduced deposition rate.

The influence of cladding speed varying from 4mm/s, 6mm/s 8mm/s and 10mm/s was investigated for the low power processing conditions for IN625 shown in Figure 5-12 and Figure 5-13. It can be observed that the microstructure variation is highly reduced and directional solidification was largely eliminated. In Figure 5-12(a), the layer boundaries were obviously presented with a good and strong metallic bonding and the most microstructures presents a homogenous distribution with equiaxed structures. It is worth to noting that some extra cladding part were deposited on the side of the walls which indicates that a lower cladding speed would provide larger amounts of powder to be deposited and eventually resulted in a higher but extra deposition existing. However, this can be further polished or use other post-processing technology without affecting material properties to give a better surface state.

The similar microstructures distribution was found in component cladding with 6mm/s shown in Figure 5-12(b). It is needed to be explained that the reason for colours metallurgic micrographs due to over-etched. Although the surface was sectioned and polished at a time, the cladding conditions were slightly different during the processing. In addition, due to the difference in phases of grains, the dissolution rate of each grain face, different orientation of the grain and differences grain and grain boundaries, the corrosion degree of the surface would be affected to presents different results under weak current.

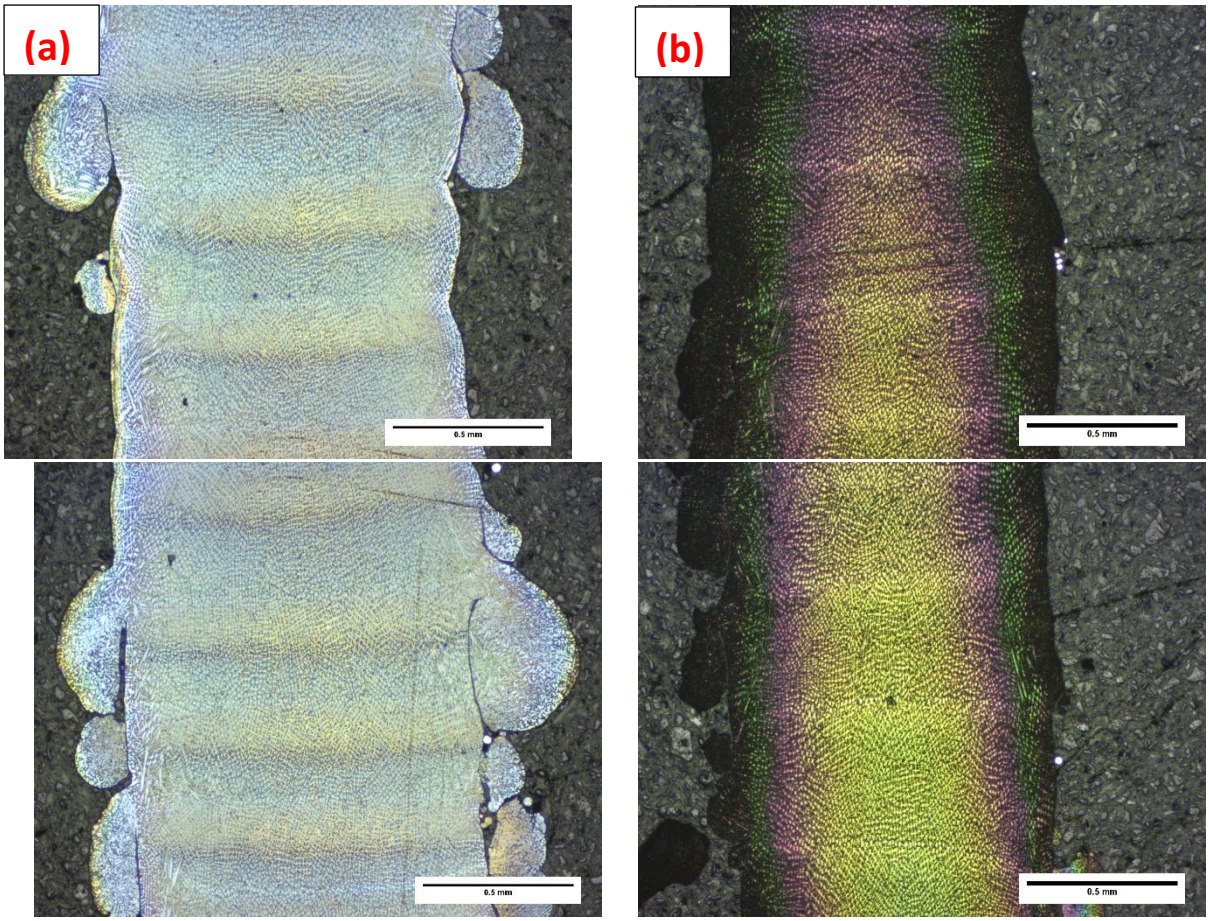

Figure 5-12: Cladding IN625 samples by power of 320W,powder carrier gas 2.5L/min, coaxial gas 4L/min, step height of 0.4mm/layer, section taken at 5mm from substrate (a) cladding speed of 4mm/s, (b) cladding speed of 6mm/s.

From Figure 5-13(a) to (b), the cladding speed is increasing. It can be seen that directional solidification was eliminated. In Figure 5-13(b), longer but still fine columnar grains were generated due to higher speed. From Figure 5-12 and Figure 5-13, it can be concluded that when the speed decrease, it leads to a better microstructure distribution and quality for each layer. All the cladding components produced here were with no relevant defects such as cracks, bonding error at the interface between deposit layers or pores in the cladding tracks.

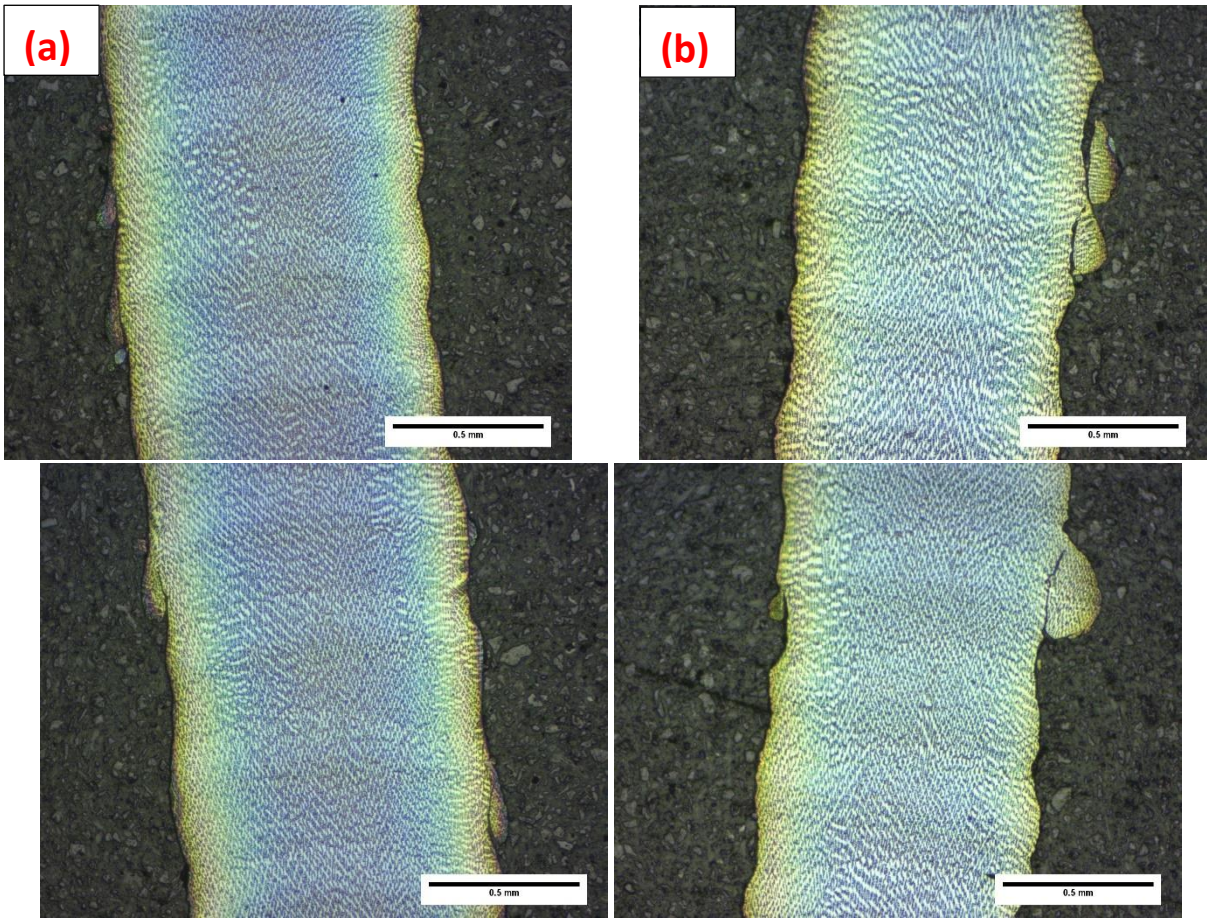

Figure 5-13: Cladding IN625 samples by power of 320W, powder carrier gas 2.5L/min, coaxial gas 4L/min, step height of 0.4mm/layer, (a) cladding speed of 8mm/s, (b) cladding speed of 10mm/s.

The cladding speeding is in relevant with the cooling rates. The results show that the number of grains per unit increases with the cooling rate. On the other hand, the grain diameter decreases with the increasing cooling. However, more measurements at different cooling rates are required to establish a lytic relation between the cooling rate and the grain size. Generally, the cooling rate has direct effect on: (1) the volumetric percentage of austenite and ferrite phases inside the microstructure, (2) formation and growth of these phases, and (3) grain boundaries and grainsize. it was realized that cooling rate variations resulted in microstructural evolutions, however, the source of these variations and the effects of speed on the cooling rate were not discussed. The increasing speed has created an increasing trend for cooling rate and a decreasing trend for the melt pool temperature. Apparently,

the traveling speed has a linear relation with the cooling rate and melt pool temperature. The traveling speed directly affects the cooling rate and hence indirectly affects the clad microstructure. Taken together, these results suggest that real time cooling rate control may be used to tailor the microstructure changes by varying laser power and traveling speed.

5.6.2 Influence of Layer height

Dinda *et al.* investigated microstructural evolution of IN625 powder thin walls built using blown powder laser cladding. The processing parameters had a significant influencing on the geometry, microstructures and hardness. Layer height which can be controlled by the step height is one of the key processing parameters which is related to the cladding cooling rate. The larger the step height resulting in larger layer height which containing a larger volume results in a deeper melt pool and a slower cooling rate. This is likely to produce directional solidifications from the solute bond shown in Figure 5-14(a). The columnar dendritic growth in the upper layer of Figure 5-14(a) is caused by epitaxial growth of primary dendrite from the partially re-melted grains of the previously deposited layer, which acts as pre-nuclei for directional growth of the crystal. The morphology of the microstructure of the horizontal section (i.e. cross-section perpendicular to the build direction) was typically cellular/equiaxed dendrites, as shown in Figure 5-15 (c).

It can be seen in the side section of Figure 5-14(b) that short directional solidification was slightly existing Near the side surface region of the deposited walls appeared horizontally growing columnar dendrites. The change in the dendrite orientation can be attributed to the change in heat flux direction due to the hemispherical shape of the melt pool at this point.

It is worth noting that the microstructure of the side walls mostly consists of near vertical columnar dendrites, which have grown epitaxially upwards, as shown in Figure 5-14(a). Moreover, the growth direction of the columnar dendrites depends on the laser cladding direction. In addition, the microstructure of each layer is composed of two regions. Directional solidification grows from the bottom part of each layer which is the solute bond. Some columnar structures are observed which often shows no secondary dendrites associated with it. The top part of the layer shows typical fine dendrites or equiaxed structures with classical secondary dendrite arms. In the BPLC process, the cooling rate of the melt pool and consequently the solidification speed is very high at the bottom part of the layer. The upper part of the layer cools down slowly compared to the bottom part. Due to the very high solidification speed of the bottom part of the melt pool, secondary dendrites could not grow. As a result, bottom part of each layer consisted of mainly primary dendrites. Because of the progressive

decrease of the cooling rate from the bottom to the top part of the melt pool, a gradual transition of microstructure form fully columnar to dendrites transition is observed.

From the comparison between step height effect shown in Figure 5-14 and Figure 5-15, it can be summarised that with the thinner step height, the fewer microstructure variation was observed and the more homogenous microstructure distribution was achieved with fine equiaxed structures shown in Figure 5-15(d) which with 4mm/s cladding speed, step height at 320W.

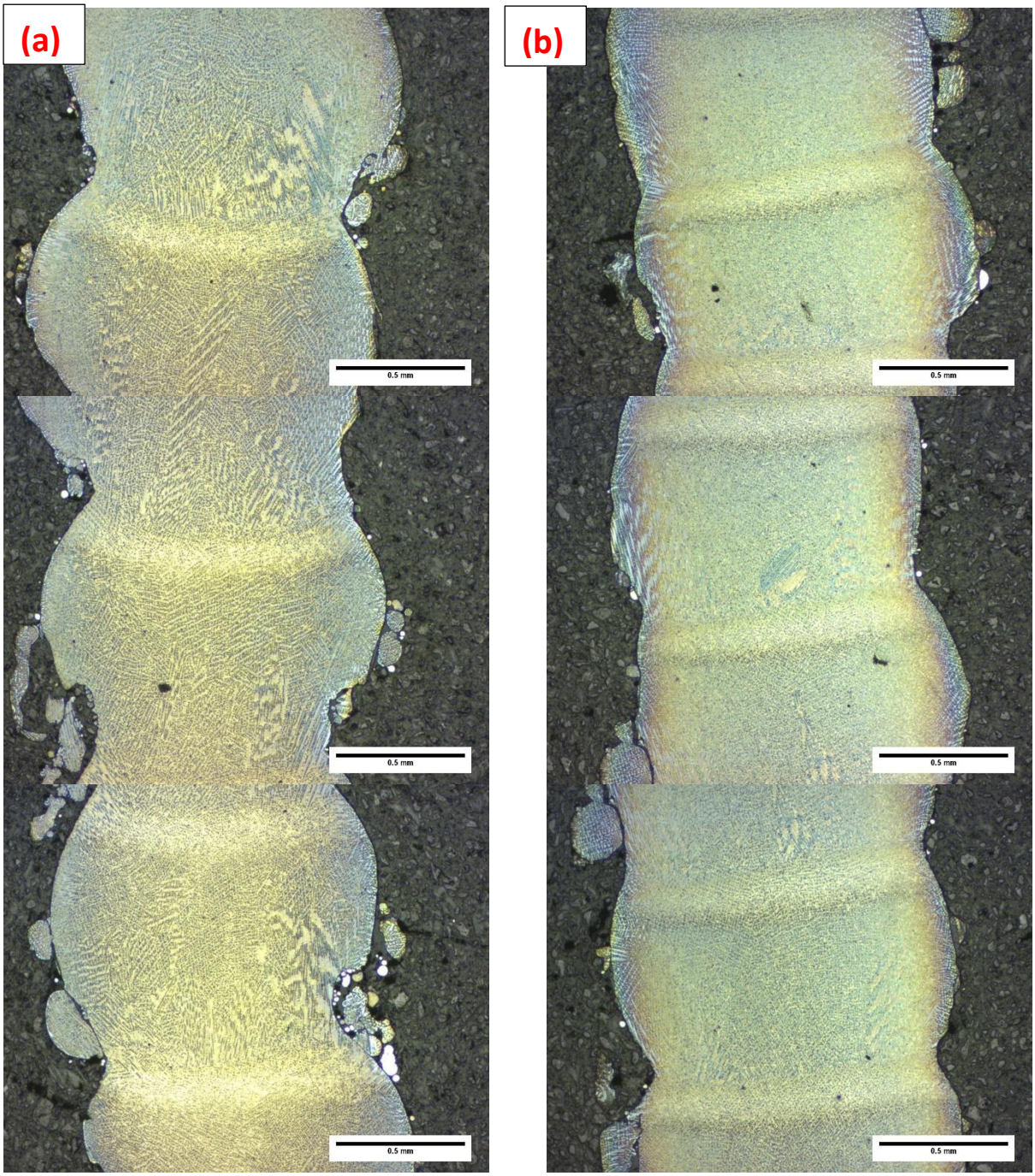

Figure 5-14: Cladding IN625 samples by power of 320W, cladding speed of 4mm/s carrier gas 2.5L/min, coaxial gas 4L/min, (a) step height of 1mm/layer, (b) step height of 0.8mm/layer.

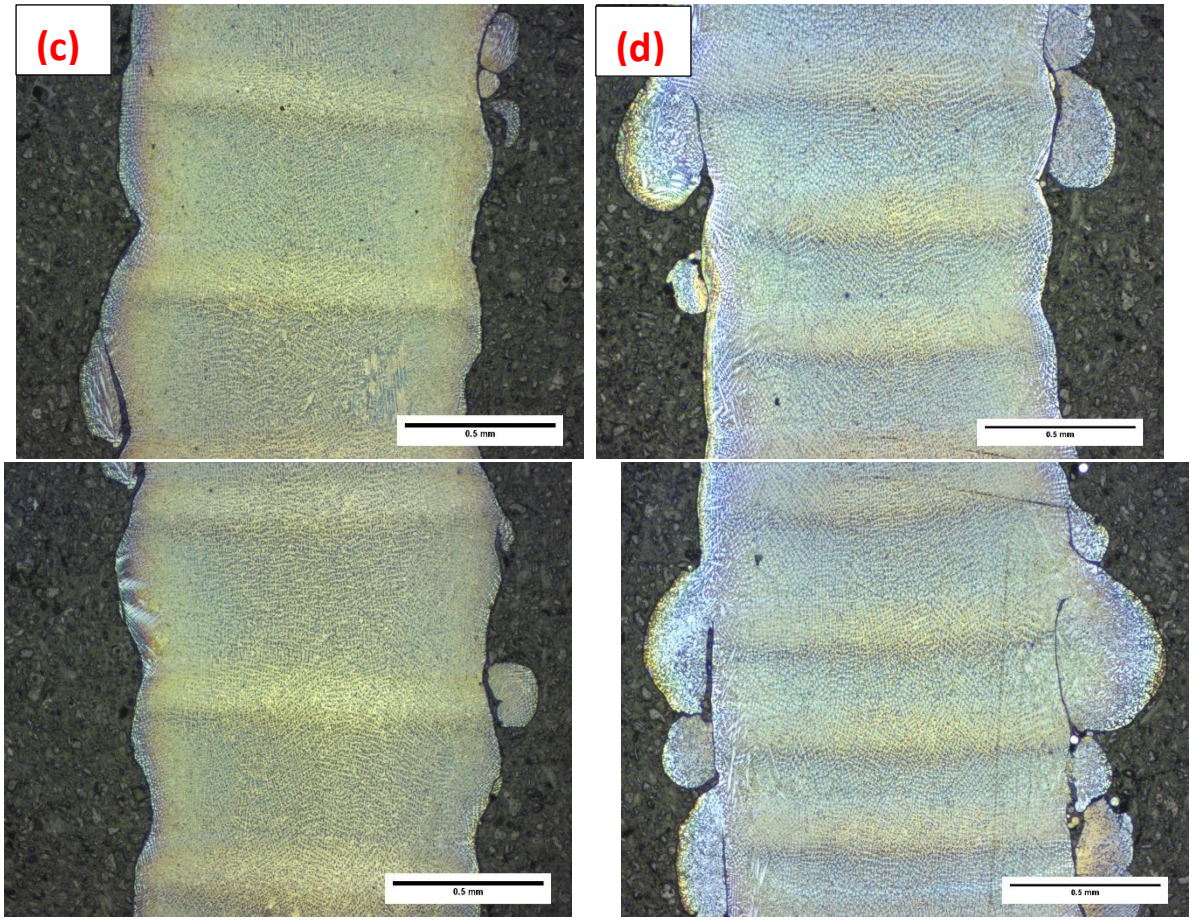

Figure 5-15: Cladding IN625 samples by power of 320W, cladding speed of 4mm/s carrier gas 2.5L/min, coaxial gas 4L/min, (C) step height of 0.6mm/layer, (d) step height of 0.4mm/layer.

5.6.3 Micro-Porosity

Laser cladding can potentially offer several advantages including a strong metallurgical bond at the clad-substrate interface, minimal distortion of the substrate, low substrate dilution and minimal porosity. An ideal track/clad is defined as one with a contact (or wetting) angle less than 90°. The cladding demonstrated in Figure 5-16 appears to meet these criteria. However, a number of pores were observed which is defined as porosity that is detrimental to mechanical performance and corrosion behaviour of the tracks.

The absence of pores in the continuous single tracks indicates that all the combinations of laser power and cladding speed gave sufficient energy density for full melting of all deposited material volumes used within the selected process window. The possible explanation for the porosity occurring in Figure 5-16 may be the presence of intra-layer porosity. It is often spherical and exists within the track area. Its cause is thought to be related to gas dissolved or entrapped within the melt pool.

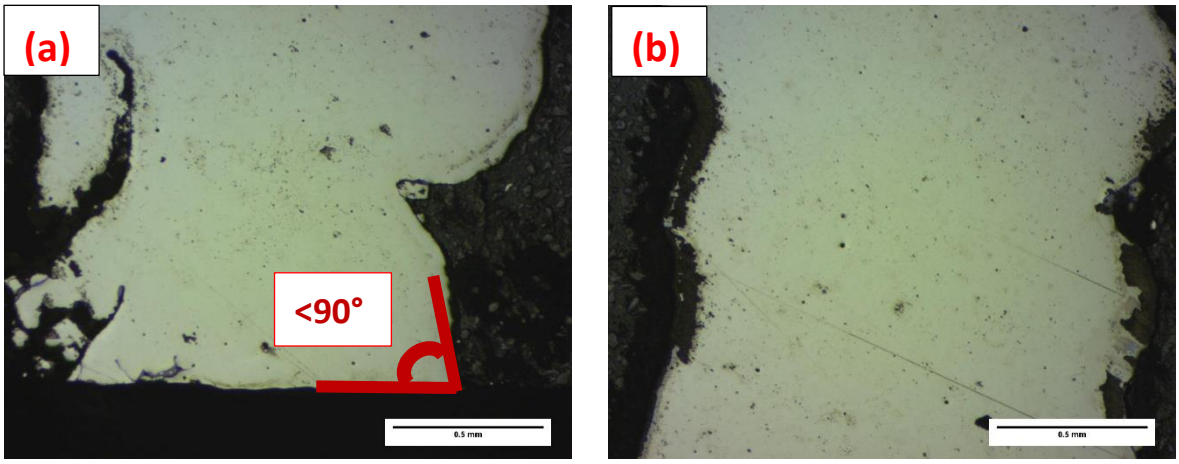

Figure 5-16: Cladding IN625 samples before etching by power of 320W, cladding speed of 4mm/s carrier gas 2.5L/min, coaxial gas 4L/min, step height of 1mm/layer, (a) first layer from the substrate, (b)3rd – 4th layer from the substrate.

During the comparison of power effect on cladding results, it is noting another type of porosity called 'Inter-layer porosity' which is due to a lack of fusion caused by incomplete bonding between adjacent tracks. This can be improved by optimising the cladding processing parameters. Figure 5-17 reveals the characteristic of this type porosity. These micrographs were taken from high power cladding conditions where directional solidifications can be observed by large amount. It can be also found that directional or columnar dendrites in nature, which grew epitaxially from the solute bond as well as the cladding bead outer face. It was worth noting that the components can be clad continuously without falling off although the existing of sufficient metallic bonding.

Both (a) and (b) in Figure 5-17 were taken from high power cladding process sectioned from different step height to the substrate. It can be seen that the overlapping deposition was not with enough fusion discontinuously across the same track layer, but still capable for more upper cladding layers.

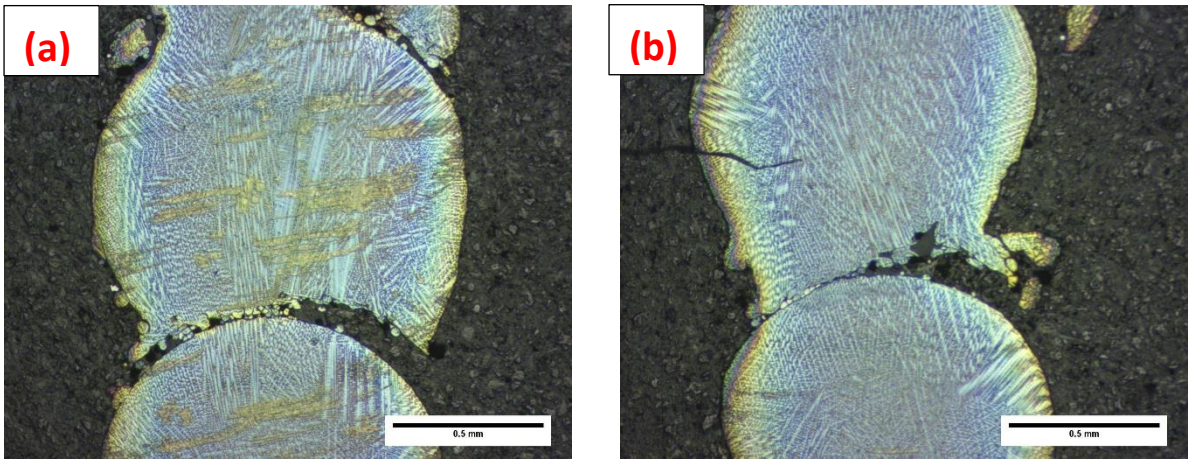

Figure 5-17: Cladding IN625 samples before etching by power of 1000W, cladding speed of 6mm/s carrier gas 2L/min, coaxial gas 8L/min, step height of 1mm/layer, (a) 3rd to 4th layer from the substrate, (b) 6th to 7th layer from the substrate.

As introduced an ideal clad should be with a contact angle less than 90°, if the angle is more than 90° which shown in Figure 5-18, this first track is called a swollen track and is not desirable. The type of porosity observed is called inter-run porosity which is caused by the horizontally aligned or offset tracks of incompatible aspect ratio (approx.< 2.5) of the single tracks from which the layers were built. As previously explained in the literature, the higher the contact angle or the lower the aspect ratio, the more spherical a single laser track becomes. Whenever the contact angle is more than 90°, a hollow groove or gap is formed at the base of the track with the substrate. During the overlapped cladding process, it becomes difficult for the molten material to flow into this gap because the laser beam radiation is obstructed from reaching the area covered by this gap due to the protruded flanks of the adjacent track. It is important to point out that both images were taken from high power cladding process. While in low powder cladding process, these defects were improved and eliminated.

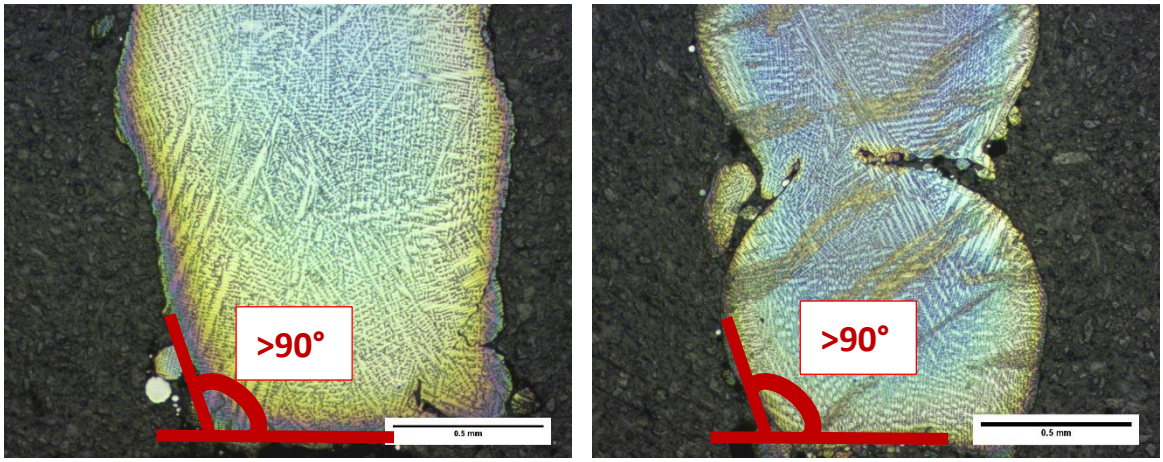

Figure 5-18: Cladding IN625 samples before etching by power of 1000W, cladding speed of 8mm/s carrier gas 2 L/min, coaxial gas 8L/min, (a) step height of 0.8mm/layer, (b) step height of 1mm/layer.

5.6.4 Microhardness

To evaluate the microhardness of the material a Rockwell hardness test was carried out on sectioned samples mounted in resin. The results can be seen in Figure 5-19. The microhardness of BPLC IN625 components were around 315-335HV, it can be observed that the step height and cladding speed have a large influence on the microhardness. There is an increase of microhardness significantly with the increase in laser cladding speed, which can be attributed to higher cooling rates and higher melt temperatures. Higher cooling rates result in shorter solidification structures and smaller the cellular and dendritic structures, which would offer higher hardness in accordance to this. This was also evident in terms of a step height effect. As the step height increases, the cooling rate is reduced as the volume of clad cross-section increases.

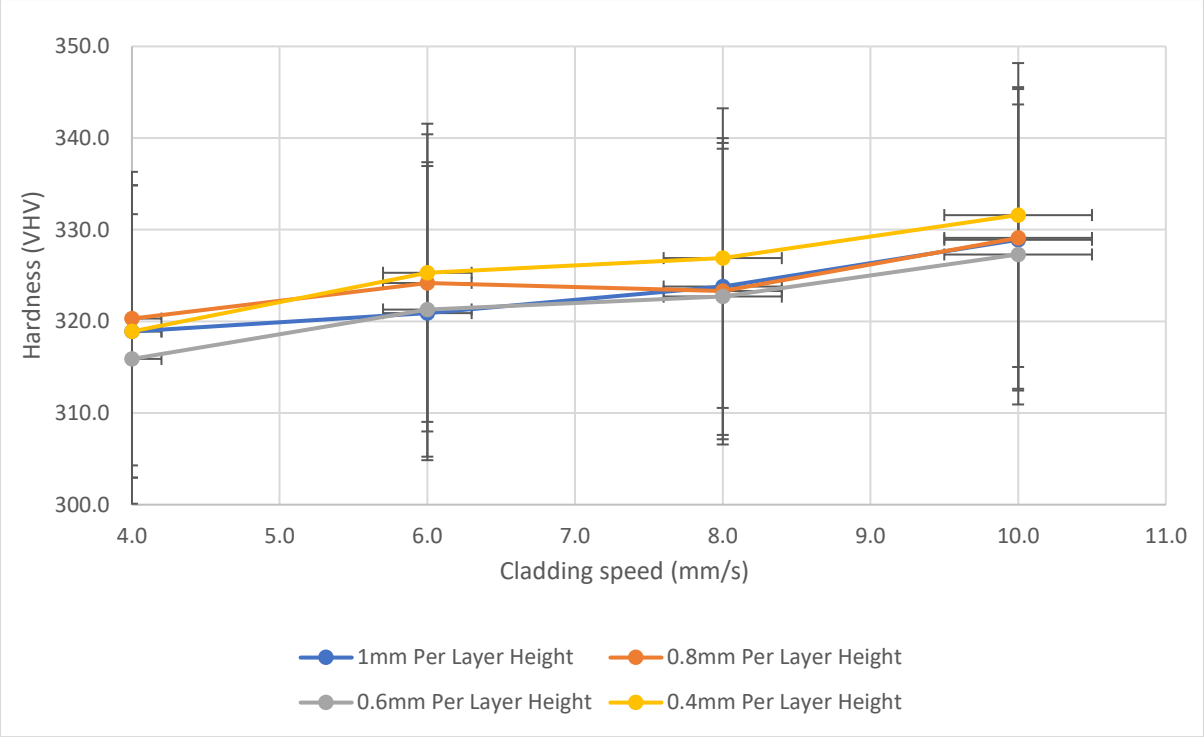

Figure 5-19: Microhardness of IN625 with varying cladding speed and step height (Power of 320W, speed at 4mm/s, flow rate of coaxial 4 and powder 2.5L/min of gas, 18g/min of feed rate).

5.6 Investigation of Cladding Track Direction Effect on Tensile Test Results of Cladding Components

Microstructures determine mechanical properties of cladding parts and the difference of tensile properties along various directions is mainly due to the anisotropy of the cellular dendrite microstructure of the samples, which was demonstrated by Amato *et al*. and, the metallurgical defects are more easily introduced into the bonding area between two neighbour cladding layers and accordingly the tensile properties of the samples fabricated along the vertical direction are inferior to those of the samples built in the horizontal direction [273, 274].

5.6.1 Design of Specific Dog-bone Samples

Another investigation into the mechanical property was achieved from tensile tests to obtain the ultimate tensile strength (UTS) and maximum load for the samples produced by laser cladding. To generate the tensile test coupons, the orientation of the deposited tracks in relation to the direction of the tensile force was designed in two directions, one was perpendicular to the tensile force (structure INC) and the other parallel (structure IND) shown in Figure 5-20. Figure 5-21 can offer a better understanding on the relations between cladding track and tensile force direction respectively.

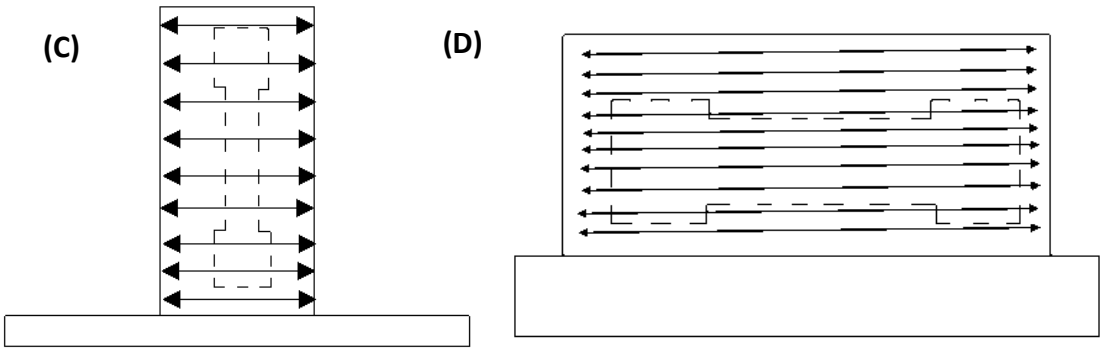

Figure 5-20: (C) Structure INC with vertical cladding and (D) Structure IND with horizontal builds used for tensile test.

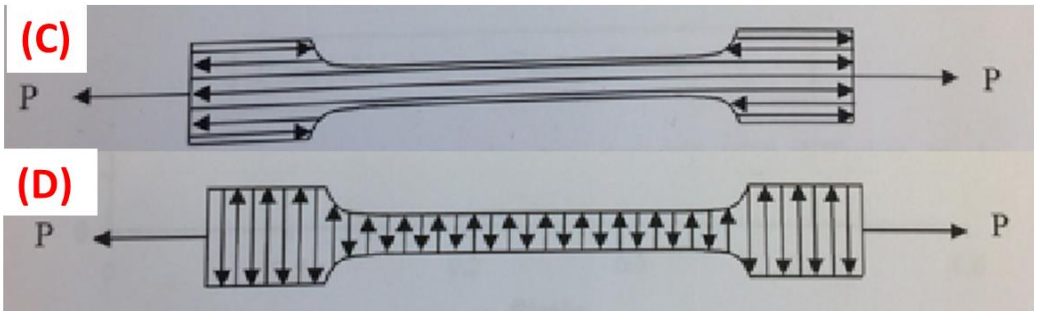

Figure 5-21: Illustration on the relations between cladding track direction and tensile force direction.

In accordance with ASTM tensile standard, the dimensions of the dog bone shape were designed as shown in Figure 5-22. LO and WO were approximately 165cm and 19cm as the originally clad finished state. The gauge length and width were shaped to 57mm and 13mm respectively. And the thickness was around 2mm as single cladding track deposited. This samples were cut using waterjet cutting to avoid chemical reaction. Laser cutting was not considered as to avoid edge hardening effects and would influence the microstructures distribution. Figure 5-23 shows the real cladding components produced in this part which were free from relevant defects such as cutting effect to the edge and alignment of placing the sample into the INTRON testing machine.

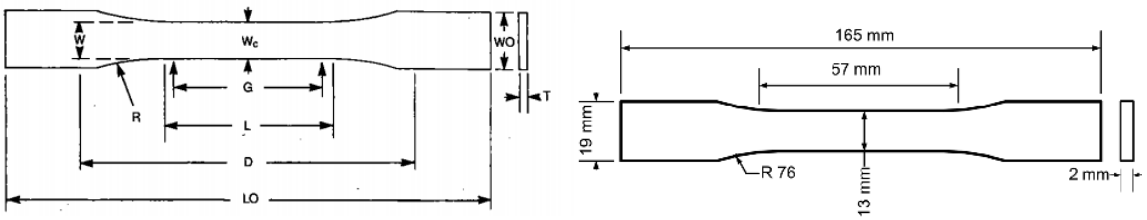

Figure 5-22 The dimensions of cladding sample INC and IND in dog-bone shape cutting for tensile test.

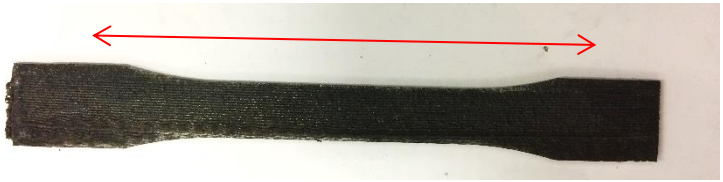

Figure 5-23: Sample made of IN625 ready for tensile test with cladding directing parallel with tensile force direction.

Table 5-5 and Table 5-6 show the processing parameters and related dimensions for the two orientations. The parameters set were to explore the power effect and two types of powder catchment efficiency combined by power feed rate and gas flow rate. All samples were laser clad with 0.8mm step height and 4mm/s cladding speed.

Table 5-5: Processing parameters for structure INC with vertical cladding tensile test samples and related dimensions (Figure 5-20(INC)).

Sample	**Processing Parameters**			**Gauge width (mm)**	**Sample thickness (mm)**
	Power (W)	Powder feed rate (g/min)	Coaxial & powder gas flow (L/min)		
INC1	320	23	8&2	13.89	1.98
INC2	320	18	4&2.5	13.94	2.11
INC3	600	18	4&2.5	13.85	2.22
INC4	1000	18	4&2.5	12.96	2.12

Table 5-6: Processing parameters for structure IND with horizontal cladding tensile test samples and related dimensions (Figure 5-20(IND)).

Sample	**Processing Parameters**			**Sample width (mm)**	**Sample thickness (mm)**
	Power (W)	Powder feed rate (g/min)	Coaxial & powder gas flow (L/min)		
IND1	320	23	8&2	13.95	2.45
IND2	320	18	4&2.5	12.98	2.12
IND3	600	18	4&2.5	13.98	1.87
IND4	1000	18	4&2.5	13.51	1.78

5.6.2 Tensile Test of Specific Dog-bone Samples Cladding of IN625

The ultimate tensile strength (UTS) is the maximum resistance to fracture which is equivalent to the maximum load (in unit kN) that can be carries by cross-sectional area (in unit mm^2) when the load is applied as simple tension and expressed in:

$$\mathbf{UTS} = \frac{\mathbf{P_{max}}}{\mathbf{A_c}} \qquad \text{Eq 5.1}$$

The structures INC and IND (Figure 5-20) were subjected to a tensile test. From the results generated in Table 5-7 and

Table 5-8, it can be summarized that the horizontal samples which the track orientation was parallel to the tensile force show higher maximum breaking load and ultimate tensile stress than perpendicular ones. As a reference, the text value of UTS is 950-1050MPa in perpendicular direction and 875-950MPa in parallel direction approximately for bulk powder (LPW Technology Ltd).

Table 5-7: Averaged mechanical properties components with perpendicular cladding track to the tensile force.

Sample	Max.Load (kN)	Ultimate Tensile Stress (MPa)	Elongation (%)
INC1	17.88	650.14	34.21
INC2	20.34	691.55	**33.15**
INC3	20.95	681.41	33.85
INC4	18.64	678.32	33.15

Table 5-8: Averaged mechanical properties for components with parallel cladding track to the tensile force.

Sample	Max.Load (kN)	Ultimate Tensile Stress (MPa)	Elongation (%)
IND1	28.78	841.95	34.45
IND2	23.42	851.24	**35.45**
IND3	22.07	844.12	35.41
IND4	18.76	780.15	35.10

The tensile test was conducted on the sub-size specimen as per ASTM standard. The test results revealed that the power, powder feed rate and gas flow rate influence the tensile properties of the material. As compared to conventionally high-power processed Inconel-625, low-power cladding material exhibited improved tensile properties without lose in percentage elongation.

Ultimate tensile strength (UTS) of cladding samples from IN625 were found around 650-850MPa, which is about 10% higher than that reported by Xue *et al* and 20% higher than that measure by Ganesh *et al* [271] but it is close to the UTS of as cast IN625. This can be easily and straightforwardly explained that the updates on blown power laser cladding system and different supplier of raw cladding material which would cause the changes in microstretches. However, the percentage elongation was found to be around 35% (for 57mm gauge length) which is close to the published results from other groups. The samples (IND1, IND2, IND3 and IND4) with cladding track parallel to the tensile force were performed better than the samples (INC1, INC2, INC3 and INC4) with cladding track perpendicular to the tensile force. The reason for a lower strength is that the interfaces are weaker compared to the solid track area which means there are easier to be pulled apart from another track. As discussed, directional solidification grains will grow from the solute band in different proportions based on changing processing parameters. In terms of microstructures under this condition, the directional solidification grains grew the same direction as the applied tensile force which allowed fewer barriers to dislocation movement; similar with being deformed or breaking easier and therefore a low mechanical strength. The failure mostly occurred from the track boundaries (Figure 5-24(a)). For the sample with track direction along with the tensile force, higher strength and stiffness were achieved. The solute boundaries retained mechanical integrity and coherence during the pulling process. Moreover, the mobility of grains dislocations can determine the different degrees and direction of deformation. If a majority of equiaxed structures could be realized this would provide more barriers to prevent distortion and improve material anisotropy. From the final failure condition shown in Figure 5-24(b), the failure path agreed with the solidification grains from different layers.

In in end, the components of 0.4mm per step height processing with 4mm/s for cladding speed, carrier gas of 2L/min, coaxial gas of 4L/min at low power to 320W can be confirmed to offer a better mechanical property which appears to agree with microstructures characteristics due to presence of equiaxed structures.

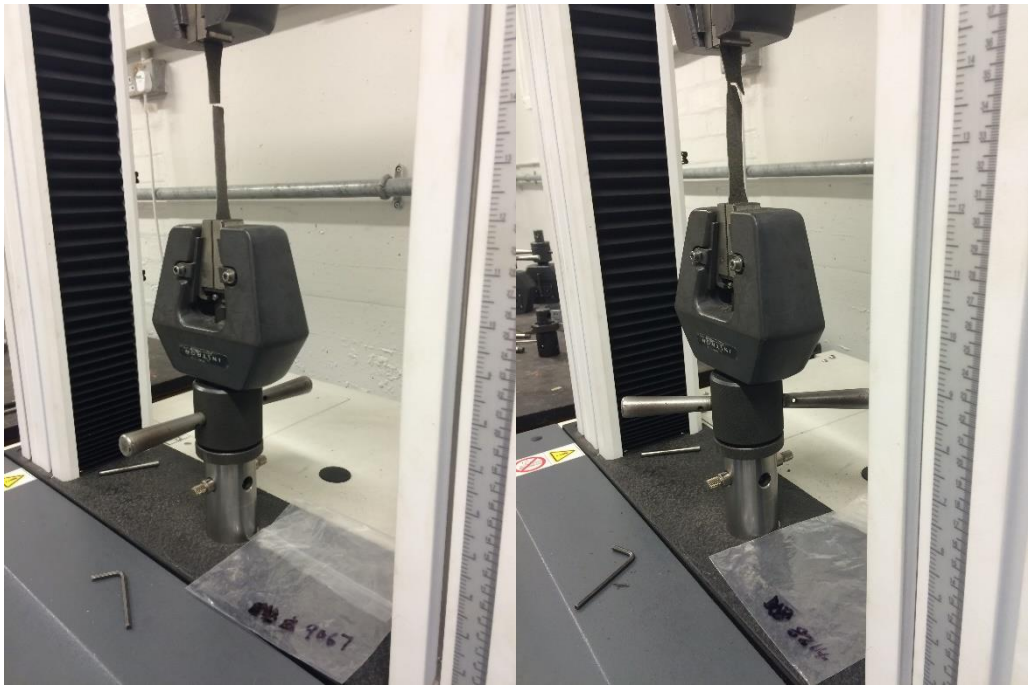

Figure 5-24: Tensile Test taking on Dog Bone Shape Made of IN625 (a) samples cladding direction perpendicular to the tensile force, (b) samples cladding direction parallel to the tensile force.

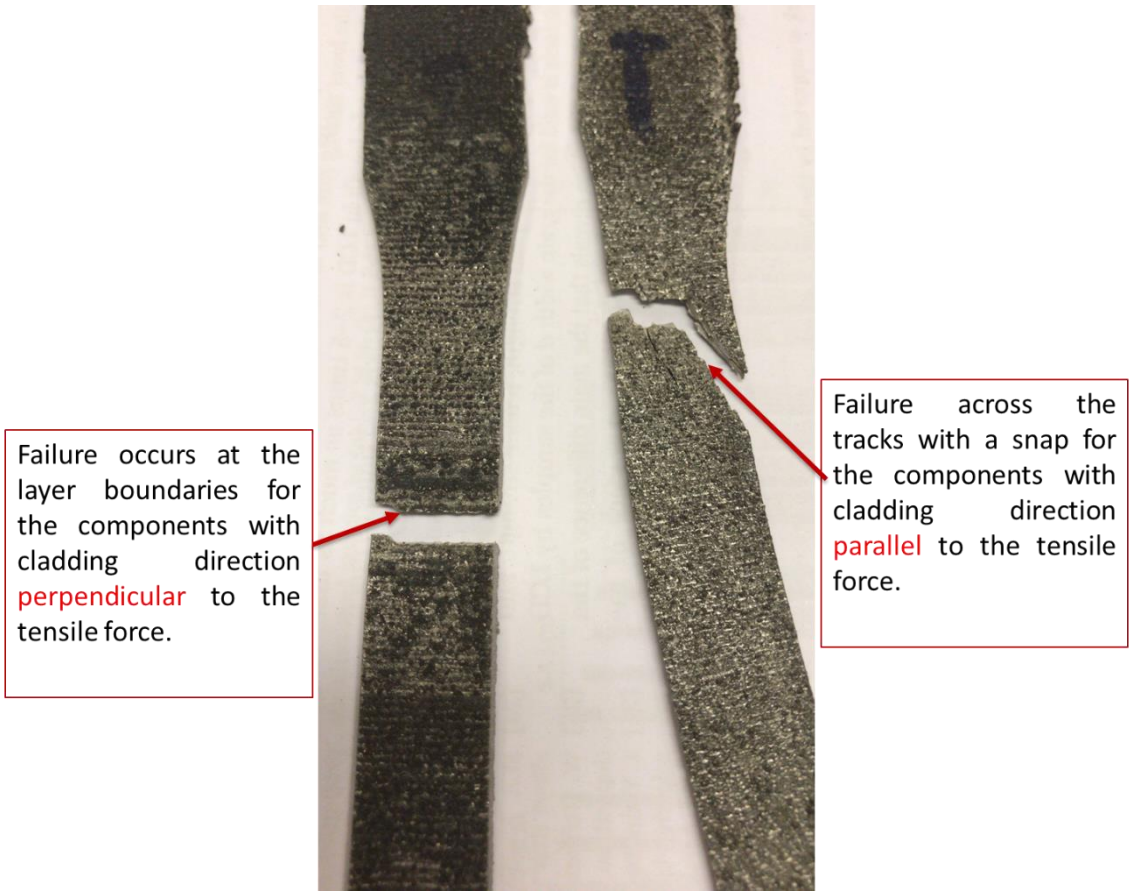

Figure 5-25: A close look at the failure area of IN625 cladding components from different cladding direct.

5.7 Conclusions of Microstructure Analysis

The micrographs clearly indicated that the laser cladding speed, laser power, powder feed rate have significant effect on microstructure features of the blown powder laser cladding part.

Overlapped-track layers of Inconel 625 powder were successfully deposited. Except for the presence of inter-run porosity in few layers, the layers were free of defects such cracks, poor fusion at the interface and lack of fusion porosity.

Generally, solidification leads to two types of solidification pattern, columnar and equiaxed dendritic. Of these two, equiaxed is usually the desired pattern since it is less prone to solidification cracking than the columnar pattern. Under this optimised novel processing parameter at low power about 320W, uniform material properties were achieved.

5.8 Conclusion of Microhardness

To investigate the microstructural features of the tracks at a range of processing parameters, hence, determining their effect on the micro-hardness of the tracks, Vickers micro-hardness measurements of the typical Inconel 625 powder laser track were performed. From this analysis, it is apparent that a laser track formed by low power blown powder laser cladding demonstrated a higher micro-hardness than the typical laser tracks formed by conventional processing parameters. The difference in the micro-hardness values of different processing parameters can be related to their microstructures. In the case of the high-value microhardness cladding track, fine equiaxed/cellular dendritic were observed. In summary, the higher micro-hardness exhibited by the clad track is mainly due to a finer grain structure and partly due to the higher volume fraction of inter-dendritic precipitates found in the track

5.9 Conclusion Mechanical Properties

The microstructure has influences on the mechanical results due to different composition of equiaxed, dendritic and directional solidifications. The most importance factor is due to the weakness of the failure layer. Once the tensile force is perpendicular to the layers, the tensile force is applied directly to this layer causing the failure; while the tensile force is parallel to the layers, the property of the specimen is averaged by all layers becoming stronger which resulting in higher strength.

Chapter 6
Final Conclusions and Recommendations for Further Research

This research focuses on the discussion of the cladding parameters effects on the blown powder laser cladding results by evaluating the microstructures, exploring the micro-hardness and analysing the mechanical testing on the built components. Multi layers cladding are realized with different values of the process parameters including cladding speed, laser power and powder feed rate *et al*. And two typical materials 316L SS and IN625 are applied and studied.

It can be summarised that the aims of this research are majority achieved. By the end, some relevant ideals to develop this research are further listed and figured out.

6.1 Overview

The original aim of this work was to investigate the production of AM parts by blown powder laser cladding with uniform material properties and the possibility of producing parts at lower average power. On the basis of acquired data to promote the generation of predominantly equiaxed grain structures and hence potentially uniform material properties not only in 316L Stainless Steel but also IN625 AM parts, confirming effects through metallurgical analysis and mechanical testing, by developing and optimising processing parameters and part geometries. This aim has been largely achieved. High uniformity of equiaxed microstructures have been observed at 320W using CO_2 laser, especially two rings intersected by the edge kind of tangential two parts. However, there is still significant scope for further research. A specific conclusion from each of the studies are given below.

6.1.1 Single-Track Cladding Bead

Laser power, cladding speed and laser stand-off distance were found to influence the geometry, microstructure, and texture in single track specimens by laser cladding. The height of the deposits decreased with increased scanning speeds. Stand-off distance had no influence on height of the deposits. The width increased with increased laser power and stand-off distance but decreased with increased scanning speeds. A single-track deposit had three distinct regions formed by varied cooling rates. Segregation of Nb-rich phases was found to be dominant in the top region of the deposit in all cases. Columnar grains dominated the deposits in all cases with a narrow region of equiaxed grains at the top. In cases of deposits that had better aspect ratio, the equiaxed grains were confined to a minute region at the top regions of the deposit. Different morphology and orientation can be achieved by varying energy conditions. The preferred growth direction for columnar grains is <100>. A centre-line solidification was noticed in cases of grains that had <110>, <111> orientations because of their high dilution rate, with interaction angles of nearly 45◦. Dilution was influenced by specific energy, and hence the texture morphology was affected by power, speed, and stand-off distances.

6.1.2 Conclusions on Blown Powder Laser Cladding of Stainless Steel 316L

The initial optimised processing parameters for structure A interlocking and structure B edge intersecting hollow cylinders: for the non-intersecting samples, sample A3 and B3 has the highest microhardness. Sample A3 and B3 displayed the lowest microstructural variation for the non-intersecting samples (320W, step height of 0.8mm, 4mm/s cladding speed, 18g/min feed rate, coaxial and powder gas flow are 8 and 2L/min). For the intersecting samples, sample A4I and B4I displays the highest microhardness value; this was again the sample with the lowest microstructural variation 320W,

step height of 1mm, 4mm/s cladding speed, 18g/min feed rate, coaxial and powder gas flow are 8 and 2L/min).

The 'ideal' sample for structure A was found in sample B5 or B5I (0.9mm per step height, 4mm/s, 18g/min powder feed rate, 2&8L/min powder and coaxial gas flow rate) to present a better uniform material property both between the non-intersection and the intersection point respectively.

Microstructures found during this investigation were primarily equiaxed cellular, with secondary phases of epitaxial cellular and columnar dendritic structures. This was a result of high cooling rates caused by low E/V values and low cladding speed. The high cooling rates promote high temperature gradients and cellular microstructures result. Due to low E/V values, low cladding speed, and possibility to use of a thin substrate, is the lack of microstructural alteration with increasing distance from the substrate has been found. The step height was found to significantly affect the microstructure of part built by BPLC. Altering the step height, i.e. altering the E/V, was found to produce a change in the microstructures and particularly the levels of microstructural variations. As the energy per unit volume decreases the microstructure coarsens due to a decrease in the cooling rate and an increase in the ratio G/R.

The microstructure at the intersection points for the selected geometry was seen to differ from the microstructure at the non-intersection points due to the added thermal process taking place. Microstructural variations were seen to increase at the intersection points. The greater complexity of the reheating/remelting process which occurs at the crossover point results in greater variations in cooling rates within the melt pool. This leads to an increase in microstructural variation. The result of this is that optimum process parameters need be defined at non-intersection points and intersection points separately.

The microhardness results can be linked to the microstructures. Varying the distance from the substrate was seen to have a negligible effect on the microhardness whilst altering the step height was seen to have a significant effect. The microhardness was seen to increase as the microstructural variation decreased. Where microstructural variation is high directionally solidified structures are present including dendritic structures and coarse cells. These structures were found to have lower hardness values than the fine cellular equiaxed microstructure.

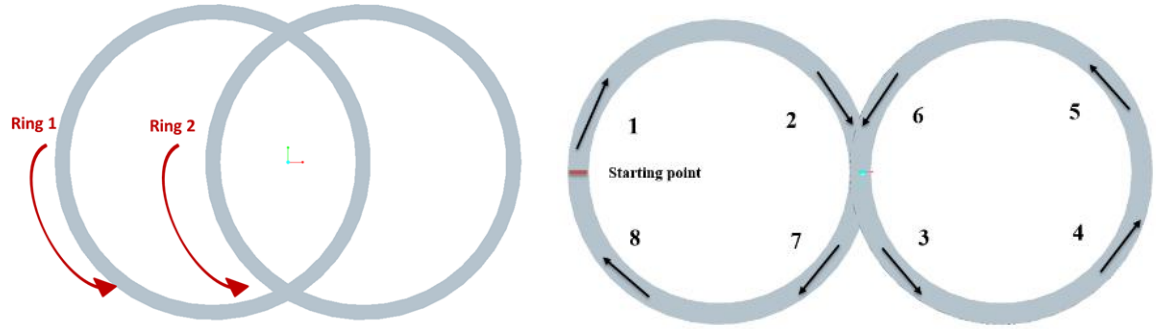

Figure 6-1: Cross Section View of structure A (left) and test structure B (right).

The test structure B build method resulted in lower microstructural variations and as such a microhardness increase was observed compared to test structure A. The test structure A samples were found to have hardness values similar that of wrought 316L Stainless Steel whilst the test structure B samples were observed to have an increase in hardness compared to the wrought material. The fine cellular microstructure found, and therefore high temperature gradients and thermal stresses, is harder.

From the compression test all samples displayed roughly similar values or the 0.2% proof stress. The 1mm step height sample was found to be the strongest sample. As the crush test samples were produced with a constant step height and cladding speed the microstructure for each sample will vary between the intersection and non-intersection points. The 1mm step height sample was found to have minimal microstructural variations and the maximum microhardness at the crossover point suggesting that the yielding occurred at the crossover points during the compression test. The 0.2mm step height sample was the weakest adding further evidence to this however only three samples were tested due to time constraints therefore any conclusions which can be gained are limited.

Tensile test conformed that a significant improvement in mechanical properties is possible with this low power technique. The horizontal and vertical UTS were found to be within in less than 500MPa and the highest UTS was greater than 389MPa which is higher than the state of art.

6.1.3 Conclusions on Blown Powder Laser Cladding of Inconel 625

The optimised processing parameters for two edge intersecting hollow cylinders were 4mm/s cladding speed, 4&2.5L/min coaxial and powder gas flow, 18g/min powder feed rate with 4mm per step height at 320W using a CO2 laser.

The Results of the study have established that blown powder laser cladding could be an alternative

technique for production of Inconel-625 components with an advantage in improved mechanical strength without sacrificing laser power.

step height was found to have a detrimental effect on the properties of the cladding results. Larger step height in clads produced with the IN625 powder leads to a decrease in micro-hardness and weaker tensile strength, which is caused by the microstructural evolution of the Ni-based and Co-based alloy. On increasing step height, cellular to dendritic transition is evidenced. This transition, explained by the lowering of the G/R ratio and the different chemical composition of the alloy, limits the formation of the eutectic constituent, within which carbides are localized, and consequently leads to the decrease in the cladding hardness. In the clads produced with Inconel 625 powder, on increasing step height, microstructural evolution is evidenced together with the decrease in clad microhardness.

A clear correlation between cladding part properties in terms of microhardness and tensile strength and laser cladding speed has also been shown. This behaviour is due to the microstructure distributions. On increasing cladding speed, the cooling rate is increased. The fine dendrite formation was due to inherent rapid cooling rate during blown powder laser cladding, while cellular microstructure is attributed to relatively reduced cooling rate during multi-layer deposition. The fine microstructures with high dislocation density are responsible for higher mechanical strength and hardness, while formation of cellular microstructure has helped in keeping ductility intact. The solidification has transformed to go in more directions, or in other words the solidification is equiaxed.

By Alphacam Mill software to slice the 3D model and output numerical code controlling the CNC working platform, the cladding strategies were designed and optimised automatically. However, cladding strategies were influencing the microstructure morphology significantly, which is related with the cooling rate as well.

Tensile test conformed that a significant improvement in mechanical properties is possible with this low power technique. The horizontal and vertical UTS were found to be within in less than 1000MPa and the highest UTS was greater than 851MPa which is higher than the state of art.

6.2 Overall Conclusions

With the results found in this research, it should be possible to eliminate the directional solidification and produce uniform material properties at lower power of 320W for both stainless steel 316L and Inconel 625.

6.3 Recommendations for Further Research

Following the study presented in this thesis, the following investigations are suggested for future research.

6.3.1 Effect of Inter-layer dwell time

Additive manufacturing involves the deposition of multiple layers and potentially large volumes of material to produce discrete shapes and components. In cases where AM processes have been investigated, the impact of changes in the dwell time between multiple passes on the accumulation of distortion and the impact of the selection of different materials has not been investigated. In the work presented here, a simple test was done to compare the tensile strength between two sample cladding under the same processing parameter but one with dwell time between each inter-layer and the other with continuous cladding (shown in Figure 6-2 and Figure 6-3). It can be observed that the samples cladding with no dwell time have a better tensile strength.

This needs to be further studied to investigate the microstructure distribution and variations. Much of this previous work on the accumulation of distortion during the deposition has concentrated on the laser cladding processes which can be explored as well.

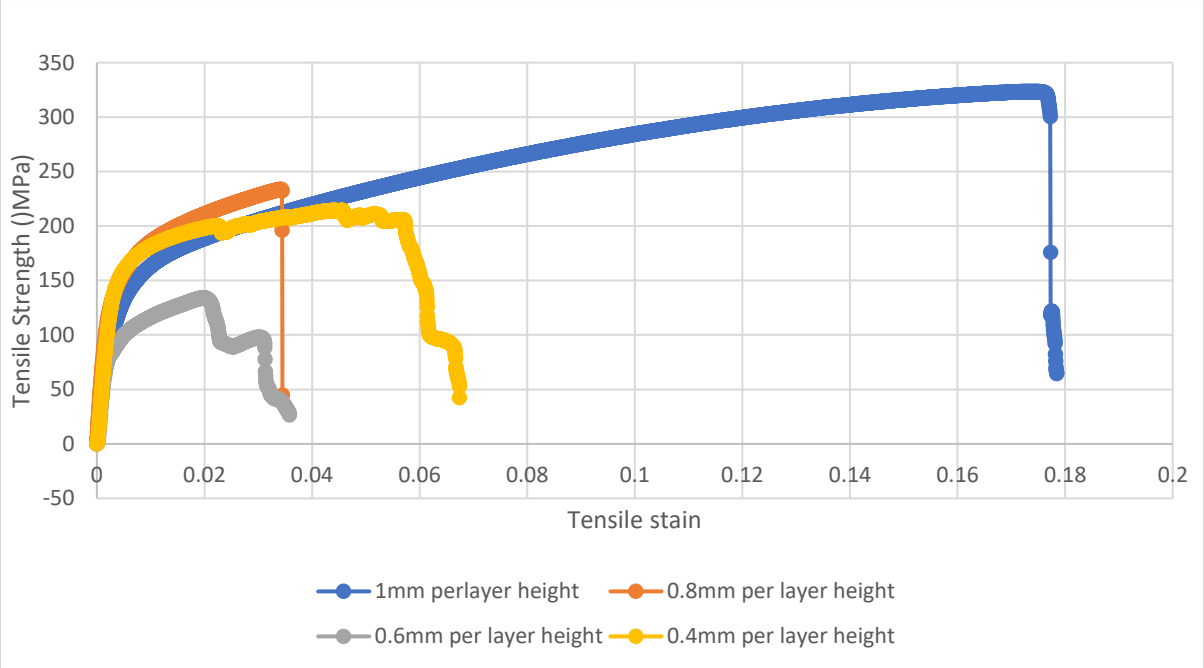

Figure 6-2: Tensile strength measured for stainless steel 316L samples under 1000W, 4mm/s cladding speed, carrier gas 4L/min, coaxial gas 2L/min with 5s dwell time between each layer.

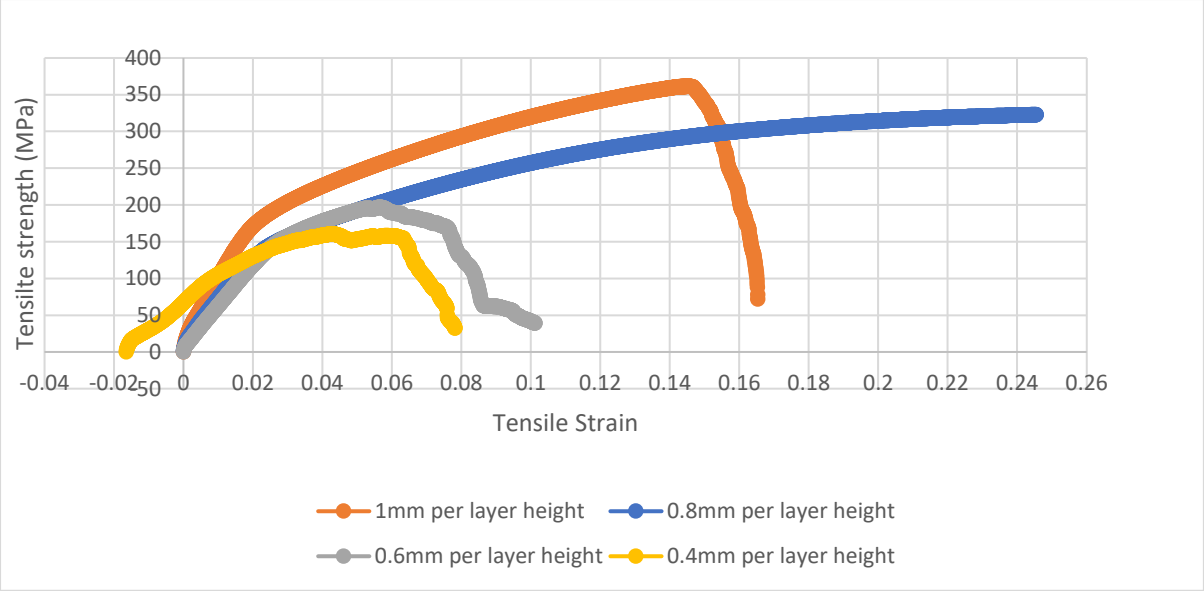

Figure 6-3: Tensile strength measured for stainless steel 316L samples under 1000W, 4mm/s cladding speed, carrier gas 4L/min, coaxial gas 2L/min with no dwell time between each layer.

6.3.2 Powder Recycling Effect

For blown powder laser cladding, the efficiency ratio of deposition can drop to 40% depending on the configuration and spot size, which means the powder needs to be sieved and recycled. It was found that the micrographs were brighter with obvious porosity inside the layers for fresh powder while the micrographs were darker with less porosity after the powder recycled several times.

The further work can be continued with the design of a procedure to collect and reuse the wasted powder of a nickel based super alloy IN625. After usage, powder could be collected, undesired fractions could be magnetically segregated, and aggregates removed by sieving. The particles would be mixed again and ready for reuse. The study could be deigned to compare fresh new powder with that recycled 5 times and 10 times to investigate the porosity and mechanism changes. The implementation of this process can allow the improvement of the final efficiency, reduce costs and decrease the amount of hazardous powder.

6.3.3 Dual-Hopper System

One of the blown powder laser cladding advantages is that parts can be built on existing components which indicates that different powders can be used in one production. As a result, a dual hopper system was designed shown in Figure 6-4. A graded sample was clad with 316L stainless steel and IN625 shown in Figure 6-5 which had a strong metallic bond between different materials but this would need to be further studied through microstructure and mechanical test analysis.

Figure 6-4: Dual-Hopper System Designed, (a) two controller to controlling the screw rotor rate, (b) dual-hopped designed.

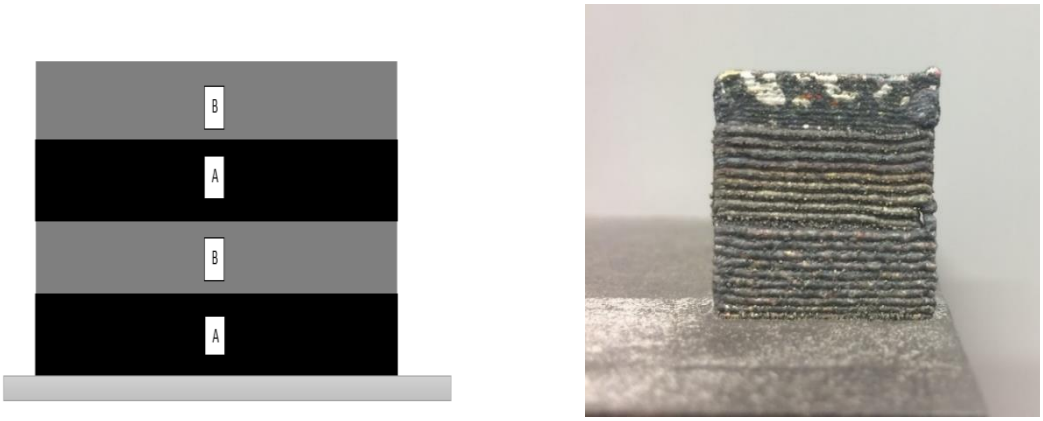

Figure 6-5: Graded structures design for Laser cladding with 316L SS and IN625.

Appendix 1: G-code for Structure A (Interlocking Hollow Cylinder)

```
DVAR $DATUM_X
DVAR $DATUM_Y
DVAR $DATUM_Z
DVAR $FEED
DVAR $LAYERHEIGHT
DVAR $LAYERSNUMBER
;### Set G54 Datums ###
$DATUM_X = 0
$DATUM_Y = 0
$DATUM_Z = 186
$LAYERHEIGHT = 1; step height IN MM
$LAYERSNUMBER = INT(30/$LAYERHEIGHT)
;### Set Feed ###
$FEED = 8; cladding speed
ENABLE X Y Z ;Turn On Servo Loop Control for the Axes
HOME Z
HOME X Y
G71 ;Metric
G76 ;Feed Speeds Units/Second
G90 ;Absolute
M52 ; CW Mode
M60 ; Beam On
M66 ; Ramp Up Laser
F$FEED ;Feed Speed mm/Second
G54 X$DATUM_X Y$DATUM_Y Z$DATUM_Z
G0 X110. Y130.085
G0 Z0.
M300 ;Gas 1 On
M302 ;Gas 2 On
M320 ;Powder On
REPEAT $LAYERSNUMBER
M100 ;Shutter Open
G90 G2 X125.072 Y138.618 I10. J-0.085
G2 X124.924 Y121.297 I-5.072 J-8.618
G2 X110. Y130.085 I-4.924 J8.703
M101 ;Close Shutter
G01 X130. Y120.016
M100 ;Shutter Open
G2 X115.016 Y111.331 I-10. J-0.016
G2 X114.988 Y128.653 I4.984 J8.669
G2 X130. Y120.016 I5.012 J-8.653
M101 ;Close Shutter
G01 X110. Y130.085
G91 G0 Z-$LAYERHEIGHT
```

```
ENDRPT
M301 ;Gas 1 Off
M303 ;Gas 2 Off
M321 ;Powder Off

M65 ;Simmer Laser
HOME Z
HOME X Y
DISABLE X Y Z ;Disable X and Y Axis Drives
M2
```

Appendix 2: G-code for Structure B (Edge Intersecting Hollow Cylinder)

```
DVAR $DATUM_X
DVAR $DATUM_Y
DVAR $DATUM_Z
DVAR $FEED
DVAR $LAYER
;### Set G54 Datums ###
$DATUM_X = 0
$DATUM_Y = 0
$DATUM_Z = 187
;### Set Feed ###
$FEED = 10
;### Set step height
$LAYER=0.4
ENABLE X Y Z ;Turn On Servo Loop Control for the Axes
HOME Z
HOME X Y
G71 ;Metric
G76 ;Feed Speeds Units/Second
G90 ;Absolute
M52 ; CW Mode
M60 ; Beam On
M66 ; Ramp Up Laser
M302 ;Gas 2 On
M320 ;Powder On
F$FEED ;Feed Speed mm/Second
$LAYER=$LAYER/-8
G54 X$DATUM_X Y$DATUM_Y Z$DATUM_Z
G0 X100. Y60.
G0 Z0.
M300 ;Gas 1 On
M302 ;Gas 2 On
M320 ;Powder On
M100 ;Shutter Open
RPT 40
G91
G2 X10. Y10. I10. J0. G1 Z$LAYER
G2 X10. Y-10. I0. J-10. G1 Z$LAYER
G3 X10. Y-10. I10. J0. G1 Z$LAYER
G3 X10. Y10. I0. J10. G1 Z$LAYER
G3 X-10. Y10. I-10. J0. G1 Z$LAYER
G3 X-10. Y-10. I0. J-10. G1 Z$LAYER
G2 X-10. Y-10. I-10. J0. G1 Z$LAYER
G2 X-10. Y10. I0. J10. G1 Z$LAYER
```

```
ENDRPT
G90
M301 ;Gas 1 Off
M303 ;Gas 2 Off
M321 ;Powder Off
M101 ;Close Shutter
M65 ;Simmer Laser
HOME Z
HOME X Y
DISABLE X Y Z ;Disable X and Y Axis Drives
M2
```

Appendix 3: G-code for Simple Wall

```
; WALLS WITH SPEED CHANGE
DVAR $DATUM_X
DVAR $DATUM_Y
DVAR $DATUM_Z
DVAR $FEED
DVAR $LAYERHEIGHT
DVAR $LAYERSNUMBER
;### Set G54 Datums ###
$DATUM_X = 100
$DATUM_Y = 100
$DATUM_Z = 186.25
$LAYERHEIGHT = 1.2; step height IN MM
$LAYERSNUMBER = INT(20/$LAYERHEIGHT)
;### Set Initial Feed ###
$FEED = 40
ENABLE X Y Z ;Turn On Servo Loop Control for the Axes
HOME Z
HOME X Y
G71 ;Metric
G76 ;Feed Speeds Units/Second
G90 ;Absolute
M52 ; CW Mode
M60 ; Beam On
M66 ; Ramp Up Laser
F$FEED ;Feed Speed mm/Second
G54 X$DATUM_X Y$DATUM_Y Z$DATUM_Z
G0 X0 Y0
G0 Z0
M300 ;Gas 1 On
M302 ;Gas 2 On
M320 ;Powder On
CALL WALL; CALL WALL 1
$FEED=$FEED-10;INCREASE FEED RATE FOR NEXT WALL
G91 G01 Y35;Y MOVE ACROSS IN INCREMENTAL COORDINATES FOR NEXT WALL
G90 G01 Z0;MOVE IN GLOBAL COORDINATES TO Z START POSITION FOR NEXT WALL
CALL WALL; CALL WALL 2
$FEED=$FEED-10
G91 G01 Y35
G90 G01 Z0
CALL WALL; CALL WALL 3
$FEED=$FEED-10
G91 G01 Y35
G90 G01 Z0
CALL WALL; CALL WALL 4
```

```
M101 ;Close Shutter
M301 ;Gas 1 Off
M303 ;Gas 2 Off
M321 ;Powder Off
M101 ;Close Shutter
M65 ;Simmer Laser
HOME Z
HOME X Y
DISABLE X Y Z ;Disable X and Y Axis Drives
M2

DFS WALL
G91; change to incremental coordinates
F$FEED ;Feed Speed mm/Second
REPEAT $LAYERSNUMBER
M100 ;Shutter Open
G01 X40
M101; Shutter closed
G0 X-40 Z-$LAYERHEIGHT
ENDRPT
ENDDFS
```

Appendix 4: G-code for Two track with 15^0 Intersecting Angle

```
;Two tracks with 15 degree angle
DVAR $DATUM_X
DVAR $DATUM_Y
DVAR $DATUM_Z
DVAR $FEED
DVAR $LAYERHEIGHT
;### Set G54 Datums ###
$DATUM_X = 125
$DATUM_Y = 160
$DATUM_Z = 50
;### ~~~ ###

$LAYERHEIGHT = 0.1; step height IN MM
;### Set Feed ###
$FEED = 8
;### ~~~ ###
;
ENABLE X Y Z ;Turn On Servo Loop Control for the Axes
HOME Z
HOME X Y
G71 ;Metric
G76 ;Feed Speeds Units/Second
G90 ;Absolute
M52 ; CW Mode
M60 ; Beam On
M66 ; Ramp Up Laser
F$FEED ;Feed Speed mm/Second
G54 X$DATUM_X Y$DATUM_Y Z$DATUM_Z
G0 X0 Y0
G0 Z0
M300 ;Gas 1 On
M302 ;Gas 2 On
M320 ;Powder On
G91
M100 ;Shutter Open
REPEAT 5
G01 X10
M101 ;Close Shutter
G90 X0.1704 Y1.2942
M100 ;Shutter Open
G90  X9.8296 Y-1.2942
M101 ;Close Shutter
G90  X0 Y0
G0 Z-$LAYERHEIGHT
ENDRPT
```

```
M101 ;Close Shutter
M301 ;Gas 1 Off
M303 ;Gas 2 Off
M321 ;Powder Off
M101 ;Close Shutter
M65 ;Simmer Laser
HOME Z
HOME X Y
DISABLE X Y Z ;Disable X and Y Axis Drives
M2
```

Appendix 5: G-code for Two track with 30^0 Intersecting Angle

```
;Two tracks with 30 degree angle
DVAR $DATUM_X
DVAR $DATUM_Y
DVAR $DATUM_Z
DVAR $FEED
DVAR $LAYERHEIGHT
;### Set G54 Datums ###
$DATUM_X = 125
$DATUM_Y = 160
$DATUM_Z = 50
;### ~~~ ###

$LAYERHEIGHT = 0.1; step height IN MM
;### Set Feed ###
$FEED = 8
;### ~~~ ###
;
ENABLE X Y Z ;Turn On Servo Loop Control for the Axes
HOME Z
HOME X Y
G71 ;Metric
G76 ;Feed Speeds Units/Second
G90 ;Absolute
M52 ; CW Mode
M60 ; Beam On
M66 ; Ramp Up Laser
F$FEED ;Feed Speed mm/Second
G54 X$DATUM_X Y$DATUM_Y Z$DATUM_Z
G0 X0 Y0
G0 Z0
M300 ;Gas 1 On
M302 ;Gas 2 On
M320 ;Powder On
G91
M100 ;Shutter Open
REPEAT 5
G01 X10
M101 ;Close Shutter
G90 X0.6693 Y2.499
M100 ;Shutter Open
G90  X9.3301 Y-2.499
M101 ;Close Shutter
G90  X0 Y0
G0 Z-$LAYERHEIGHT
ENDRPT
```

```
M101 ;Close Shutter
M301 ;Gas 1 Off
M303 ;Gas 2 Off
M321 ;Powder Off
M101 ;Close Shutter
M65 ;Simmer Laser
HOME Z
HOME X Y
DISABLE X Y Z ;Disable X and Y Axis Drives
M2
```

Appendix 6: G-code for Two track with 45^0 Intersecting Angle

```
;Two tracks with 45 degree angle
DVAR $DATUM_X
DVAR $DATUM_Y
DVAR $DATUM_Z
DVAR $FEED
DVAR $LAYERHEIGHT
;### Set G54 Datums ###
$DATUM_X = 125
$DATUM_Y = 160
$DATUM_Z = 50
;### ~~~ ###

$LAYERHEIGHT = 0.1; step height IN MM
;### Set Feed ###
$FEED = 8
;### ~~~ ###
;
ENABLE X Y Z ;Turn On Servo Loop Control for the Axes
HOME Z
HOME X Y
G71 ;Metric
G76 ;Feed Speeds Units/Second
G90 ;Absolute
M52 ; CW Mode
M60 ; Beam On
M66 ; Ramp Up Laser
F$FEED ;Feed Speed mm/Second
G54 X$DATUM_X Y$DATUM_Y Z$DATUM_Z
G0 X0 Y0
G0 Z0
M300 ;Gas 1 On
M302 ;Gas 2 On
M320 ;Powder On
G91
M100 ;Shutter Open
REPEAT 5
G01 X10
M101 ;Close Shutter
G90 X1.4645 Y3.5355
M100 ;Shutter Open
G90  X8.5355 Y-3.5355
M101 ;Close Shutter
G90  X0 Y0
G0 Z-$LAYERHEIGHT
ENDRPT
```

```
M101 ;Close Shutter
M301 ;Gas 1 Off
M303 ;Gas 2 Off
M321 ;Powder Off
M101 ;Close Shutter
M65 ;Simmer Laser
HOME Z
HOME X Y
DISABLE X Y Z ;Disable X and Y Axis Drives
M2
```

Appendix 7: Austenitic Stainless-Steel Grades and Process Parameters from Literature Review

Austenitic stainless-steel grades:

Austenitic Group	Common AISI Grades
Conventional Austenitics	301, 302, 303, 304, 305, 308, 309, 310, 316, 317
Stabilized Compositions	321, 347,348
Low-Carbon Grades	304L, 316L, 317L
High Nitrogen Grades	201, 202, 304N, 316N
High Alloyed Austenitics	317LM, 317LX, JS700, JS777, 904L

References

1. Ngo, T.D., et al., *Additive manufacturing (3D printing): A review of materials, methods, applications and challenges.* Composites Part B: Engineering, 2018. **143**: p. 172-196.
2. Thomas, D., *Costs, Benefits, and Adoption of Additive Manufacturing: A Supply Chain Perspective.* The International journal, advanced manufacturing technology, 2016. **85**(5-8): p. 1857-1876.
3. Prakash, K.S., T. Nancharaih, and V.V.S. Rao, *Additive Manufacturing Techniques in Manufacturing -An Overview.* Materials Today: Proceedings, 2018. **5**(2, Part 1): p. 3873-3882.
4. Singh, S., S. Ramakrishna, and R. Singh, *Material issues in additive manufacturing: A review.* Journal of Manufacturing Processes, 2017. **25**: p. 185-200.
5. Bourell, D., et al., *Materials for additive manufacturing.* CIRP Annals, 2017. **66**(2): p. 659-681.
6. Bandyopadhyay, A. and B. Heer, *Additive manufacturing of multi-material structures.* Materials Science and Engineering: R: Reports, 2018. **129**: p. 1-16.
7. Stratasys. *A New Mindset in Product Design- 3D PRINTING CAN HELP BRING BETTER PRODUCTS TO MARKET FASTER*. 2015; Available from: http://usglobalimages.stratasys.com/Main/Secure/White%20Papers/WP_FDM_NewMindset.pdf?v=635905246245235050.
8. Liverani, E., et al., *Characterization of Lattice Structures for Additive Manufacturing of Lightweight Mechanical Components*. 2017. V002T01A012.
9. Queheillalt, D.T. and H.N.G. Wadley, *Pyramidal lattice truss structures with hollow trusses.* Materials Science and Engineering: A, 2005. **397**(1): p. 132-137.
10. Attaran, M., *The rise of 3-D printing: The advantages of additive manufacturing over traditional manufacturing.* Business Horizons, 2017. **60**(5): p. 677-688.
11. Li, Q., I. Kucukkoc, and D.Z. Zhang, *Production planning in additive manufacturing and 3D printing.* Computers & Operations Research, 2017. **83**: p. 157-172.
12. Tofail, S.A.M., et al., *Additive manufacturing: scientific and technological challenges, market uptake and opportunities.* Materials Today, 2018. **21**(1): p. 22-37.
13. Eyers, D.R. and A.T. Potter, *Industrial Additive Manufacturing: A manufacturing systems perspective.* Computers in Industry, 2017. **92-93**: p. 208-218.
14. Zhai, Y., D.A. Lados, and J.L. LaGoy, *Additive Manufacturing: Making Imagination the Major Limitation.* JOM, 2014. **66**(5): p. 808-816.
15. Bak, D., *Rapid prototyping or rapid production? 3D printing processes move industry towards the latter.* Assembly Automation, 2003. **23**(4): p. 340-345.
16. Khajavi, S., *Improving Additive Manufacturing Enabled Operations – A Forward Looking Empirical Study*. 2018.
17. Abdulrahman, K.O., et al., *Laser Metal Deposition of Titanium Aluminide Composites: A Review.* Materials Today: Proceedings, 2018. **5**(9, Part 3): p. 19738-19746.
18. Khademzadeh, S., N. Parvin, and P. F. Bariani, *Production of NiTi alloy by direct metal deposition of mechanically alloyed powder mixtures*. Vol. 16. 2015. 2333-2338.
19. Powell, J., P. S. Henry, and W. M. Steen, *Laser cladding with preplaced powder: Analysis of thermal cycling and dilution effects*. Vol. 4. 1988. 141-149.
20. Bhavar, V., et al., *A review on powder bed fusion technology of metal additive manufacturing*. 2014.
21. Liu, Z.Y., et al., *Energy Consumption in Additive Manufacturing of Metal Parts.* Procedia Manufacturing, 2018. **26**: p. 834-845.
22. Gu, D., *Laser Additive Manufacturing (AM): Classification, Processing Philosophy, and Metallurgical Mechanisms*. 2015. p. 15-71.
23. Emmelmann, C., et al., *Laser Additive Manufacturing and Bionics: Redefining Lightweight Design.* Physics Procedia, 2011. **12**: p. 364-368.

24. Taheri, H., et al., *Powder-based additive manufacturing - a review of types of defects, generation mechanisms, detection, property evaluation and metrology*. Vol. 1. 2017. 172.
25. DebRoy, T., et al., *Additive manufacturing of metallic components – Process, structure and properties.* Progress in Materials Science, 2018. **92**: p. 112-224.
26. Adebiyi, D., P. Popoola, and S. Pityana, *Phase constituents and microhardness of laser alloyed Ti–6Al–4 V alloy*. Vol. 27. 2015. S29104.
27. Ma, M., et al., *Control of shape and performance for direct laser fabrication of precision large-scale metal parts with 316L Stainless Steel.* Optics & Laser Technology, 2013. **45**: p. 209-216.
28. Nowotny, S., et al., *COAXn: Modular System of Powder Nozzles for Laser Beam Build-Up Welding*. 2003.
29. Adesina, O., P. Popoola, and O. Fatoba, *Laser Surface Modification — A Focus on the Wear Degradation of Titanium Alloy*. 2016.
30. Clare, A., et al., *Laser cladding for railway repair and preventative maintenance*. Vol. 24. 2012.
31. Thompson, S., et al., *An Overview of Direct Laser Deposition for Additive Manufacturing; Part I: Transport Phenomena, Modeling and Diagnostics*. Vol. 8. 2015. 36-62.
32. Fayazfar, H., et al., *A critical review of powder-based additive manufacturing of ferrous alloys: Process parameters, microstructure and mechanical properties.* Materials & Design, 2018. **144**: p. 98-128.
33. Heiden, M.J., et al., *Evolution of 316L stainless steel feedstock due to laser powder bed fusion process.* Additive Manufacturing, 2019. **25**: p. 84-103.
34. Thomas-Seale, L.E.J., et al., *The barriers to the progression of additive manufacture: Perspectives from UK industry.* International Journal of Production Economics, 2018. **198**: p. 104-118.
35. Shamsaei, N., et al., *An overview of Direct Laser Deposition for additive manufacturing; Part II: Mechanical behavior, process parameter optimization and control.* Additive Manufacturing, 2015. **8**: p. 12-35.
36. Levy, G.N., R. Schindel, and J.P. Kruth, *RAPID MANUFACTURING AND RAPID TOOLING WITH LAYER MANUFACTURING (LM) TECHNOLOGIES, STATE OF THE ART AND FUTURE PERSPECTIVES.* CIRP Annals, 2003. **52**(2): p. 589-609.
37. Gu, D.D., et al., *Laser additive manufacturing of metallic components: materials, processes and mechanisms.* International Materials Reviews, 2012. **57**(3): p. 133-164.
38. Wang, Z., et al., *The microstructure and mechanical properties of deposited-IN718 by selective laser melting.* Journal of Alloys and Compounds, 2012. **513**: p. 518-523.
39. Pei, Y.T. and J.T.M. De Hosson, *Functionally graded materials produced by laser cladding.* Acta Materialia, 2000. **48**(10): p. 2617-2624.
40. Zhou, S., et al., *Analysis of crack behavior for Ni-based WC composite coatings by laser cladding and crack-free realization.* Applied Surface Science, 2008. **255**(5, Part 1): p. 1646-1653.
41. Wang, Q.Y., et al., *Microstructures, mechanical properties and corrosion resistance of Hastelloy C22 coating produced by laser cladding.* Journal of Alloys and Compounds, 2013. **553**: p. 253-258.
42. Fang, Q., et al., *5kW Near-diffraction-limited and 8kW High-brightness Monolithic Continuous Wave Fiber Lasers Directly Pumped by Laser Diodes*. Vol. PP. 2017. 1-1.
43. Picasso, M. and M. Rappaz, *Laser-Powder-Material Interactions in the Laser Cladding Process*. Vol. 04. 1994.
44. Zhong, M., et al., *Microstructural evolution in high power laser cladding of Stellite 6+WC layers.* Surface and Coatings Technology, 2002. **157**(2): p. 128-137.
45. Baitimerov, R., et al., *Influence of Powder Characteristics on Processability of AlSi12 Alloy Fabricated by Selective Laser Melting*. Vol. 11. 2018. 742.
46. Rombouts, M., et al., *Fundamentals of Selective Laser Melting of alloyed steel powders.* CIRP Annals, 2006. **55**(1): p. 187-192.

47. Lévesque, D., et al., *Inspection of additive manufactured parts using laser ultrasonics*. Vol. 1706. 2016. 130003.
48. Ng, G.K.L., et al., *Porosity formation and gas bubble retention in laser metal deposition.* Applied Physics A, 2009. **97**(3): p. 641.
49. Gong, H., et al., *Analysis of defect generation in Ti–6Al–4V parts made using powder bed fusion additive manufacturing processes.* Additive Manufacturing, 2014. **1-4**: p. 87-98.
50. Hanemann, T., et al., *Rapid Prototyping and Rapid Tooling Techniques for the Manufacturing of Silicon, Polymer, Metal and Ceramic Microdevices*. 2007. p. 801-869.
51. Joesbury, A.M., et al., *Weld-bonded stainless steel to carbon fibre-reinforced plastic joints.* Journal of Materials Processing Technology, 2018. **251**: p. 241-250.
52. Reddy, L., et al., *Process parameter optimisation of laser clad iron based alloy: Predictive models of deposition efficiency, porosity and dilution.* Surface and Coatings Technology, 2018. **349**: p. 198-207.
53. Wong, K.V. and A. Hernandez, *A Review of Additive Manufacturing.* ISRN Mechanical Engineering, 2012. **2012**: p. 10.
54. Gurr, M., et al., *Acrylic Nanocomposite Resins for Use in Stereolithography and Structural Light Modulation Based Rapid Prototyping and Rapid Manufacturing Technologies.* Advanced Functional Materials, 2008. **18**(16): p. 2390-2397.
55. D Gu, D., et al., *Laser additive manufacturing of metallic components: Materials, processes and mechanisms*. Vol. 57. 2012. 133-164.
56. Singh, R. and M. Chhabra, *Rapid casting solutions: a review.* Rapid Prototyping Journal, 2011. **17**(5): p. 328-350.
57. Seifi, M., et al., *Overview of Materials Qualification Needs for Metal Additive Manufacturing.* JOM, 2016. **68**(3): p. 747-764.
58. Ion, J.C., *Chapter 12 - Cladding*, in *Laser Processing of Engineering Materials*, J.C. Ion, Editor. 2005, Butterworth-Heinemann: Oxford. p. 296-326.
59. Spears, T.G. and S.A. Gold, *In-process sensing in selective laser melting (SLM) additive manufacturing.* Integrating Materials and Manufacturing Innovation, 2016. **5**(1): p. 16-40.
60. Tan, C., et al., *Selective laser melting of high-performance pure tungsten: parameter design, densification behavior and mechanical properties*. Vol. 19. 2018. 370-380.
61. Watkins, T.R., et al., *Residual stress determination of direct metal laser sintered (DMLS) inconel specimens and parts*. 2018: United States.
62. King, W.E., et al., *Laser powder bed fusion additive manufacturing of metals; physics, computational, and materials challenges.* Applied Physics Reviews, 2015. **2**(4): p. 041304.
63. Kruth, J.P., et al., *Binding Mechanisms in Selective Laser Sintering and Selective Laser Melting*. Vol. 11. 2005. 26-36.
64. Everton, S.K., et al., *Review of in-situ process monitoring and in-situ metrology for metal additive manufacturing.* Materials & Design, 2016. **95**: p. 431-445.
65. Bartolomeu, F., et al., *316L stainless steel mechanical and tribological behavior—A comparison between selective laser melting, hot pressing and conventional casting.* Additive Manufacturing, 2017. **16**.
66. Kumar, S. and S. Pityana, *Laser-Based Additive Manufacturing of Metals*. Vol. 227. 2011.
67. Vaezi, M., et al., *Multiple Material Additive Manufacturing – Part 1: A Review*. Vol. 8. 2013.
68. Ding, D., et al., *Wire-feed additive manufacturing of metal components: technologies, developments and future interests*. Vol. 81. 2015.
69. Martina, F. and S. W. Williams, *Wire+arc additive manufacturing vs. traditional machining from solid: a cost comparison*. 2015.
70. *Chapter 1 - Deposition Technologies: An Overview*, in *Handbook of Deposition Technologies for Films and Coatings (Third Edition)*, P.M. Martin, Editor. 2010, William Andrew Publishing: Boston. p. 1-31.

71. Fuchs, J., C. Schneider, and N. Enzinger, *Wire-based additive manufacturing using an electron beam as heat source.* Welding in the World, 2018. **62**(2): p. 267-275.
72. Ding, D., et al., *Adaptive path planning for wire-feed additive manufacturing using medial axis transformation.* Journal of Cleaner Production, 2016. **133**: p. 942-952.
73. Shi, J., et al., *Geometry characteristics modeling and process optimization in coaxial laser inside wire cladding.* Optics & Laser Technology, 2018. **101**: p. 341-348.
74. Naghiyan Fesharaki, M., et al., *Microstructure investigation of Inconel 625 coating obtained by laser cladding and TIG cladding methods.* Surface and Coatings Technology, 2018. **353**: p. 25-31.
75. Wen, P., et al., *Microstructure and mechanical properties of hot wire laser clad layers for repairing precipitation hardening martensitic stainless steel.* Optics & Laser Technology, 2015. **75**: p. 207-213.
76. Xu, X., et al., *Research on microstructures and properties of Inconel 625 coatings obtained by laser cladding with wire.* Journal of Alloys and Compounds, 2017. **715**: p. 362-373.
77. Chohan Jasgurpreet, S. and R. Singh, *Pre and post processing techniques to improve surface characteristics of FDM parts: a state of art review and future applications.* Rapid Prototyping Journal, 2017. **23**(3): p. 495-513.
78. Zhang, Z., et al., *Surface quality and forming characteristics of thin-wall aluminium alloy parts manufactured by laser assisted MIG arc additive manufacturing.* International Journal of Lightweight Materials and Manufacture, 2018. **1**(2): p. 89-95.
79. Kruth, J.P., M.C. Leu, and T. Nakagawa, *Progress in Additive Manufacturing and Rapid Prototyping.* CIRP Annals, 1998. **47**(2): p. 525-540.
80. Zavala-Arredondo, M., et al., *Laser diode area melting for high speed additive manufacturing of metallic components.* Materials & Design, 2017. **117**: p. 305-315.
81. Bidare, P., et al., *Fluid and particle dynamics in laser powder bed fusion.* Acta Materialia, 2018. **142**: p. 107-120.
82. Xiang, Z., et al., *Modeling of the thermal physical process and study on the reliability of linear energy density for selective laser melting.* Results in Physics, 2018. **9**: p. 939-946.
83. Chiumenti, M., et al., *Numerical simulation and experimental calibration of additive manufacturing by blown powder technology. Part I: thermal analysis.* Rapid Prototyping Journal, 2017. **23**(2): p. 448-463.
84. Arrizubieta, J.I., et al., *Evaluation of the relevance of melt pool dynamics in Laser Material Deposition process modeling.* International Journal of Heat and Mass Transfer, 2017. **115**: p. 80-91.
85. Gedda, H., et al., *Laser wire casting*. Vol. 46. 2003. 199-201.
86. Anisimov, S.I. and V.A. Khokhlov, *Instabilities in Laser-Matter Interaction*. 1995.
87. Saqib, S., R.J. Urbanic, and K. Aggarwal, *Analysis of Laser Cladding Bead Morphology for Developing Additive Manufacturing Travel Paths.* Procedia CIRP, 2014. **17**: p. 824-829.
88. Weerasinghe, V.M. and W.M. Steen, *LASER CLADDING WITH BLOWN POWDER*. Vol. 19. 1987. 581-585.
89. Lin, J. and W. M. Steen, *Design characteristics and development of a nozzle for coaxial laser cladding*. Vol. 10. 1998.
90. Hayhurst, P., et al., *Coaxial laser cladding nozzle for use with a high power diode laser*. 2002.
91. Lin, J. and W. M. Steen, *Design characteristics and development of a nozzle for coaxial laser cladding*. 1996. A27-A36.
92. Zhang, Y., G. Yu, and X. He, *Numerical study of thermal history in laser aided direct metal deposition process*. Vol. 55. 2012.
93. Arrizubieta, J.I., et al., *Instantaneous powder flux regulation system for Laser Metal Deposition.* Journal of Manufacturing Processes, 2017. **29**: p. 242-251.

94. Liu, S., Y. Zhang, and R. Kovacevic, *Numerical Simulation and Experimental Study of Powder Flow Distribution in High Power Direct Diode Laser Cladding Process.* Lasers in Manufacturing and Materials Processing, 2015. **2**(4): p. 199-218.
95. Liu, H., et al., *A Numerical Study on Metallic Powder Flow in Coaxial Laser Cladding*. Vol. 9. 2016. 2247-2256.
96. Fearon, E. and K. G. Watkins, *Optimisation of layer height control in direct laser deposition*. 2004. 1708.
97. Fearon, E., *Laser Free Form Fabrication Applied to the Manufacture of Metallic Components*. 2004.
98. G. Watkins, K., *Achieving the potential of direct fabrication with lasers*. 2001.
99. Lewis, G.K. and E. Schlienger, *Practical considerations and capabilities for laser assisted direct metal deposition.* Materials & Design, 2000. **21**(4): p. 417-423.
100. Sexton, L., et al., *Laser cladding of aerospace materials*. Vol. 122. 2002. 63-68.
101. Sun, S., et al., *Analysis of defects in laser cladding of high strength steel for aerospace Applications*. 2010. p. 1-7.
102. Frazier, W.E., *Metal Additive Manufacturing: A Review.* Journal of Materials Engineering and Performance, 2014. **23**(6): p. 1917-1928.
103. Nadal-Serrano, J.M., A. Nadal-Serrano, and M. Lopez-Vallejo, *Democratizing science with the aid of parametric design and additive manufacturing: Design and fabrication of a versatile and low-cost optical instrument for scattering measurement.* PLOS ONE, 2017. **12**(11): p. e0187219.
104. Krantz, D., et al., *On-demand spares fabrication during space missions using Laser Direct Metal Deposition*. Vol. 552. 2001.
105. Larimian, T. and T. Borkar, *Additive Manufacturing of In Situ Metal Matrix Composites*. 2019. p. 1-28.
106. Lander, M.L., et al., *High power calibration of commercial power meters using an NIST-traceable secondary standard.* Journal of Laser Applications, 1996. **8**(2): p. 103-107.
107. Majumdar, J.D. and I. Manna, *Introduction to LaserAssisted Fabrication of Materials*, in *Laser-Assisted Fabrication of Materials*, J.D. Majumdar and I. Manna, Editors. 2013, Springer Berlin Heidelberg: Berlin, Heidelberg. p. 1-67.
108. Rohde, M., C. Markert, and W. Pfleging, *Laser micro-welding of aluminum alloys: experimental studies and numerical modeling.* The International Journal of Advanced Manufacturing Technology, 2010. **50**(1): p. 207-215.
109. Lin, J. and W.M. Steen. *Powder flow and catchment during coaxial laser cladding*. in *Lasers and Optics in Manufacturing III*. 1997. SPIE.
110. Kumar, A., Y.-P. Lee, and D.-M. Chen, *Photodissociation of glycidyl azide polymer with a Nd:YAG laser at 1.064 µm.* Combustion and Flame, 2001. **126**(3): p. 1736-1745.
111. Arias-González, F., et al., *Fiber laser cladding of nickel-based alloy on cast iron.* Applied Surface Science, 2016. **374**: p. 197-205.
112. Gabler, F., *Fiber Laser Improves Cladding and Additive Manufacturing*, in *Industrial Laser Solutions* 2016.
113. Steen, W.M., *Laser material processing—an overview.* Journal of Optics A: Pure and Applied Optics, 2003. **5**(4): p. S3.
114. Kogelnik, H. and T. Li, *Laser Beams and Resonators.* Applied Optics, 1966. **5**(10): p. 1550-1567.
115. Tseng, W. and J.-N. Aoh, *Experimental Validation of a Laser Heat Source Model for Laser Melting and Laser Cladding Processes*. Vol. 8. 2014. 370-381.
116. Kim, J.W., et al., *High-power Er:YAG laser with quasi-top-hat output beam.* Optics Letters, 2012. **37**(9): p. 1463-1465.
117. Valentin, C., et al., *Top-hat beam output of a single-mode microstructured optical fiber: Impact of core index depression*. Vol. 21. 2013. 23250.
118. Mazumder, J., *LIA handbook of laser materials processing*. Vol. 13. 2001. 177-177.

119. Fatoba, O., et al., *Computational Dynamics of Anti-Corrosion Performance of Laser Alloyed Metallic Materials*. 2018.
120. Val, J.d., et al., *Laser cladding of Co-based superalloy coatings: Comparative study between Nd:YAG laser and fibre laser.* Surface & Coatings Technology - SURF COAT TECH, 2010. **204**: p. 1957-1961.
121. Haglund, R.F., *Laser Physics for Materials Scientists: A Primer*, in *Lasers in Materials Science*, M. Castillejo, P.M. Ossi, and L. Zhigilei, Editors. 2014, Springer International Publishing: Cham. p. 1-28.
122. M. Steen, W. and J. Mazumder, *Laser material processing: Fourth edition*. 2010. 1-558.
123. Collins, P., *A combinatorial approach to the development of composition-microstructure-property relationships in titanium alloys using directed laser deposition*. 2004.
124. Collins, P.C., et al., *Microstructural Control of Additively Manufactured Metallic Materials.* Annual Review of Materials Research, 2016. **46**: p. 63-91.
125. Patwa, R., et al., *Multi-beam laser additive manufacturing*. 2013. 376-380.
126. Buls, S., S. Clijsters, and J.-P. Kruth, *Homogenizing the melt pool intensity distribution in the SLM process through system identification and feedback control*. 2014.
127. Catchpole-Smith, S., et al., *Fractal scan strategies for selective laser melting of 'unweldable' nickel superalloys.* Additive Manufacturing, 2017. **15**: p. 113-122.
128. Anam, M.A., et al., *Effect of Scan Pattern on the Microstructural Evolution of Inconel 625 during Selective Laser Melting*. 2014.
129. Luo, Z. and Y. Zhao, *A survey of finite element analysis of temperature and thermal stress fields in powder bed fusion Additive Manufacturing*. Vol. 21. 2018. 318-332.
130. Carter, L.N., et al., *The influence of the laser scan strategy on grain structure and cracking behaviour in SLM powder-bed fabricated nickel superalloy.* Journal of Alloys and Compounds, 2014. **615**: p. 338-347.
131. Aursand, E., et al., *A multi-phase ferrofluid flow model with equation of state for thermomagnetic pumping and heat transfer.* Journal of Magnetism and Magnetic Materials, 2016. **402**: p. 8-19.
132. Gibson, I., D. Rosen, and B. Stucker, *Software Issues for Additive Manufacturing*, in *Additive Manufacturing Technologies: 3D Printing, Rapid Prototyping, and Direct Digital Manufacturing*, I. Gibson, D. Rosen, and B. Stucker, Editors. 2015, Springer New York: New York, NY. p. 351-374.
133. Wauthle, R., et al., *Revival of pure titanium for dynamically loaded porous implants using additive manufacturing*. Vol. 54. 2015.
134. Bartkowiak, K., et al., *New Developments of Laser Processing Aluminium Alloys via Additive Manufacturing Technique.* Physics Procedia, 2011. **12**: p. 393-401.
135. Buchbinder, D., et al., *High Power Selective Laser Melting (HP SLM) of Aluminum Parts.* Physics Procedia, 2011. **12**: p. 271-278.
136. Louvis, E., P. Fox, and C.J. Sutcliffe, *Selective laser melting of aluminium components.* Journal of Materials Processing Technology, 2011. **211**(2): p. 275-284.
137. Vora, H.D., et al., *Laser Assisted Additively Manufactured Transition Metal Coating on Aluminum.* JOM, 2016. **68**(7): p. 1819-1829.
138. Gorsse, S., et al., *Additive manufacturing of metals: a brief review of the characteristic microstructures and properties of steels, Ti-6Al-4V and high-entropy alloys*. Vol. 18. 2017. 584-610.
139. Santos-Ortiz, R., et al., *Effect of deposition energy on the microstructure and phase purity of pulsed laser deposited iron fluoride thin films*. Vol. 120. 2015. 863.
140. Dinda, G.P., L. Song, and J. Mazumder, *Fabrication of Ti-6Al-4V Scaffolds by Direct Metal Deposition.* Metallurgical and Materials Transactions A, 2008. **39**(12): p. 2914-2922.
141. Li, P., *On the Fatigue Performance of Additively Manufactured Ti-6Al-4V to Enable Rapid Qualification for Aerospace Applications*. 2016.

142. Krishna, B.V., S. Bose, and A. Bandyopadhyay, *Low stiffness porous Ti structures for load-bearing implants.* Acta Biomaterialia, 2007. **3**(6): p. 997-1006.
143. Liu, Y., G. Jiang, and G. He, *Enhancement of entangled porous titanium by BisGMA for load-bearing biomedical applications.* Materials Science and Engineering: C, 2016. **61**: p. 37-41.
144. Dobrzańska-Danikiewicz, A.D., T. Gaweł, and W. Wolany, *Ti6Al4V titanium alloy used as a modern biomimetic material*. Vol. 76. 2015. 150-156.
145. Brånemark, R., et al., *Bone response to laser-induced micro- and nano-size titanium surface features.* Nanomedicine: Nanotechnology, Biology and Medicine, 2011. **7**(2): p. 220-227.
146. Singh, R., A. Kurella, and N. Dahotre, *Laser Surface Modification of Ti—6Al—4V: Wear and Corrosion Characterization in Simulated Biofluid*. Vol. 21. 2006. 49-73.
147. Banerjee, R., S. Nag, and H.L. Fraser, *A novel combinatorial approach to the development of beta titanium alloys for orthopaedic implants.* Materials Science and Engineering: C, 2005. **25**(3): p. 282-289.
148. Olorunfemi, O., *Nickel Based Super Alloys For Gas turbine Applications*. 2015.
149. Morad, A., *Nickel Base Superalloys used for Aero Engine Turbine Blades*. 2014.
150. Matthews, M.J., et al., *Denudation of metal powder layers in laser powder bed fusion processes.* Acta Materialia, 2016. **114**: p. 33-42.
151. Fauchais, P., G. Montavon, and G. Bertrand, *From Powders to Thermally Sprayed Coatings.* Journal of Thermal Spray Technology, 2010. **19**(1): p. 56-80.
152. Hirsch, M., et al., *Assessing the capability of in-situ nondestructive analysis during layer based additive manufacture.* Additive Manufacturing, 2017. **13**: p. 135-142.
153. Fang, Y., C. Selomulya, and X. D. Chen, *On Measurement of Food Powder Reconstitution Properties*. Vol. 26. 2008. 3-14.
154. Slotwinski, J.A., *Additive manufacturing: Overview and NDE challenges.* AIP Conference Proceedings, 2014. **1581**(1): p. 1173-1177.
155. Spierings, A.B., et al., *Powder flowability characterisation methodology for powder-bed-based metal additive manufacturing.* Progress in Additive Manufacturing, 2016. **1**(1): p. 9-20.
156. Herzog, D., et al., *Additive manufacturing of metals.* Acta Materialia, 2016. **117**: p. 371-392.
157. Galati, M. and L. Iuliano, *A literature review of powder-based electron beam melting focusing on numerical simulations.* Additive Manufacturing, 2018. **19**: p. 1-20.
158. Boley, C., S. Khairallah, and A. Rubenchik, *Calculation of laser absorption by metal powders in additive manufacturing*. Vol. 54. 2015. 2477.
159. K. Tolochko, N., et al., *Absorptance of powder materials suitable for laser sintering*. Vol. 6. 2000. 155-161.
160. Gusarov, A.V. and I. Smurov, *Radiation transfer in metallic powder beds used in laser processing.* Journal of Quantitative Spectroscopy and Radiative Transfer, 2010. **111**(17): p. 2517-2527.
161. Kruth, J.-P., et al., *Lasers and Materials in Selective Laser Sintering*. Vol. 23. 2003.
162. Steen, W. and J. Mazumder, *Laser material processing: Fourth edition*. 2010. 1-558.
163. Science, K.I. *What is Contact Angle?* 2012; Available from: https://www.face-kyowa.co.jp/english/en_science/en_what_contact_angle.html.
164. Romano, V., et al., *Modeling of near infrared pulsed laser sintering of metallic powders*. 2003.
165. Swift, D.L., *The thermal conductivity of spherical metal powders including the effect of an oxide coating.* International Journal of Heat and Mass Transfer, 1966. **9**(10): p. 1061-1074.
166. Hadley, G.R., *Thermal conductivity of packed metal powders.* International Journal of Heat and Mass Transfer, 1986. **29**(6): p. 909-920.
167. Lindgren, L.-E., et al., *Simulation of additive manufacturing using coupled constitutive and microstructure models.* Additive Manufacturing, 2016. **12**: p. 144-158.
168. Hofmeister, W. and M. Griffith, *Solidification in direct metal deposition by LENS processing*. Vol. 53. 2001. 30-34.

169. Wood, N. and D. Hoelzle, *On the feasibility of a temperature state observer for powder bed fusion additive manufacturing*. 2018. 321-328.
170. Haeri, S., *Optimisation of blade type spreaders for powder bed preparation in Additive Manufacturing using DEM simulations.* Powder Technology, 2017. **321**: p. 94-104.
171. Ghaffar, S.H., J. Corker, and M. Fan, *Additive manufacturing technology and its implementation in construction as an eco-innovative solution.* Automation in Construction, 2018. **93**: p. 1-11.
172. Jinoop, A.N., C.P. Paul, and K.S. Bindra, *Laser assisted direct energy deposition of Hastelloy-X.* Optics & Laser Technology, 2019. **109**: p. 14-19.
173. Attallah, M., et al., *Additive manufacturing of Ni-based superalloys: The outstanding issues*. Vol. 41. 2016. 758-764.
174. Bauereiß, A., T. Scharowsky, and C. Körner, *Defect generation and propagation mechanism during additive manufacturing by selective beam melting.* Journal of Materials Processing Technology, 2014. **214**(11): p. 2522-2528.
175. Zhong, C., et al., *Experimental study of effects of main process parameters on porosity, track geometry, deposition rate, and powder efficiency for high deposition rate laser metal deposition*. Vol. 27. 2015.
176. Liang, Y.-J., D. Liu, and H.-M. Wang, *Microstructure and mechanical behavior of commercial purity Ti/Ti–6Al–2Zr–1Mo–1V structurally graded material fabricated by laser additive manufacturing.* Scripta Materialia, 2014. **74**: p. 80-83.
177. Marya, M., et al., *Microstructural Development and Technical Challenges in Laser Additive Manufacturing: Case Study with a 316L Industrial Part.* Metallurgical and Materials Transactions B, 2015. **46**(4): p. 1654-1665.
178. Salsi, E., M. Chiumenti, and M. Cervera, *Modeling of Microstructure Evolution of Ti6Al4V for Additive Manufacturing*. Vol. 8. 2018.
179. Carroll, B.E., T.A. Palmer, and A.M. Beese, *Anisotropic tensile behavior of Ti–6Al–4V components fabricated with directed energy deposition additive manufacturing.* Acta Materialia, 2015. **87**: p. 309-320.
180. Smith, C.J., et al., *Dimensional accuracy of Electron Beam Melting (EBM) additive manufacture with regard to weight optimized truss structures.* Journal of Materials Processing Technology, 2016. **229**: p. 128-138.
181. Moroni, G., W.P. Syam, and S. Petrò, *Towards Early Estimation of Part Accuracy in Additive Manufacturing.* Procedia CIRP, 2014. **21**: p. 300-305.
182. Lee, Y. and D. Farson, *Surface tension-powered build dimension control in laser additive manufacturing process*. Vol. 85. 2015.
183. Gockel, J. and J. Beuth, *Understanding Ti-6Al-4V microstructure control in additive manufacturing via process maps*. 2013. 666-674.
184. Shifeng, W., et al., *Effect of molten pool boundaries on the mechanical properties of selective laser melting parts.* Journal of Materials Processing Technology, 2014. **214**(11): p. 2660-2667.
185. Scharowsky, T., et al., *Observation and numerical simulation of melt pool dynamic and beam powder interaction during selective electron beam melting*. 2012.
186. Malcolm Benson, J. and E. Snyders, *The need for powder characterisation in the additive manufacturing industry and the establishment of a national facility*. Vol. 26. 2015. 104.
187. Stencel, J., et al., *Removal of Ceramic Defects From a Superalloy Powder Using Triboelectric Processing*. 2000.
188. Moylan, S., et al., *Infrared Thermography for Laser-Based Powder Bed Fusion Additive Manufacturing Processes*. Vol. 1581. 2014.
189. Abd-Elghany, K. and D. Bourell, *Property evaluation of 304L stainless steel fabricated by selective laser melting*. Vol. 18. 2012.
190. Ataollahi Oshkour, A., et al., *Mechanical and physical behavior of newly developed functionally graded materials and composites of stainless steel 316L with calcium silicate and*

hydroxyapatite. Journal of the Mechanical Behavior of Biomedical Materials, 2015. **49**: p. 321-331.
191. Prajapati, A., et al., *CHARACTERIZATION OF STAINLESS STEEL 316L COATED BY THERMAL SPRAY COATING*. Vol. Volume2. 2016.
192. Hinojos, A., et al., *Joining of Inconel 718 and 316 Stainless Steel using electron beam melting additive manufacturing technology*. Vol. 94. 2016.
193. Thoma, D.J., G.K. Lewis, and R.B. Nemec, *Solidification behavior during directed light fabrication*. 1995: United States. p. 7.
194. Zhang, Y., et al., *Effect of Cooling Rate on the Microstructure of Laser-Remelted INCONEL 718 Coating*. Vol. 44. 2013.
195. Wu, D., et al., *Laser Rapid Manufacturing of Stainless Steel 316L/Inconel718 Functionally Graded Materials: Microstructure Evolution and Mechanical Properties*. Vol. 2010. 2010.
196. Juric, D. and G. Tryggvason, *A Front-Tracking Method for Dendritic Solidification.* Journal of Computational Physics, 1996. **123**(1): p. 127-148.
197. Ocelík, V., I. Furár, and J.T.M. De Hosson, *Microstructure and properties of laser clad coatings studied by orientation imaging microscopy.* Acta Materialia, 2010. **58**(20): p. 6763-6772.
198. El Cheikh, H., et al., *Direct Laser Fabrication process with coaxial powder projection of 316L steel. Geometrical characteristics and microstructure characterization of wall structures.* Optics and Lasers in Engineering, 2012. **50**(12): p. 1779-1784.
199. Amine, T., J. Newkirk, and F. Liou, *An investigation of the effect of direct metal deposition parameters on the characteristics of the deposited layers*. Vol. 3. 2014. 21–34.
200. Cullum, R.D., *Handbook of Engineering Design*. 2013: Elsevier
201. Liu, P.S. and G.F. Chen, *Chapter Two - Making Porous Metals*, in *Porous Materials*, P.S. Liu and G.F. Chen, Editors. 2014, Butterworth-Heinemann: Boston. p. 21-112.
202. Saluja, R. and K. Moeed, *The emphasis of phase transformations and alloying constituents on hot cracking susceptibility of type 304L and 316L stainless steel welds*. Vol. 4. 2012. 2206-2212.
203. Saied, M., *Experimental and numerical modeling of the dissolution of delta ferrite in the Fe-Cr-Ni system : application to the austenitic stainless steels*. 2016.
204. Mas, F., *Solidification and phase transformations in a dissimilar steel weld 18MND5/309L/308L : evolution of microstructure and mechanical properties*. 2014.
205. Junwei, F., et al., *Effect of cooling rate on solidification microstructures in AISI 304 stainless steel*. Vol. 24. 2008. 941-944.
206. El Nayal, G. and J. Beech, *Relationship between composition, impurity content, cooling rate, and solidification in austenitic stainless steels*. Vol. 2. 1986. 603-610.
207. Junwei, F., et al., *Microstructure evolution in AISI 304 stainless steel during near rapid directional solidification*. Vol. 25. 2009. 1013-1016.
208. Tang, L. and R. G. Landers, *Layer-to-Layer Height Control for Laser Metal Deposition Process*. Vol. 133. 2011. 021009.
209. Flynn, J.M., et al., *Hybrid additive and subtractive machine tools – Research and industrial developments.* International Journal of Machine Tools and Manufacture, 2016. **101**: p. 79-101.
210. Tabernero, I., et al., *Geometric Modelling of Added Layers by Coaxial Laser Cladding.* Physics Procedia, 2012. **39**: p. 913-920.
211. Mazumder, J., J. Choi, and A. Schifferer, *Direct materials deposition: Designed macro and microstructure*. Vol. 3. 1999.
212. Murr, L.E. and W.L. Johnson, *3D metal droplet printing development and advanced materials additive manufacturing.* Journal of Materials Research and Technology, 2017. **6**(1): p. 77-89.
213. Mazumder, J., et al., *Closed loop direct metal deposition: art to part.* Optics and Lasers in Engineering, 2000. **34**(4): p. 397-414.
214. Goodarzi, D.M., J. Pekkarinen, and A. Salminen, *Analysis of laser cladding process parameter influence on the clad bead geometry.* Welding in the World, 2017. **61**(5): p. 883-891.

215. Gedda, H., J. Powell, and A. Kaplan, *A process efficiency comparison of Nd:YAG and CO2 laser cladding.* Welding in the World, Le Soudage Dans Le Monde, 2002. **46**: p. 75-86.
216. Kuznetsov, A., et al., *Annular Laser Beam Cladding Process Feasibility Study.* Physics Procedia, 2016. **83**: p. 647-656.
217. Parekh, R., R.K. Buddu, and R.I. Patel, *Multiphysics Simulation of Laser Cladding Process to Study the Effect of Process Parameters on Clad Geometry.* Procedia Technology, 2016. **23**: p. 529-536.
218. Ibarra-Medina, J. and A.J. Pinkerton, *A CFD model of the laser, coaxial powder stream and substrate interaction in laser cladding.* Physics Procedia, 2010. **5**: p. 337-346.
219. Pinkerton, A., *Advances in the modeling of laser direct metal deposition.* Journal of Laser Applications, 2015. **27**: p. S15001.
220. Dadbakhsh, S., L. Hao, and N. Sewell, *Effect of selective laser melting layout on the quality of stainless steel parts.* Rapid Prototyping Journal, 2012. **18**: p. 241-249.
221. Abouda, E., et al., *Effect of Laser Cladding Parameters on the Microstructure and Properties of High Chromium Hardfacing Alloys.* Physics Procedia, 2016. **83**: p. 684-696.
222. Song, B., T. Hussain, and K.T. Voisey, *Laser Cladding of Ni50Cr: A Parametric and Dilution Study.* Physics Procedia, 2016. **83**: p. 706-715.
223. Sun, R.L., et al., *Laser cladding of Ti-6Al-4V alloy with TiC and TiC+NiCrBSi powders*. Vol. 135. 2001. 307-312.
224. Mazumder, J., *1 - Laser-aided direct metal deposition of metals and alloys A2 - Brandt, Milan*, in *Laser Additive Manufacturing*. 2017, Woodhead Publishing. p. 21-53.
225. Flood, A. and F. Liou, *Modeling and Simulation of Metal AM*. 2018.
226. Gunenthiram, V., et al., *Analysis of laser–melt pool–powder bed interaction during the selective laser melting of a stainless steel*. Vol. 29. 2017. 022303.
227. Liou, F., et al., *Modeling and Simulation of a Laser Deposition Process*. 2007. 13.
228. Iždinská, Z., A. Nasher, and K. Iždinský, *STUDY OF THE STRUCTURE AND MECHANICAL PROPERTIES OF NICRBSI COATINGS PREPARED BY LASER BEAM CLADDING*. Vol. 17. 2010.
229. Sun, S., et al., *Microstructure and Mechanical Properties of Laser Cladding repair of AISI 4340 Steel*. Vol. 6. 2012.
230. Sun, S.D., et al., *Mechanical Properties of Laser Cladding Repair of Aermet 100 High Strength Low Alloy Steel*. 2013.
231. Liu, S. and R. Kovacevic, *Statistical analysis and optimization of processing parameters in high-power direct diode laser cladding*. Vol. 74. 2014. 867-878.
232. Lawrence, J., et al., *Contributor contact details*, in *Advances in Laser Materials Processing*, J. Lawrence, et al., Editors. 2010, Woodhead Publishing. p. xiii-xvii.
233. Ziółkowski, G., et al., *Application of X-ray CT method for discontinuity and porosity detection in 316L stainless steel parts produced with SLM technology.* Archives of Civil and Mechanical Engineering, 2014. **14**(4): p. 608-614.
234. Facchini, L., et al., *Metastable Austenite in 17–4 Precipitation-Hardening Stainless Steel Produced by Selective Laser Melting.* Advanced Engineering Materials, 2010. **12**(3): p. 184-188.
235. Burkert, T. and A. Fischer. *The Effects of Heat Balance on the Void Formation within Marage 300 Processed by Selective Laser Melting*. 2015.
236. Islam, M., et al., *Temperature Profile and Imaging Analysis of Laser Additive Manufacturing of Stainless Steel.* Physics Procedia, 2013. **41**: p. 835-842.
237. Krakhmalev, P., et al., *In situ heat treatment in selective laser melted martensitic AISI 420 stainless steels.* Materials & Design, 2015. **87**: p. 380-385.
238. Cormier, D., O. Harrysson, and H. West, *Characterization of H13 Steel Produced via Electron Beam Melting.* Rapid Prototyping Journal - RAPID PROTOTYPING J, 2004. **10**: p. 35-41.
239. Yadollahi, A., et al., *Effects of process time interval and heat treatment on the mechanical and microstructural properties of direct laser deposited 316L stainless steel.* Materials Science and Engineering: A, 2015. **644**: p. 171-183.

240. E.Abouda, M.D., O. Aubry, T.N. Tarfa, I. Demirci. *Effect of Laser Cladding Parameters on the Microstructures and Properties of High Chromium Hardfacing Alloys*. in *9th International Coference on Photonic Technologies - LANE2016*. 2016. Physics Procedia
241. *Stainless Steel - Grade 316L - Properties, Fabrication and Applications (UNS S31603)*, in *AZO Materials*. 2013.
242. Weerasinghe, V.M., W.M. Steen, and D.R.F. West, *Laser Deposited Austenitic Stainless Steel Clad Layers.* Surface Engineering, 1987. **3**(2): p. 147-153.
243. Gao, J., et al., *Numerical simulation and experimental investigation on three-dimensional modelling of single-track geometry and temperature evolution by laser cladding.* Optics & Laser Technology, 2020. **129**: p. 106287.
244. Flemings, M.C., *Solidification processing.* Metallurgical Transactions, 1974. **5**(10): p. 2121-2134.
245. Choudhary, S.K. and S. Ganguly, *Morphology and Segregation in Continuously Cast High Carbon Steel Billets.* Isij International - ISIJ INT, 2007. **47**: p. 1759-1766.
246. Krauss, G., *Solidification, segregation, and banding in carbon and alloy steels.* Metallurgical and Materials Transactions B, 2003. **34**(6): p. 781-792.
247. DuPont, J.N., *Fundamentals of Weld Solidification*, in *Welding Fundamentals and Processes*. 2011, ASM International. p. 96-114.
248. Trivedi, R., et al., *In situ observations of weld pool solidification using transparent metal-analog systems.* Journal of Applied Physics, 2003. **93**: p. 4885-4895.
249. David, S.A., S.S. Babu, and J.M. Vitek, *Welding: Solidification and microstructure.* JOM, 2003. **55**(6): p. 14-20.
250. Segerstark, A., J. Andersson, and L.-E. Svensson, *Investigation of laser metal deposited Alloy 718 onto an EN 1.4401 stainless steel substrate.* Optics and Laser Technology, 2017. **97**(Supplement C): p. 144-153.
251. Fearon, E., *Laser Free Form Fabrication Applied to the Manufacture of Metallic Components, PhD Thesis*. 2002, University of Liverpool: Liverpool.
252. Fearon, E. and K. Watkins, *Optimization of layer height control in direct laser deposition.* 23rd International Congress on Application of Laser & Electro-Optics (ICALEO 2004) Paper, 2004.
253. Lu, Y., et al., *Microstructure and Element Distribution during Partial Remelting of an Al4Cu-Mg alloy.* Journal of Materials Engineering and Performance - J MATER ENG PERFORM, 2008. **17**: p. 25-29.
254. Kraft, T. and Y.A. Chang, *Discussion of "Effect of dendrite arm coarsening on microsegregation".* Metallurgical and Materials Transactions A, 1998. **29**(9): p. 2447-2449.
255. Flemings, M., *Coarsening in Solidification Processing.* Materials Transactions - MATER TRANS, 2005. **46**: p. 895-900.
256. Long, M., L. Zhang, and F. Lu, *A Simple Model to Calculate Dendrite Growth Rate during Steel Continuous Casting Process.* ISIJ International, 2010. **50**: p. 1792-1796.
257. *CES Edupack Software*. 2014, Granta Designs Ltd: Cambridge.
258. Quested, P.N. and M. McLean, *Solidification morphologies in directionally solidified superalloys.* Materials Science and Engineering, 1984. **65**(1): p. 171-180.
259. Lee, J., et al., *Microstructure evolution in directionally solidified Fe–18Cr stainless steels.* Materials Science and Engineering: A, 2005. **413-414**: p. 306-311.
260. Majumdar, J.D., et al., *Microstructure characterisation and process optimisation of laser assisted rapid fabrication of 316L stainless steel.* Applied Surface Science, 2005. **247**: p. 320-327.
261. Armstrong, R.W., *The (cleavage) strength of pre-cracked polycrystals.* Engineering Fracture Mechanics, 1987. **28**(5): p. 529-538.
262. De Lima, M.S.F. and S. Sankaré, *Microstructure and mechanical behavior of laser additive manufactured AISI 316 stainless steel stringers.* Materials & Design, 2014. **55**: p. 526-532.

263. Liu, S. and Y.C. Shin, *Additive manufacturing of Ti6Al4V alloy: A review.* Materials & Design, 2019. **164**: p. 107552.
264. Yu, J., M. Rombouts, and G. Maes, *Cracking behavior and mechanical properties of austenitic stainless steel parts produced by laser metal deposition.* Materials & Design, 2013. **45**: p. 228-235.
265. Syed, W.U.H., A.J. Pinkerton, and L. Li, *A comparative study of wire feeding and powder feeding in direct diode laser deposition for rapid prototyping.* Applied Surface Science, 2005. **247**(1): p. 268-276.
266. Li, C., et al., *Influence of overlapping ratio on hardness and residual stress distributions in multi-track laser surface melting roller steel.* Optics and Lasers in Engineering, 2010. **48**(12): p. 1224-1230.
267. Lin, J., *A simple model of powder catchment in coaxial laser cladding*, in *Optics and Laser Technology*. 1999, Elsevier Ltd. p. 233-238.
268. Gedda, H., et al., *Energy redistribution during CO2 laser cladding.* Journal of Laser Applications, 2002. **14**.
269. Shaikh, A.S., *Development of a γ' Precipitation Hardening Ni-Base Superalloy for Additive Manufacturing*. 2018.
270. Rombouts, M., et al., *Laser metal deposition of Inconel 625: Microstructure and mechanical properties*. Vol. 24. 2012.
271. Qin, L., et al., *The microstructure and mechanical properties of deposited-IN625 by laser additive manufacturing*. Vol. 23. 2017. 00-00.
272. Leo Hulten, P.J., *Investigation and Evaluation of Metal Powder Characterization Techniques*, in *SCHOOL OF INDUSTRIAL ENGINEERING AND MANAGEMENT*. 2018, KTH ROYAL INSTITUTE OF TECHNOLOGY.
273. Amato, K.N., et al., *Microstructures and mechanical behavior of Inconel 718 fabricated by selective laser melting.* Acta Materialia, 2012. **60**(5): p. 2229-2239.
274. Ma, M., et al., *Layer thickness dependence of performance in high-power selective laser melting of 1Cr18Ni9Ti stainless steel.* Journal of Materials Processing Technology, 2015. **215**: p. 142-150.